2014

Nano-derived sensors for high-temperature sensing of H2, SO2 and H2S

Engin Ciftyurek

Recommended Citation
Ciftyurek, Engin, "Nano-derived sensors for high-temperature sensing of H2, SO2 and H2S" (2014). *Graduate Theses, Dissertations, and Problem Reports*. 7305.
https://researchrepository.wvu.edu/etd/7305

NANO-DERIVED SENSORS FOR HIGH-TEMPERATURE SENSING OF H_2, SO_2 and H_2S

Engin Çiftyürek

A dissertation submitted to the
Statler College of Engineering
at West Virginia University
in partial fulfillment of the requirements
for the degree of

Doctor of Philosophy
In
Mechanical Engineering

Edward M. Sabolsky, Ph.D., Chair
Konstantinos Sierros, Ph.D.
Charter Stinespring, Ph.D.
Xueyan Song, Ph.D.
Nianqiang Wu, Ph.D.

Department of Mechanical Engineering
Morgantown, West Virginia
2014

Keywords: Sulfur and Hydrogen Sensors, High temperature, Chemiresistive, Electrode, Platinum

ProQuest LLC.
789 East Eisenhower Parkway
P.O. Box 1346
Ann Arbor, MI 48106 - 1346

Abstract

Nano-Derived Sensors for High-Temperature Sensing of H_2, SO_2 and H_2S

Engin Çiftyürek

The emission of sulfur compounds from coal-fired power plants remains a significant concern for air quality. This environmental challenge must be overcome by controlling the emission of sulfur dioxide (SO_2) and hydrogen sulfide (H_2S) throughout the entire coal combustion process. One of the processes which could specifically benefit from robust, low cost, and high temperature compatible gas sensors is the coal gasification process which converts coal and/or biomass into syngas. Hydrogen (H_2), carbon monoxide (CO) and sulfur compounds make up 33%, 43% and 2% of syngas, respectively. Therefore, development of a high temperature (>500°C) chemical sensor for in-situ monitoring H_2, H_2S and SO_2 levels during coal gasification is strongly desired. The selective detection of SO_2/H_2S in the presence of H_2, is a formidable task for a sensor designer. In order to ensure effective operation of these chemical sensors, they must inexpensively function within the gasifier's harsh temperature and chemical environment. Currently available sensing approaches, which are based on gas chromatography, electrochemistry, and IR-spectroscopy, do not satisfy the required cost and performance targets.

There is also a substantial necessity for microsensors that can be applied inexpensively, have quick response time and low power consumption for sustained operation at high temperature. In order to develop a high temperature compatible microsensor, this work will discourse issues related to sensor stability, selectivity, and miniaturization. It has been shown that the integration of nanomaterials as the sensing material within resistive-type chemical sensor platforms increase sensitivity. Unfortunately, nanomaterials are not stable at high temperatures due to sintering and coarsening processes that are driven by their high surface to volume ratio. Therefore, new hydrogen and sulfur selective nanomaterial systems with potentially highly selective and stable properties in the proposed harsh environment were investigated. Different tungstates and molybdates (WO_3, MoO_3, $MgMoO_4$, $NiMoO_4$, $NiWO_4$, Sr_2MgWO_6 (SMW), Sr_2MgMoO_6 (SMM), $SrMoO_4$, and $SrWO_4$) were investigated at the micro- and nano-scale, due to their well-known properties as the reversible absorbents of sulfur compounds. Different morphologies of aforementioned compounds as well as microstructural alterations were also the subject of the investigation. The fabrication of the microsensors consisted of the deposition of the selective nanomaterial systems over metal based interconnects on an inert substrate. This work utilized the chemi-resistive (resistive-type) microsensor architecture where the chemically and structurally stable, high temperature compatible electrodes were sputtered onto a ceramic substrate. The nanomaterial sensing systems were deposited over the electrodes using a lost mold method patterned by conventional optical lithography.

Development of metal based high temperature compatible electrodes was crucial to the development of the high temperature sensor due to the instability of typically used noble metal (platinum) based electrode material over ceramic substrates. Therefore, the thermal stability limitations of platinum films with various adhesion layers (titanium (Ti), tantalum (Ta), zirconium (Zr), and hafnium (Hf)) were characterized at 800 and 1200°C. Platinum (Pt)-zirconium (Zr)-hafnium (Hf) were investigated. The high-temperature stable composite thin film architecture was developed by sequential sputter deposition of Hf, Zr and Pt. In addition to this multilayer architecture, further investigation was carried out by using an alternative DC sputtering deposition process, which led to the fabrication of a functionally-gradient platinum and zirconium composite microstructure with very promising high temperature properties. The final process investigated reduced labor, time and material consumption compared to methods for forming multilayer architectures previously discussed in literature.

In addition to electrical resistivity characterization of the different thin film electrode architectures, the chemical composition, and nano- and micro-structure of the developed nanomaterial films, as well as sensing mechanism, were characterized by means of scanning electron microscopy (SEM), energy dispersive X-ray spectroscopy (EDS), X-ray and ultraviolet photoelectron spectroscopies (XPS and UPS), atomic absorption spectroscopy (AAS), X-ray diffraction (XRD), Raman spectroscopy, temperature programmed reduction (TPR) and transmission electron microscopy (TEM). The macro-configurations of the sensors were tested and analyzed for sensitivity and cross-sensitivity, response time and recovery time, as well as long term stability. The microsensor configuration with optimized nanomaterial system was tested and compared to a millimeter-size sensor platform in terms of sensitivity and accuracy. Electrochemical relaxation (ECR) technique was also utilized to quantify the

surface diffusion kinetics of SO_2 over the chosen sensor material surface. The outcomes of this research will contribute to the economical application of sensor arrays for simultaneous sensing of H_2, H_2S, and SO_2.

Dedication

This dissertation is dedicated to my mother, father, brother and my late grandmother and grandfather…

Acknowledgement

I am most grateful to my advisor/mentor Dr. Edward M. Sabolsky for his time, enthusiasm, encouragement, and vast expertise as well as his patience throughout my Ph.D. research. I would also like to thank his wife Katarzyna Sabolsky, for her guidance and support. I would like thank to my friends and colleagues Christina, Tim, Josh, Phil, Sheldon, Patrick, Fanke. Special thanks goes to Mr. Charles Coleman for his willing help and encouragement. I would also like to thank my committee for their help and understanding. Finally I would like to thank to my family for their constant support during my doctoral studies.

Table of Contents

List of Figures

List of Tables

List of Symbols and Abbreviations

δ	Oxygen deficiency
E_G	Energy Gap
k	Boltzmann Constant
E_F	Fermi Level
L_D	Debye Length
ε	Dielectric Constant
ε_0	Permittivity of Free Space
T	Temperature
e^-	Electron Charge
Φ	Work function
n_d	Carrier Concentration
d	Grain Size
L	Thickness of Sensing Layer
ppm	Parts Per Million
ppb	Parts Per Billion
k	Boltzmann Constant
MOS	Metal Oxide Semiconductor
IDEs	Interdigitated Electrodes

EDS	Energy Dispersive X-ray Spectroscopy
PVD	Physical Vapor Deposition
CVD	Chemical Vapor Deposition
SEM	Scanning Electron Microscope
SMM	Strontium Magnesium Molybdenum Oxide
SMW	Strontium Magnesium Tungsten Oxide
TEM	Transmission Electron Microscope
XRD	X-ray Diffraction
DMM	Digital Multimeter
XPS	X-ray Photoelectron Spectroscopy
AES	Auger Electron Spectroscopy
W_{DL}	Depletion Layer
ECR	Electrochemical Relaxation
Uv-Vis	Ultraviolet–Visible Light Spectroscopy
UPS	Ultraviolet Photoelectron Spectroscopy
FT-IR	Fourier Transformed Infrared Spectroscopy
TCE	Coefficient of thermal expansion
TPR	Temperature Programmed Reduction
XANES	X-ray Absorption Near Edge Structure

Chapter 1: Introduction-Statement of Problem

1.1 Statement of Problem

Industrialization comes with advantages and disadvantages, as well as, a series of significant issues related to sustained technological development and its effects on the environment and human health. Coal is a cheap and abundant energy source compared to oil and natural gas; therefore, it is predicted that the coal consumption will increase 2.5% per year between 2003 and 2030 [1]. Although its abundance and relative low cost, coal brings palpable environmental challenges throughout its energy life-cycle (from mining and energy conversion). Coal as an energy source results in more CO_2 emission compared to oil and natural gas; in addition, it contains critical pollutants such as SO_2, H_2S, PH_3 and NO_x. The emissions of SO_2/H_2S from coal-fired power plants remain a significant concern for air quality, since these gasses are major contributors to green-house effects.

Monitoring the level of air pollutants has become a significant challenge for scientists and engineers especially after 1970s due to extensive usage of coal among the developing and underdeveloped countries [1, 2]. Assertive environmental challenges must be overcome by controlling the emission of sulfur compounds (SO_2/H_2S) through the entire coal process. In order to overcome this obstacle, it is necessary to develop reliable and robust chemical sensors that can fulfil the requirements of harsh environmental conditions that coal is processed. The coal gasification process, an advanced clean-coal conversion process currently be researched, could critically benefit from a reliable SO_2 sensor, as well as, an advanced H_2 sensor which may be incorporated within the gasification reactor. The gasification process converts coal directly to a syngas at elevated temperature (>1000°C). This process has shown to be more effective than conventional combustion of the coal.

State-of-the-art chemical sensor technology is restricted to devices that operate only at temperatures lower than <500°C due to their compositions, processing conditions, and metallization materials (IDEs and interconnects) [3]. Therefore, as a first step for micro-sensor fabrication, work must be focused on the development of highly stable electrodes for high-temperature sensor applications. In the current work, bilayer, multilayer and composite Ti, Ta, Hf, and Zr metals with Pt thin films were investigated and tested up to 1200°C for 48 h. Multiple electrode architectures were developed that would maintain the needed microstructure and electrical properties over the duration of the sensor processing and sustained testing at 1000°C. In addition, a modified lift-off patterning process was developed for the composite electrode thin film fabrication.

Available literature regarding to chemical sensors has made known that the utilization of nanomaterials as the active sensing material system results in extraordinary gas sensing capabilities (high sensitivity). Therefore, developing low priced, micro scale chemical sensors that are derived from metal oxide nanomaterials to sense gases within the high-temperature environments (>500°C) is existing necessity [4]. Nanomaterials are known to be unstable at high temperatures due to sintering and coarsening mechanisms, and these issues drawback their prospective utilization within advanced sensors at high temperature. In order to retain the high surface area of the synthesized nanomaterials, this work focused on strategies to limit the sintering and grain growth processes. Two different strategies with different stabilizing mechanisms were proposed in order to hinder/stop the coarsening/sintering process. The strategies chosen were grain and substrate pinning of the chosen nanomaterial through the distribution of coarsening resistant secondary phase among nanomaterial grains and the bonding of nano-granular microstructure over a stable refractory substrate.

The current work also investigated the tungstate and molybdate compositional families as sensing nanomaterials towards H_2, SO_2 and H_2S at levels of 5 to 4000 ppm within a resistive-type sensor platform (also termed as chemi-resistive platform). Carbon monoxide (CO) tests were completed in the range of 1000 to 4000 ppm in order to evaluate level of possible interference to chemi-resistive response. Multiple hydrogen (H_2) and sulfur (H_2S and SO_2) sensing materials were developed with different morphologies via hydrothermal method. The compositions synthesized and tested were: tungsten trioxide (WO_3), molybdenum trioxide (MoO_3), and molybdates, including $SrMoO_4$ and $MgMoO_4$. Double-perovskites were also synthesized by solid state reactions, and compositions such as strontium magnesium molybdate ($SrMgMoO_6$) and strontium magnesium tungstate ($SrMgWO_6$) and commercially available nickel tungstate ($NiWO_4$) and molybdate ($NiMoO_4$), strontium tungstate ($SrWO_4$) are also among the compounds that were tested for H_2S, H_2 and SO_2 sensing.

The chemical composition and nano- and micro-structure of the developed nanomaterials were compared against the sensing mechanism. The work also attempted to correlate the sensor activity and stability to the high-temperature compatible thin film electrode architecture which were investigated in this work. The sensing materials and electrodes were characterized by means of scanning electron microscopy (SEM), energy dispersive X-ray spectroscopy (EDS), X-ray and ultraviolet photoelectron spectroscopies (XPS and UPS), atomic absorption spectroscopy (AAS), X-ray diffraction (XRD), Raman spectroscopy, temperature programmed reduction (TPR) and transmission electron microscopy (TEM). The macro- and micro-configurations of the sensors were tested and analyzed for sensitivity and cross-sensitivity, long-term stability, response and recovery times. Electrochemical relaxation (ECR) technique was also utilized to quantify the surface diffusion kinetics of sulfur dioxide (SO_2) over chosen sensor material surface.

1.2 Goals of Research

High sensing performance demands microstructural and chemical stability, as well as, a high surface-to-volume ratio of the designated sensing material system. The primary emphasis of this study is to produce high performance micro-scale H_2S, SO_2 and H_2 sensors with the stabilized thin film electrode composition and nanomaterial, where both components are capable of operating at temperatures beyond 500°C (up to 1000°C). In order to accomplish this goal, the following work was completed in this thesis:

1. High temperature compatible interdigitated electrodes (IDEs) were developed with different coating architectures. In order to
2. Sensing oxide nanomaterials were synthesized via hydrothermal method with a high surface area in order to enhance solid-gas interaction.
3. Different approaches for stabilizing the sensing nanomaterials at high temperature were investigated, where strategies to control diffusional anisotropic morphologies, grain and substrate pinning were also employed.

4. Microsensors for H_2 and SO_2 with the designated nanomaterial systems were developed and tested. The microsensors were fabricated by thin film deposition and optical lithography.
5. Research over the sensing mechanism and surface dissociation kinetics, sensitivity, and selectivity of the H_2S, H_2 and SO_2 sensing materials were also completed.

1.3 Thesis Organization

This dissertation is comprised of seven chapters. Chapter 1 contains a systematic outline of the thesis and the objectives. Chapter 2 introduces a comprehensive background regarding the overall view of chemical sensors, current sensing technology together with different types of electrode materials and deposition techniques of them, as well as, the sensing material systems used for detecting gas species such as H_2, SO_2 and H_2S. The deposition and characterization of the high temperature compatible thin film electrodes are also covered in Chapter 3. Chapter 4 provides the synthesis of nano-tungstates and -molybdates. Chapter 5 explorers testing of micro- and nano-size tungstates and molybdates for H_2, H_2S and SO_2, as well as, explores the sensing mechanism and surface diffusion kinetics of SO_2 over chosen material system by means of electrochemical relaxation technique (ECR). The microsensor fabrication equipped with the optimized nanomaterial systems and testing results for H_2, SO_2 and H_2S are discussed in Chapter 6. Conclusions and recommendations for future work are detailed in Chapter 7.

Chapter 2: Background

2.1 Solid State Sensors for Chemical Detection

2.1.1 Introduction to chemical sensors and catalysis aspect of the chemical sensing

Figure 1 quantitatively shows the different metal oxides compositions utilized as an active sensing layer for chemical sensing applications. Although the schematic presentation does not provide any data for effective decision making for sensor designer; however, it provides insight into the relation between chemistry and specific sensing capabilities. As seen from the Figure 1, among all oxides previously utilized for gas sensing, SnO_2 is the most common choice of material for chemical sensor applications. All materials presented in the Figure 1 have their own advantages and disadvantages, and before deciding over the active layer, must be evaluated in accordance with the operational conditions such as target gas type and its concentration, temperature, chemical environment, humidity, existence of oxygen and corrosion resistance.

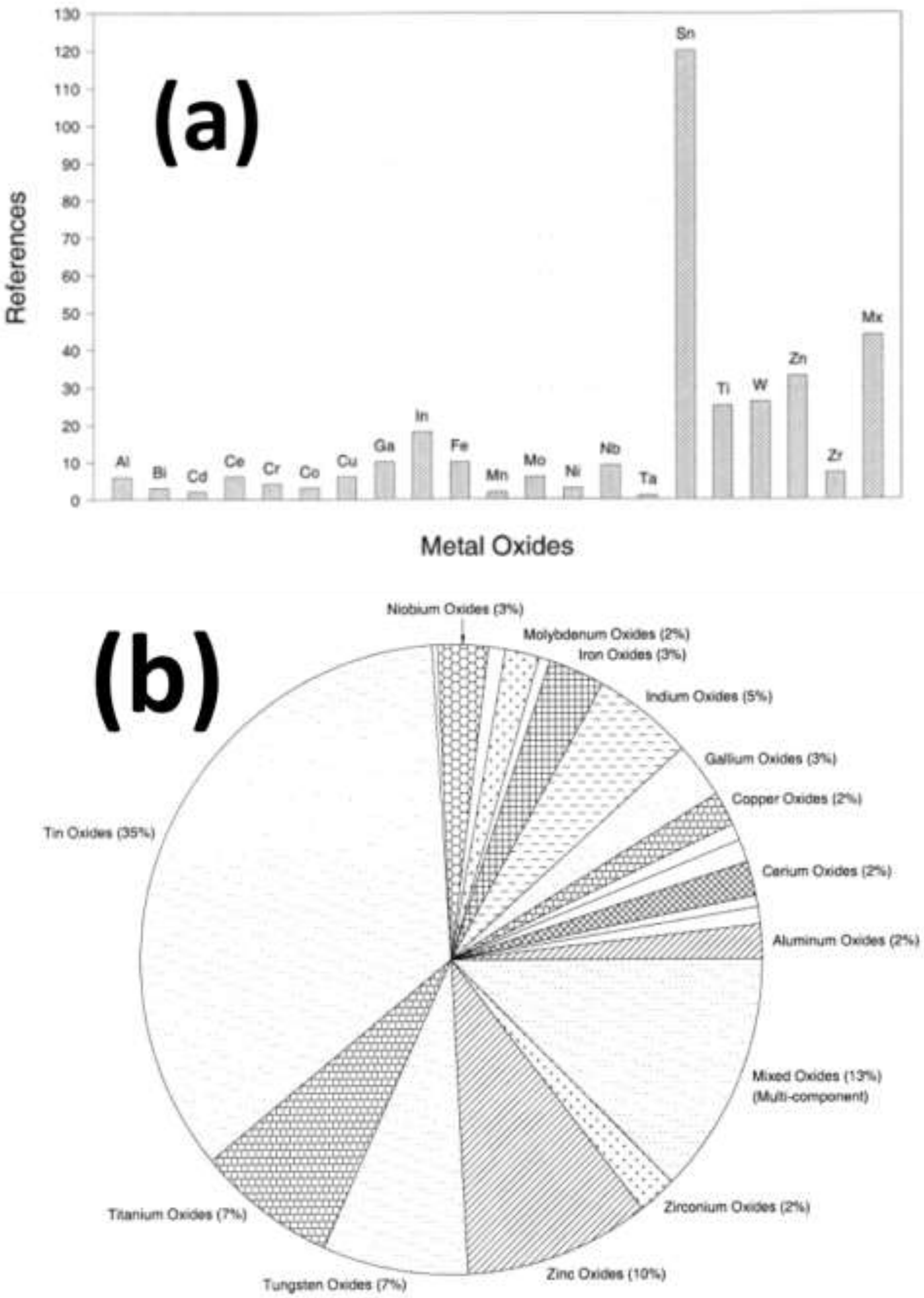

Figure 1: Different metal oxides shown against the amount of work on them referred in **(a)** normalized application frequency **(b)** relative comparison pie graph **[5].**

Solid state type gas sensors` sensing operation is not only related to surface activity of sensing material against target species, but also their selectivity and sensitivity are also affected by catalytic interaction. A catalytic reaction can be expressed in other words as a sensing process of a semiconducting metal oxide material since both processes include surface dissociation and chemical reactions with the gas environment [5]. The electrical response characteristics of sensors depend on the existing electrical polarization at the semiconducting surface that depends on the electronic surface states due to chemical interaction occurring on its surface as interaction with the target gas. Two related phenomena must be defined; physisorption and chemisorption. Surfaces in nature are high energy states and in constant search for satisfaction to their unbalanced electronic distribution that leads to an appetite for approaching molecules to vicinity. Physisorption is the first kind of absorption and features weak interaction mainly based on van der Walls force but strong enough to prevent the molecule from diffusing around the surface. The second type is chemisorption, which is stronger and stiffer, because of chemical bond formation. In chemical sensor applications, there are two types of electronic materials typically used as the catalyst, metals and semiconductors. In each subset, the unbalanced d-orbitals play the leading role [6, 7, 5]. In addition to the abovementioned phenomena, adsorption of different reducing or oxidizing specious changes the work functions *(ɸ)* of the metal or semiconductor sensing material surfaces. The work function *(ɸ)* itself also depends on the cation oxidation state together with the absorption characteristic of the surface. Therefore, the monitoring/measuring of the *ɸ* of known metals or semiconductors can provide significant insight regarding the nature of surface-target gas interactions [6, 8].

2.1.2 Solid state semiconductor sensors for chemical detection

Solid state gas sensors are based on semiconductor devices possessing junction structures of metal and semiconductor materials. These sensors are usually deposited onto an electrochemically non-active surface in the form of a thick or thin film with via different deposition techniques including but not limited to physical/chemical vapor deposition and/or other thick film deposition techniques. The electrochemically active sensor material is usually connected to the measurement system through metal interconnects. The former subset can further be classified into three major clusters by modifying the junction order or type. Those are either MS (metal-semiconductor, Schottky barrier device), MIS (metal-insulator-semiconductor), or MOSFETs (metal-oxide-semiconductor field effect transistors). In the subset of semiconducting surface film devices, one can distinguish two main clusters; bulk and surface conductivity sensors [6]. Figure 2 shows Saaman and Bergveld`s general classification scheme of semiconductor-type of solid state sensors. The schematic provides a micro-machined representative device, an example of standard sensor output signal, and chemically active material composition and target gas [9].

2.1.2.1 Metal-semiconductor (Schottky barrier) devices

Unlike the surface film and capacitive type sensors, which are generally fabricated on binary oxide ceramic substrates such as ZrO_2 or Al_2O_3, however taking the TCE match, chemical inertness and electrical characteristic into account may complicated the design. Metal semiconductor sensors are realized only on a semiconductor platform, which further requires compatibility and increases the required labor and technology. In this sense, compatibility means silicon (Si) processing concurrency that further increase the manufacturing cost and labor requirements. First example of this subset is the Schottky barrier devices (MS), where the operation principle of these sensors is based on the fact that Fermi level of the semiconductor adjusts itself to the neighboring metals` Fermi level at the metal-semiconductor interface. The competence adjustment even existed under the condition that dielectric layer occupies the interface between two, however this type is classified under different subset. A barrier height (φ_{B_n}) can be obtained by subtracting the electron affinity of the semiconductor (χ) from the work function of metal (φ_m), and this difference is then multiplied by the elementary charge. Equation 1 shows the mathematical formulation of the barrier height (φ_{B_n}) [6].

$$q\varphi_{B_n} = q(\varphi_m - \chi)\text{ , } q{=}e^{-} \qquad \textbf{(Eq. 2.1)}$$

The target gas composition dictates the barrier height change in conjunction with the changes in catalytic metals` work function (φ_m). The work function bending sets the detection mechanism for the Schottky devices. Figure 3 shows the Schottky device energy schematic for an n-type doped semiconductor and catalytic metal which is exposed to a target gas. MS devices have been utilized to sense hydrogen (H_2) by using palladium (Pd), which is known for its high H_2 uptake capability. The restrictions on the usage of semiconducting substrates are mainly chemical instability and insensitivity of Fermi level under the existence of target gas (H_2). A typical example of a MS device using a Pd metal catalyst and cadmium sulfate (CdS) semiconducting substrate as well as sensor signal output upon exposure to target gas can be seen in Figure 2-g [6].

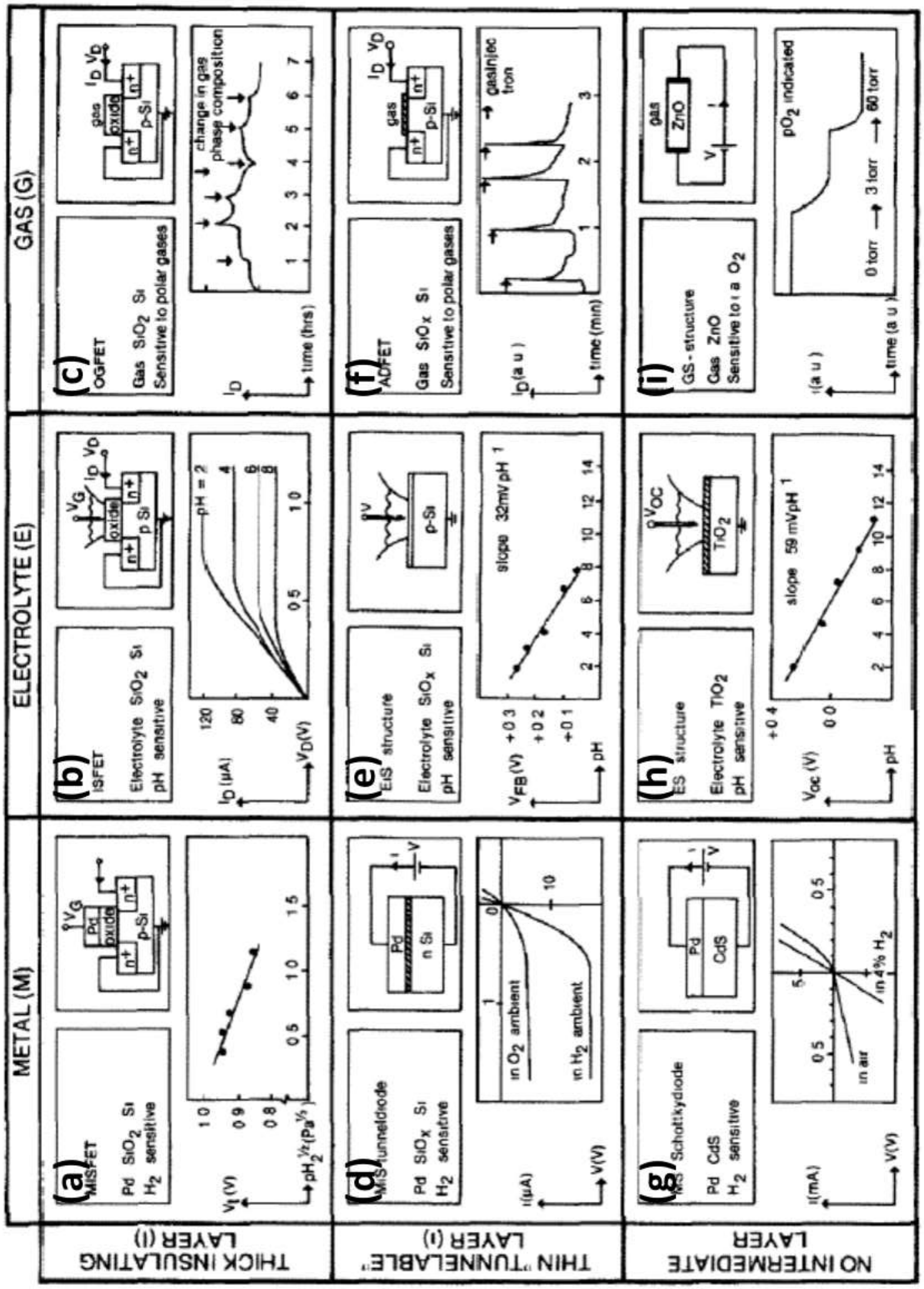

Figure 2: Classification of chemically sensitive semiconductor gas sensors including a micro-machined representative device, an example of standard sensor output signal, and chemically active material composition and target gas **[9]**.

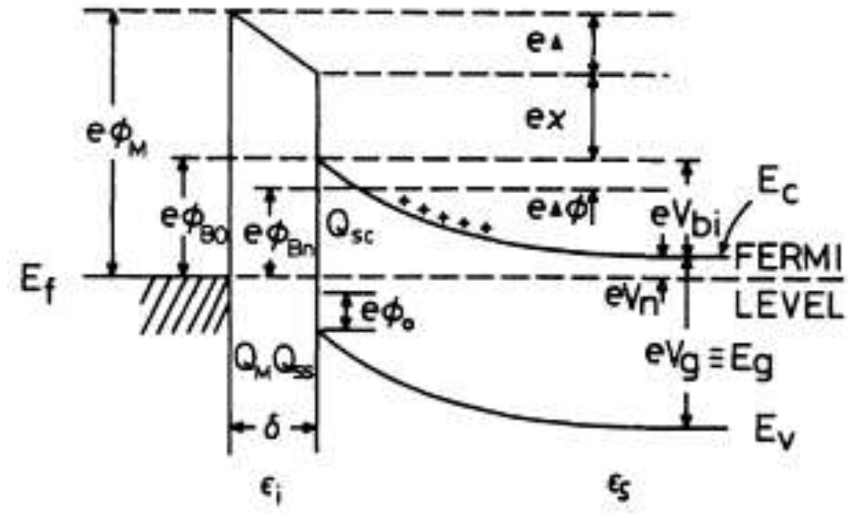

Figure 3: Schottky device energy schematic under the presence of surface states **[6]**.

2.1.2.2 Metal-insulator-semiconductor (MIS) devices

The most important member of the MIS (metal-insulator-semiconductor) family is MOS (metal-oxide-semiconductor) devices, which utilizes SiO_2 and silicon (Si) as a structural component. MOS devices are the most common choice for sensor designers not only due to their high sensitivity capabilities, but also its relatively simple design. In order to utilize the MOS device as a sensor element a conventional aluminum (Al) gate metal has exchanged with catalytic active metals. The sensing mechanism is based on the formation of an ionic charge dipole layer at the metal-insulator interface, which causes a voltage drop upon exposure to the target gas. The example of the device is presented in Figure 2-d. The presented H_2 sensitivity MOS device configuration includes palladium (Pd) as an active catalytic metal and thin SiO_x insulation and Si semiconductor layers. The increase in H_2 partial pressure results in a decrease in the current flow between the Pd and the Si. MiS tunnel diode is the other example of MIS devices. A MiS tunnel diode resembles a Schottky device regarding the general design and components; however, it does not only differ in the choice of semiconductor material by utilization of extrinsic type semiconductor (n-Si) instead compound semiconductor (TiO_2 or CdS) used in Schottky devices, but also insulating layer between metal-semiconductor interface. The difference in two designs (a Schottky and a MiS device) regarding to sensing mechanism studied by Sullivan et *al.* In this study authors used Pd metallization accompanied by ultrathin SiO_x insulator and Si (100). It was concluded that change in output signal from MiS to MS structure is the direct result of a barrier height (φ_{B_n}) change between the two systems [10, 6, 4].

Another configuration is metal-insulator-field effect transistor (MISFET) which differs from MIS device due to its thick insulating layer. Other acronyms can also be found in the literature in order to describe MISFET; those are MOSFET, IGFET and MOST. Figure 2-a represents example of the device. Again, the MISFET device is sensitive to H_2 and is able to distinguish different partial pressures of the H_2. The MISFET sensors vary in the design of gate metallization and can be classified in further to four subsets. The first of them is open gate field effect transistor (OGFET) which basically does not utilize the gate metal. Adsorption field effect transistor is the second type and utilizes ultrathin gate oxide, which is less than ~5 nm. The surface accessible field effect transistor which has utilizes direct access to target gas via air gap in the gate insulator [6, 4].

2.1.2.3 Surface film devices

The surface film devices possess relatively simple design in comparison to previously explained sensor architectures. The surface film devices are consist of deposited semiconducting thin film onto an insulating substrate. They were first demonstrated in the early 1960s. Crystalline defects and non-stoichiometry are the basic characteristic differences of the type compare to single crystalline semiconducting systems mentioned in previously. The advantages of these devices are the simple design, low production cost and robust operating mechanism. The operation mechanism of surface films devices is based on the change of thin film conductivity upon exposure reducing or oxidizing atmospheres. The most proposed electrochemical reaction which dictates the sensing mechanism is the chemical interaction of the adsorbed oxygen (O_2) in redox reaction with the approaching gas stream. This chemical interaction results in an increase in the surface conductivity, which was previously lowered since the adsorbed oxygen acted as an acceptor on the surface and decreased the electron density of the surface. The adsorption can be occurred on the surface of the sensing material through either a physical or chemical mechanism. These two mechanisms are typically termed as physisorption or chemisorption, respectively. As a rule of thumb as the material approaches (oxide semiconductors, e.g. transition metal oxides) to stoichiometry (d^0), the resistance increases and eventually become extremely high [7, 6]. Typical design and sensor output of this type of sensor can be seen in Figure 2-i at the right bottom corner.

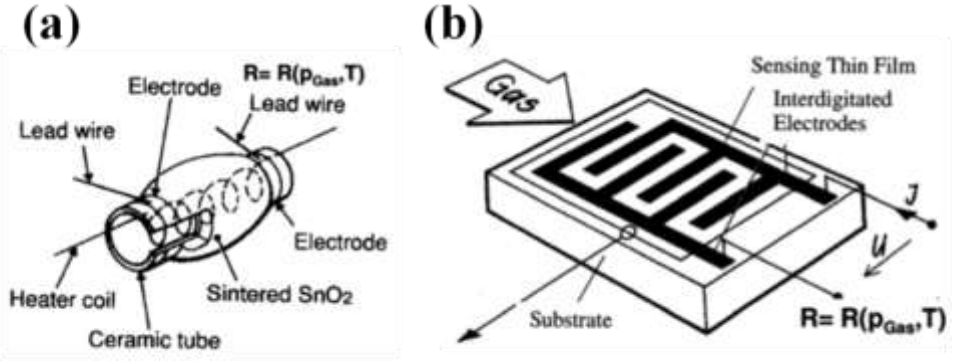

Figure 4 : (a) Conventional tubular setup; and **(b)** Planar structure fabricated by thin film technology **[11]**.

Figure 4-a shows Taguchi type sensor designed. As seen in the schematic heating element located in ceramic cylinder and reference and sensing electrode in this case tin oxide (SnO_2). Figure 4-b shows a schematic of a planar resistive-type sensor architecture. The figure shows two electrodes printed into a comb-structure, where the electrodes are the positive and negative polar electrodes. The two electrode are separated by a distance which is named gap. The electrodes are electrically connected by the sensing materials, which are typically a semiconducting material that is sensitive to basic surface redox reactions. These redox (reduction-oxidations) reactions were briefly discussed in the proceeding sections, but will be further discussed in Chapter 5. The sensor manufactured by flat design with the choice of alumina substrate whereupon metallizations including electrode and heater can be deposited on opposite sides and finally sensing material can be positioned over electrode [11].

Two different type of sensing mechanism can be distinguished; one subset contains bulk conductivity while other involves changes in the surface conductance. The former sensitive to changes in the oxygen partial pressure and defect chemistry controls sensing behavior as the oxide tends to equilibrate itself with the environmental oxygen partial pressure while the other basically depends on surface-target gas interactions, adsorbed gas molecules, surface crystal defects, interstitials and physic or chemisorbed material.

2.1.2.3.1 Bulk conductivity sensors

Bulk conductivity (potentiometric) sensors owe their usefulness to high ionic conductivity via solid electrolyte material in the temperature regime 500 to 1300°C. Sensors made of TiO_2 and ZrO_2 are the example of the bulk conductivity family type of sensors. The latter is the choice of material in the automobile industry for detection of the air/fuel ratio in the exhaust gas. The electrical (Ionic and electronic) conductivity (σ) in the bulk type of sensors is given in Eq. 2, where μ_n and μ_p are electron and hole motilities, respectively. A change in the partial pressure of the ambient oxygen creates oxygen vacancies and titanium (Ti) interstitials [12, 5, 4, 6].

$$\boldsymbol{\sigma = q(n\mu_n + \mu_p p)} \qquad \textbf{(Eq. 2.2)}$$

The activation energies for a bound electron to move into the conduction band of TiO_2 can be extracted from the solid state reactions described by Marucco et *al.* using Kröger-Vink notation. Equations 2.3, 2.4 and 2.4 show the corresponding reactions during the sensor operation. The total activation energy for the creation of electrons into the conduction band can be obtained through adding the activation energy for reaction shown in Eq. 2.3 plus the ionization energy (E_D) for the removal of electron from donor state (Ti^-) to the conduction band [13, 6]. Eq. 2.6 shows the conductance upon oxygen vacancy formation. Another mechanism contributing to electrical conduction in semi-conducting material is electron excitation from valence band to conduction band without chemical interaction due to thermal excitation (an intrinsic thermal mechanism).

$$\boldsymbol{2Ti^0 + O^0 \rightarrow 2Ti^- + V_O^{2+} + \frac{1}{2}\, O_2 \uparrow} \qquad \textbf{(Eq. 2.3)}$$

$$\boldsymbol{Ti^- \rightarrow Ti^0 + e^-} \qquad \textbf{(Eq. 2.4)}$$

$$\boldsymbol{O^0 \rightarrow V_O^{2+} + 2e^- + \frac{1}{2}\, O_2 \uparrow} \qquad \textbf{(Eq. 2.5)}$$

$$\boldsymbol{\sigma = \sqrt{2}\, q\mu_n [p(O_2)]^{\frac{1}{6}}\, e^{\left\{\left[\left(\frac{\Delta G_2}{2}\right)+E_D\right]/kT\right\}}} \qquad \textbf{(Eq. 2.6)}$$

This type of sensor has a strong temperature dependence of the conductivity and requirement for high temperature for fast oxygen ion transfer in TiO_2 bulk conductivity sensors are the main disadvantages, however continuous monitoring, simple sensor output (conductance), accuracy, relatively simple design are among the advantageous of it. In order to compensate the deficiencies mainly regarding the vulnerability to temperature fluctuations, new material systems were the subject of intense research in the scientific community. Those materials include complex perovskites, multivalent oxides, a few simple oxides, and alkaline-earth substituted ferrites [14]. The electrical conductivity of the some alkaline-earth (Ca, Ba and Sr) ferrites is provided in Figure 5 for comparison purposes. All material system show temperature dependence conductivity and composition. Among the materials investigated, $SrFeO_{2.5+x}$ showed less temperature dependence, which is desirable for feature for sensor designer; however, the $CaFeO_{2.5+x}$ showed high sensitivity to temperature change (see Figure 5-a). Another important aspect is the compositional integrity and stoichiometry of the material. Figure 5-b shows all three different ferrites show high reduction after 500°C. $BaFeO_{2.5+x}$ and $CaFeO_{2.5+x}$ reduced significantly lost significant amount of O_2 around 1000°C, however $SrFeO_{2.5+x}$ was still able preserve O_2 to relatively large extent compare to other ferrites. This shows the potential applicability of the material as an active layer for chemical sensor applications.

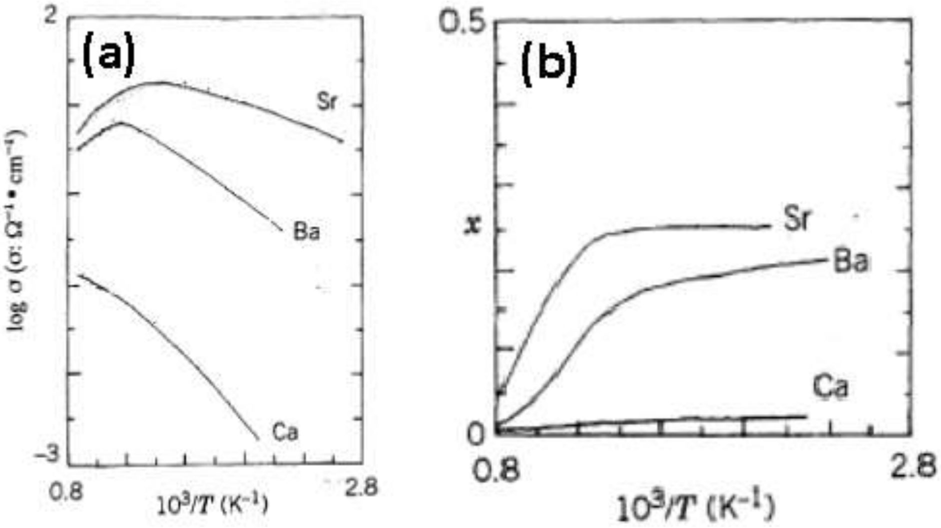

Figure 5 : Comparison of the **(a)** conductivities and **(b)** compositions of $MFeO_{2.5+x}$ where M = Sr, Ba, or Ca **[14]**.

2.1.2.3.2 Surface conductivity sensors

Surface conductivity sensors benefit from adsorption and redox reactions to alter the conductivity of the underlying sensing material. The second and most widely studied solid state gas sensors are based on semiconducting surface thin/thick film architecture (see Figure 4-b). A sensor detection mechanism lies on the alteration in the electrical resistance of a sensing element upon change in the gas atmosphere. It has been long known that chemical interaction between adsorbed species and the gas environment drastically changes the electronic surface states, subsequent surface charge exchange process yields drastic changes in resistance of the semiconductor dictated by the nature (reducing or oxidizing) of the gas environment [12, 4, 6, 5]. In the surface thin/thick film devices, oxide semiconductor materials have been utilized to a greater extent as the sensing material compared to organic materials (such as polyimide, polyamide, polyimidazole materials) or elemental or compound semiconductors (such as Si, Ge, GaAs, etc.) [12]. The basic reactions regarding the sensing operation in n-type of semiconductor are; first adsorption of O_2 to the surface of the sensing material either by physisorption and/or chemisorption, which consumes electrons as seen in Eq. 2.7. A subsequent reducing gas counters acts the oxidation layer through a process that extracts the absorbed O_2 from the surface and releases an electrons back as seen in Eq. 2.8.

$$\boldsymbol{O_2 + 2e^- \rightarrow 2O^-_{ads}} \qquad \textbf{(Eq. 2.7)}$$

$$\boldsymbol{R + O^-_{ads} \rightarrow RO_{des} + e^-} \qquad \textbf{(Eq. 2.8)}$$

Adsorption of oxygen to the surface requires the ionization of the donor state (activation energy E_D) and desorption of oxygen, which follows the reverse reaction during desorption (activation energy E_S) of oxygen form surface. Eq. 2.9 shows the conductance of the surface thin film device. The formula includes the reaction rate constants shown in Eq. 2.7 and 2.8, as well as, the reaction order with respect to O_2 and the reducing gas. The model given in the Eq. 2.9 can be further modified by treating the surface states as an electronic density of states and apart from these different absorption types of oxygen also included [6].

$$\boldsymbol{\sigma = \left(\frac{q\mu_n N_D h^2}{N_s K_1^0}\right)\left\{e^{\frac{-[E_S - E_D]}{kT}}\right\} [p(O_2)]^{\frac{-m}{2}}(K^0_{-1} + K_2^0[p(R)^m])} \qquad \textbf{(Eq. 2.9)}$$

The kinetics of the sensing reactions are mainly altered by microstructure for surface conductivity films. Thin film surface conductivity sensors give prompt responses compared to thick film surface conductivity sensors because the adsorption of the target gas molecules occur only on the surface of the sensing material grains as schematically illustrated in the Figure 6 [15]. The successful operation of thick film sensor is reliant on the flow of the gas species deep inside material down to sensor electrode interface via percolation paths. The active available surface area for gas specious is increased to great extent in the case of thick film with engineered porosity as seen in the illustration shown in Figure 6-b. It should be noted that the reaction near the electrode interface is the active location. Reactions occur far towards the surface do not contribute to the performance as much as the reactions near the electrode interface. Therefore, diffusion limitations are more important over the sensing material in thick film sensor compare to thin films counterparts. Also, redox reactions towards the outer surface may produce product there which may also limit mass transport into the active sensing material, this phenomenon termed as poisoning of the sensing material surface [15, 16, 17].

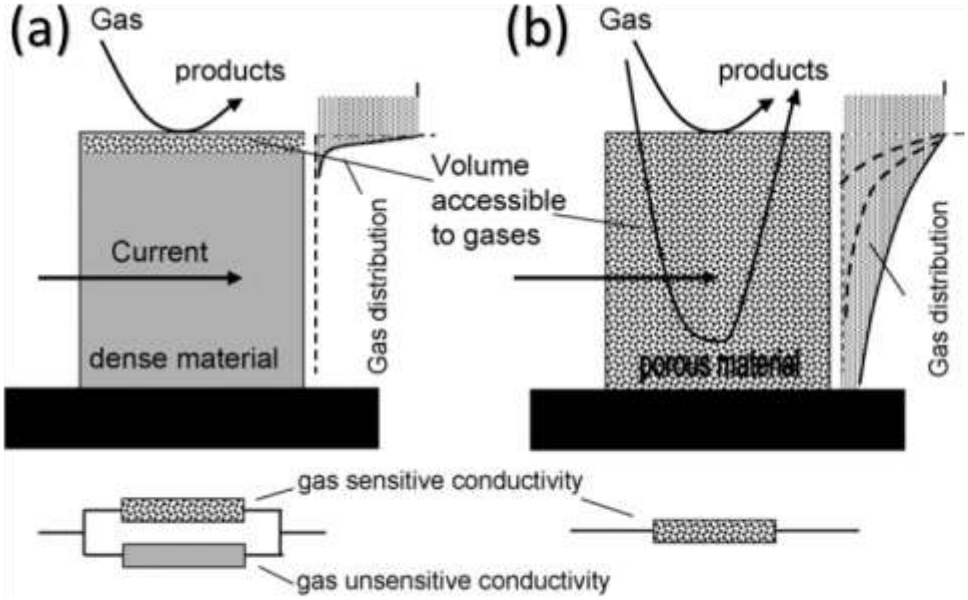

Figure 6: Microstructural effect on sensing operation **[15]**.

For thick porous surface conductivity films, there are three main conduction models depending on the intergranular contacts and necking. The electrical conductance of the thick film can be controlled by the grain boundaries, the necks between the grains, or just by the grains due to formation of Schottky barriers at transition locations in each of them. If the particle diameter, D, is too much larger than the Debye length (2L, depletion length), the conductance is controlled by the grain boundaries as schematically demonstrated in Figure 7-a [15, 17, 18].

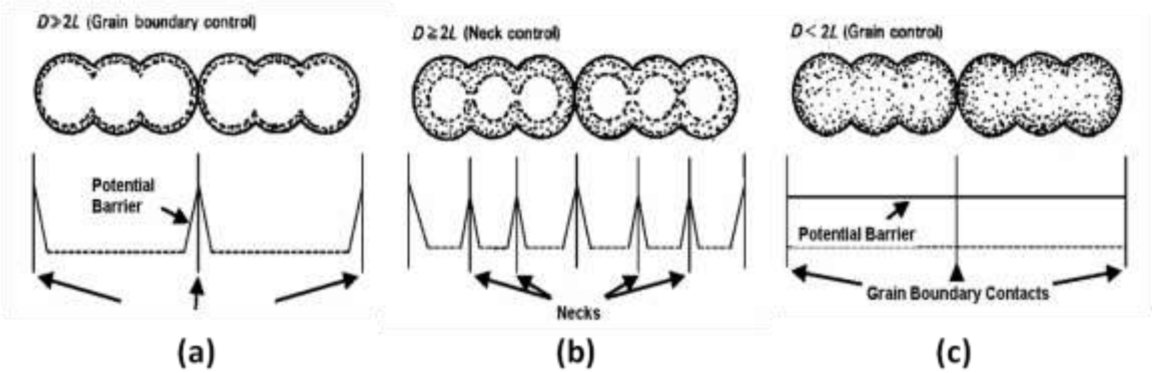

Figure 7: The neck formation and importance of the width of it **[15]**.

As illustrated in Figure 7-b, when D becomes equal or slightly larger than 2L, the depletion zones of the grains begin to overlap and the necks between the grains start to control the conductivity thorough the thick film. As the grains become smaller to D<<2L, as seen in Figure 7-c, they are totally depleted and the conduction is dominated by the grain itself [15]. The thickness of the depletion layer is shown in Eq. 2.10, which corresponds to approximately 10 nm, which makes photoelectron spectroscopy (XPS) very useful technique. The nanomaterials with the grain size up to 10 nm can be classified under the third subset, grain control electrical conductivity. The very thin layer (depletion layer) with the high electrical resistance occurs due to chemisorbed or ionosorped O^{2-}; however, it is known that oxygen cannot be chemisorbed on stoichiometric oxides [12, 6]. It was reported that CeO_2 showed high corrosive resistance when compared to Ga_2O_3 and $SrTiO_3$ material at temperatures as high as 800°C againts highly reactive gases such as NO, Cl_2, SO_2, H_2S and CO. In the same study, it was also concluded that CeO_2 did not show measurable resistance change at 800°C under O_2 and SO_2 containing atmospheres. That type of behaviour can be explained by very low oxygen incoporation to the stoichiometric surface of the CeO_2. In additon to that it also shows that the compound is redoz resistance at this temperature. In the same study, the stoichiometry of the compound was further confirmed by Auger depth profiling [19].

$$\boldsymbol{W_{DL} = \sqrt{\left(\frac{2\epsilon_s kT}{qN_d}\right)} = \sim 10\ nm} \qquad \textbf{(Eq.2.10)}$$

The interstitial oxygen ions and oxygen vacancies act as acceptor/donor species as the way chemisorbed oxygen on the surface of oxides materials. Defect equilibriums are given in Eq. 2.11 and Eq. 2.15 and reaction with SO_2 is provided in Eq. 2.12 through 2.16 [12]. Reintroducing the sensing semi conduction oxide material into an oxygen-rich atmosphere will retreat the surface of the sensing material and deploy the missing oxygen vacancies as well as extra interstitials. The replacement of the oxygen vacancies and redeployment of the interstitial states with physisorption of the oxygen to the surface that is immediately followed by chemisorption of the oxygen by gaining an electron from the surface states and decreases the electrical conductance. The whole process is given in Eq. 2-17, 2-18, 2-19 and 2-20 [4, 12, 20, 19].

$$\boldsymbol{O_o \leftrightarrow O_i^{\cdot\cdot} + V_{\ddot{o}}} \qquad \textbf{(Eq. 2.11)}$$

$$\boldsymbol{SO_2\ (g) + O_i^{''} \leftrightarrow SO_3(g) + 2e\text{-}\ (interstitial)} \qquad \textbf{(Eq. 2.12)}$$

$$\boldsymbol{SO_2\ (g) + O_o \leftrightarrow SO_3\ (g) + V_O + 2e^-\ (lattice)} \qquad \textbf{(Eq. 2.13)}$$

$$\boldsymbol{SO_2 + O_{lattice} \rightarrow SO_3 + V_O^x} \qquad \textbf{(Eq. 2.14)}$$

$$\boldsymbol{V_O^x \rightarrow V_O^{\cdot\cdot} + 2e^-} \quad \textbf{(Eq. 2.15)}$$

$$\boldsymbol{SO_3 + e^- \rightarrow SO_{3(ads)}^{`}} \quad \textbf{(Eq. 2.16)}$$

$$\boldsymbol{O_2 + e^- \rightarrow O_{2,ads}^-} \quad \textbf{(Eq. 2.17)}$$

$$\boldsymbol{O_{2,ads}^- + e^- \rightarrow O_{2,ads}^{2-}} \quad \textbf{(Eq. 2.18)}$$

$$\boldsymbol{O_{2,ads}^{2-} \rightarrow 2\, O_{ads}^-} \quad \textbf{(Eq. 2.19)}$$

$$\boldsymbol{O_{ads}^- + V_{\ddot{o}} + e^- \rightarrow O_0} \quad \textbf{(Eq. 2.20)}$$

The conduction band charge carrier concentration in the semiconductor is proportional to the partial pressure of the reducing gas in the sensor environment. The oxygen is chemisorbed as O^- or O_2^{2-} (O^{2-} is excluded) [20, 21, 22, 12] . Figure 8 shows the valance and conductance bands bending after oxygen and the reducing gas absorption on the thin film semiconducting oxide over aluminum oxide (Al_2O_3) substrate. Alumina has larger band gap compare to sensing material semiconducting compound therefore remains electrically inert during operation and do not interfere with the sensor signal output. The most important feature of the surface film conductivity devices (resistive type) is the depletion of conductance band electrons by being transferred to chemisorbed O_2 ions in the thickness defined by space charge region (W_{DL}). Both the physisorption of oxygen and subsequent chemisorption by electron transfer are exothermic reactions. For a functional sensor, kT_0 in which T_0 is operating temperature. In other words operation temperature must be high enough to promote the reactions. The sensor response starts with physisorption of the approaching reducing gas which is followed by the capture of the approaching molecule via chemisorption. The rate determining reaction in the sequence determined by many is the chemical interaction of the reducing gas such as SO_2, H_2S, H_2, CO and the chemisorbed oxygen which is followed by thermally activated irreversible desorption of the final compound from surface otherwise is defined as poisoning of the surface of the sensing material. [20, 12, 23, 4].

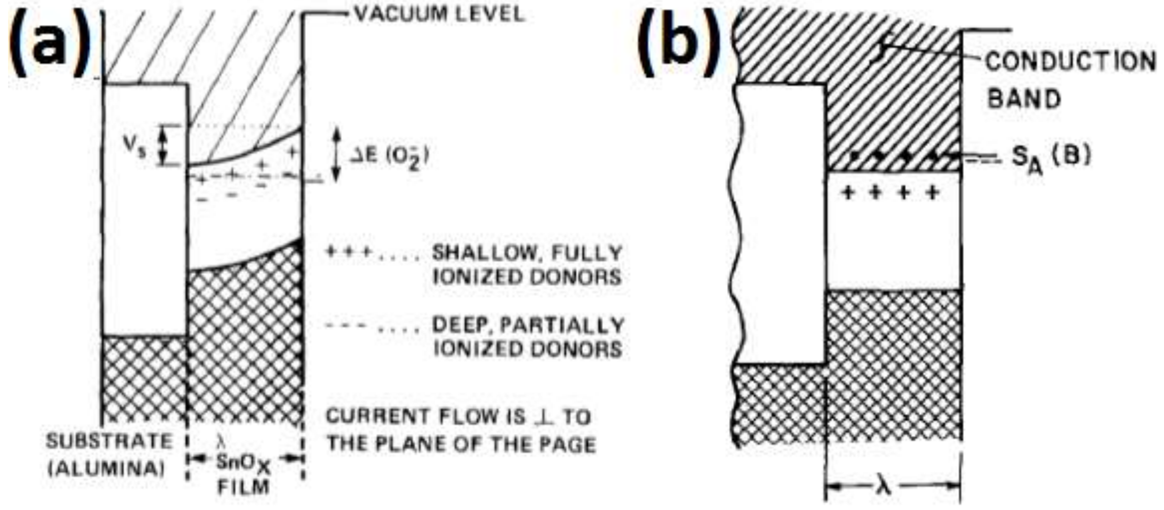

Figure 8 : (a) Chemisorption of oxygen consumes the electrons and enlarge the band gap by bending it from the **(b)** recovery due to electron emission from compound formation between oxygen and reducing gas **[20].**

One of the problems associated with surface film conductivity sensors is the non-selectivity due to the materials response to wide range of reducing or oxidizing gases in the same sense. The common solutions to the problem are utilization of initial treatment of the sensor, filters which let certain type of molecules go and certain others do not, another method is usage of catalytically active materials such as noble metals and/or occasionally different oxides. It was also reported that significant change in both magnitude of response and exclusive targeted selectivity of TiO_2 [23] semiconducting surface film device when the sensing material mixed with favorable d^0 configuration secondary phases such as Y_2O_3, Al_2O_3 or ZrO_2, it is believed that the reason behind this exclusive sensing capabilities is the formation of space charge region between second phase and semiconducting oxide material [23, 12, 20, 4, 24, 22].

2.2 Current Sensing Materials for H_2, SO_2, and H_2S

2.2.1 Hydrogen (H_2)

Figure 9-a provides the statistical data over the number of works devoted to certain types of gases in the literature. As seen from the image, pollutants such as CO_2 and NO_x dominate the list. Figure 9-b provide relative percentages from which can be concluded that 32% of the sensor/sensing related work focused on aforementioned two pollutants, after these gases, H_2 takes the third most cited works with 11%, due to its potential commercial value in the market [5]. Hydrogen is the most suitable substitution of hydrocarbon based fuels for future energy demands. The biggest obstacle in front of that hydrogen vision is the difficulties in safe and effective infrastructure [25]. A common application regarding the hydrogen sensor technology is leak detection due to hydrogen`s ability to diffuse through almost all known materials; concentration monitoring is another demanding application since H_2 has significant importance over the general performance of the solid oxide fuel cell (SOFC) which utilizes H_2 as a fuel. H_2 sensors are required for industrial processes in order to quantify the concentration of H_2. Hydrogen sensors are needed in catalytic hydrogenation process in foods, processing of metals such as aluminum, atmospheric control, pharmaceutical and petrochemical applications [26].

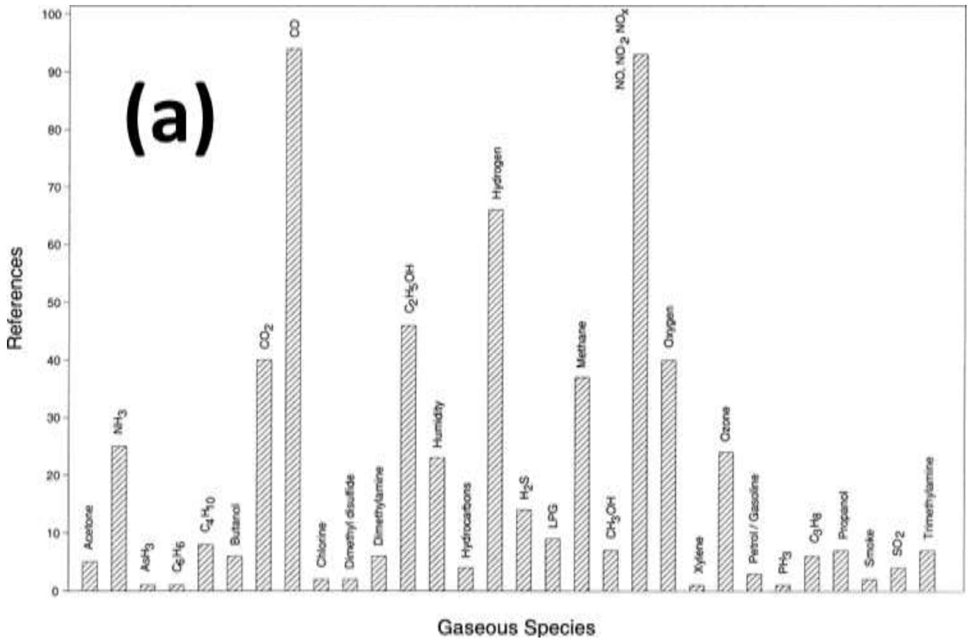

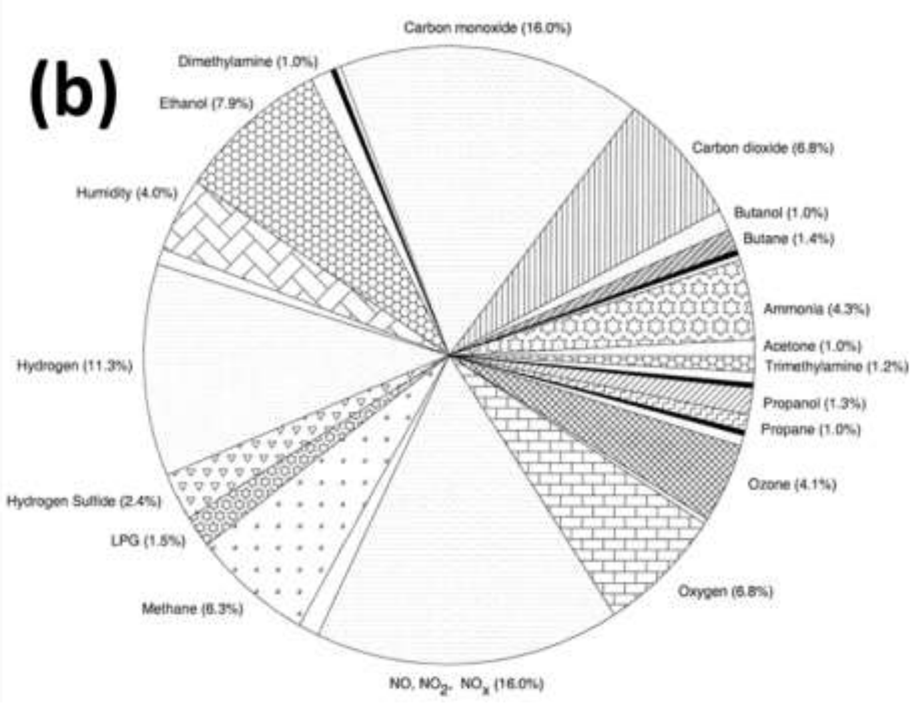

Figure 9: Relative frequency of gas specious on which sensor designed **(a)** normalized **(b)** relative comparison **[5].**

It is necessary to develop H_2 sensors that are capable of working under room temperature, without the need of an internal heater or at high temperatures up to 1000°C. For the abovementioned purposes, a wide range of materials with different microstructures, morphologies, compositions and dopants have been tried as a H_2 sensor in the literature. Table 1 summarizes the materials of interest for H_2 sensing at different temperatures under different conditions together with their manufacturing methods. As can be seen from Table 1, numerous types of materials utilized for H_2 sensor application including binary oxide semiconductors (Al_2O_3, ZrO_2, Fe_2O_3, CuO, NiO, SnO_2 ZnO, TiO_2, Cr_2O_3, WO_3, MoO_3, Bi_2O_3, In_2O_3, YSZ, CeO_2), ternary oxides ($SrCeO_3$, $CaZrO_3$, , $SrTiO_3$, $SmCoO_3$, $BiCuVO_x$) compound semiconductors (CdO, $SrGe_{0.95}$), complex oxides such as $BaCe_{0.8}Gd_{0.2}O_3$, $BaZr_{0.4}Ce_{0.4}In_{0.2}O_3$, and many more complex oxide and/or compound semiconductor with different dopants as well as composites. SnO_2 has been the main choice of material for H_2 sensing [25, 17, 5]. As seen form Table 1, only a few sensors are capable of working beyond 500°C with sustained operation time. This is mainly due to structural and phase stability problems of the utilized sensing material composition at these higher temperatures under reducing atmospheres.

Table 1: Materials for H_2 detection **[25]**.

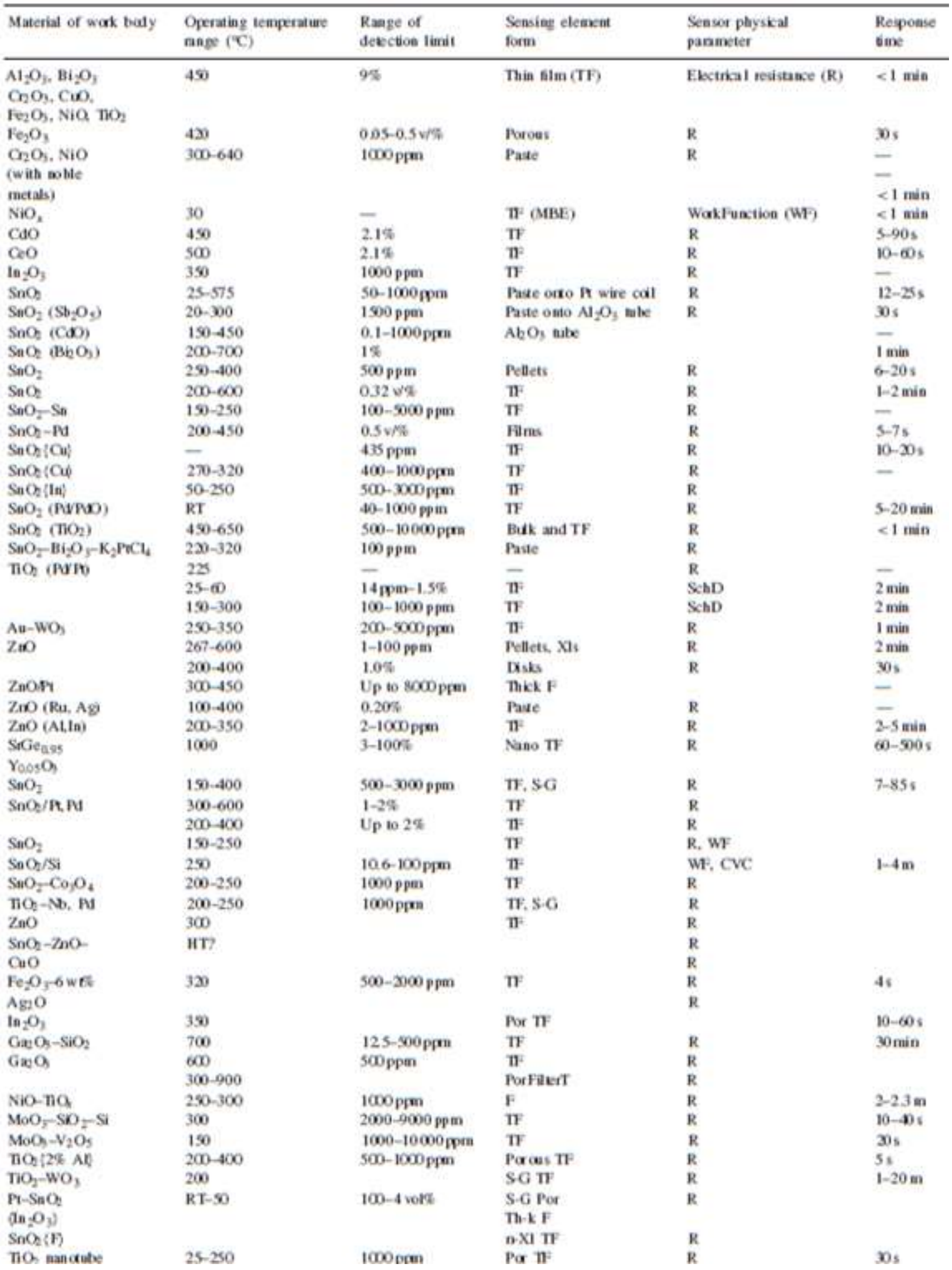

Material of work body	Operating temperature range (°C)	Range of detection limit	Sensing element form	Sensor physical parameter	Response time
Al_2O_3, Bi_2O_3 Cr_2O_3, CuO, Fe_2O_3, NiO, TiO_2	450	9%	Thin film (TF)	Electrical resistance (R)	<1 min
Fe_2O_3	420	0.05–0.5 v/%	Porous	R	30 s
Cr_2O_3, NiO (with noble metals)	300-640	1000 ppm	Paste	R	— — <1 min
NiO_x	30	—	TF (MBE)	WorkFunction (WF)	<1 min
CdO	450	2.1%	TF	R	5–90 s
CeO	500	2.1%	TF	R	10–60 s
In_2O_3	350	1000 ppm	TF	R	—
SnO_2	25-575	50–1000 ppm	Paste onto Pt wire coil	R	12–25 s
SnO_2 (Sb_2O_5)	20–300	1500 ppm	Paste onto Al_2O_3 tube	R	30 s
SnO_2 (CdO)	150-450	0.1–1000 ppm	Al_2O_3 tube		—
SnO_2 (Bi_2O_3)	200-700	1%			1 min
SnO_2	250-400	500 ppm	Pellets	R	6–20 s
SnO_2	200-600	0.32 v/%	TF	R	1–2 min
SnO_2–Sn	150-250	100–5000 ppm	TF	R	—
SnO_2–Pd	200-450	0.5 v/%	Films	R	5–7 s
SnO_2{Cu}	—	435 ppm	TF	R	10–20 s
SnO_2(Cu)	270-320	400–1000 ppm	TF	R	—
SnO_2{In}	50-250	500-3000 ppm	TF	R	
SnO_2 (Pd/PdO)	RT	40-1000 ppm	TF	R	5-20 min
SnO_2 (TiO_2)	450-650	500–10 000 ppm	Bulk and TF	R	<1 min
SnO_2–Bi_2O_3–K_2PtCl_4	220-320	100 ppm	Paste	R	
TiO_2 (Pd/Pt)	225	—	—	R	—
	25-60	14 ppm-1.5%	TF	SchD	2 min
	150-300	100–1000 ppm	TF	SchD	2 min
Au–WO_3	250-350	200-5000 ppm	TF	R	1 min
ZnO	267-600	1–100 ppm	Pellets, Xls	R	2 min
	200-400	1.0%	Disks	R	30 s
ZnO/Pt	300-450	Up to 8000 ppm	Thick F		—
ZnO (Ru, Ag)	100-400	0.20%	Paste	R	—
ZnO (Al,In)	200-350	2–1000 ppm	TF	R	2-5 min
$SrGe_{0.95}$ $Y_{0.05}O_3$	1000	3–100%	Nano TF	R	60–500 s
SnO_2	150-400	500–3000 ppm	TF, S-G	R	7-85 s
SnO_2/Pt, Pd	300-600	1-2%	TF	R	
	200-400	Up to 2%	TF	R	
SnO_2	150-250		TF	R, WF	
SnO_2/Si	250	10.6-100 ppm	TF	WF, CVC	1-4 m
SnO_2–Co_3O_4	200-250	1000 ppm	TF	R	
TiO_2–Nb, Pd	200-250	1000 ppm	TF, S-G	R	
ZnO	300		TF	R	
SnO_2–ZnO–	HT?			R	
CuO				R	
Fe_2O_3–6 wt%	320	500–2000 ppm	TF	R	4 s
Ag_2O				R	
In_2O_3	350		Por TF		10–60 s
Ga_2O_3–SiO_2	700	12.5–500 ppm	TF	R	30 min
Ga_2O_3	600	500 ppm	TF	R	
	300-900		PorFilterT	R	
NiO–TiO_x	250-300	1000 ppm	F	R	2-2.3 m
MoO_3–SiO_2–Si	300	2000–9000 ppm	TF	R	10–40 s
MoO_3–V_2O_5	150	1000–10 000 ppm	TF	R	20 s
TiO_2{2% Al}	200-400	500–1000 ppm	Porous TF	R	5 s
TiO_2–WO_3	200		S-G TF	R	1-20 m
Pt–SnO_2 (In_2O_3)	RT-50	100–4 vol%	S-G Por Th-k F	R	
SnO_2{F}			n-Xl TF	R	
TiO_2 nanotube	25-250	1000 ppm	Por TF	R	30 s

All the sensors, but a few provided in the Table 1, function by the interaction between a chemisorbed reducing gas and surface oxygen (where there is an electrical resistance change). In the case of SnO_2, the hydrogen molecule (H_2) is first dissociated over SnO_2 surface and the atomic hydrogen reacts with the oxygen ions producing water, which injects electrons to the conduction band of the semiconducting sensing material, thus increases the conductance. The reactions regarding the briefly abovementioned sensor operation is given by the Kröger-Vink notation in Figure 10 [17, 25].

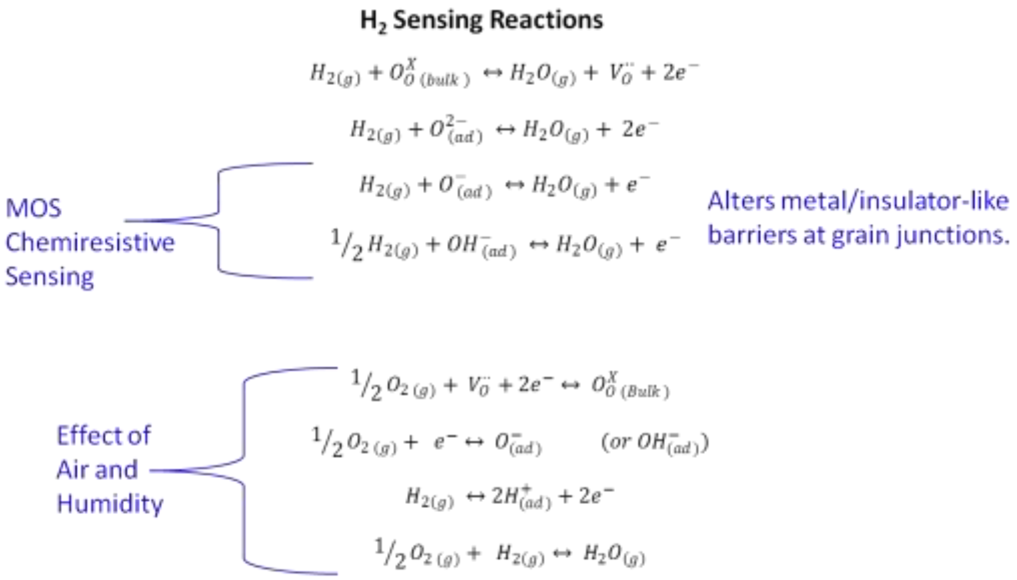

$$H_{2(g)} + O_{O\,(bulk)}^{X} \leftrightarrow H_2O_{(g)} + V_O^{\cdot\cdot} + 2e^-$$

$$H_{2(g)} + O^{2-}_{(ad)} \leftrightarrow H_2O_{(g)} + 2e^-$$

$$H_{2(g)} + O^{-}_{(ad)} \leftrightarrow H_2O_{(g)} + e^-$$

$${}^{1}/{}_{2}\,H_{2(g)} + OH^{-}_{(ad)} \leftrightarrow H_2O_{(g)} + e^-$$

$${}^{1}/{}_{2}\,O_{2\,(g)} + V_O^{\cdot\cdot} + 2e^- \leftrightarrow O_{O\,(Bulk)}^{X}$$

$${}^{1}/{}_{2}\,O_{2\,(g)} + e^- \leftrightarrow O^{-}_{(ad)} \qquad (or\ OH^{-}_{(ad)})$$

$$H_{2(g)} \leftrightarrow 2H^{+}_{(ad)} + 2e^-$$

$${}^{1}/{}_{2}\,O_{2\,(g)} + H_{2(g)} \leftrightarrow H_2O_{(g)}$$

Figure 10: Possible reactions during H_2 sensor operation **[17]**.

Another noteworthy point is the effect of the microstructure of the films or bulk sensing material on the sensing mechanism, which is strongly influenced by deposition technique of the sensing material and metal interdigitated metallization system. As explained in the previous section, the importance of the morphology is based on the understanding of the sensing mechanism as a semiconducting metal oxide sensor, which operates by a change in the electrical conductance determined by interaction of the reducing gas with the accessible volume of the sensing material. Thick film sensors with limited surface area tend to have longer response/recover times and low sensor signal output due to limited accessible volume for interaction of the target gas and sensing material. The sensing material target gas species interaction, as well as the level of percolation throughout the sensing material, and the diffusion rate through the intra or inter-grain diffusion (see Figure 6) affect the response/recover times. Incorporation of nanomaterials as a sensing material is the subject of extensive research currently since nanomaterials possess extraordinary high surface to volume ratios.

Much work has been devoted to increase the sensitivity of gas sensing films by microstructural engineering by adjusting the pore/grain size and distribution. Optimization of the microstructure and tailoring the sensing element of the ceramic sensing materials would result in optimum crystallinity and pore structure as well as small grain size with a high active surface area. [27, 28, 29, 30, 31, 32, 33, 34]. Microstructural control/engineering alone is not sufficiently enough to improve the capabilities of the sensor device, so significant amount of work has been devoted to the incorporation of catalyst to the sensor architecture and surface engineering as well. Catalytic additives such as noble metals (Pt, Pd, Au, and Ag) increased the surface coverage of the active layer by target gas via so-called spill-over mechanism [25, 5, 35, 36]. Apart from noble metals [37, 25] [38] [39], chromium(Cr), cobalt (Co), nickel (Ni), niobium (Nb), titanium (Ti), indium (In), iridium (Ir) and cupper (Cu) either in metallic phase or as an oxide [40, 25, 5, 41, 42, 43] [44, 45, 46, 47, 48, 49] are among the most frequently used catalyst/dopants/additives for sensor applications and all are well-known to increase sensitivity against H_2. Abovementioned metals/oxides not only catalyze the dissociation reaction of the hydrogen molecules that leads to subsequent spill-over but also the aforementioned metals/oxides provide additional surface sites for the chemical interaction of hydrogen atoms with the sensing material [50, 51, 52, 25, 53]. In addition to materials presented above Wildfire et *al.* developed coarsening resistant perovskite/pyrochlore gadolinium zirconates materials by using hydrothermal technique for H_2 sensing at high temperature. It was reported in the same study that use micro platforms of this material showed higher sensitivity toward H_2 in comparison to thin film counterparts [54].

2.2.2 Sulfur dioxide (SO_2)

Sulfur dioxide (SO_2) is one of the most major pollutants that has to be monitored and then transformed to the other compounds that do not present such a danger to the environment. SO_2 released into the atmosphere mainly originates from the combustion of hydrocarbons and natural reactions, such as volcanic eruptions and wild forest fires. As seen from Figure 9, the previous works on sulfur sensing focused on the use of semiconducting metal oxides to sense compounds such as SO_2 and H_2S, but the number of these publications are very limited compared to other gas sensing. In the case of SO_2, the percentage of the literature completed over the past few decades is less than 1% of the entire literature. Much of this work focused on the development of SO_2 sensors using liquid and solid electrolytes, as well as polymeric materials [55, 56, 57]. Table 2 provides the generalized results for sensing behaviors of different metal oxides against the most common target gases. The cross mark indicates possible usability of the metal oxide against the target gas [5].

The number of oxide compounds investigated for SO_2 is limited to W, Ni and Sn with a few exceptions. Among those few exceptions that are able to work at high temperature, three studies deserved to be mentioned in detail due to their unique employed strategies in order to increase the sensitivity and selectivity. Liang et *al.* and Morris et *al.* have modified a compact tubular sensor based on V_2O_5 modified NASICON (sodium superionic conductor) and a vanadium (V)-doped TiO_2, respectively [58, 59]. In the research conducted by Liang et *al.*, a NASICON composition was used as the basic material in the sensor design and V_2O_5-doped TiO_2 as the sensing electrode. The sensor which showed the best sensing properties toward SO_2 had a thick film of NASICON and 5 wt% V_2O_5-doped TiO_2 as sensing electrode tested at 300°C. Beyond this temperature, the sensing capabilities of the sensor drastically decreased and diminished especially after 500°C.

Table 2: Sensing behavior of different metal oxides to various gaseous species **[5]**.

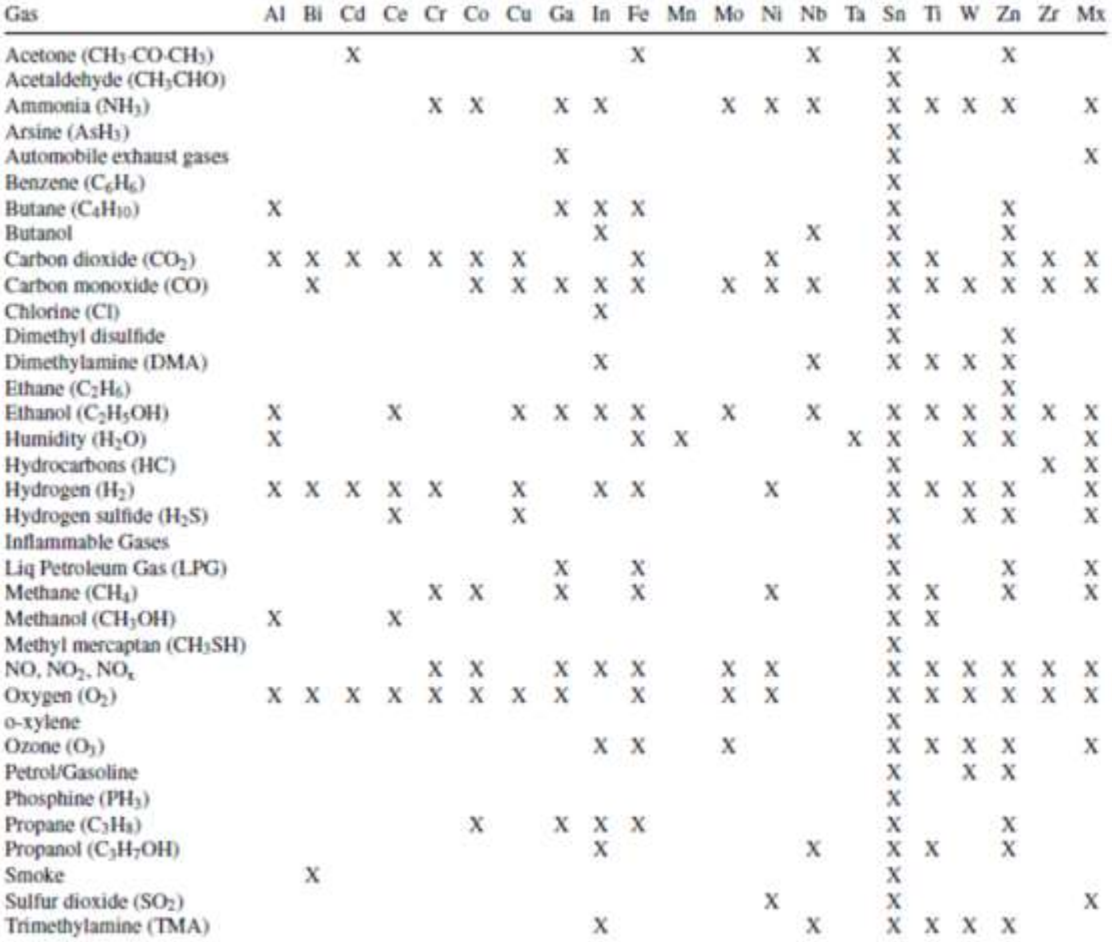

Gas	Al	Bi	Cd	Ce	Cr	Co	Cu	Ga	In	Fe	Mn	Mo	Ni	Nb	Ta	Sn	Ti	W	Zn	Zr	Mx
Acetone (CH_3-CO-CH_3)			X							X				X		X			X		
Acetaldehyde (CH_3CHO)																X					
Ammonia (NH_3)					X	X		X	X			X	X	X		X	X	X	X		X
Arsine (AsH_3)																X					
Automobile exhaust gases								X								X					X
Benzene (C_6H_6)																X					
Butane (C_4H_{10})	X							X	X	X						X			X		
Butanol									X					X		X			X		
Carbon dioxide (CO_2)	X	X	X	X	X	X	X			X			X			X	X		X	X	X
Carbon monoxide (CO)		X				X	X	X	X	X		X	X	X		X	X	X	X	X	X
Chlorine (Cl)									X							X					
Dimethyl disulfide																X			X		
Dimethylamine (DMA)									X					X		X	X	X	X		
Ethane (C_2H_6)																			X		
Ethanol (C_2H_5OH)	X			X			X	X	X	X		X		X		X	X	X	X	X	X
Humidity (H_2O)	X									X	X				X	X		X	X		X
Hydrocarbons (HC)																X				X	X
Hydrogen (H_2)	X	X	X	X	X		X		X	X			X			X	X	X	X		X
Hydrogen sulfide (H_2S)				X			X									X		X	X		X
Inflammable Gases																X					
Liq Petroleum Gas (LPG)								X		X						X			X		X
Methane (CH_4)					X	X		X		X			X			X	X		X		X
Methanol (CH_3OH)	X			X												X	X				
Methyl mercaptan (CH_3SH)																X					
NO, NO_2, NO_x					X	X		X	X	X		X	X			X	X	X	X	X	X
Oxygen (O_2)	X	X	X	X	X	X	X	X		X		X	X			X	X	X	X	X	X
o-xylene																X					
Ozone (O_3)									X	X		X				X	X	X	X		X
Petrol/Gasoline																X		X	X		
Phosphine (PH_3)																X					
Propane (C_3H_8)						X		X	X	X						X			X		
Propanol (C_3H_7OH)									X					X		X	X		X		
Smoke		X														X					
Sulfur dioxide (SO_2)													X			X					X
Trimethylamine (TMA)									X					X		X	X	X	X		

Morris et *al.* investigated sensing capabilities of TiO_2 with different levels of doping with vanadium (V) against different levels of SO_2 balanced with dry air (nearly 20% O_2 conditions). The sensitivity graphs shown in Figure 11-a indicate that upon exposure to 1000 ppm SO_2 at 440°C, there was almost a 30% resistance decrease observed with the response time 17 min. As seen in Figure 11-b, the maximum response obtained with a 60% decrease in the resistivity with 0.5% V-doped TiO_2 at 375°C upon exposure to 1000 ppm SO_2. An increase in the temperature decreased the sensitivity and eventually at ~600°C sensitivity (S) was about 0.05 [58]. The same researchers indicated that their interest in developing the resistive-type sensor using semi-conducting type materials centered on the simple architecture and control of selectivity compared to galvanic cell type of sensors. Galvanic types of sensors typically utilize a solid sulfate electrode as a sensing material. The decay in resistance after switching from a dry air to a flow of 1000 ppm SO_2 in dry air was fitted to a modified Arrhenius-type equation. It was claimed that at low temperature the recovery occurred with activation energy of about 80 kJ mol^{-1} [58]. This activation energy may be interpreted simply as desorption of the product of SO_2 oxidation i.e. SO_3 or SO^{-2}_4. At high temperatures (>600°C), we presume that the loss of the oxidation product (SO_3 or SO^{-2}_4) is diffusion limited with an essentially negligible temperature dependence for temperatures close to 800°C [58].

It is noteworthy to indicate that TiO_2 is the most successful semi-conducting metal oxide for detection of SO_2 at high temperature. Unfortunately, the sensitivity (S) decreases towards 0.01 as the temperature increases beyond 500°C [58].

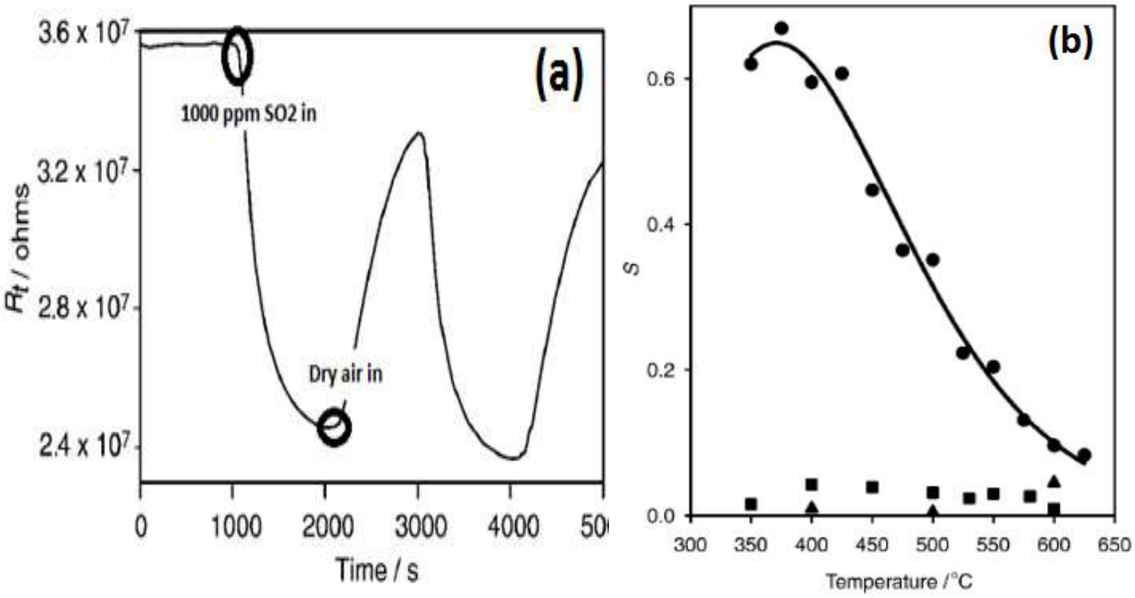

Figure 11 : (a) V-doped TiO_2 sensor operated at 440°C response curve against 1000 ppm of SO_2 **(b)** sensitivity (s) curves of un-doped (squares) and vanadium doped TiO_2 (spheres) **[58].**

CeO_2 is the last example of a semiconducting metal oxide tested and tailored for SO_2 sensor applications at high temperature. Varhegyi et *al.* concluded that resistance of the CeO_2 is not affected by the presence of SO_2 up to 500 ppm, unless the oxygen is not present in the testing environment in the wide temperature window from 300 to 800°C. In other words, chemically or physically adsorbed oxygen does not create surface states by extracting electrons from the conduction band, and/or physi-chemi adsorption do not occur due to stoichiometric perfection of the CeO_2 surface. Authors basically developed a better understanding of the SO_2-CeO_2 surface interaction, and bulk interactions and proposed several mechanisms regarding surface and bulk interactions of CeO_2 and SO_2 [60]. Authors first explained that the addition of O_2 to the N_2 flow, which resulted in resistance increase, is due to incorporation of oxygen into the oxygen vacancies and/or interstitial sites. Basically occupation of conduction band electrons and/or annihilation donor level associated with conduction band. Authors also stated that, the formation of surface space-charge regions cannot be excluded, but its role in the overall conduction cannot be distinguished by resistance measurements.

The resistance change caused by SO_2 can be attributed to the interaction of the SO_2 with the lattice oxygen as shown in the equations 2.21 through 2.24 in Kröger-Vink notation. The equations indicate that these electrochemical reactions eventually decrease resistance due to the release of electrons to the bulk of the material, however the formation of SO_3^- (Eq. 2.23) results in an electron transfer event, as expected the negative ion formation on the surface increases the sample resistance. Authors proposed that the interaction between the lattice oxygen and SO_2 as the controlling reaction within the possible mechanism provided through Eq. 2.21 to 2.24, instead much anticipated surface adsorbed oxygen with approaching SO_2 interaction. The reason behind the proposed sensing mechanism was proved by Auger electron spectroscopy (AES) of the sensor surface after long term exposure to SO_2 at 550°C. AES spectrum proved that the stoichiometry (atomic ratio of Ce to O) of the compound changed from 1:2 to 1:1. In other words, the surface of the compound transformed from CeO_2 to CeO by losing oxygen to SO_2 during exposure [19]. Two very important outcomes of this paper were the unexpected sensing mechanism and the utilization of surface sensitivity techniques for characterization.

$$SO_2 + O_{lattice} \rightarrow SO_3 + V_O^X \qquad \text{(Eq. 2.21)}$$

$$V_O^X \rightarrow V_O^{\cdot\cdot} + 2e^- \qquad \text{(Eq. 2.22)}$$

$$SO_3 + e^- \leftrightarrow SO_{3(ads)}^- \qquad \text{(Eq.2.23)}$$

$$2SO_{2(gas)} + O_{2(gas)} \rightarrow 2SO_{3(gas)} \qquad \text{(Eq. 2.24)}$$

Even though nickel oxide (NiO) is not common as a gas sensor material, it was the one very first materials tested for SO_2 sensing. Neubecker et *al*. studied gas sensing properties ultra-thin films of NiO_x as an active layer deposited by molecular beam epitaxy (MBE) over Si substrate for detection of H_2, NH_3, NO_2 and SO_2. Authors concluded that the potential work function (ϕ) change could be used as the prime sensor signal at room temperature upon exposure of the target gas. The material showed high cross sensitivity to NH_3 and NO_2, when using either stoichiometric (NiO) or highly oxygen contained forms (NiO_x, x>1) [61].

The most common semiconducting metal oxide used as a sensor material SnO_2 for various types of gases including but not limited to, NO_x, CH_3CHO, Benzene, H_2, CO, CO_2 as well as evaluation of deodorants [20, 62, 5], was also utilized in both the bulk and thin/thick film forms and tested at 200-500°C temperature window for SO_2 by Lee et *al.* Response time was quite large up to 20 min and the micromachining process compatibility was not satisfactory. The micromachined thin film of SnO_2 also showed low potential for SO_2 sensor, since it was also highly sensitive to H_2, C_2H_5OH, CO, NO_x, CH_4, H_2S, and CO_2 from room temperature up to 500°C with varying sensitivities. Another novel approach of SnO_2 for SO_2 sensors was realized by Lee et *al.* in which the authors mixed SnO_2 with different promoters such as MgO, CeO_2, Al_2O_3, Sb_2O_3, MoO_3 and V_2O_5. Among those oxides, MgO and V_2O_5 showed not only increased sensitivity, but also a decrease in the response time. However, the recovery was diminished by irreversible sulfate formation especially in the case of MgO beyond the temperatures of 500°C [63]. Girardin et *al.* studied SO_2 adsorption over pressed powders of SnO_2 through the use of Fourier transform infrared spectroscopy (FT-IR). It was concluded that adsorption of the SO_2 was drastically decreased after 200°C; this was further proved by conductivity measurements in which the change of the conductance was identical without using a reducing atmosphere up to 200°C. Especially after 500°C, the total desorption of SO_2 observed for the adsorbed SO_2 onto the SnO_2 surface occurs by a chemical reaction where the SO_2 and adsorbed oxygen ions (O_2^-, O^-) react to form SO_3, which subsequently leaves the surface in the gas phase. This behavior will be second the assumption in the model developed in the Chapter 6. Bakun et *al.* concluded that in the 250-500°C temperature range, chemisorption dominates the SO_2 inclusion into the surface of the oxide material. In the case of the Sb-modified SnO_2 surface, the kinetics of that reactions is further improved due to the interaction with the surface oxygen, which reacted to form the SO_3 complexes. [64, 65, 66].

Tungsten has numerous forms of stable oxides and suboxides. Those are WO, WO_2, W_2O_3, W_4O_3, $W_{17}O_{47}$, $W_{18}O_{49}$ and WO_3, corresponding to different oxidation states of W ranging from W^{+2} to W^{+6}. Due to these different oxidation states, W possesses high catalytic activity toward different types of reducing or oxidizing gases. WO_3 is a d^0 compound in a stoichiometric form, therefore it exhibits an insulator behavior. However, the non-stoichiometric forms of W oxides (WO_{3-x}) shows an n-type semi-conducting metal oxide with the band gap 2.7 eV and it is an important compound for various industrial applications. The W/O determines the semiconducting characteristic of the compound. The material has also good adhesion properties over other oxide, nitride and polycrystalline silicon surfaces, as well as, it can easily be chemically and physically etched, which makes it MEMS processing compatible. [35, 7, 5].

WO_3 has been tested for H_2S, O_3, NO, NO_2, NO_x, H_2, DMA, TMA, NH_3, ethanol, petrol, O_2, SO_2 and humidity with various morphologies as well as deposition techniques [5, 67, 68, 69, 55]. Among those wide range of reducing and oxidizing agents, it was observed that NO_x, H_2S and SO_2 were detected with high sensitivity compared to the other gasses. Different noble metal additives (Ag, Pt, Pd) were shown to increase the sensitivity as observed for other semiconducting metal oxides [5, 36]. Izu et *al.* sought a new directions by mixing prominent oxides such as V_2O_5, WO_3 and TiO_2 in the SO_2 sensing literature on the planar-type resistive sensor utilized two different electrode metallizations (interconnects or electrodes); those are gold (Au) and platinum (Pt). Authors concluded that the response value did not depend on the content of vanadium (V) but the type of electrode utilized and significant enhancement on the sensitivity was reported in comparison to WO_3 and TiO_2 stand-alone sensors [70]. Stankova et *al.* focused on deposition method and doping level of WO_3 as well as electrode geometry. A micromachined WO_3 based micro-hotplate sensor was deposited by RF (radio frequency) sputtering. They reported that the electrode geometry and effect of dopant agent have significant importance to sensitivity. SO_2 sensitivity tests were conducted in a CO_2 stream down to 1 ppb level. The grain size of the thin film was 15-20 nm. While the Pt doped sensors showed high sensitivity toward SO_2 balanced with CO_2, the un-doped sensor performed with better sensitivity towards 100 ppb of H_2S balanced with again CO_2. In addition to that, the authors also concluded that the geometry of the interdigitated electrodes regarding the gap size has an important effect on the sensor performance. The sensor equipped with 50 µm gap size electrode showed significant performance increase compare to sensor equipped with 100 µm gap size electrodes. In the case of the smaller gap size, the sensors showed better performance [71].

Shin et *al.* studied phase stabilities of WO_3-based noble metal loaded metal oxides by using a computational thermodynamic approach in an effort to correlate them with the reported sensing properties toward SO_2. According to these authors, there is not a notable change in the phase stabilities of W-S-O as temperature increased up to 800°C, except that the two phase region, gas and $WO_{2.96}$, slightly expands. It was noted by the authors that the thermodynamic phase stabilities near the stoichiometry of W-O in WO_3 are very complex and not yet completely understood or confirmed. Thus, there are many different versions of the W-O phase diagram and the existence of certain tungsten oxide phases, e.g., $W_{17}O_{47}$ and $W_{18}O_{49}$, are still controversial in the scientific community. As Shimizu et *al.* concluded that the change of the type of response from n-type to p-type (or vice versa), at temperatures higher than 500°C, might be associated with the eutectoid reaction at ~585°C involving the $W_{18}O_{49}$ and WO_2 phases. The solubility of dissociated SO_2 in WO_3 also may have an impact on the phase transformation temperature [72].

Shimizu et *al.* compared the sensing properties of WO_3, SnO_2, ZnO, TiO_2, In_2O_3 and 5.0 mol% MgO-In_2O_3 toward SO_2 in the 100-800°C temperature window. As shown in Figure 12-a, WO_3 showed superior sensitivity toward SO_2. Another point is that all semiconductors showed complicated temperature dependent responses. At 400°C WO_3, the oxide showed a resistance increase up to 1100%. In contrast, a resistance decrease up to 400% was observed at 600°C. It was stated that for temperatures lower than 500°C, the increase in the resistance due to formation of SO_2^- adsorbents and further electron extraction from the bulk on different oxygen adsorbed sites, which seems to be very unlikely due to electron density of the surface. However, no further explanation was given regarding the change in the response characteristic with the increasing temperature. In the same study, the authors also examined the effect of different types of noble metal loadings on the sensing behavior of the WO_3. It was revealed that 1% Ag addition significantly increased the sensitivity; however, in any case there was no response after 750°C. Figure 12-b shows the sensitivity-temperature response of the sensor. Both WO_3 and noble metal loaded sensors showed significant cross sensitivity problem when tested for NO_x [36] .

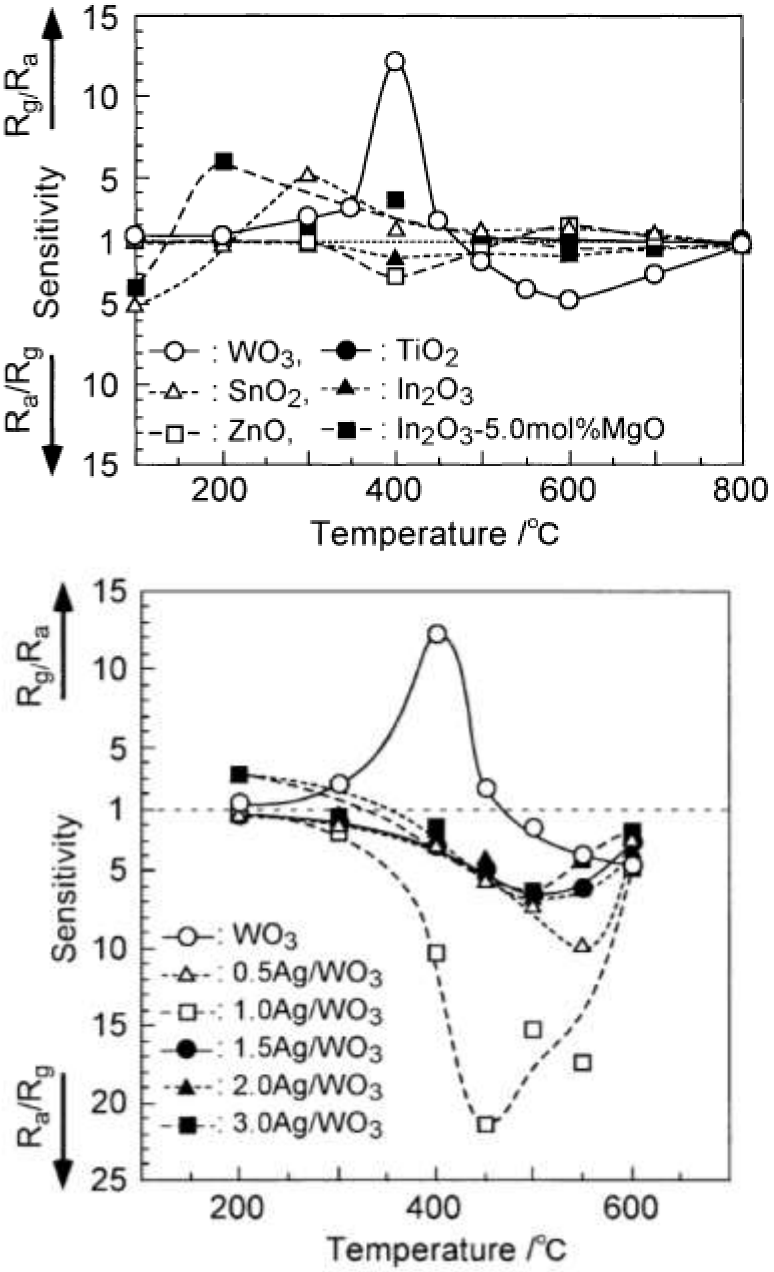

Figure 12 : (a) Temperature dependence of sensitivity to 800 ppm SO_2 of different semi-conductors **(b)** effect of different noble metal loadings to WO_3 **[36]**.

MoO_3 is another transition metal oxide has been utilized for sensors applications. Among different phases of molybdenum oxides, MoO_3 phase is the common choice for gas sensing applications. The material is an n-type semi-conductor with a band gap of 3.2 eV and it possesses very high electrical resistivity (10^{10} Ω·cm) with a low melting point (795°C). The latter two identify the basic restrictions of the material for high temperature sensor material applications. One of the special features of this material is its natural sensitivity without any promoters in the temperature range of 200 to 450°C toward NH_3 and NO_2. MoO_3 was first tested for NH_3, CO, CH_4, SO_2 and NO_2 by the Azad et *al.* either as a binary oxide or composite structure with ZrO_2. Authors discuss that redox reactions were primarily occurred on the surface. Another noteworthy point in this study is that author claimed that absorption of O_2 to stoichiometric surface at relatively high temperature is impossible [22]. It was proposed that interstitial oxygen ions and lattice oxygen were primary source of the redox reactions [22]**.** MoO_3 was also used as a sensing material by depositing over oxidized silicon with a 30 nm Al_2O_3 adhesion layer and Pt interdigitated electrodes. It was concluded that MoO_3 in the temperature regime of 250°C to 500°C was two times as sensitive to NO_2 than H_2 [73].

Imawan et *al.* Investigated gas sensing properties of MoO_3 modified with V_2O_5. Authors indicated that the electrical resistivity of the MoO_3 was drastically reduced when modified with V_2O_5, which is a convenient progress for gas sensor application. MoO_3 has a very high intrinsic resistance and is not well suited for sensor applications due to the difficulty in modifying the electrical conductance through redox reactions. Authors coated MoO_3 thin film with 50 nm V_2O_5 by RF sputtering and they were able to reduce the electrical resistivity by the creation of substitutional solid solution between the two oxides. Authors claimed that multilayer deposition of MoO_3 by the sputtering process increased the H_2 sensitivity, with very low NH_3 cross-sensitivity (see Figure 13). The H_2 concentration was 500 times higher than that of NH_3 and $SO_{2;}$ moreover the response to H_2 was 12 times that of SO_2. It is not possible to correlate the results of tests due to high concentration differences in the target gases [74]. The same group also stated that the improved sensitivity towards NH_3 through the addition of a Ti overlayer (deposited by a sputtering process. Another group discussed improved sensitivity and response time towards CO by addition of TiO_2 to MoO_3 [75, 76]. Prasad et *al.* tested MoO_3 and WO_3 at 450°C for NO_2/NH_3 balanced in synthetic air that is similar to automotive exhaust. Authors concluded that MoO_3 showed superior sensitivity toward NH_3 rather than NO_2 once compared with WO_3 that showed vice-versa. The authors commented on the sensing mechanism of MoO_3 towards NH_3 was the result of a stable chemical reaction during sensing; however, the NO_2 sensing behavior of WO_3 was dictated by a surface physic/chemi adsorption led mechanism [77]. The cross-sensitivity problem explained above (high NO_2 sensitivity) is the disadvantage of WO_3 for SO_2 sensing applications since many gas environments contains SO_2 also contains NO_2. This is because MoO_3 and complex molybdates are added to choice of sensing material list for SO_2 in our case. It is well-known that coal-powered power plants does contain significant amount of NO_2 but not NH_3.

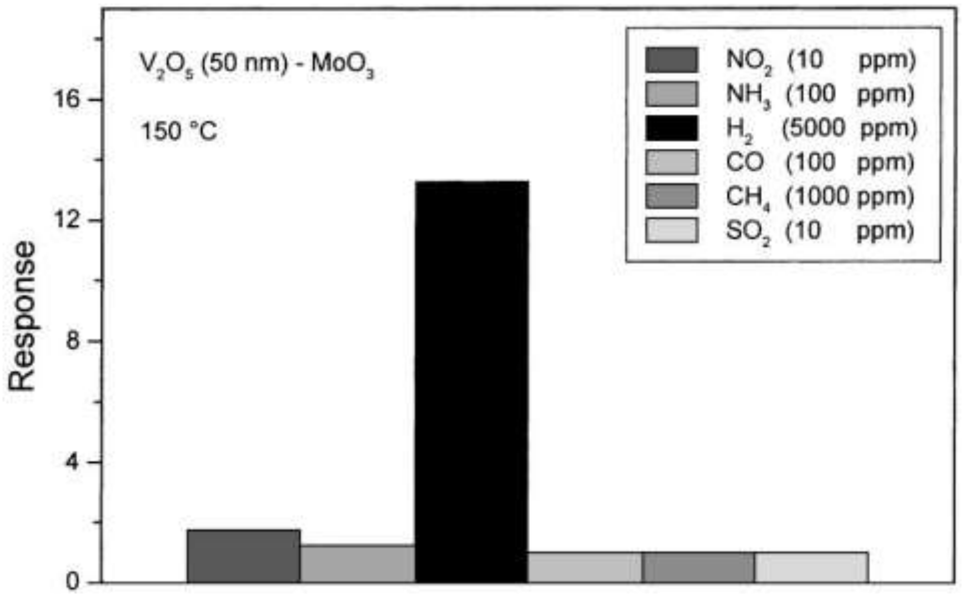

Figure 13 : Cross-sensitivity of the V_2O_5 (50 nm)-MoO_3 sensor toward various test gases at operating temperature of 150°C.

The semiconducting metal oxide, especially binary oxides, as a sensing material for SO_2 is limited to low temperature (<500°C) applications due to stability problem of the oxide in the highly reducing atmospheres. West *et al.* summarized the current situation of the SO_2 sensors for both types that employ semi-conducting metal oxide and solid electrolytes. It was concluded that current SO_2 sensor technology limited to near room temperature (~50°C) applications in the market. The same authors developed amperometric-type of sensor consisted of two different oxides ($LaCr_{0.98}O_3$ and $LaCr_{0.85}Mg_{0.15}O_3$) and Pt reference electrode by screen-printing over on oxygen-ion conducting YSZ substrates. In order to operate this sensor, a DC current 0.1 mA was driven between two electrodes and the voltage between one of these electrodes. The platinum electrode is the output as a sensor signal. The authors claimed that operating at temperatures near 900°C with 2 ppm of SO_2 (with a background 7 vol% O_2 balanced with N_2), the sensor showed 10% change in the resistance as a sensing signal. It was also claimed that such a change would easily be detected. The authors reported a nominal change of 0.1% drift after 1 month operation time. The authors did not mention either the sensing mechanism of the sensor cell or chemical state changes of the oxides during testing [56].

Among various physical and chemical strategies employed in order to detect reducing gases (CO_x, SO_x, H_2S, H_2, and NO_x), the solid state (electrochemical and semi-conducting metal oxide) sensors have been found to be more successful. Currie et *al.* developed micromachined solid state electrochemical sensors for CO_2, NO_2 and SO_2 by utilizing corresponding sulfates of Na, Ba and Ag. In order to fabricate the thin film sensors, the first target materials were prepared with the correct stoichiometry. The materials were patterned on the electrodes using a five sequential lift-off processes with at least six sputtering processes. The final sensor was composed of a thin film pattern with reference electrode, working electrode, sensing electrolyte, RTD, heater, and reference electrode. The final sensor architecture is shown in the Figure 14. The sensors were tested at 200-250°C and the sensors showed reasonable sensitivity to target gases with insignificant cross-sensitivity over 1000 ppm. The sensors showed cross-sensitivity to other aforementioned gases at the 0.1-100 ppm concentration level. It was also reported that SO_2 micro-sensors showed 1-2 s response time and 5 sec recovery time at 250°C [78].

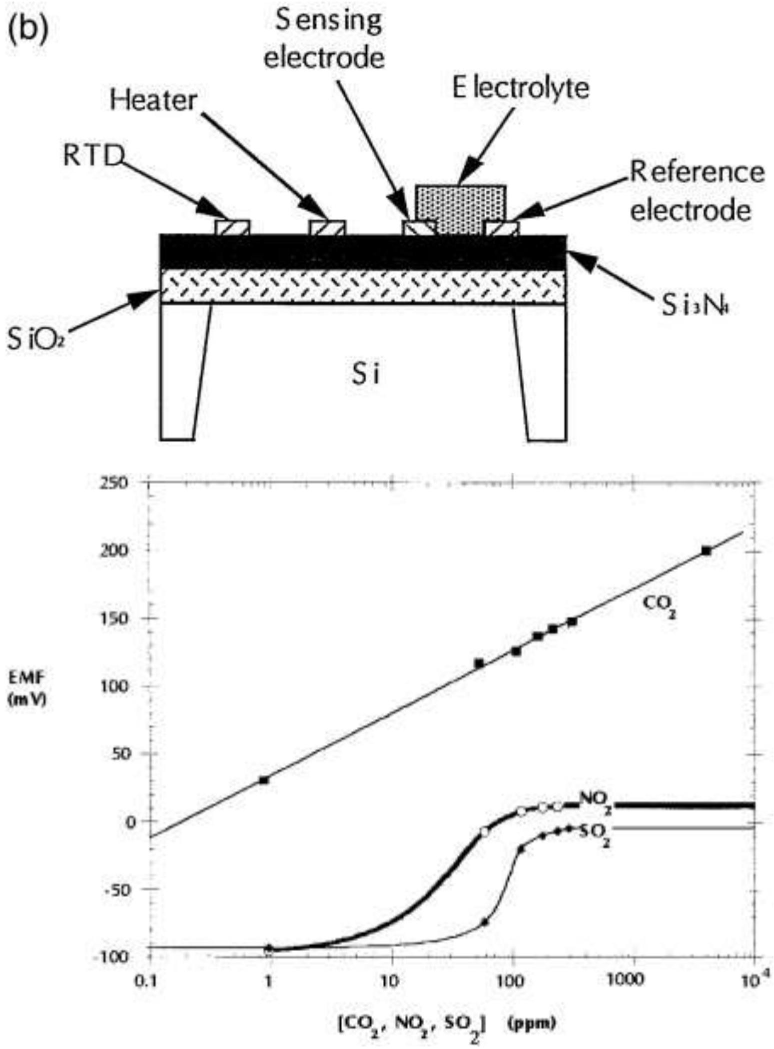

Figure 14 : (a) Sketch of cross-section of the micro-sensor and electrode structures on the self-supporting membrane **(b)** Sensitivity of the carbon dioxide sensor to other gases [4].

2.2.3 Hydrogen sulfide (H_2S)

Figure 9-a delivers the statistics over the number of works focused on different types of gases used in the scientific community. As seen from the image, although pollutants such as CO_2 and NO_x lead the list, developing H_2S sensors takes considerable attention in the scientific community. Figure 10-b provide relative percentages from which can be concluded that 32% of the sensor/sensing related work focused on CO_2 and NO_x pollutants, after that H_2 takes the third place with 11% due to its potential commercial value in the market. The research of H_2S gas sensors is roughly 2.5% of total research on gas sensors, which is far more than that of SO_2.

Semiconducting metal oxide sensors for H_2S detection have received much more attention than similar sensors to for SO_2. The main driving force behind this was the higher value in health/safety sensors over environmental sensors. The threshold exposure limit for H_2S is 10 ppm and one of the main gases utilized as a warfare agent during WWI [79]. With concentrations above 250 ppm, H_2S has a major effect on the human body, causing instantaneous death [80]. The following transition metal oxide based sensors have been successfully designed to detect H_2S; WO_3 and WO_3-based materials, CeO_2, SnO_2, ZnO, CuO, platinum and palladium oxides, indium oxides, silver based materials, TiO_2 and CdO sensors. Figure 15 provides a detailed description of H_2S sensing material systems, including the deposition techniques, operational usage and working principle of the designated sensor [80, 81, 82, 5, 83].

Literature related to H_2S sensor applications is quite a bit larger than that of SO_2. Although the size of the literature is remarkable, most of the works again are devoted to the semi-conducting metal oxides and the operation temperature of these sensors have been reported from room temperature to only 300°C. Most of the reports that have been presented have shown utilization of WO_3 and SnO_2 with stability and cross sensitivity issues.

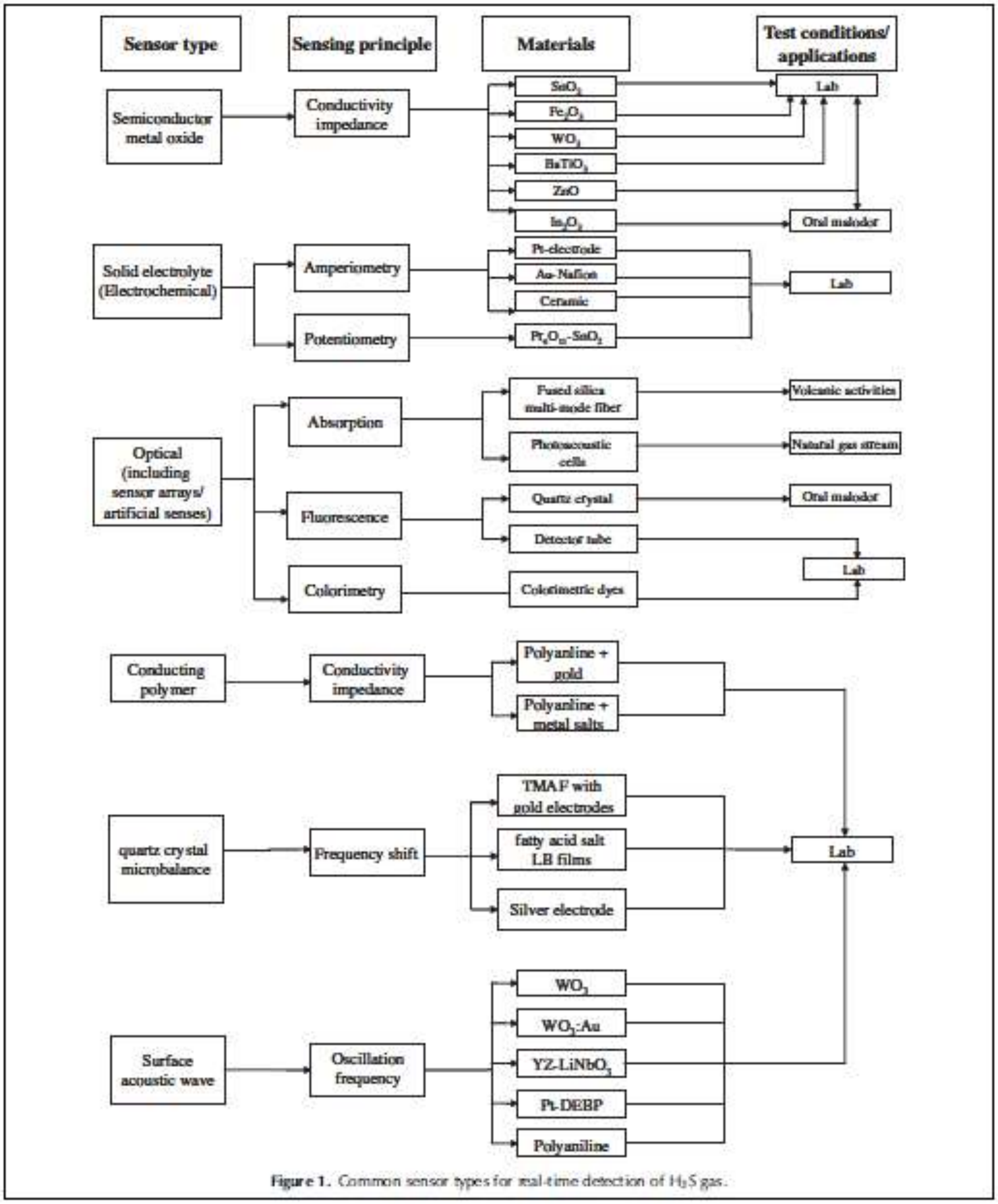

Figure 15 : A schematic classification of different sensor types for detection of H_2S **[80]**.

Dawson et *al.* utilized $Cr_{2-y}Ti_yO_{3+x}$ as a sensing material for H_2S. The material has a p-type characteristic at elevated temperatures (>250°C) and showed an increase in resistance upon exposure to H_2S (50 ppm) within a testing range of 250-500°C. It is the sole paper, at least to our knowledge, in the literature that provided temperature desorption curves for both H_2S and SO_2.

Figure 16 provides the temperature depended desorption curves. It is seen that H_2S exhibited two maxima at about 150°C and 470°C. The loss of SO_2 from the surface occurred at 470°C. It was concluded that a sensor that operates at 350°C can be cleaned by heat treatment, and a pre-treatment will increase the sensitivity of the sensor [84]. The data provided here will be one of the basic assumptions in the model developed by this work (in Chapter 5) using ECR to characterize the kinetics of SO_2 over oxide material.

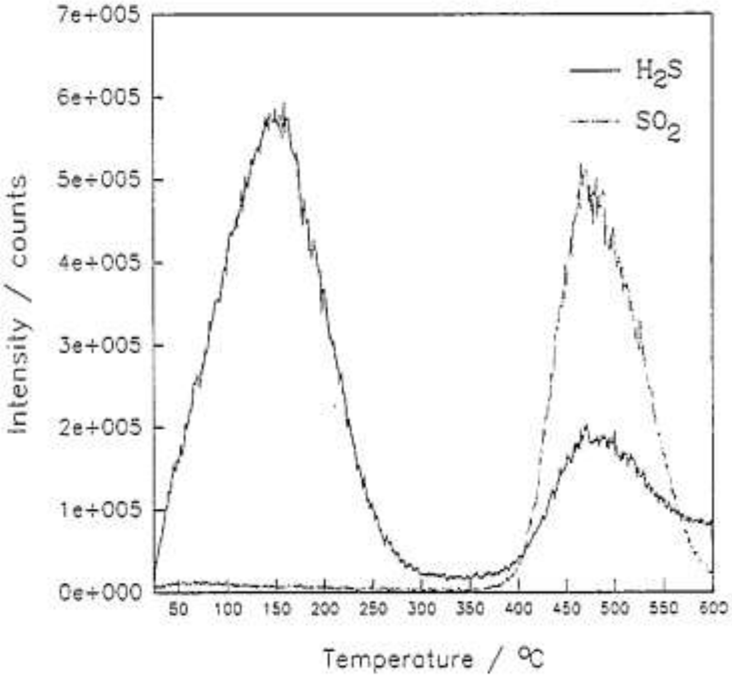

Figure 16 : Temperature desorption curves for H_2S and SO_2 **[84]**.

Barret et *al.* were performed a series of experiments with WO_3 and WS_2 for 200 ppm H_2S diluted in air. Sensitivity is defined in Eq. 25, in which R_a is the resistance in air, and R_g is the resistance in the test gas. The response time is the time taken by the sensor to achieve 90% of the total resistance change due to the chance in concentration of the test gas [85]. Figure 17 provides correlation between sensitivity, temperature and concentration in the study.

$$\boldsymbol{S = R_a - \frac{R_g}{R_a} = \frac{\Delta R}{R_a}} \qquad \text{(Eq. 2.25)}$$

Even though the conductivity of the WO_3 is much less than WS_2, WO_3 showed its highest sensitivity at lower temperature compare to WS_2; however, WS_2 was more sensitive compare to WO_3 at all temperature regimes as seen in the data given Figure 17. Also it has been shown that after 100 ppm of H_2S exposure, the sensor selectivity did not change at all and saturated; therefore, the both material are not able distinguish different concentration of the target gas.

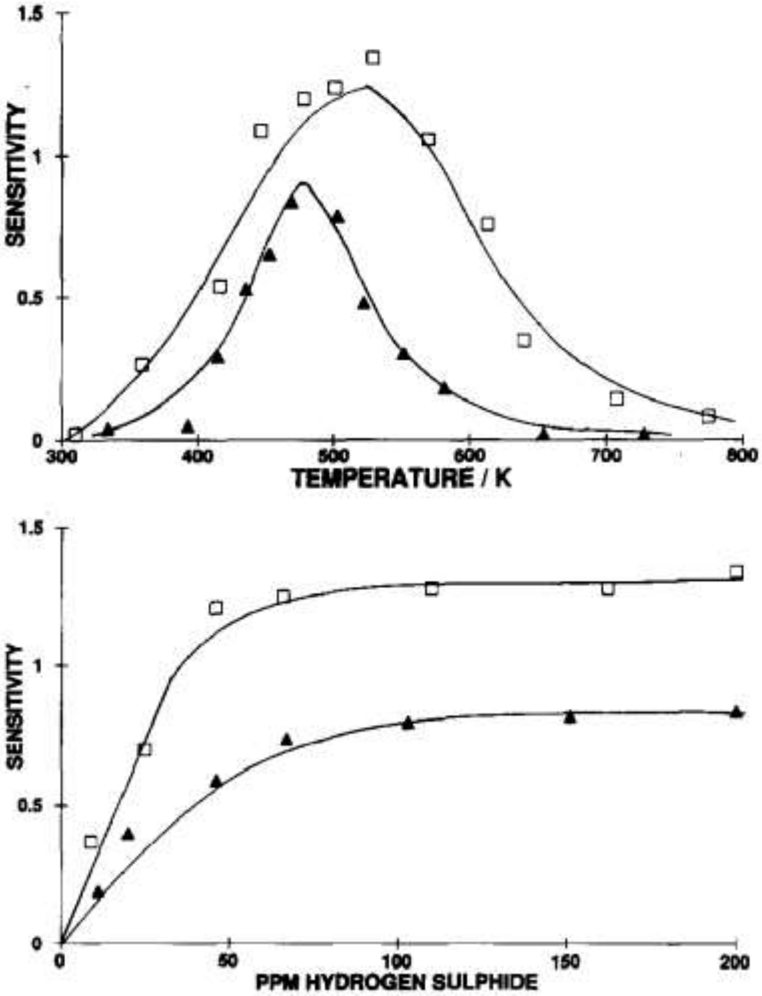

Figure 17 : **(a)** Sensitivity of WO_3 shown with solid triangles and WS_2 showed with rectangles with varying temperatures **(b)** Sensitivity of WO_3 and WS_2 at 195°C with varying H_2S concentration **[85]**.

Barret et *al.* conducted thermo-gravimetric analysis (TGA) which showed that there was no weight change in WO_3 on heating in air to 223°C; however, after introducing 50% H_2S to the test chamber for 30 sec, a significant weight gain occurred (up to 2%). In other words, the whole surface was covered by WS_2. Re-introduction of air to the sample surface resulted in a return to its original weight. The same authors confirmed that the product consisted of WO_3 and WS_2 by XRD analysis. It must be recalled here that XRD is not surface sensitive technique, so it fair to claim that the material surface is covered by WS_2. One of the most important outcomes of this paper is that the transformation between the two aforementioned phases was characterized. In addition, electrical conduction mechanisms of the two compounds were further established, where WO_3 is an n-type semiconductor and WS_2 is a p-type semiconductor. This data may explain the switch in the type of response characteristic of the WO_3 upon exposure to SO_2 (n-type to p-type or vice versa) which was observed by Shimizu. It is noteworthy to recall that SO_2 is byproduct of the oxidation of the H_2S. [36]. However, there was no comment indicating so in the Barret`s work. It was also observed in the same paper that the sensitivity diminished to a great extent after 375°C [85]. Fruhberger et *al.* conducted detailed XPS and UPS analysis at 200°C in order to obtain final chemical state of the H_2S exposed WO_3 surface at 200°C. Authors indicated that sensing mechanism is totally depended on the creation of oxygen vacancies (H_2S and lattice oxygen interaction and subsequent desorption of by product, SO_2) on the surface and excluded the chemical reaction between surface adsorbed oxygen and H_2S [86], however in the same study it was confirmed that transformation of WO_3 to WS_2 under very high H_2S partial pressures is substantial as Barret et *al.* reported the same validity but for very low H_2S partial pressures. Another point in the Fruhberger`s work is that, authors themselves found quite surprising occurrence of the S 2p around 167-168 eV and attributed to this binding energy SO_4^{2-}, however it is known that 2p peak positions for S in SO_2 (which is by product of H_2S and O_2 reaction) and SO_3 (which is by product of SO_2 and O_2 reaction) sit at the same binding energy position like SO_4^{2-} [87, 88, 89]. Dawson et *al.* showed that desorption of SO_2 from another transition metal oxide (TMOs) type sensor material ($Cr_{2-y}Ti_yO_{3+x}$) does not occur before 400°C which directly opposes Fruhberger`s sensing mechanism description. Under these circumstances it is fair to speculate that n-type/p-type response transition in WO_3 upon exposure to H_2S or SO_2 may be (but not limited to) attributed formation of sulfide and subsequent total/partial coverage of the surface by this phase.

Antonik et *al.* investigated the microstructural effects on the sensing capabilities of WO_3 thin films deposited by RF sputtering over *yz*-cut $LiNbO_3$ as an active layer for H_2S sensing. It was concluded that the as deposited amorphous state of the films were less sensitive for H_2S detection compared to crystalline films, which were obtained though annealing at 350°C. It was shown that film roughness was increased with the increasing annealing time, potentially due to polycrystalline grain growth. Therefore, the authors attributed the increased sensitivity with an increase in surface roughness by polycrystalline growth of the material [90]. Niu et *al.* studied $REFeO_3$ (RE: Eu, Gd) rare-earth mixed oxides with the perovskite structure for detecting C_2H_5OH, H_2S, gasoline and H_2. Figure 18 shows the relative sensitivities and temperature dependencies of the different $REFeO_3$ structures. The sensors were set up in a glass chamber and kept under a continuous flow of fresh air for 10 min before the measurement. $EuFeO_3$ showed reasonable sensitivity; however, the sensor response diminished at 400°C. $GdFeO_3$ showed better sensing characteristic after 400°C, but no data was given after this point [91].

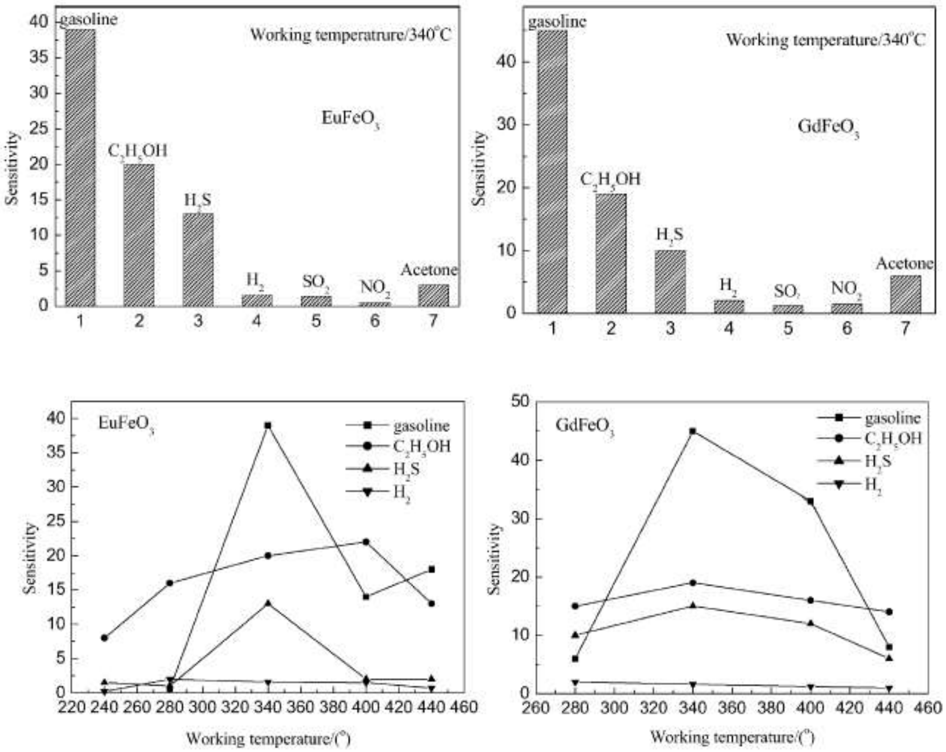

Figure 18 : $REFeO_3$ (RE: Eu, Gd) sensors cross-sensitivity and temperature dependency **[91]** .

More recently Liewhiran et *al.* studied the H_2S sensing capabilities of SnO_2 by using 5 -20 nm in size functionalized nanoparticles produced by flame-spraying. The flame-spraying is a simple method which is similar to thermal spraying techniques. It may be further classified as a physical deposition technique. The nano-particles showed a very high surface area, where the specific surface area was 141.6 m^2. The sensing layer was deposited over alumina substrate by spin coating. At 300°C, the sensitivity (S) of the sensor against 10 ppm H_2S was 8, while sensitivities against 200 ppm CO, 500 ppm H_2 and 200 ppm C_2H_2 were 1.8, 1.5 and 2.0, respectively. Response time was in the range 3-5 sec in the case of H_2S. Authors indicated that the high sensitivity against H_2S, compare to SO_2 sensitivity, is the natural result of the surface interactions and transformation of H_2S to SO_2 after extracting chemisorbed oxygen ions from surface [92]. The possible reactions during H_2S exposure of any kind of semiconducting metal oxide utilized sensor are given in the Eq.26 through 2.30 [92].

$$H_2S\,(ads) + 3O_s^{2-} \leftrightarrow SO_2(g) + H_2O + 6e^- \tag*{(Eq. 2.26)}$$

$$2H_2S\,(g) + 3O_s^{2-} \leftrightarrow 2SO_2(g) + 2H_2O + 3e^- \tag*{(Eq. 2.27)}$$

$$H_2S\,(ads) + 3O_s^{2-} \leftrightarrow SO_2(g) + H_2O + 3e^- \tag*{(Eq. 2.28)}$$

$$H_2S\,(g) + 3SnO_2 \leftrightarrow SnS_2(g) + 2H_2O \tag*{(Eq. 2.29)}$$

$$SO_2\,(g) + O_i^{''} \leftrightarrow SO_3(g) + 2e^-\,(interstitial) \tag*{(Eq. 2.30)}$$

In addition to materials discussed thus far for H_2S sensor applications, some novel materials were also examined for their ability to detect H_2S. The operation temperatures for those alternative materials were restricted to 25-300 °C. Fe_2O_3-$Fe_2(MoO_4)_3$ was one composition that showed high sensitivity towards H_2S at 225°C. $La_{0.7}Pb_{0.3}Fe_{0.4}Ni_{0.6}O_3$ and $CdIn_2O_4$ were also used but did not exhibit sufficient sensing at a temperature range of 100-350°C. Different ferrites were utilized but sensitivity was too low in the range of 0-10% resistivity change even at temperatures between 100-400°C [93, 94, 95, 96]. Literature given above is complementary to summary of the sensing materials shown in Figure 11. Another type of sensor deserves to be mentioned is Nernst type electrochemical sensors where the potential difference is the sensing signal (for the thermodynamic electrochemical reaction through the electrolyte). These type of electrochemical sensors can be divided into two groups such as liquid and solid electrolyte sensors. For hydrogen sulfur sensor applications, solid electrolyte type design is frequently utilized in comparison to liquid electrolyte type design. Electrochemical design can be further divided into two subset, based on their operational mechanism. Those are called amperometric and potentiometric electrochemical sensors [80].

CdS was found to be the only sulfide which demonstrates predominantly an ionic conduction mechanism at very low partial pressures of sulfur (0.00007 Torr). Schneeberg et *al.* used AgI solid electrolytes with auxiliary Ag_2S phase and Ag reference electrode. Unfortunately, the low melting point of compound and onset of electronic conduction at about 450°C limited the usage of material [97]. CaS with CaF_2 produced promising results, however the response time was too slow. Vangrunderbeek et *al.* worked on sodium ß-alumina based sensors which showed an increase in the sensitivity; however, the use of the Na_2S auxiliary dispersed phase was unsuccessful. Interestingly, the contact mode of those phases showed superior sensing behavior. The Na-ß-Al_2O_3 family exhibited reasonable sensing behavior at 500-600°C [98]. Surface acoustic wave (SAW) sensors have been used for detection of H_2S [86, 80]. A SAW sensors for H_2S were fabricated on a single crystalline $LiNbO_3$ and $LiTaO_3$ substrates by using WO_3 and SnO_2 as an active layers, respectively. This type of sensor does not suit to high temperature applications since the active sensing material was SnO_2 as well as WO_3, which possess serious stability problems at elevated temperatures under reducing atmospheres. Nevertheless, SAW sensor design has proven to be one of the best choices for high temperature applications and further improvement may be seen once the active SAW area is decorated with high temperature stable nanomaterials [99, 100, 80].

Recently, Kersen and Holappa studied non-conventional sensing material for H_2S by modifying Fe_2O_3 with $Fe_2(MoO_4)_3$ thick oxide films. Iron oxides were shown to be well studied in the literature as a H_2S sensor, and molybdenum oxides are known for their reversible reactions with sulfur compounds. The authors prepared $Fe(MoO_4)_3$ by a solvothermal method and deposited the material over alumina substrates as a thick film. The material was heat treated at 650°C, which converted the surface of iron molybdate to iron oxide. The sensing tests were carried out with 1, 10 and 20 ppm of H_2S diluted in N_2. It was reported that material showed a decrease in resistance upon exposure to H_2S and the response and recovery times were 7 and 15 min, respectively at 225°C [96].

As discussed by many researchers, it is desirable for sensor applications to deposit the sensing material with highly porous network in order to maximize solid-gas phase interaction. For this purpose, Sun et *al.* utilized carbon nanotubes as a template for subsequent hematite (α-Fe_2O_3) growth by thermal decomposition of $Fe(NO_3)_3$ in a super critical CO_2 temperature modified via ethanol at 150°C. The catalytic chemi-luminescence was used as a sensor signal and it was observed that the response and recovery times were less than minute. The sensor recovery was almost perfect against as low as 10 ppm H_2S balanced in air at 109 and 134°C, respectively [83]. Chaudhari et *al.* utilized 50-60 nm in grain size TiO_2 with different additives including Al_2O_3, CuO, MnO_2 and Pb_3O_4 as H_2S sensing material. Authors concluded that 5 wt% Al_2O_3 together with 0.5 wt% Pd is the best composition that increased the sensitivity (S) up to 0.8. The maximum sensitivity was reached at 250°C against 200-1000 ppm of H_2S, after this point the sensitivity was almost unchanged until 325°C, but after this peak point, there was a step decrease observed in sensitivity [101]. Shirsta et *al.* reported that H_2S sensors were fabricated using polyaniline (PANI) nanowires decorated with gold nano-particles for room temperature applications. Functionalization of the PANI with gold nano particles resulted in room temperature operation. The sensors were highly sensitive down to 0.1 ppb concentration of H_2S, which was accompanied by a resistance decrease upon exposure to target gas. The sensing mechanism of the gold decorated conductive polymers were based on the compound formation between gold and sulfur, where the AuS formation results in subsequent replacement of two protons [102].

Chapter 3. High Temperature Electrodes for Chemical Sensing Applications

Initial experiments of the micro scale sensors showed that the Pt IDEs were degrading during stabilizing thermal processing and testing as well. Therefore, research was directed to the development of highly stable Pt based electrodes for high-temperature sensor applications. Bilayer and composite Ti, Ta, Hf, Zr and Pt thin films were investigated and tested up to 1200°C for 48 h. Two different electrode architectures with specific composition and deposition sequence were developed that would maintain the needed microstructure and electrical properties over the duration of the sensor processing and testing to 1000°C. In addition, a lift-off patterning process was developed for the composite electrode film permitting the fabrication of the desired H_2 and H_2S micro-sensors composed of the compositional nanomaterial systems previously described [103].

3.1. Introduction

Thin films of noble metals (silver (Ag), gold (Au), platinum (Pt), palladium (Pd), ruthenium (Rh)) have widespread applications in various microelectromechanical (MEMS) devices such as electrodes for micro-sensors, interconnects, bridge structures, cantilevers or active electrical leads for micro-heaters, structural monitoring sensors and thermocouples for gas turbines, and fuel cell systems operates at 600-800°C, as well as with the increased necessity for enhancing functionality together with miniaturization requirements for integral passive parts of low temperature (1000°C) co-fired ceramic (LTTC) microelectronic devices such as piezoelectric/electrostrictive actuators, resistor and capacitors. Among other noble metals, Pt is well-suited for high-temperature or corrosive environment applications, since it possesses a high melting point and is resistant to oxidation and chemical reaction. However, Pt has several drawbacks especially processed or operate at high temperatures (>800°C), where the metal demonstrates a high level of coarsening/agglomeration and weak adhesion when deposited on oxide or nitride surfaces, such as those typically utilized in MEMS design (such as Al_2O_3, SiO_2, Si_3N_4). In other words, upon exposure to high temperature processing or operation, thin Pt films uncover the underlying oxide or nitride substrate, and the film separates into a discontinuous array of islands.

Platinum thin films are used in various microelectronic and micro-sensor applications. The microstructural, chemical, and electrical stability of these films under high-temperature conditions are of major concern. In addition, stability is also a concern for potential extended use in specialized microelectronic applications, especially when the films are used as thin, two-dimensional interconnects or electrodes connecting active components at elevated temperatures. Typical applications of these high-temperature films are aligned with electrodes/interconnects for chemical sensors, micro-heaters and -hotplates within microelectromechanical systems (MEMS) [104, 105, 106, 107, 108, 109] Recently, more advanced MEM systems have been applied within extreme environments, which includes high temperatures and harsh chemical reactants, such as micro-chemical emission sensors, -structural monitoring sensors,-thermocouples, and -fuel cell systems that are utilized at temperatures >600-800°C [110, 111, 112, 113, 114, 115, 116].

High melting point noble metals are most suited for extreme environment applications. Platinum, with its relatively high melting point (1773°C) and excellent chemical inertness, has long been utilized for MEMs devices capable of operating at elevated temperatures. Pt and other noble metals have a great chemical inertness; however, these metals show poor adhesion and high surface tension towards oxide surfaces. Budhani et *al.* demonstrated an interface modification between thermally grown aluminum oxide (Al_2O_3) and thin Pt films via reactive sputtering with low levels of oxygen in order to obtain a 20-30 nm Pt_xO_{1-x} layer prior to pure platinum metal deposition. Adhesion tests showed a higher level of adhesion compared to the conventional Pt over Al_2O_3 couple. The authors indicated that strong Pt_xO_{1-x} to Al_2O_3 bonding and interdiffusion at the interface were responsible for the enhanced adhesion [117]. Although the controlled oxidation of a sub-layer of Pt showed promise for enhanced wetting and adhesion to oxide substrates, various researchers have focused on incorporating alternative metal/metal oxide layer compositions. These thin coatings were deposited to improve noble metal adhesion, as well as, to improve the thermal stability over prolonged exposure to high temperatures. High temperature operating conditions lead to the development of many structural defects, such as hillocks, film delamination, surface cracking, voids

---

and grain coarsening, which all eventually result in non-uniform film morphology and variable electrical response, [104, 106, 105, 107, 108, 118, 119, 120, 121]. At high temperatures (≥700°C), grain coarsening and hillock formation are the major mechanisms that break the percolated granular network across the polycrystalline film [105, 122, 123, 124, 125]. Since low-temperature sputtering and evaporation techniques typically produce films with high surface area granular structures, these films possess an extremely high driving force for sintering and grain growth processes. High-temperature operation permits the required diffusional kinetics for accelerated grain growth, resulting in the coalescence of the grains and the formation of a poorly percolated structure [124, 126]. In other words, the total interfacial and surface energy of the thin film can be minimized by reducing ceramic-metal contact area by creating islands of Pt material. The destruction of the integrity of the continuous film eventually results in complete loss of electrical continuity, which diminishes the functionality, reliability and sensitivity of the micromachined devices.

Metals such as Ti and Ta have been proposed and demonstrated with variable success to decrease both Pt grain coarsening and hillock formation. Lee et *al.* optimized the procedure first defined by Budhani et *al.* for deposition of Pt over insulating oxide layers with improved adhesion. According to this procedure, platinum deposition under an oxidation atmosphere, followed by inert atmosphere deposition of Pt and subsequent annealing of silicon substrate at 400-1300°C, removed the remaining O_2 in the Pt film [127]. Recently, Tiggelaar et *al.* compared the use of the Pt_xO_{1-x} adhesion layer to the use of Ti or Ta adhesion layers. These layers were deposited by sputtering onto silicon and Si_3N_4 substrates. After annealing between 400-950°C under inert and oxygen containing atmospheres, their electrical and structural performances were characterized [128]. The authors concluded that the operational reliability of Pt films with Ti and Ta adhesion layers are limited to temperatures below 650°C and 850°C, respectively. In the same study, the fast diffusion behavior of Ti and the resultant changes to the wetting characteristics of Pt on the Ti layer over different ceramic layers (Al_2O_3, Ta_2O_5, SiO_2 and Si_3N_4) were also described. Firebaugh *et al.* used a similar Ta adhesion strategy on silicon rich silicon nitride. This study states that the adhesion layer migration and coarsening were the major contributors to the Pt film degradation processes. The same group showed that utilizing a thin Ta adhesion layer and a thick Pt top layer with a ceramic capping layer as an oxygen diffusion barrier (Si_3N_4, Al_2O_3) improved the durability of the Pt thin films utilized in microreactors. A significant lifetime increase was reported in the case where a 300 nm Al_2O_3 capping layer was used. Firebaugh *et al.* showed that also, the use of a thicker Pt films delays the formation of the initial hole defect, as well as, lower the hillock growth rate [105]. In addition, Jeong *et al.*

investigated the effect of Ta capping layers over a thick Pt top coating and reported an increase in the lifetime of the Pt film with an increase in the thickness of the capping layer [108].

A few researchers have recently shown the use of a Zr adhesion layer for Pt thin films which resulted in greater stabilization of the Pt films to oxide surfaces during high-temperature operation. Maeder *et al.* compared the use of a Zr adhesion layer to that of Ti and Ta adhesion layer over a Pt electrode within a Pb-based ferroelectric thin film structure [129]. The Ti layer showed its inability to restrict microstructural changes and chemical interdiffusion between the active layers and the substrate. The authors demonstrated the superior features of Zr as an adhesion layer, compared to the Ta counterpart, in terms of the lower reactivity towards lead (Pb), as well as, the desirable diffusion and oxidation characteristics. Mardare et *al.* proposed the use of a Zr adhesion layer for PZT-capacitor electrodes. These authors showed that it is possible to deposit Pt films at lower temperatures with a Zr adhesion layer compared to the Ti counterpart [119]. Howard *et al.* utilized a similar strategy for thin Pt films for capacitor applications by utilizing Zr or Hf as an adhesion layer; these adhesion layers enhanced Pt bonding through the formation of an intermetallic phase. The authors also indicated that self-limiting nature of these adhesion layers prevented excessive diffusion to the top of the film when the bottom electrode was subjected to high temperature annealing (500-1000°C) [104]. Cunha *et al.* also reported improved high temperature stability of Pt thin films on sapphire substrates by utilizing both a Zr adhesion layer and a thin 1.5 nm ZrO_2 layer deposited between multiple Pt films in an alternating fashion to form the complete composite electrode structure. The researchers demonstrated the method of co-sputtering a Pt/10%Rh alloy with Zr (10^{-5} O_2 partial pressure) as the composite electrode, which showed further stability. These works, as well as a few others [107, 130, 131, 132, 133] showed that alloying or the inclusion of impurities has a significant effect on the grain boundary mobility, which is valid for both thin films and bulk materials.

The sintering and coarsening mechanisms have a significant impact on the high-temperature behavior of sputtered Pt films, as well as, the electrical conductivity of these films. The addition of an intermediate metal thin film layer has been shown to initially improve the adhesion between oxide substrates and noble metal thin films; however, these films have shown significant microstructural alterations when processed at temperatures between 200 and 800°C. The aim of this study is to better understand the degradation mechanism of sputtered Pt films with common adhesion layers (such as Ti, Ta, and Zr) at temperatures ≥1000°C. This temperature regime has not been investigated by previous researchers in the area. In addition, the information gained on the microstructural evolution of both the adhesion layer and Pt film (and their interrelation) will be used to develop an efficient strategy to control the overall degradation of the continuous film. The main focus of this work will be to suppress coarsening and hillock formation through the distinct control of the composition and thickness of the adhesion layer, as well as, the control of the interdiffusion and migration of adhesion layer atoms throughout the Pt film. As shown by a few researchers [130, 131, 132, 133], the intentional addition of refractory metal-metal oxide secondary precipitates within the Pt grain boundaries can limit the sintering/coarsening mechanism by Zener-pinning. This work will show the utilization of refractory metal Zr, and further investigation of a more durable and less mobile Hf adhesion layer [103].

3.2. Experimental

The adhesion layer compositions and Pt electrodes were sputtered on polished Al_2O_3 substrates through a magnetron sputtering technique (CVC 610 DC Magnetron Sputtering Station) at 100 W. Primary gas (argon) pressure was 50 mTorr for all coatings. All metal depositions were completed with a base pressure of 3×10^{-6} Torr. The sputtering unit is equipped with a 2 inch diameter sputtering target. The platinum thin films were all deposited onto alumina ceramic substrates that were heated to 200°C by a quartz lamp heater located behind the sample holder. The deposition temperature was elevated to this temperature to improve atomic surface mobility. The temperature was restricted to 200°C to permit the future use of high-temperature, stable photoresists for patterning electrodes through a lift-off process. All adhesion layers were deposited to the same ~35 nm thickness, as well as Pt layer with ~425 nm in thickness, in order to retain consistency between each film alteration. Prior to the experiments, processing correlation was completed for each adhesion layer individually in order to insure a consistent thickness. Thicknesses were confirmed with a Tencor Alpha-Step 200 profilometer to an accuracy of ±3 nm and SEM cross-sectional observations. The annealing studies, which mimics the high temperature operation conditions of the Pt coated samples, were completed at 800°C and 1200°C in a conventional tube furnace (MTI GSL 1600X). The heating/cooling rates for the isothermal annealing steps were kept constant at 5°C/min. The annealing time was varied from 1 to 48 h under a N_2 atmosphere (with a background O_2 and H_2O content of 2 ppm and 3 ppm, respectively) in order to evaluate microstructural alteration of the Pt film. In order to evaluate the thin film morphology, the surfaces of the samples were examined by Scanning Electron Microscopy (SEM, JEOL 7600F) after each annealing step. Migration behavior of the different adhesion layers, and the surface chemical state after 800°C and high-temperature 1200°C annealing processes, were examined by Energy-dispersive X-ray Spectroscopy (EDS) and X-Ray Photoelectron Spectroscopy (XPS, PHI 5000 Versaprobe XPS). The EDS spectra was obtained using an Oxford INCA 350 connected to JEOL 7600F SEM. XPS spectra was recorded by PHI SUMMIT software. XPS was also used to verify the intermetallics Pt species. The X-ray source was operated at 15 kV and 25 watts using Al Kα (1486.6 eV) radiation. The films were analyzed by a combination of 117.40 eV survey scan and 23.50 eV detailed scans of relevant peaks. A 0.5 eV step was used for the survey scan and a 0.05 eV step for the detailed scan. Prior to spectral analysis all coatings surfaces were cleaned to remove atmospheric and post-depositional contamination with Ar ion sputter cleaning at 2 kV accelerating voltage for 30 seconds. During measurement, the analysis chamber pressure was maintained at (~10^{-11} Torr). Resistivity of the Pt films with different adhesion layers were measured using van der Pauw's technique after heat treatment [134]. Finally, micro electrode fabrication was completed by a modified lift-off process. A positive resist (AZ 3330-F) typically used for reactive-ion etching (RIE) procedures was spin-coated over an alumina substrate to a thickness of 3.5 µm. A conventional lithography process was carried out to define an interdigitized electrode (IDE) pattern. After pattern transfer, the wafers were given a post-bake at 120°C for 5 min to strengthen the photoresist [103].

3.3. High Temperature Degradation of Pt Films with Conventional Adhesion Layers

3.3.1 Platinum without adhesion layer

Platinum films were deposited onto polished alumina substrates without any adhesion layer by the sputtering method previously described. The as-deposited Pt films were ~425 nm in thickness. After annealing at 1000°C for 1 h, a vermicular-shaped Pt microstructure was formed with an average Pt grain size of ~300 nm (Figure 19). The SEM micrograph (not included) also shows that further annealing of a similar sample to 1200°C for 1 h further separated the structure into distinct Pt islands with the increased grain size of ~1-3 µm. As previously discussed, the grain coarsening and hillock formation is typical of low-temperature sputtered Pt films on oxide substrates after high-temperature annealing. The high-temperature annealing process resulted in the complete destruction of the desired conductive film structure. The initial fine granular structure (with high surface to volume ratio) was significantly altered by sintering and grain coarsening. After each annealing shown in these micrographs, there was nearly a magnitude increase in average grain size. The annealed Pt films on bare alumina substrates shown in Figure 19 will be considered as the baseline samples for the rest of the paper. Adhesion layer incorporation and compositional film modifications will be contrasted to these experiments. The adhesion layers were examined in terms of their diffusion behavior and microstructural evolution after heat treatments at different temperatures, and these results will be described in the next subsections.

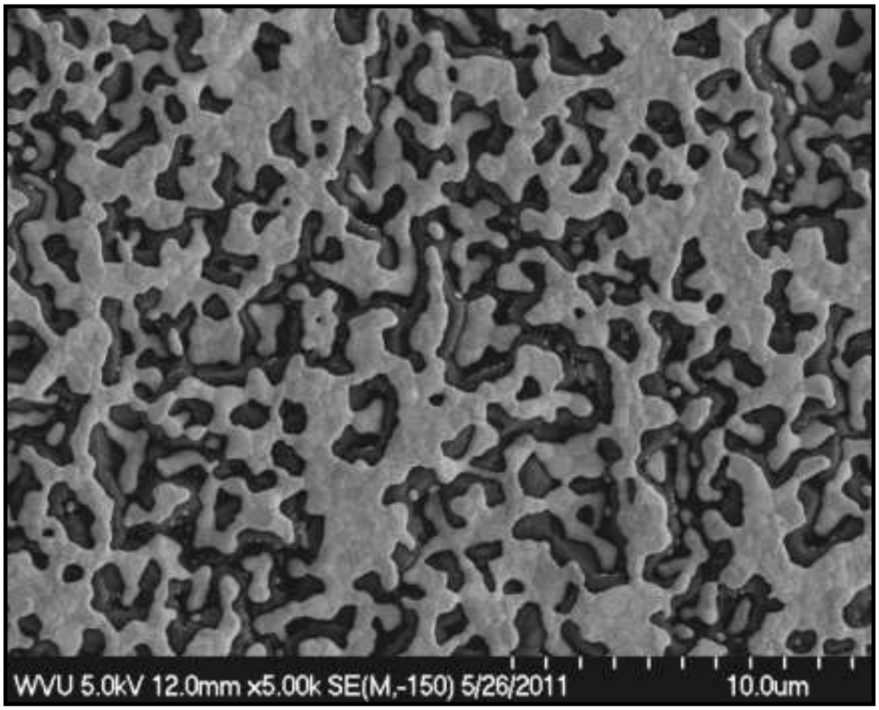

Figure 19 : Pt film surface after annealing 1000°C for 1 h.

3.3.2 Platinum with tantalum adhesion layer (Ta+Pt)

The investigation of the effect of adhesion layers for Pt sputtered films was initiated with titanium (Ti) thin films, but the behavior of these films were shown to be inferior to Ta, and therefore, the discussion of the microstructural stability of adhesion layers will start with tantalum (Ta) films. The instability of Ti adhesion films has also been well-documented in literature [135, 105, 110]. In the case of Ta, the material is a refractory metal that has been previously utilized as an adhesion layer for Pt metallization films, but the primarily focused on operation at temperatures <800°C [105, 107, 108]. The Pt film with the Ta adhesion layer was annealed at 800°C for 1 h in N_2. XPS analyses of the top surface of the Pt film showed that Ta diffused through the entire film thickness (see Figure 20). At the surface, the Ta was present in the stable oxide form (Ta_2O_5). The broadness of the peaks suggests that there are two distinct chemical states, elemental Ta and Ta_2O_5. The determined binding energies of the Ta $4f_{7/2}$ (26.5 eV) and $4f_{5/2}$ (28.4 eV) peaks match well with the values reported in the literature for Ta_2O_5 [136]. When a similar Ta+Pt film was processed at 1200°C for 1 h annealing, the film displayed significant Pt granular segregation. SEM and EDS analysis showed that the Ta adhesion layer partially remained on the substrate surface in sparse areas (as seen in Figure 21 -a and -b). EDS analysis (not shown) confirmed the presence of a higher level of Ta in the area circled within the figure. This remaining adhesion layer which consisted of Ta/Ta_2O_5 agglomerates provided an intermediate for the Pt grain surface retention and grain boundary pinning.

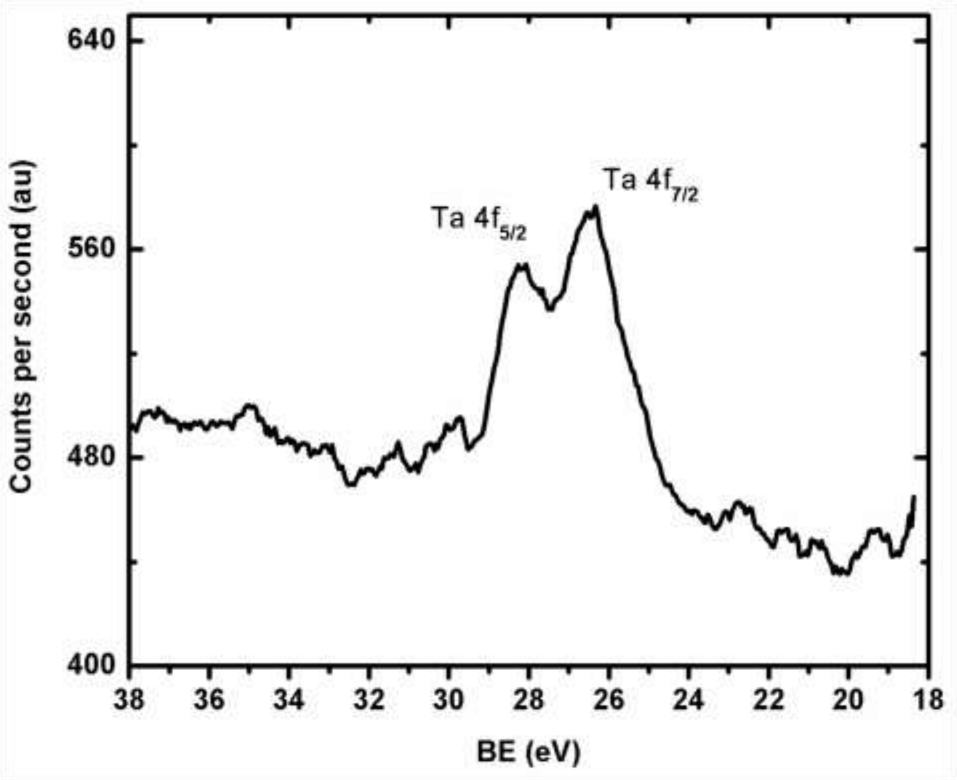

Figure 20 : XPS detailed spectrum of Ta+Pt film after annealing at 800°C for 1 h.

As the XPS analysis showed for the 800°C annealed Ta+Pt metallization, the presence of Ta on the Pt film surface shows that there is significant Ta migration, and thus, significant depletion of adhesion layer. Such fast Ta diffusion to the surface is not desired for platinum metallization. It is important to note that for these processing conditions the incorporation of the more refractory metal/metal oxide (due to grain boundary migration) within the Pt grain boundaries did not significantly impede the Pt grain coarsening. The result was a low percolated granular network, as shown in the SEM micrograph in Figure 21-a. Regardless of the improvement compare to Ti+Pt film, it can be stated that Ta is not the appropriate candidate for Pt film adhesion for operation temperatures ≥800°C.

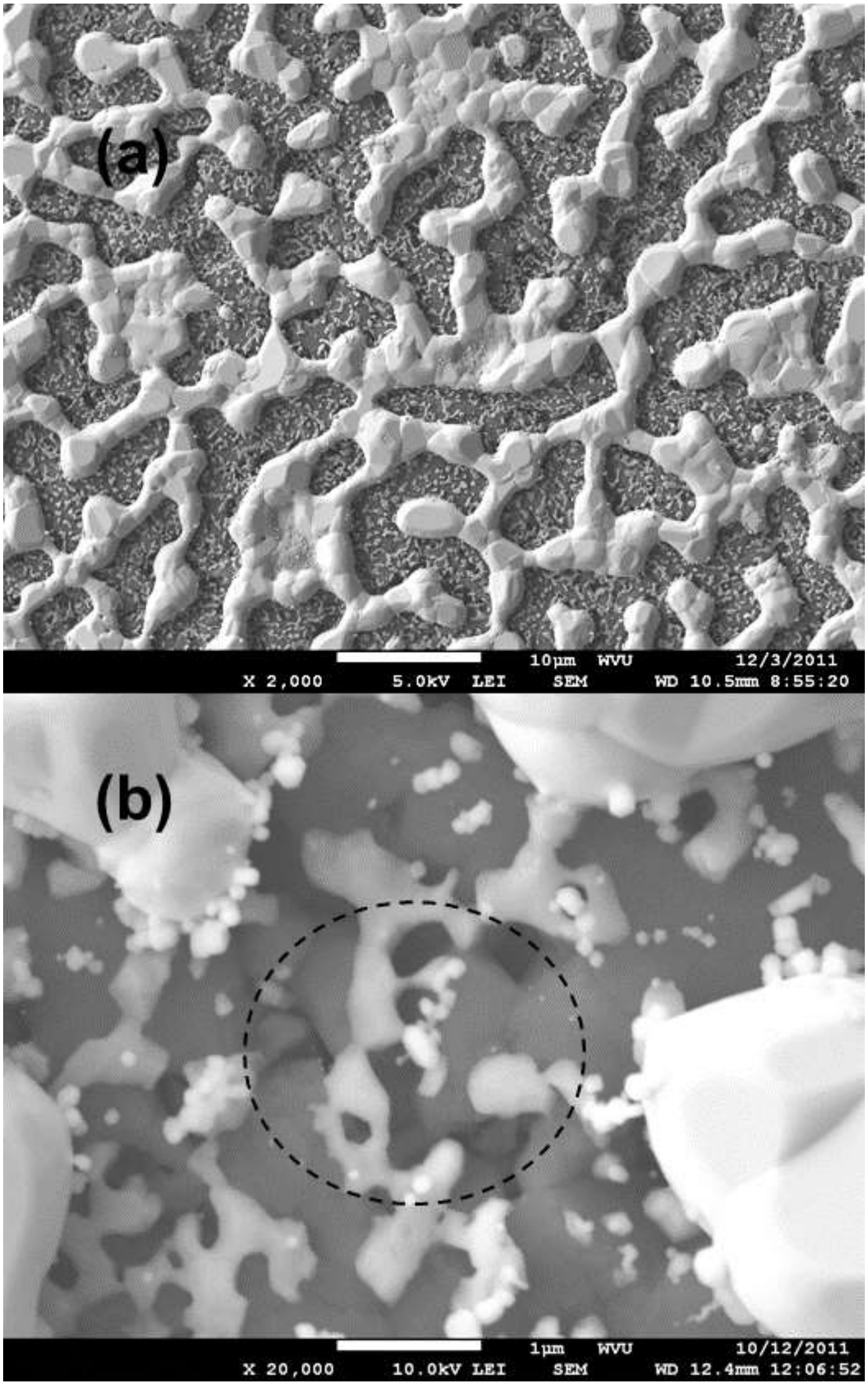

Figure 21 : (a) SEM micrograph of Ta+Pt film after 1200°C for 1 h annealing. **(b)** High magnification SEM micrograph of the Ta+Pt film annealed at the 1200°C for 1 h **[103]**.

3.3.3 Platinum with zirconium adhesion layer (Zr+Pt)

The stabilization of the Pt thin film can be enhanced by choosing an adhesion layer which forms an intermetallic and/or oxide phase with Pt with an even greater refractory nature [104, 110, 137]. Two such compositions are Zr and Hf. Both of these metals easily oxidize at high temperature, similar to Ta and Ti, but the oxidation states of Zr and Hf are stable at 4+, which limits their defect states and diffusivity. Zr and Hf are prone to form strong intermetallic phases with Pt which enhances adhesion to Pt. Ficalora et *al.* reported that $HfPt_3$ and $ZrPt_3$ are highly stable refractory materials with greater bond strength and chemical stability compared to their carbide counterparts [137]. The sheet resistivities of these intermetallics are shown to be comparable or lower than platinum metal [104, 138]. A Zr adhesion layer was deposited with a similar thickness (~35 nm) onto the alumina substrates using the same procedures discussed for the Ta composition. Again, the ~425 nm Pt thin film was sputtered over the Zr adhesion layer. The Zr+Pt film was annealed at 800°C for 1 h and XPS was completed on the top surface of the Pt film. The XPS spectrum (see Figure 22) showed no presence of Zr on the top surface within the detectable limit of the XPS unit. This result indicates that Zr diffusion was far below that shown by Ta for the 800°C annealing condition [103].

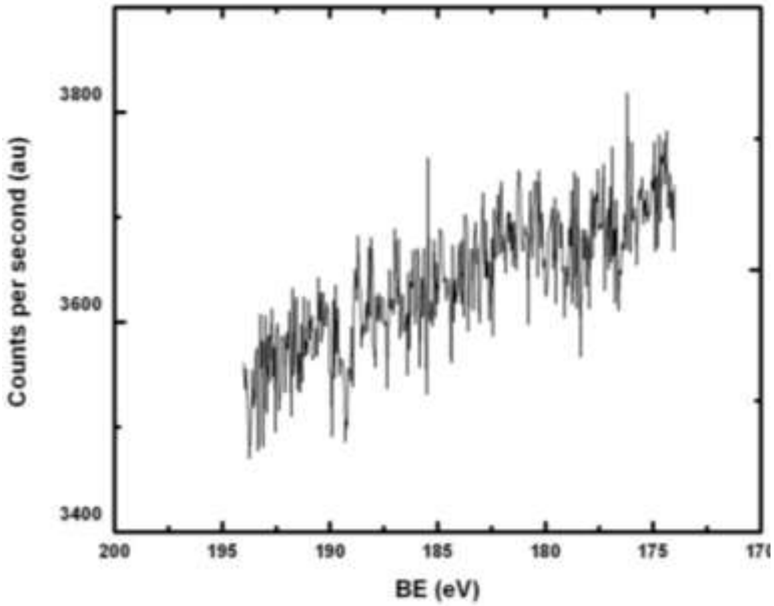

Figure 22 : XPS detailed surface scan of the 800°C annealed Zr+Pt bilayer coating.

When the as-deposited films were processed at 1200°C for 1 h, the SEM micrograph showed that the Zr adhesion layer retained a high level of Pt percolation over the entire area (Figure 23-a). The overall Pt granular structure consisted of a few islands of large Pt grains (and large pores) surrounded by a fine mixture of submicron Pt grains. This is in far contrast to that seen for the Pt film that utilized the Ta adhesion layer annealed at 1200°C for 1 h (see Figure 21-b).

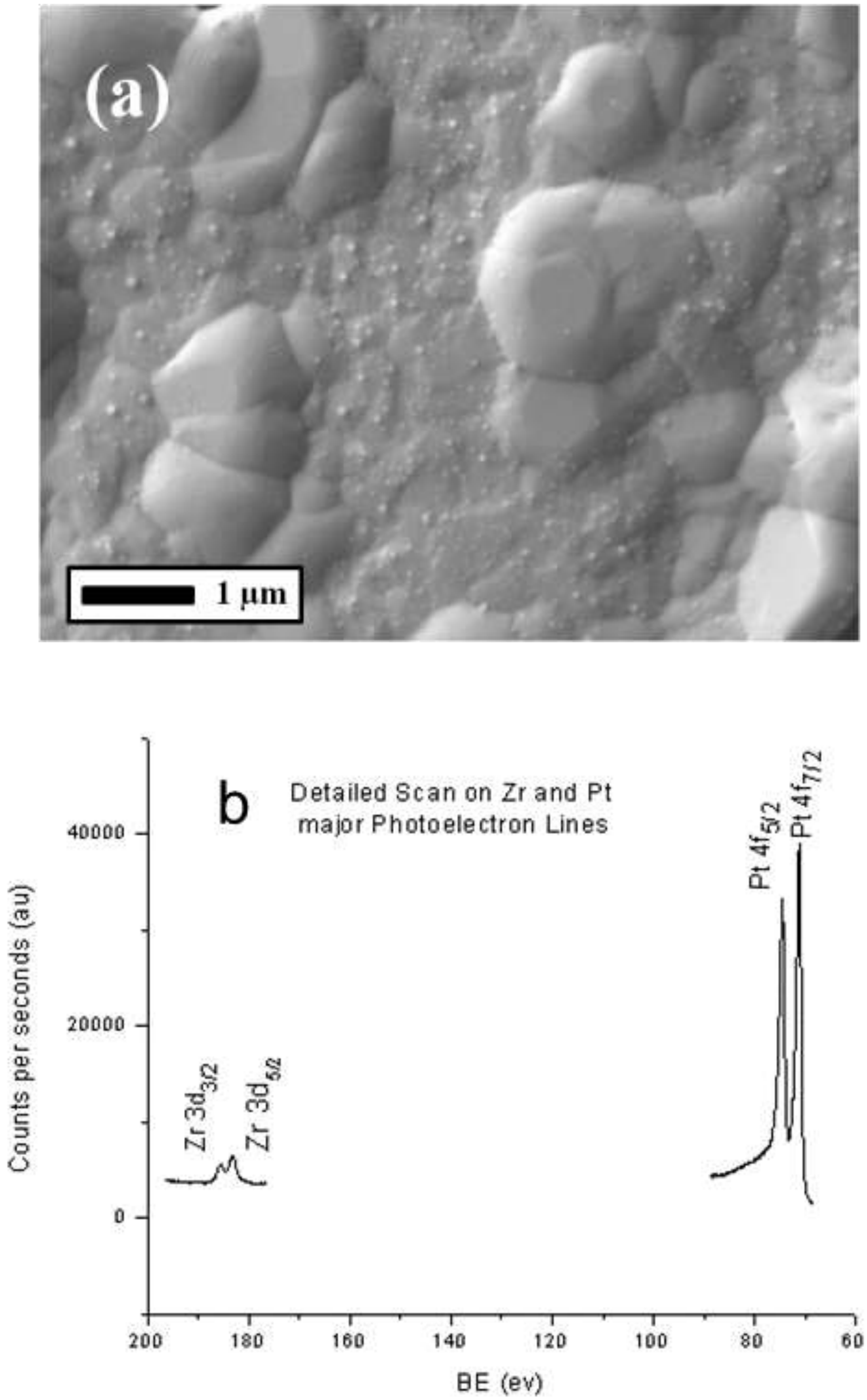

Figure 23 : (a) SEM micrograph of the Zr+Pt bilayer coating annealing after 1 h at 1200°C. **(b)** XPS detailed spectra of the Pt and Zr 4f peak positions after 1 h at 1200°C.

The XPS detailed spectrum obtained for this higher annealing temperature showed the presence the Zr 3d and Pt 4f photoelectron lines (Figure 23-b). The doublet was composed of the Zr the $3d_{3/2}$ and $3d_{5/2}$ peaks positioned at 185.7 eV and 183.3 eV, respectively, and the Pt $4f_{5/2}$ and $4f_{7/2}$ positioned at 71.1 eV and 74.4 eV, respectively. These binding energies match well with the values reported in the literature for both ZrO_2 and pure metal Pt [136]. Although the Zr+Pt microstructure showed an improvement over the samples that included the Ta adhesion layer, the early stages of the microstructural rearrangement and Pt grain coarsening was still present. It was evident from Figure 23-a that the microstructure had the potential to evolve and progress to the stages seen for the other experiments, although at a slower rate. It could be assumed that the percolated Pt network would be destroyed with extended exposure to 1200°C. This progression can be seen in Figure 24-a, where the SEM micrograph shows that after the sample was thermally processed for 5 h at 1200°C, the fine Pt microstructure was completely consumed by the large Pt grains. The final microstructure included large interconnected lines of Pt grains with average sizes ~2 μm. The Zr/ZrO_2 adhesion layer was shown to be still intact and evenly distributed over the alumina substrate (see Figure 24-a); although, it was now composed of a coarsened granular structure. Figure 24-b displays the grain morphology of the Zr adhesion layer after 5 h annealing at 1200°C. In this case, the Pt grains coarsened at their natural rate and the kinetics of this process was not impeded by the presence of migrating Zr, intermetallics or the development of ZrO_2 precipitates within the Pt grain boundaries. The low migration of the Zr from the adhesion layer into the bulk Pt film allowed for the retention of the Pt layer, which is in contrast to the Ti+Pt and Ta+Pt films at these temperatures. The ultimate example of the progressive destruction of Pt film can be seen in Figure 25, in which the morphology of the Zr+Pt bilayer coating is shown after 15 h at 1200°C.

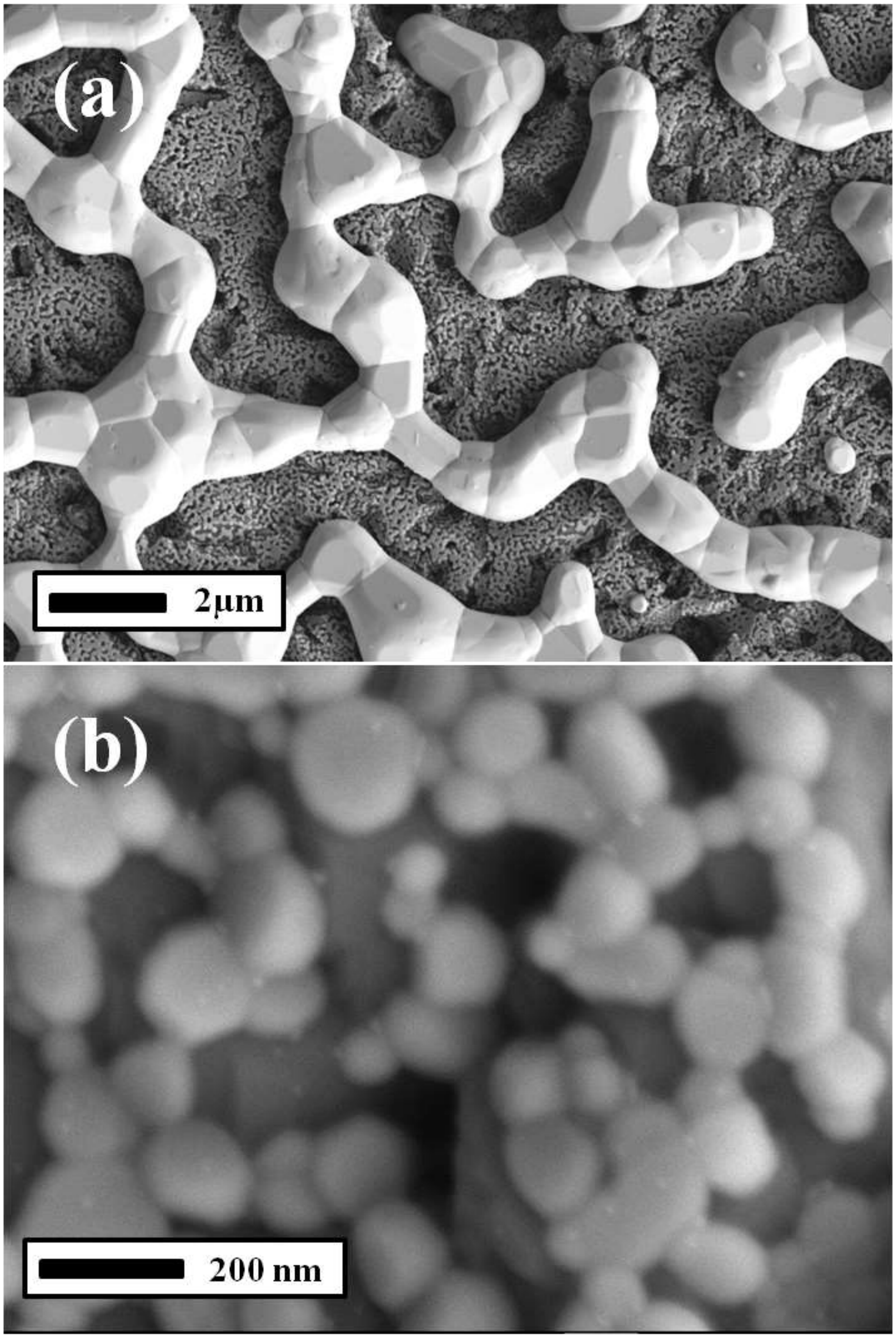

Figure 24 : (a) SEM micrograph of the Zr+Pt bilayer coating annealing after 5 h at 1200°C. **(b)** SEM micrograph of the Zr adhesion layer after 5 h annealing at 1200°C.

As a conclusion for the bilayer Pt films, as seen from Figure 21-a and -b, the greater part of the ~35 nm Ta adhesion migrated into Pt film and accumulated within the bulk Pt film as fine intergranular precipitates (which was similarly found to an even greater extent for the Ti+Pt composite film). In the case of Zr+Pt, the adhesion layer remained intact even when processed to 1200°C for 15 h. This phenomenon can be explained in terms of the low diffusion of Zr into the Pt bulk, unlike that showed for the Ti or Ta compositions. However, as seen in Figure 24-a and Figure 25, the Zr+Pt combination had finally succumb to the natural grain coarsening after the extended thermal treatment at 1200°C. These results show that even though an adhesion layer may be stabilized to retain wetting of the Pt film to the oxide substrate (or oxide film), a strategy must be implemented to limit the coarsening of the Pt grains for the thermal exposure. The diffusion or precipitation of a dissimilar second phase within the Pt grain boundaries is required in order to restrict grain growth migration, and thus, retain the percolated Pt electrode at temperatures ≥800°C. Therefore, strategies which incorporate a specific adhesion layer composition and a separate composite-Pt bulk film layer are required in order to address the influence of the two failure mechanisms. An example would be the sputtering of pure Zr as the adhesion layer, while sputtering a composite of Zr and Pt as the bulk electrode composition. The formation of phases such as ZrO_2 or intermetallics ($ZrPt_3$) within the Pt electrode may therefore limit the Pt grain coarsening and retain the fine microstructure over various operations or processes [104] [129, 130, 131, 103].

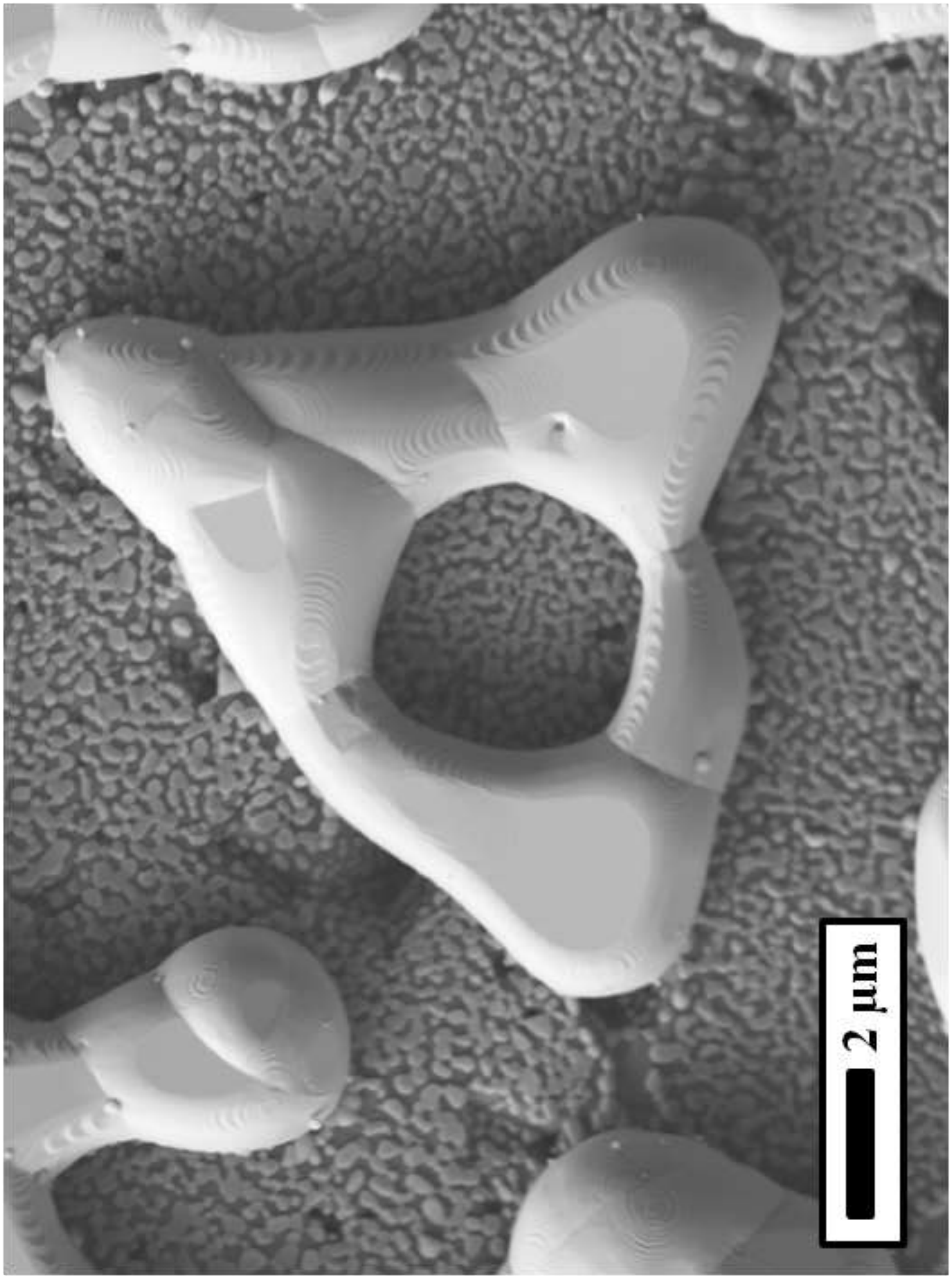

Figure 25 : SEM micrograph of the Zr+Pt coating after 15 h at 1200°C **[103]**.

3.4. Alternative Adhesion Layers and composite Conductive multilayers

3.4.1 Layer-by-layer deposition of zirconium and platinum (L-Zr+Pt)

In order to increase the presence of Zr throughout the platinum film, a layered coating of Zr and Pt (L-Zr+Pt) was synthesized with low temperature deposition (200°C). For convenience, this multilayer coating will be termed L-Zr+Pt. The proposed coating would allow for two-dimensional clamping of the Pt granular structure, in addition to decreasing diffusional distance and increasing dispersion of Zr into the bulk Pt film. The intent of these two strategies is to constrain the grain boundary mobility which would result in a drastic decrease in the Pt grain growth kinetics. This strategy was originally demonstrated by Cunha et *al.* for surface acoustic wave devices for high temperature sensor applications, but detailed microstructural and chemical characterization was not completed and the maximum testing temperature was limited to 1000°C [130]. In our study, the Zr+Pt multilayer coating (L-Zr+Pt) was obtained by introducing thin Zr layers (~10 nm thickness) between thin Pt layers (~77 nm thickness). After ~35 nm of the adhesion layer was deposited, alternating Pt and Zr thin films were deposited over the Zr adhesion layer (consisting of 5 Pt thin film layers and 4 Zr layers) to a total thickness of ~460 nm. Total multilayer coating thickness was comparable to the previous bilayer coating thicknesses in this study. The films were annealed to 1200°C in N_2 in order to rapidly evaluate applicability for high temperature operation conditions. The SEM micrograph of the top Pt surface of this film is shown in Figure 26 after the 1200°C annealing process for 1 h [103].

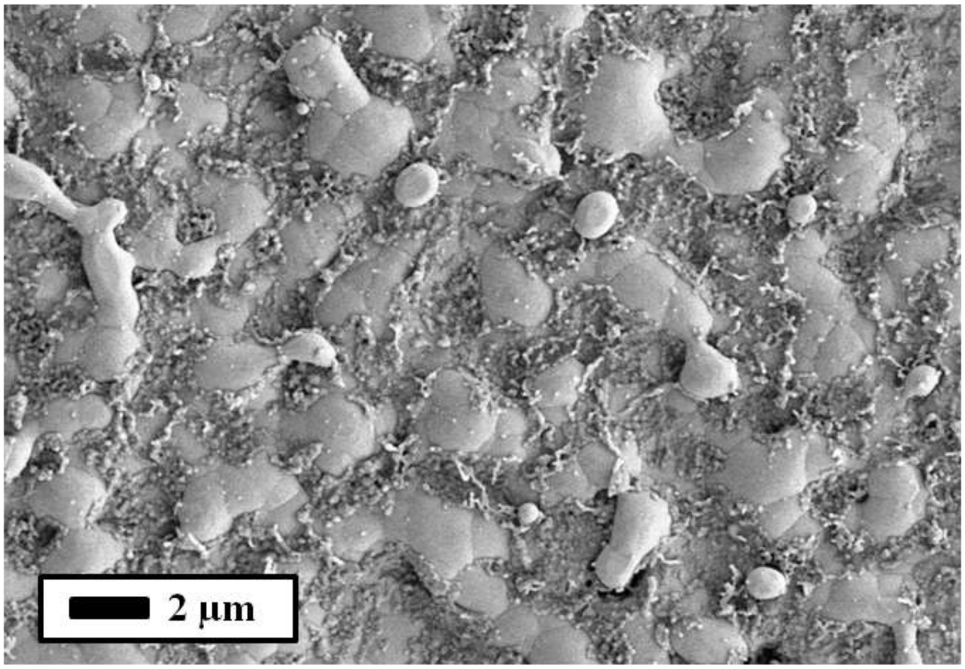

Figure 26 : SEM micrograph of the L-Zr+Pt multilayer coating surface after annealing at 1200°C for 1h **[103].**

The SEM micrograph reveals a continuous Pt film with a low level of pore formation across the viewed area. This structure is in contrast to that seen for the Pt films with a single adhesion layer of Ti, Ta or Zr. Similarly, L-Zr+Pt films were also processed at 1200°C for 5, 8, 15 and 48 h (see Figure 27-a, -b, -c and -d.). Again, these micrographs were taken from the surface of the L-Zr+Pt multilayer structure after annealing. After separate 5 and 8 h annealing at 1200°C, the integrity of the film (i.e. adhesion to the substrate and percolation across the substrate surface) was retained. The contrast between these two annealing times was slight. The 5 and 8 h annealing times produced films that contained a few isolated exaggerated Pt grain surrounded by a dispersed mixture of fine grains. As expected, the increased annealing time from the 1 h resulted in the growth of both the exaggerated grains and the fine grain structure. A significant change to the microstructure occurred after the 15 h annealing at 1200°C annealing. As seen in the SEM micrograph shown in Figure 27-c, the growth and coalescence of exaggerated Pt grains resulted in limited degradation of the percolated Pt network. In addition, the integrity of the Zr adhesion layer was not compromised due to similar sintering/grain growth processes previously identified [103].

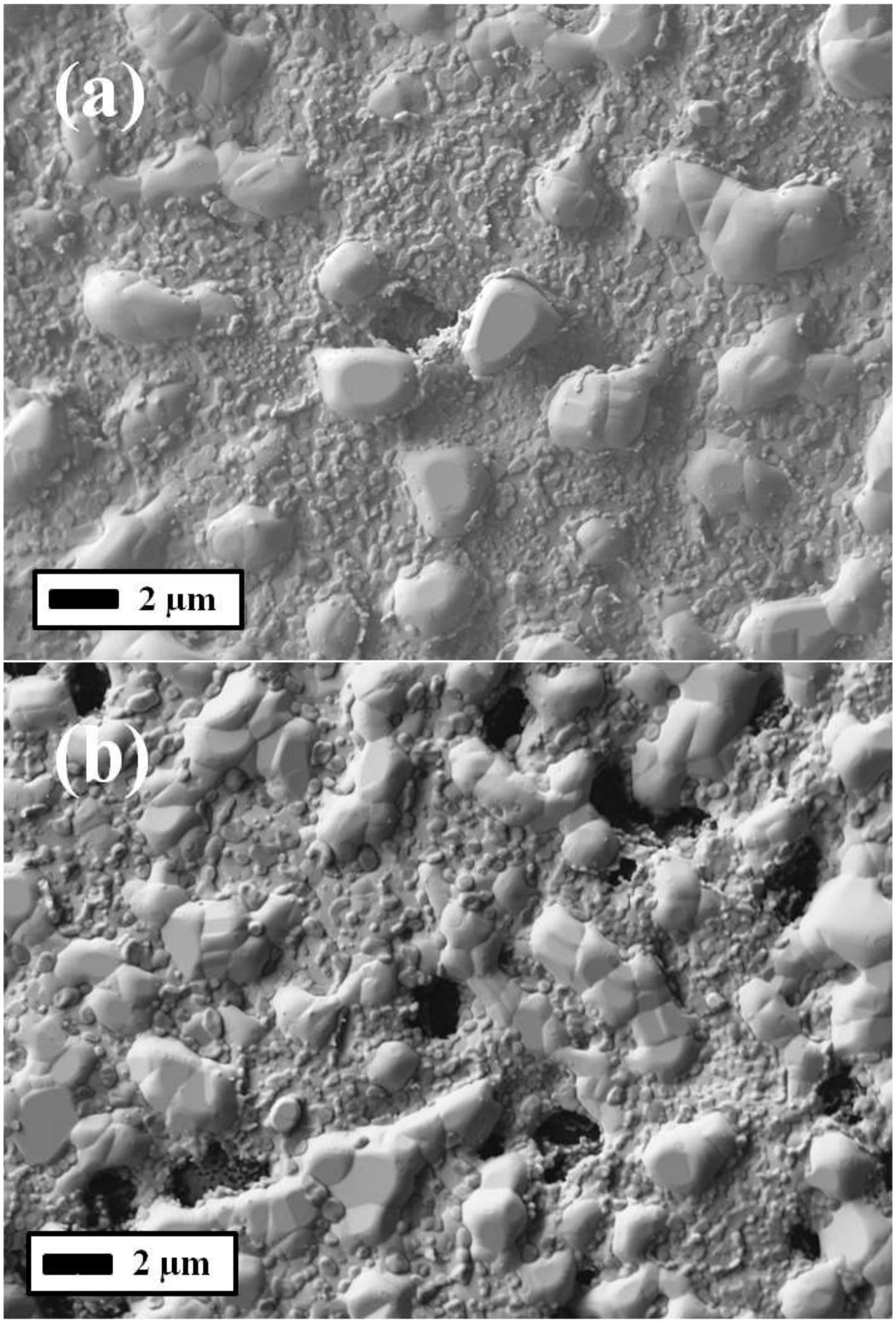
(a)
2 µm
(b)
2 µm

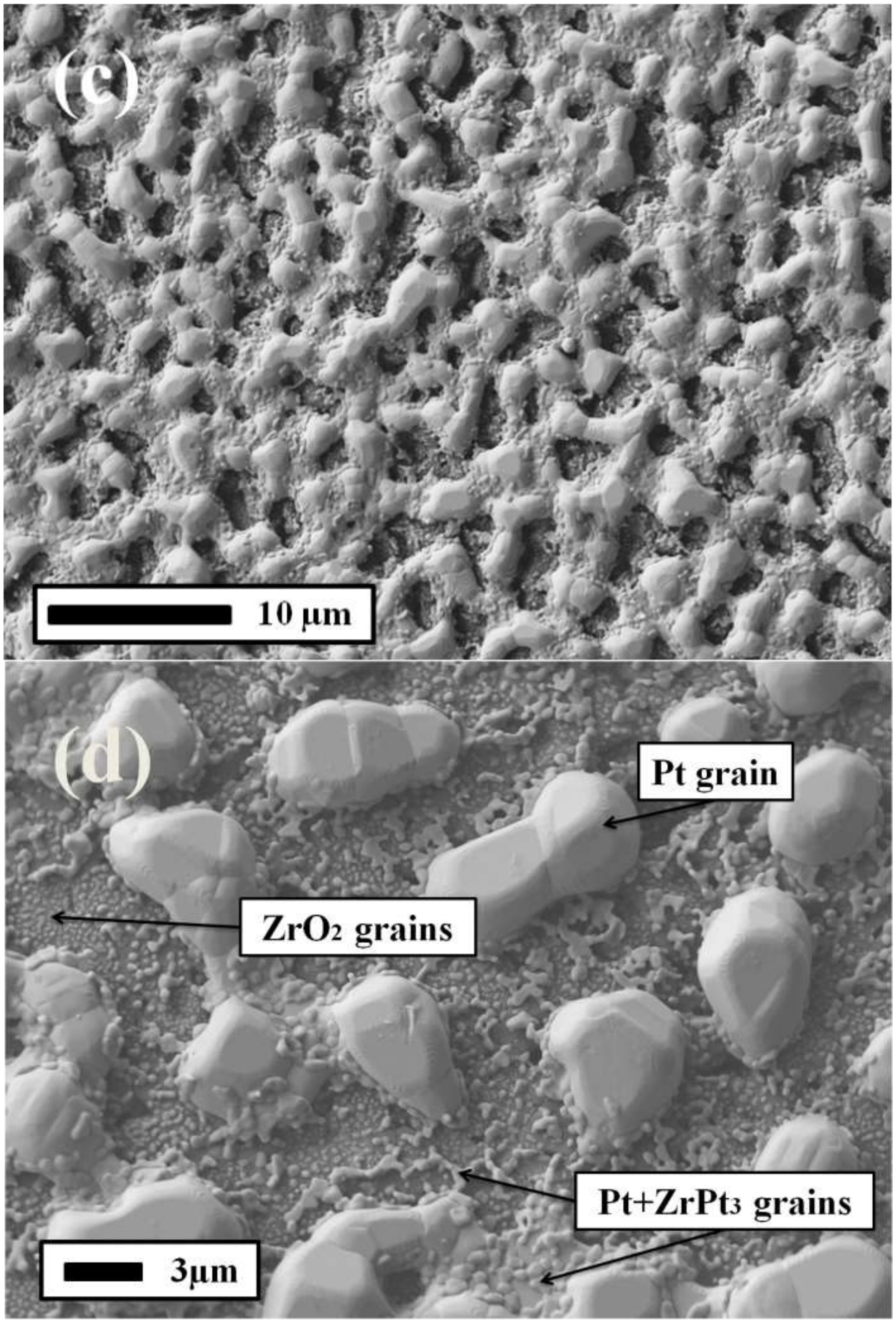

Figure 27 : SEM micrographs of L-Zr+Pt multilayer coating surface after annealing at 1200°C **(a)** 5 h **(b)** 8 h **(c)** 15 h **(d)** 48 h **[103]**.

The final annealing step was the 48 h at 1200°C in order to determine the limitation of the multilayer L-Zr+Pt coating. After 48 h annealing, total destruction of the film was observed. The formations within the agglomerated Pt grains shown in the Figure 27-d are believed to be precipitates of ZrO_2 and $ZrPt_3$. Ficalora et *al.* defined the $ZrPt_3$ intermetallic as the second most stable intermetallic compound after $HfPt_3$ in their study [137]. Future work will include Auger Electron Spectroscopy (AES) and Transmission Electron Microcopy (TEM) for point analyses in order to obtain more detailed information about the aforementioned second phases. The L-Zr+Pt multilayer coating showed satisfactory microstructural retention for extended annealing and/or processing at 1200°C. This multilayer coating has shown that Pt coarsening and hillock formation can be hindered considerably to temperatures up to 1200°C by introducing second-phase refractory $Zr/ZrO_2/ZrPt_3$ inclusions within the bulk Pt film [103].

3.4.2 Platinum with hafnium adhesion layer (Hf+Pt)

The successful result obtained from Zr+Pt and L-Zr+Pt is the motivation behind the investigation of Hf as an adhesion layer. Hf is also a refractory material which shares similar oxidation and chemical properties with Zr; however, the stronger bond strength of the metal and oxide (and thus, higher melting temperature and lower diffusion rates compared to the Zr counterparts) indicates that this would be a logical substitution.

There are three different known crystal structures of HfO_2; monoclinic, tetragonal and cubic. The monoclinic HfO_2 transforms into the tetragonal phase at ~1700°C, and the tetragonal to cubic phase transformation occurs at ~2200°C. The monoclinic to tetragonal phase transformation for ZrO_2 is at ~1150°C, which must be considered when heating zirconia thin films to >1150°C temperatures. Transformation temperatures observed in HfO_2 are higher than the ZrO_2 counterpart. The phase transformations accompanied by significant volume changes lead to stress accumulation in the thin film and eventually will turn into crack formations at the adhesion layer in order to be stress released. Initial crack formations have crucial importance since these points can behave as pore growth centers in the adhesion layer. Therefore, the physical properties and phase equilibria of Hf make this composition a good candidate for both the adhesion layer and Zener-pinning inclusions within bulk Pt film. In order to make a clear comparison between Hf and Zr, both bilayer Hf+Pt and layer-by-layer sputtered L-Hf+Pt multilayer coatings were fabricated in this work. The sputtering of the Hf adhesion layer and subsequent platinum deposition were completed utilizing the same methodology used for the deposition of the Ti, Ta and Zr adhesion layers. Again, a ~425 nm thick Pt film was deposited over a ~35 nm Hf film, as characterized by profilometer. The Hf+Pt samples were similarly annealed at 1200°C for 1 h and XPS was again completed on the top surface of the Pt film. The XPS spectrum of the Pt film surface presented in Figure 28 indicated the presence of Hf with low peak intensities. This was similar to the presence of Zr identified by XPS for the Zr+Pt film after the same annealing conditions (Figure 23-b). Again, major peaks of Pt were positioned at 71.1 eV ($4f_{7/2}$) and 74.4 eV ($4f_{5/2}$), which agree with the literature values for pure Pt metal [136, 103].

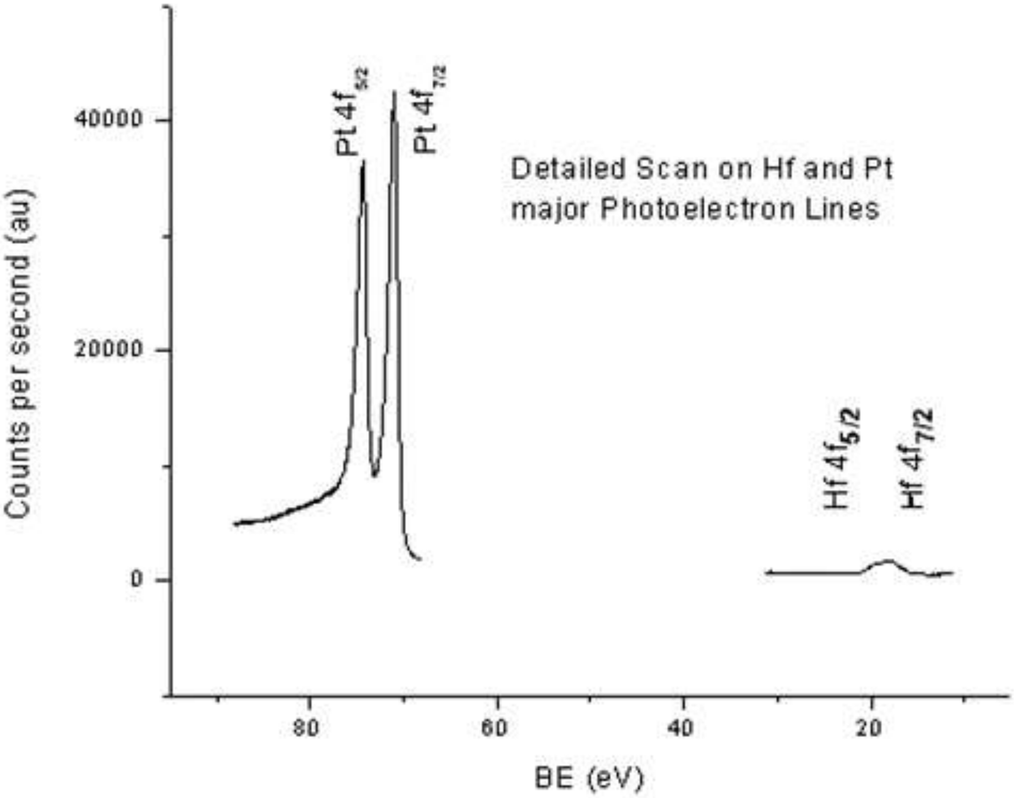

Figure 28 : XPS detailed spectrum of the Pt and Hf 4f peak positions from the surface of the Hf+Pt bilayer coating after annealing at 1200°C for 1 h **[103]**.

As was seen for the major Zr peaks in the Zr+Pt film, a peak-shift was observed in the position of the Hf major peaks due to corresponding oxide formation (as also observed in Ti and Ta cases). Since detailed spectra were obtained in the binding energy range for the Hf 4f peaks, Zr 3d peaks and major Pt 4f peaks, it was possible to conduct elemental analysis. The composition was calculated from the intensities obtained for the doublets of Zr at 185.7 eV ($3d_{3/2}$) and 183.3 eV ($3d_{5/2}$), Hf at 19.3 eV ($4f_{5/2}$) and 17.6 eV ($4f_{7/2}$), and Pt at 74.4 eV ($4f_{5/2}$) and 71.1 eV ($4f_{7/2}$). These binding energies match well with the value reported in literature for both ZrO_2 and HfO_2 [136]. A concentration of

~4.5% Hf was calculated from the Hf+Pt film surface; this value is nearly a third of the Zr measured (13% Zr detected) for the Zr+Pt structure processed at the same condition. This indicates that the Hf migration rate was nearly a third of that shown by the Zr under the same thermal budget (1200°C, 1 h). The SEM micrograph of the Hf+Pt bilayer coating after annealing at 1200°C for 1 h is shown in Figure 29-a. This result was similar to that shown for the Zr+Pt film (see Figure 23-a). The increased uniformity of the Hf+Pt film for the 1 h at 1200°C annealing time can be attributed to the stability of the adhesion layer, and thus, the slower migration of the Hf layer into the bulk Pt film. Conversely, as seen in Figure 29-b, after annealing Hf+Pt film for 5 h at 1200°C, a greater difference between the Hf+Pt and Zr+Pt bilayer films became evident [103].

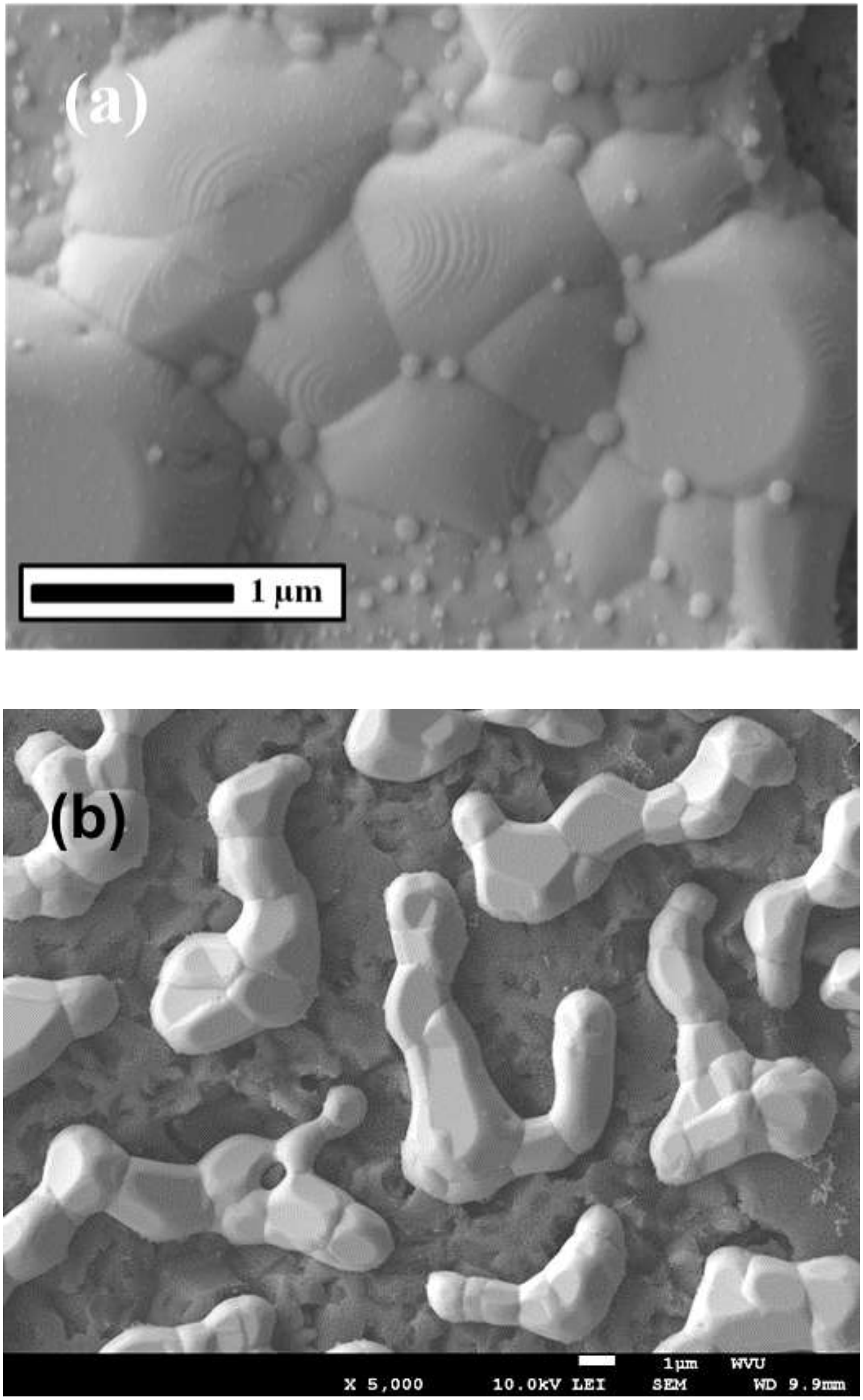

Figure 29 : SEM micrographs of the Pt coating with Hf adhesion layer after annealing at 1200°C for **(a)** 1 h **(b)** 5 h **[103]**.

The contrast is related to the higher Zr interdiffusion into the bulk Pt film, resulting in the presence of a secondary-phase within Pt grain boundaries. The relatively fast migration of Zr retarded the coarsening process of the Pt, compared to that seen for the Hf+Pt structure. As seen in Figure 24-a, the collection of the Zr-based secondary-phases within the remaining grain boundaries preserved some portion of the percolated microstructure by limiting the final grain size. In the Hf+Pt film (Figure 29-b), the same mechanism cannot be claimed and distinct island formation was observed. As expected, the Hf adhesion layer remained a dense and continuous layer over the entire substrate area even after extended annealing at 1200°C (in contrast to the ZrO_2 coarsening and grain growth). The average grain size for the adhesion layer was ~50 nm (Figure 30), which was half of that shown for the Zr/ZrO_2 adhesion layer grain size (~100 nm grain size) in the Zr+Pt film for the same annealing condition (see Figure 24-b) [103].

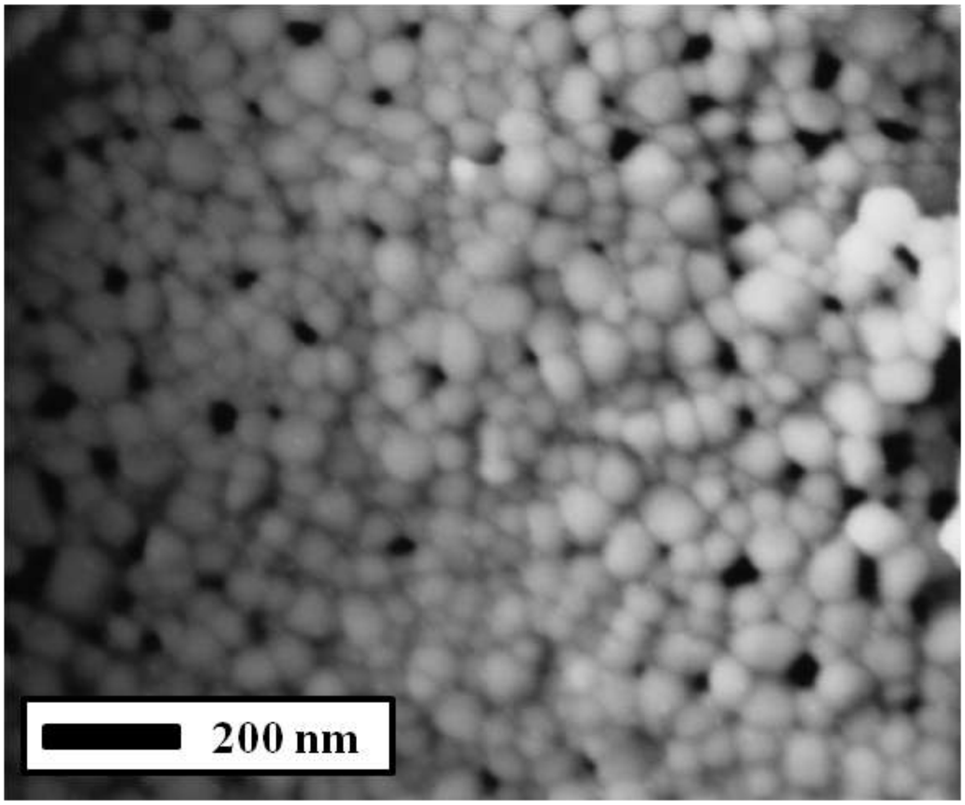

Figure 30 : SEM micrograph of the Hf layer after 5 h at 1200°C **[103]**.

3.4.3 Layer-by-layer deposition of hafnium and platinum (L-Hf+Pt)

The Hf+Pt bilayer film structure proved that hafnium is a promising adhesion layer with its durability and low migration behavior. The L-Zr+Pt multilayer coating showed the success of the layer-by-layer deposition strategy for the bulk Pt film. Therefore, the incorporation of the same layer-by-layer strategy for Hf (L-Hf+Pt), while incorporating an Hf base adhesion layer, has the potential to provide the required stability at high-temperature electrode film.

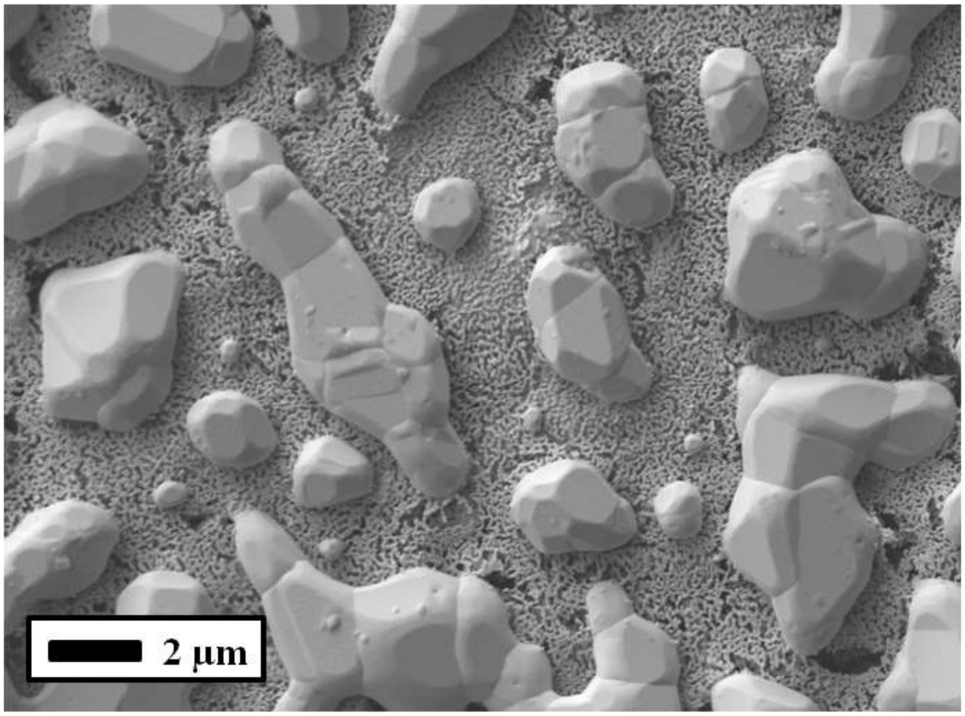

Figure 31 : SEM micrograph of the L-Hf+Pt coating surface after annealing at 1200°C for 5 h.

The sputtering of the L-Hf+Pt multilayer coating with the same layer thicknesses previously utilized for the L-Zr+Pt coating was repeated. In order to efficiently evaluate the difference between L-Hf+Pt and L-Zr+Pt, the annealing condition of 1200°C for 5 h was chosen. This thermal budget previously showed the onset of the degradation for the L-Zr+Pt film. The SEM micrograph obtained for the L-Hf+Pt film shows extensive Pt island formation throughout the whole platinum film and the elimination of all continuity across the film (Figure 31). For the same annealing conditions, the L-Zr+Pt film showed an intact microstructure with no distinguishable pore formation even after the 5-8 h annealing time (seen in Figure 27-a and -b). For both composite films, no appreciable adhesion layer depletion was observed. Due to this result, the difference in the degradation kinetics must be aligned with the diffusional behavior of each composition.

As discussed previously, the Zr was found to move through to the top surface of the Pt film after the 1200°C annealing times for >1 h; small Zr based grains were distinguishable on the top of the Pt (seen in Figure 26 and Figure 27-a). However, there is no such formation in L-Hf+Pt; clear Pt islands are the dominant microstructure formation seen within Figure 31. Therefore, it can be concluded that the loss of film continuity in the L-Hf+Pt film was due to the low Hf diffusion into the Pt film and the low precipitation of Hf-based secondary-phases within the Pt film granular structure.

3.4.4 Single layer Hf adhesion layer in addition to the L-Zr+Pt multilayer coating

Following the same logic presented in the last subsection, the layer-by-layer Zr+Pt film over stable Hf adhesion layer (Hf/L-Zr+Pt) was evaluated. A single Hf layer with a thickness of ~35 nm was sputtered over the ceramic substrate. The similar layer-by-layer sputtering methodology previously defined was utilized to deposit the Zr (~10 nm thickness) and Pt layers (~85 nm thickness) over the adhesion layer. The samples were annealed at the two highest thermal budgets used in this work (1200°C for 15 and 48 h). The annealing of the L-Zr+Pt multilayer film for 8 h was previously shown to result in minimal microstructural degradation; however, the L-Zr+Pt network was totally destroyed after the 48 h annealing at 1200°C (see Figure 27-d). In comparison to L-Zr+Pt multilayer structure, the Hf/L-Zr+Pt multilayer coating showed a different behavior. Figure 32 displays SEM micrographs of the top surface of the Hf/L-Zr+Pt multilayer film. As seen in Figure 32-a, the Pt grains are connected partially under the dense and continuous layer, which, as previous publications suggested might be ZrO_2 and intermetallics of Pt and Zr. There are also a few large exaggerated grains and well-distributed pores are surrounded by a fine matrix of Pt and/or $PtZr_3$ grains. Figure 32-b shows the Hf/L-Zr+Pt composite microstructure after 48 h at 1200°C. Well-distributed second phase precipitations are easily distinguishable over the coarsened Pt grains. Another distinctive feature of this coating is the presence of 0.1-1 µm size, prism-shaped grains distributed evenly over the Al_2O_3 substrate (seen in Figure 32-c). These structures are believed to be intermetallics of $HfPt_3$ and/or $ZrPt_3$. Hf/L-Zr+Pt composite multilayer coating did not evolve into separated islands of material as observed in L-Zr+Pt multilayer coating (Figure 27-d), instead a percolated network of Pt grains was observed. The reason for the improved high temperature behavior of the Hf/L-Zr+Pt multilayer composite film may be due to the formation of an intermediate intermetallic phase between Pt and Hf layer. The formation of the intermetallic phase (such as $HfPt_3$) may provide a coherent layer over the alumina with high wetting characteristics for both substrate and Pt film. A high level of compatibility between the wetting of the adhesion layer between both layers reduces the need for a reduction of the overall contact area between either oxide or metal phases [103].

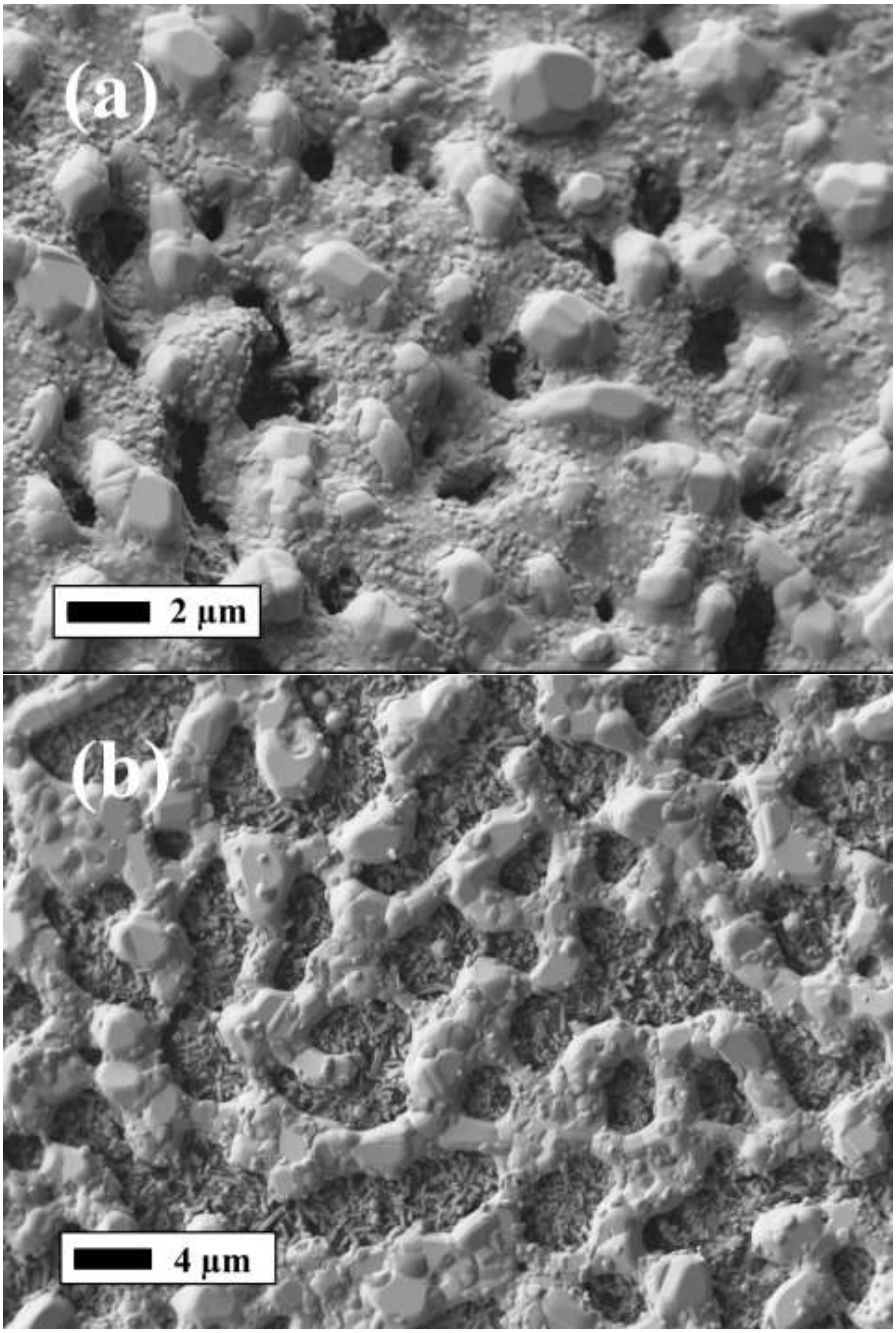
(a)
2 µm
(b)
4 µm

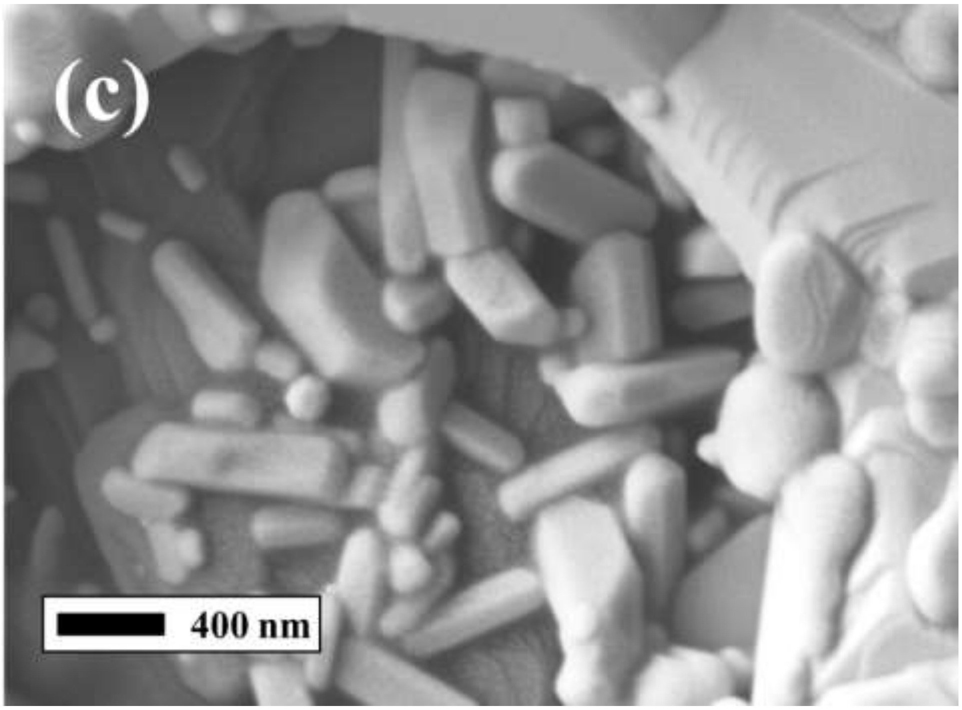

Figure 32 : SEM micrographs of **(a)** Hf/L-Zr+Pt multilayer coating after 15 h annealing at 1200°C and **(b-c)** after 48 h 1200°C annealing **[103]**.

3.5. Functionality Growth Adhesion Layer Approach (Zr/Zr+Pt/Pt)

The main focus of this part is to suppress the granular coarsening/sintering mechanism at temperatures ≥800°C for the low-temperature sputtered Pt thin films with minimum time and labor. The current approach was initiated by investigating the thermal stability of sputtered Pt films utilizing common adhesion promoters such as Ti and Zr over an alumina (Al_2O_3) substrate as also was case for the sequential deposition route explained in the previous chapter. The work then focused upon a method of controlling these processes by manipulating the microstructure and thickness of the Zr adhesion promoter by utilizing an alternative DC sputtering process. By manipulating the deposition parameters (such as sputtering power and primary deposition gas pressure) during the adhesion layer deposition a functionally gradient composite Zr/Pt film was formed that demonstrated similar stability as the Zr-Pt layer-by-layer structure demonstrated by Cunha [130] and Çiftyürek [103]. The dispersion of refractory particles (such as nano- or micro-ZrO_2

or Zr/Pt intermetallics) drastically reduces the low- and high- angle grain boundary mobility within the polycrystalline film. This mechanism is usually termed as Zener pinning in the literature. However, these previously demonstrated strategies are energy consuming, and/or require specialized deposition control (for co-deposition and processing control) to balance varying deposition rates of the two species. In order to access a similar grain-pinning strategy, this work proposes a two-layer adhesion film which consists of an initial Zr adhesion layer in contact with the oxide substrate and a secondary defective layer of Zr film deposited over the initial adhesion layer.

Pt-based thin films and electrodes were fabricated by a magnetron sputtering technique (CVC 610 DC Magnetron Sputtering Station) at 100 W with a primary gas (argon) pressure of 50 mTorr for Ti and Zr adhesion films and the primary Pt electrode film (unless otherwise indicated). The films were deposited upon polycrystalline Al_2O_3 substrates polished to ~35 nm thickness. All adhesion layers were deposited to the same 50 nm thickness, as well as, the Pt layer with 425 nm in thickness (unless otherwise indicated), in order to provide consistency among deposited thin films. The film thicknesses were measured with a Tencor Alpha-Step 200 profilometer with an accuracy limit of ±3 nm. The sputtering chamber was sustained with a base pressure of 1×10^{-7} Torr, and 2 inch sputtering targets were utilized.

The post-deposition annealing was completed at 1200°C in a conventional tube furnace (MTI GSL 1600X) in order to mimic potential high temperature operation conditions. A 5°C/min heating and cooling rates were chosen. The annealing time was varied from 1 to 24 h under a N_2 atmosphere (with a O_2 and H_2O content of 2 ppm and 3 ppm, respectively) in order to clearly examine microstructural alterations that may have occurred in the Pt, Ti and Zr films. In order to evaluate the thin film microstructure, the film surfaces were examined by Scanning Electron Microscopy (SEM, JEOL 7600F). Energy-dispersive X-ray Spectroscopy (EDS) and X-ray Photoelectron Spectroscopy (XPS, PHI 5000 Versaprobe) was utilized in order to determine the surface composition and chemical state of the elements, and was later used for depth profiling of the films. The EDS spectra were obtained using an Oxford INCA attached to JEOL 7600FE-SEM. The XPS source was operated at 15 kV and 25 watts using Al Kα (1486.6 eV) radiation. The films were analyzed by a combination of 117.40 eV survey scans and 23.50 eV detailed scans of peaks of interest. A 0.5 eV step was used for each survey scan and a 0.05 eV step for the detailed scan. Prior to spectral analysis, all coating surfaces were cleaned against atmospheric and post-depositional contaminations with Ar^+ sputter using a 2 kV accelerating voltage for 30 seconds. The depth profile analysis was conducted with Ar^+ stepwise sputtering using an accelerating voltage of 2 kV and an etching area of 1×1 mm. The X-ray induced photoelectron data acquisition area was chosen to be 100 µm x 100 µm in order to increase the accuracy in the depth profiling. All binding energies of Pt, Zr, Ti and O were referenced to Au $4_{f7/2}$ at 84.0 eV. During measurements, the analysis chamber pressure was maintained at ~10^{-11}Torr. Finally, the room temperature electrical resistivities of the as-deposited and annealed Pt and composite films were measured using a van der Pauw's four probe technique [134].

3.5.2 High temperature behavior of platinum films with titanium and zirconium adhesion layers

3.5.2.1 Platinum with Ti and Zr adhesion layers (Ti/Pt and Zr/Pt)

Titanium was initially investigated as an adhesion promoter for high temperature applications (≥800°C) of Pt films due to its widespread application in the micro-electronics and sensor field [105, 139]. As indicated in the experimental section, 425 nm Pt film was deposited over a 50 nm thick Ti and Zr adhesion layers. The corresponding bilayer coatings will be expressed as Ti/Pt and Zr/Pt throughout the paper. Figure 33 shows the SEM micrographs of the Ti/Pt and Zr/Pt bilayer coatings after annealing at 1200°C for 1 and 5 h, respectively. The SEM micrograph shown in Figure 33-a presents a general view of the Pt network with a highly disturbed structure and a low degree of percolation. The microstructure is separated into collection of islands due to the rapid depletion of the Ti adhesion promoter from substrate surface and the simultaneous grain coarsening of the Pt metallization. The protruding formations (see regions shown in the dashed-circles in Figure 33-a inset) on the Pt grains were shown to be Ti rich through EDS analysis (not presented). Therefore, the high mobility of Ti within sputtered Pt film makes it neither a stable adhesion layer nor capable of remaining within the grain boundaries of the Pt film to retard the coarsening processes.

Zirconium (Zr) was the second choice as an adhesion promoter. A few research groups have recently demonstrated the use of a Zr film as an adhesion layer or grain pinning phase for Pt thin films [130, 133, 107, 103, 131, 132]. Figure 33-b shows the SEM micrograph of the Pt film with the Zr adhesion layer (Zr/Pt) after 5 h at 1200°C. The resulting microstructure consists of micron-size Pt grains with a low degree of percolation across the microstructure.

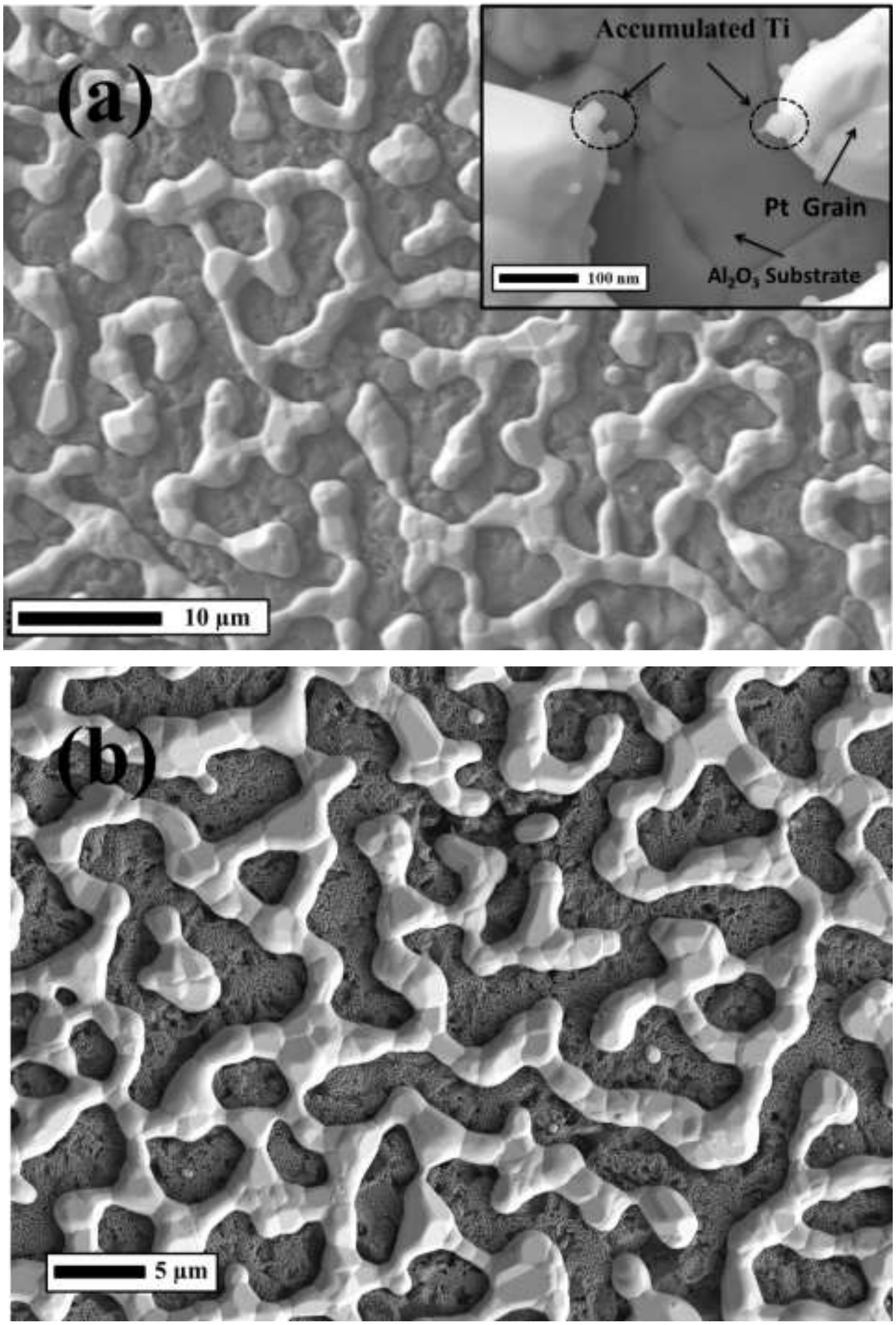

Figure 33: SEM images from surface of **(a)** Ti/Pt after annealing at 1200°C for 1 h, inset shows the migrated Ti accumulation on the Pt grains **(b)** Zr/Pt after annealing at 1200°C for 5 h.

It can be concluded that Ti and Zr are not suitable adhesion promoters in the bilayer thin film form, since they showed high instability and rapid adhesion depletion near the substrate interface, and the latter could not stop the coarsening of the Pt metallization. However, the Zr showed adequate stability as an adhesion promoter, in part due to the slow Zr diffusion kinetics (even at 1200°C). Therefore, Zr would be an applicable candidate for the realization of a functionally gradient composite Zr and Pt film.

3.5.1.2 Platinum with double zirconium adhesion layer

As demonstrated by the degradation of the bilayer film, the use of only an adhesion layer of Ti or Zr below the sputtered Pt film resulted in the unwanted dewetting and coarsening/sintering of the film after high-temperature exposure. A strategy is required to control the migration of the adhesion layer away from the substrate interface and to limit the migration of the Pt grain boundaries, which results in unwanted grain growth. One method recently [103, 140, 130] demonstrated for controlling the later mechanism is through the introduction of Zr metal into the Pt layer through a co-sputtering of Zr and Pt, or through sequential depositions of each of these constituents. The dispersion of refractory particles (such as nano- or micro-ZrO_2 or Zr/Pt intermetallics) drastically reduces the low- and high- angle grain boundary mobility within the polycrystalline film. This mechanism is usually termed as Zener pinning in the literature. However, these previously demonstrated strategies are energy consuming, and/or require specialized deposition control (for co-deposition and processing control) to balance varying deposition rates of the two species. In order to access a similar grain-pinning strategy, this work proposes a two-layer adhesion film which consists of an initial Zr adhesion layer in contact with the oxide substrate and a secondary defective layer of Zr film deposited over the initial adhesion layer. After the deposition of the second defective Zr film, the Pt film is deposited over the Zr film, where it both infiltrates and coats over the secondary Zr layer. This deposition procedure results in the formation of a functionally gradient film from the original Zr adhesion layer to the outer Pt top layer, as shown in the cross-sectional illustration in Figure 34-a. Figure 34-b shows the typical cross-sectional illustration of simple bilayer coating for visualization purposes.

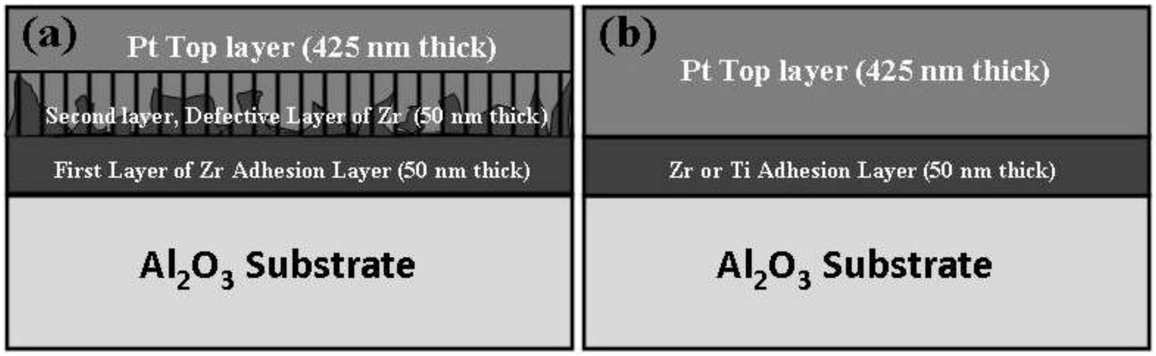

Figure 34 : Cross-sectional schematic illustrations of **(a)** functionally gradient composite Zr and Pt films (Zr/Zr+Pt/Pt), during Pt film deposition, in-situ formation of co-continuous composite of Zr and Pt, called Zr+Pt shown in shaded region. **(b)** Bilayer coatings of Zr/Pt or Ti/Pt (Illustrations are not scaled to real dimensions of the abovementioned layers

Figure 35 shows the high magnification SEM images of the above-mentioned two Zr layers. Figure 35 shows as-deposited state of the first adhesion Zr thin film deposited with the same processing parameters and thickness (50 nm) used in the deposition of the adhesion layer for the Zr/Pt bilayer coating. This layer shows significantly high surface coverage compared to the second defective layer, which is shown in Figure 35-b. The second Zr layer is also deposited to 50 nm thickness, but a 25 W power input and a primary gas pressure of 150 mTorr was utilized instead 100 W and 50 mTorr, respectively. The defective layer was generated by modification of the deposition parameters, where the parameter change resulted in a decrease in the incident energy of the deposited Zr. This effect of primary gas pressure and power on the microstructure formation is well documented in literature for sputtered thin films [141, 142]. The initial layer provided a durable adhesion layer, while the latter layer provided a porous Zr framework, which would be later infiltrated with the deposition of 425 nm thick Pt top layer to form a co-continuous composite microstructure. This in-situ formed co-continuous network of Zr and Pt layer will be termed Zr+Pt throughout the paper (see Figure 34-a). The Zr granular network between the Pt grains would further assist in pinning of the Pt grain boundaries by upward diffusion beyond the Zr+Pt co-continuous layer. The total thin film coating, with the first layer being the Zr adhesion layer, second layer being the Zr+Pt co-continuous layer and top layer being pure Pt, will be termed as Zr/Zr+Pt/Pt thorough the current work.

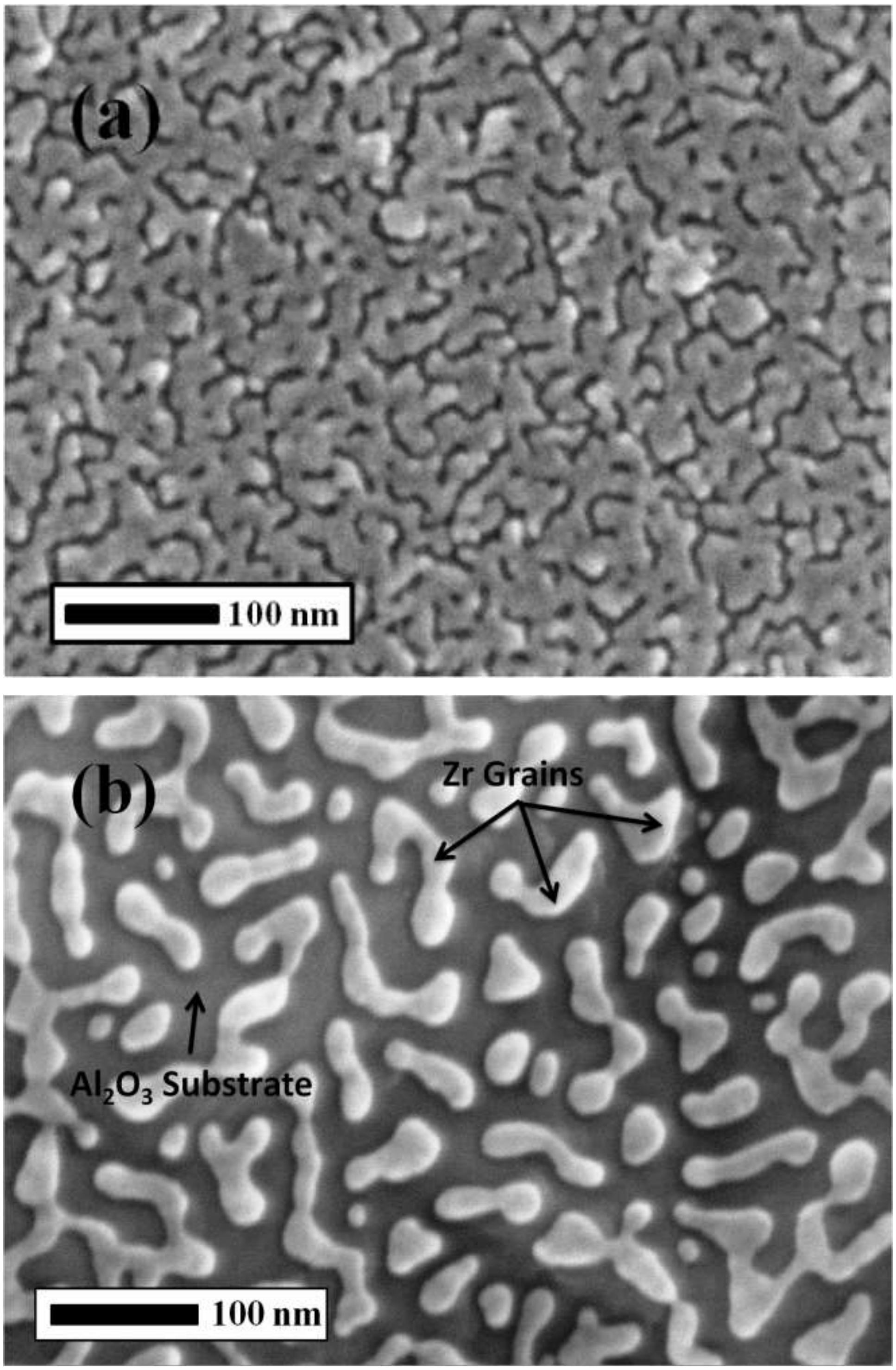

Figure 35 : SEM micrographs of as-deposited state of **(a)** First layer of Zr adhesion layer common in Zr/Pt and Zr/Zr+Pt/Pt **(b)** Defective layer of Zr utilized in Zr/Zr+Pt/Pt coating as a second layer of double adhesion layer.

Figure 36-a through -f displays SEM micrographs of the Zr/Zr+Pt/Pt coating after annealing at 1200°C for 0-24 h. The as-deposited state of Pt is shown in Figure 36-a, and this SEM micrograph displays an average grain size of ~15 nm. The other micrographs show the successive destruction of the thin film microstructure as the isothermal hold is increased. The microstructure remained continuous during the annealing process, but larger, isolated pores with a size of 3-5 μm began to emerge throughout the microstructure after 1 h at 1200°C (as shown in Figure 36-b). After annealing for 5 h at 1200°C, the coarsening of these isolated pores began to accelerate and merge with other larger isolated pores. Figure 36-c displays the SEM micrograph of the Zr/Zr+Pt/Pt coating after an annealing time of 5 h. Although the Zr/Zr+Pt/Pt microstructure appeared to begin to evolve, the percolation was not compromised and was far superior over that displayed by the Pt film with only the Zr adhesion layer (Zr/Pt). The rate of coarsening and coalescence of the exaggerated pores began to subside after the 5 h annealing, where the microstructure did not alter between the 5 h and 8 h isothermal annealing. Figure 36-d shows the SEM micrograph of the 8 h annealing at 1200°C. Figure 36-e displays the microstructure after 15 h annealing. After the 15 h annealing, the larger pores grew extensively and the coalescence of these pores began to compromise the percolation of the Pt phase. The percolated granular network of Zr/Zr+Pt/Pt thin film was finally destroyed after 24 h annealing, as shown in the SEM micrograph presented in Figure 36-f.

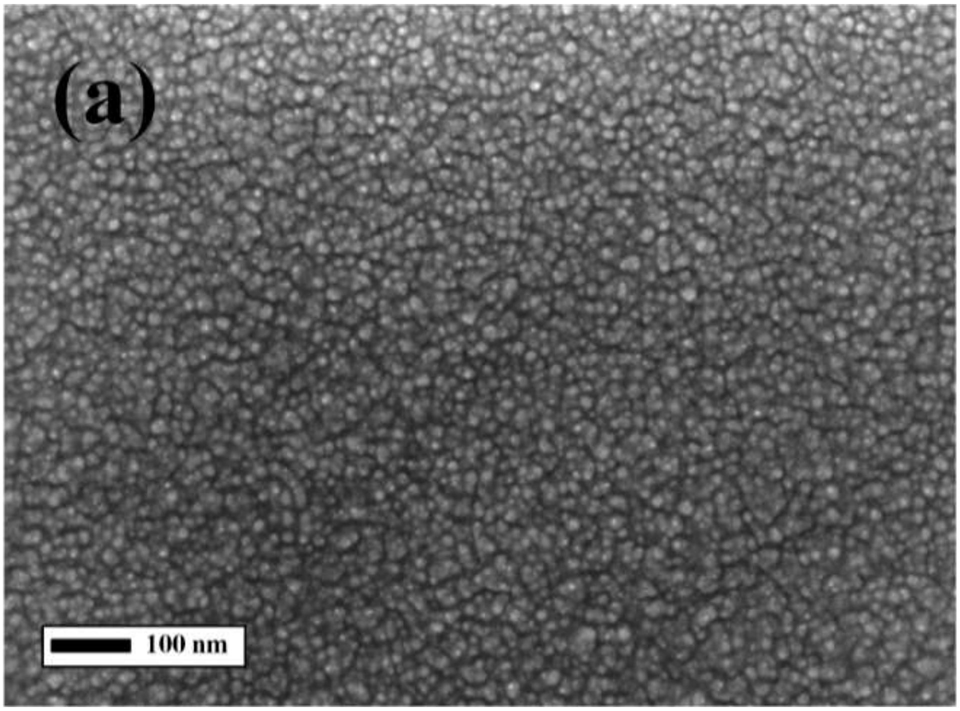

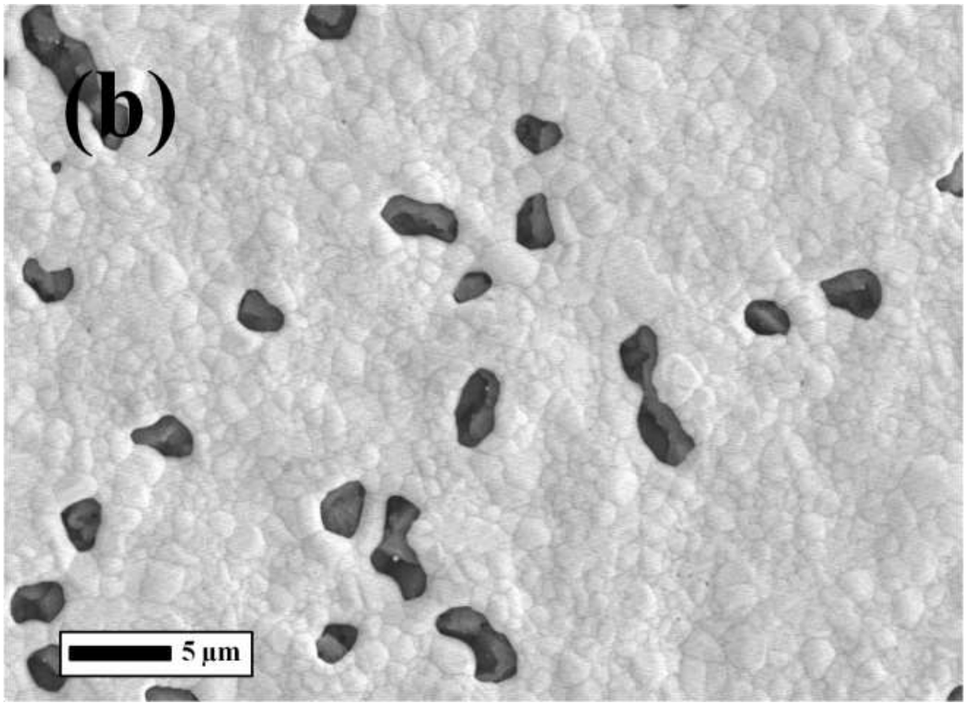
(b)
5 µm

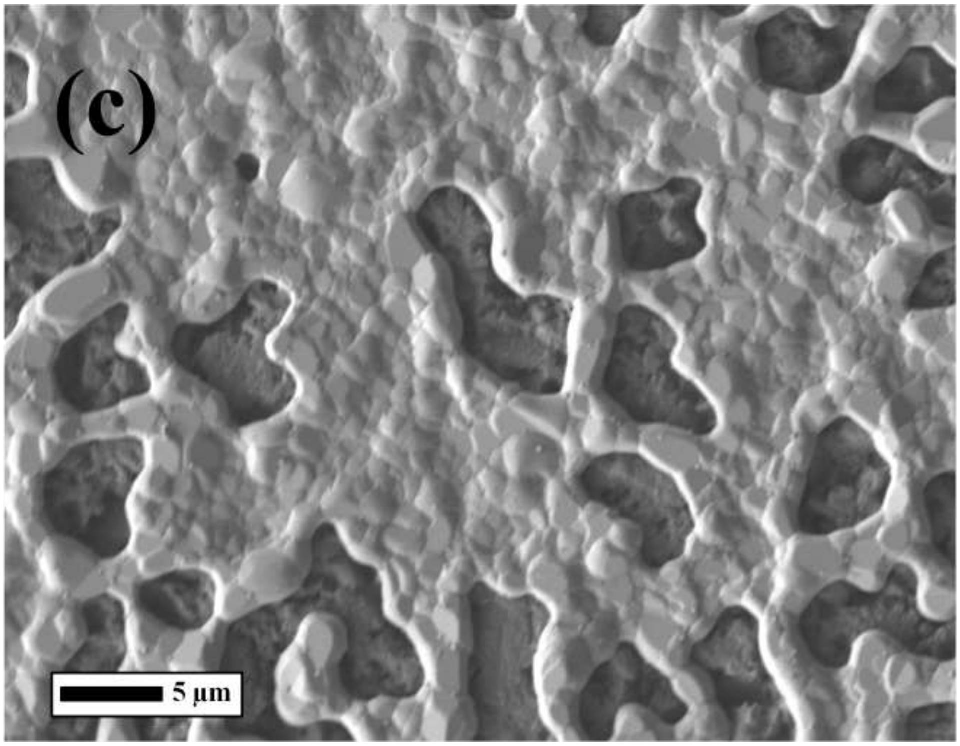
(c)
5 µm

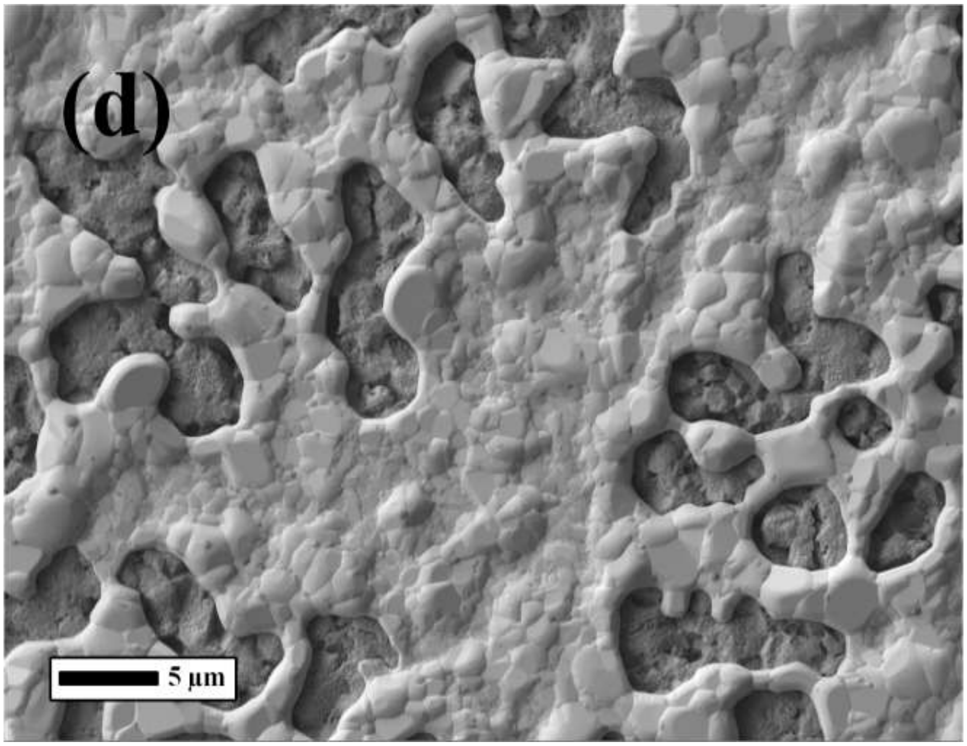
(d)
5 μm

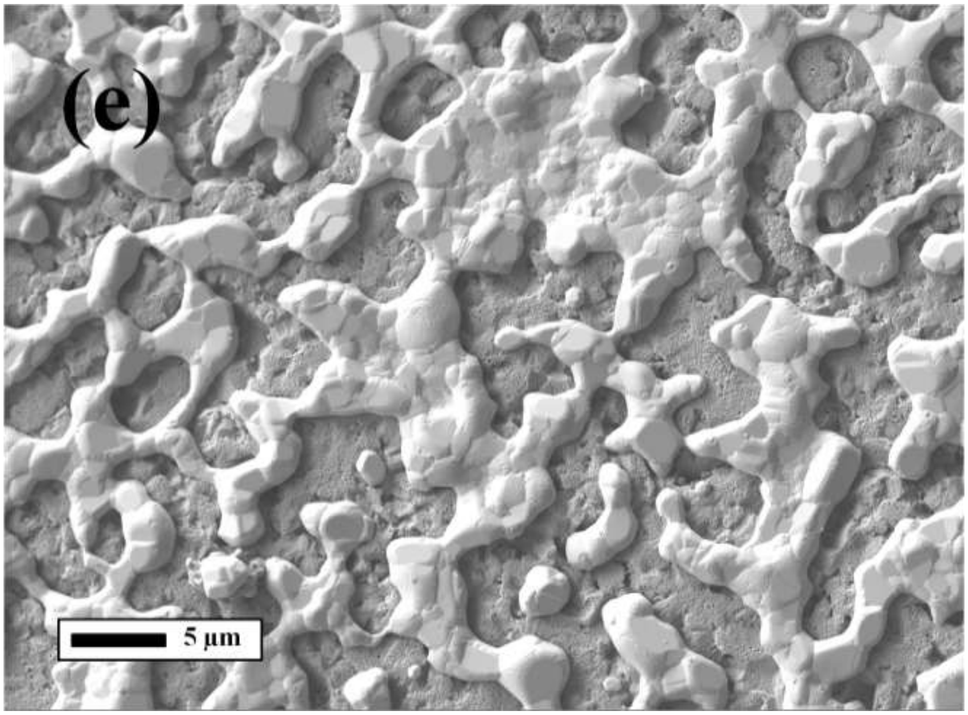
(e)
5 μm

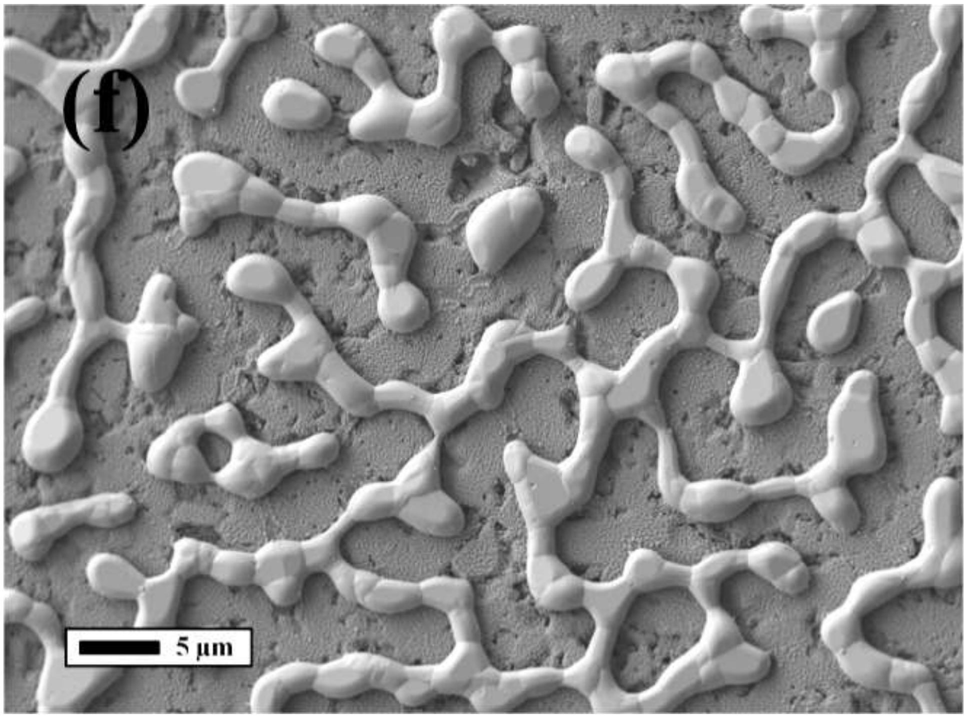

Figure 36 : Zr/Zr+Pt/Pt thin film **(a)** as-deposited state, after annealing at 1200°C for **(b)** 1 h **(c)** 5 h **(d)** 8 h **(e)** 15 h **(f)** 24 h **[103]**.

In contrast to the Pt coatings utilizing just the Ti and Zr adhesion layers (Figure 33), the Pt coating consisting of the double Zr adhesion layer demonstrated superior stability over the extended high-temperature annealing. Higher magnification SEM micrographs of the Zr adhesion layer (which may be observed through pores in the Pt thin film) are shown in Figure 37-a and -b after 5 and 15 h annealing practices, respectively. It is worthy to note that the grain growth also occurred in the Zr adhesion layer, where the grains were growing at an average rate of ~5 nm/h. The pores grew at a similar rate, but the kinetics was considerably slower than that of shown for the Pt films. Figure 37-c shows an SEM micrograph of the Zr adhesion layer after the 24 h annealing. This annealing practice highly disturbed the Zr adhesion layer as well as the Pt top layer (see Figure 36-f). The image shows that the Zr adhesion layer was thoroughly disturbed beneath the Pt top layer. At some locations, the alumina substrate became visible due to the coarsening of the adhesion layer.

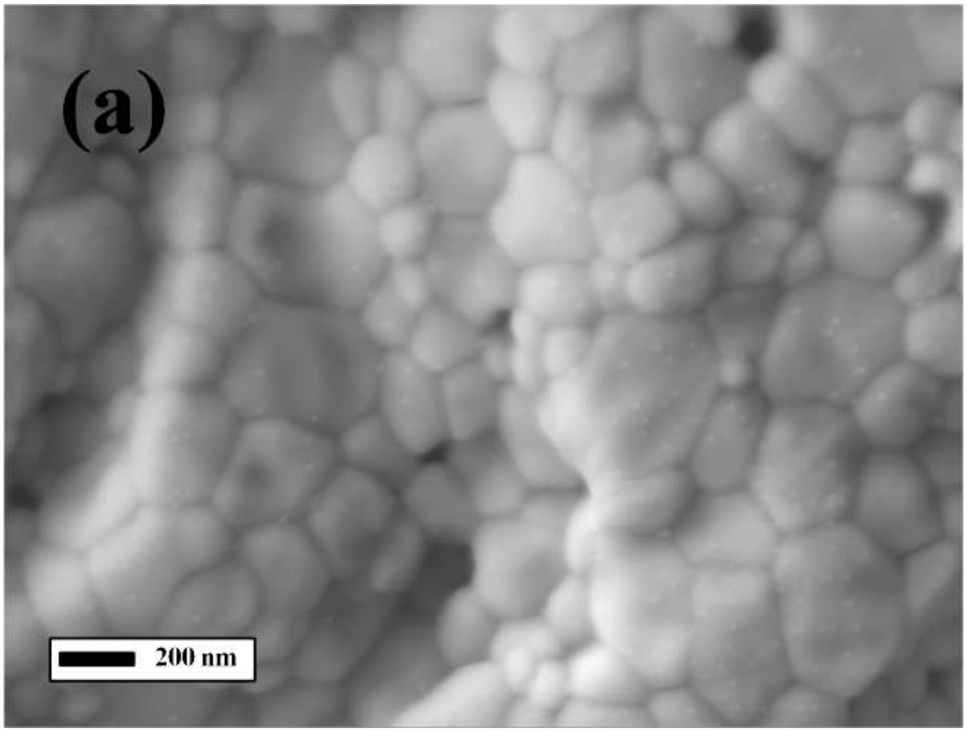
(a)
200 nm

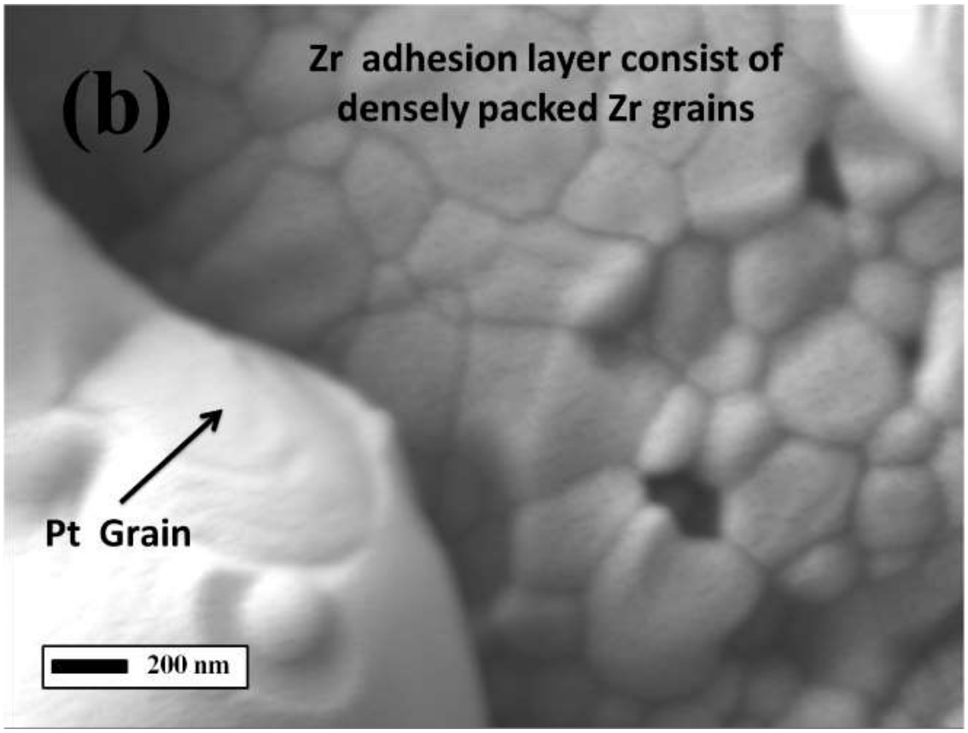
(b)
Zr adhesion layer consist of densely packed Zr grains
Pt Grain
200 nm

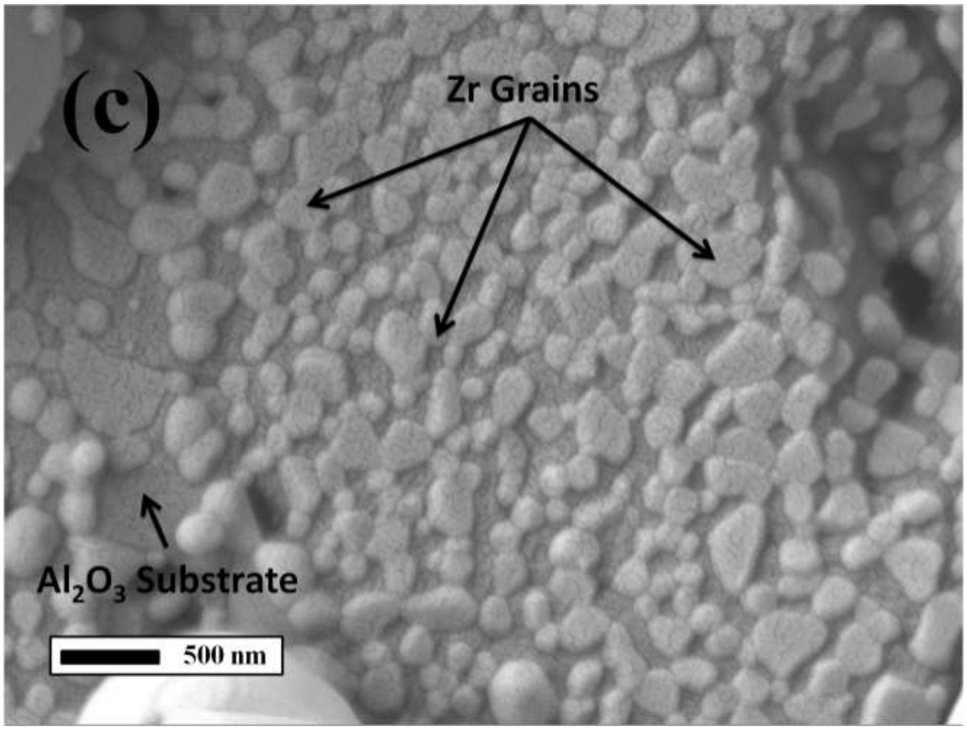

Figure 37 : High magnification SEM micrographs of adhesion layer in Zr/Zr+Pt/Pt after annealing at 1200°C for **(a)** 5 h **(b)** 15 h **(c)** 24 h.

3.5.1.3 XPS depth profiling of Zr/Pt and Zr/Zr+Pt/Pt

The superior high-temperature stability of the Zr/Zr+Pt/Pt thin film compared to the Zr/Pt thin film demonstrates the applicability of the Zener pinning effect on the control of the Pt grain growth and dewetting characteristics. By introducing Zr into the Pt bulk composition from the start, the driving force for the diffusion of Zr from the adhesion layer into the bulk was decreased. This diffusion is driven by the chemical gradient across the thickness of the film. Therefore, the incorporation of the Zr into the Pt film limited migration of Zr from the adhesion layer, as is typically the case for various adhesion metals such as Ti, Ta, and Zr [103]. Therefore, the preservation of the adhesion layer between the oxide and Pt film resulted in the desired effect where the hillock and dewetting degradation mechanisms were minimized. Also, the coarsening/sintering of the Pt grains was controlled by the presence of the Zr, which limited the microstructural evolution of the bulk electrode thin film. In order to shed light over the distribution of the Zr in Pt, XPS depth profiles of the Zr/Pt and the Zr/Zr+Pt/Pt thin films were completed by Ar ion etching through the Pt metallization towards the alumina substrate (as described in detail within the experimental section). XPS depth profile spectra were taken in the vicinity of the Zr, Pt and O main photoelectron lines.

The XPS depth profiles of the thin films are shown in Figure 38, where the 0 nm marker represents the outside surface of the Pt metallization, and the entire thin film thicknesses were roughly 450 and 475 nm for Zr/Pt and the Zr/Zr+Pt/Pt, respectively (thus, the alumina substrate interfaces is located accordingly). The figures show that the Pt concentration throughout the thin films does not change considerably; however, the Zr concentration increases rapidly toward the interface at different depths from surface for the above-mentioned thin films, as expected. As seen from the graphs in Figure 38, detection of Zr started at the 375 nm and 275 nm depths from the surface for Zr/Pt and Zr/Zr+Pt/Pt thin films, respectively. The early detection of the Zr in Zr/Zr+Pt/Pt is in direct consequence of the Pt deposition over the defective Zr layer, where the Pt infiltrated the Zr architecture during deposition (Figure 35-b). In the Zr/Pt layer, the Zr content gradually rose from the 375 nm until a depth of ~412.5 nm. In the case of double-layered thin film, the Zr was first detected at the 275 nm depth and gradually rose to 375 nm, and this concentration was finally limited to a constant value between ~375-425 nm. In the Zr/Pt case, the adhesion layer identified in Figure 35-a could not provide the same diffusional source of Zr. The stable phases such as $ZrPt_3/ZrO_2$ are formed within the Pt grain boundaries during the high-temperature annealing process, which has an important effect on the high temperature behavior of the Pt thin film due to the pinning of the Pt bulk grains.

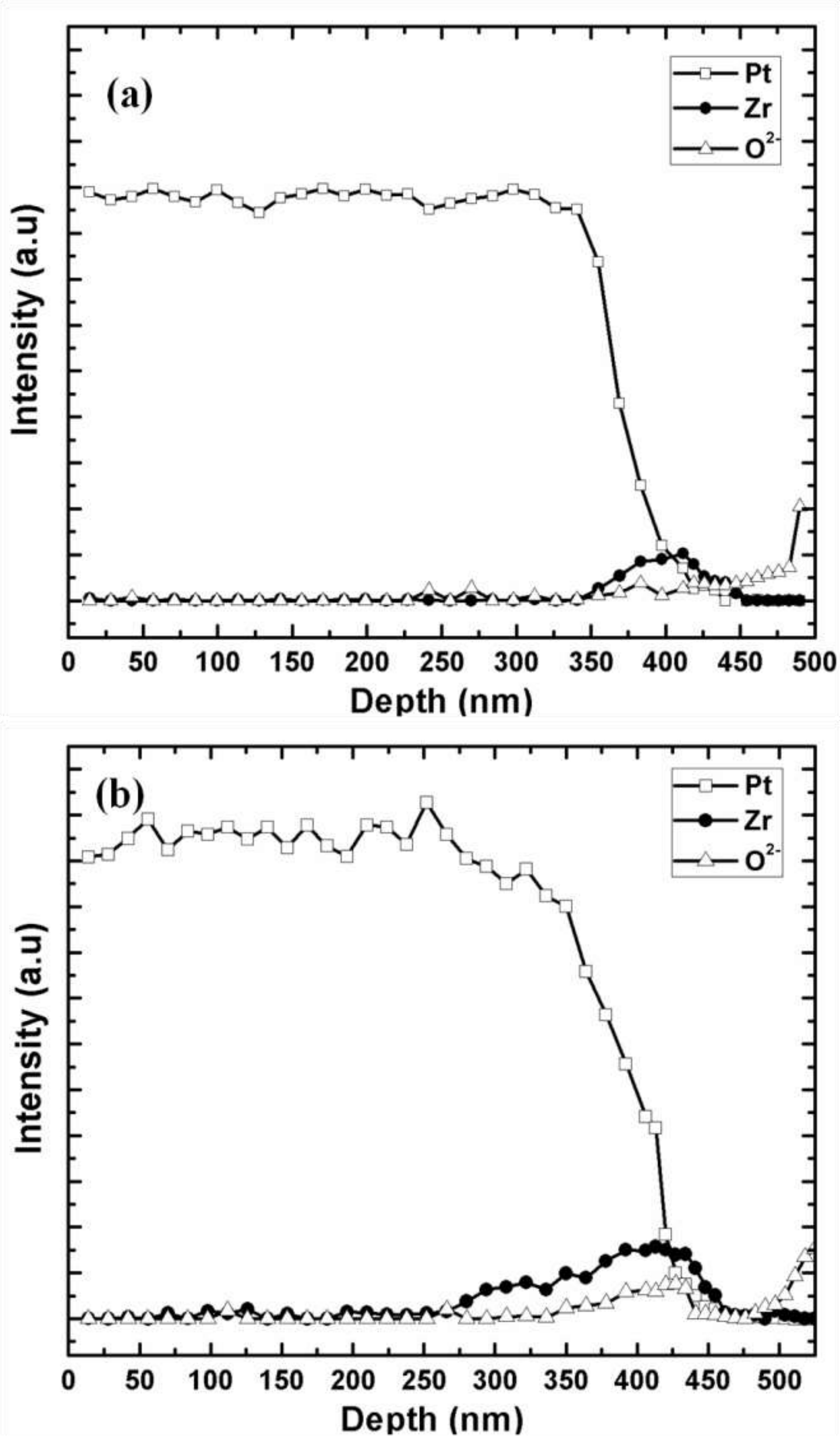
(a)
Pt
Zr
O2-
Intensity (a.u)
0
50
100
150
200
250
300
350
400
450
500
Depth (nm)
(b)
Pt
Zr
O2-
Intensity (a.u)
0
50
100
150
200
250
300
350
400
450
500
Depth (nm)

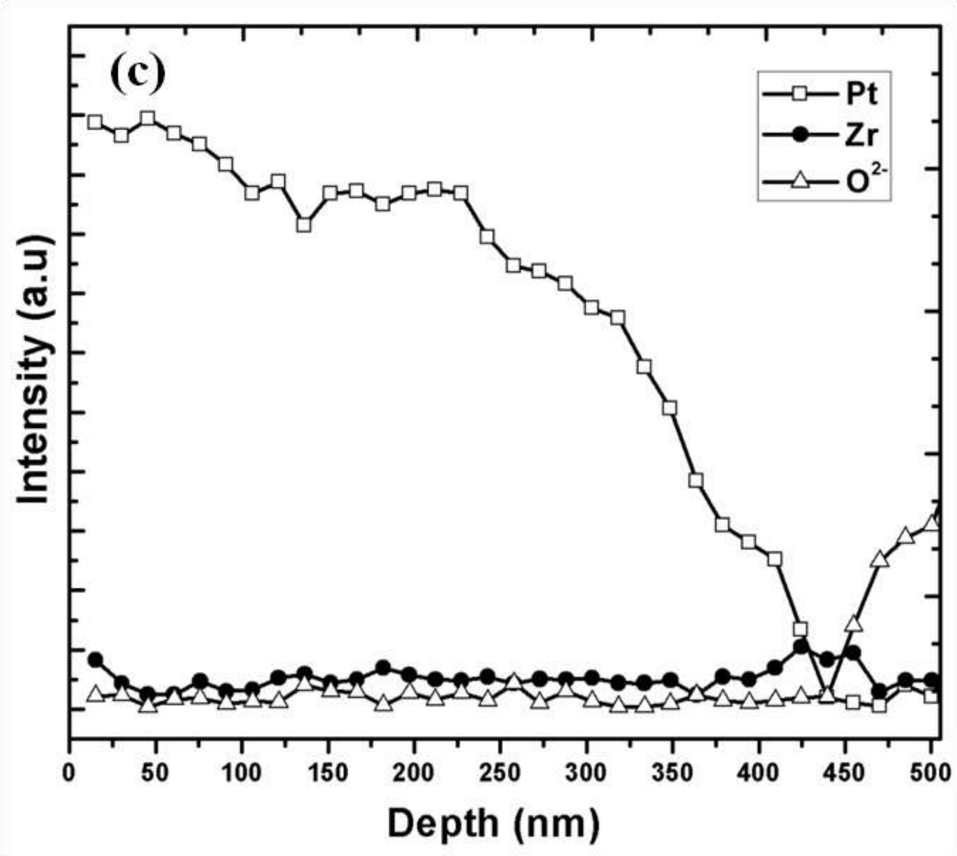
(c)
Pt
Zr
O^{2-}
Intensity (a.u)
Depth (nm)
0
50
100
150
200
250
300
350
400
450
500

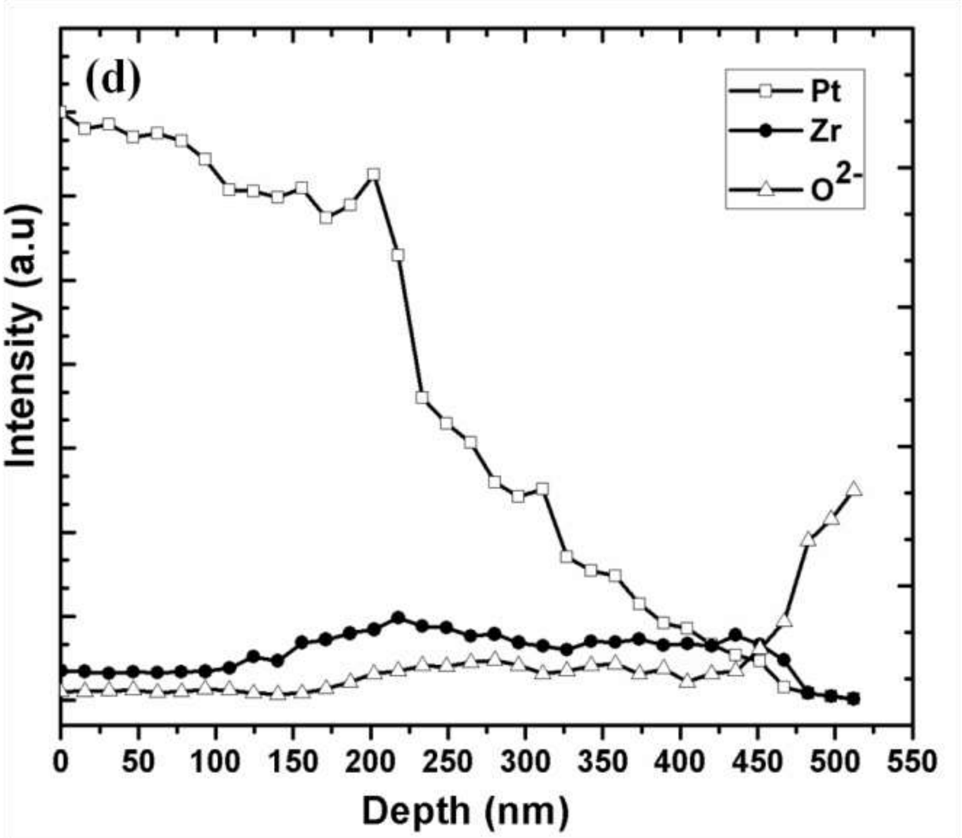

Figure 38 : XPS depth profiling of as-deposited **(a)** Zr/Pt **(b)** Zr/Zr+Pt/Pt and annealed for 1h at 1200°C for the **(c)** Zr/Pt **(d)** Zr/Zr+Pt/Pt thin films.

The higher stability at the elevated temperature for the Zr/Zr+Pt/Pt thin film was previously attributed to the distribution and amount of the second phase precipitants among the Pt grain boundaries in the form of ZrO_2 and $ZrPt_3$. Further XPS depth profiling analysis was conducted in order to examine the concentration/distribution of the Zr through the thin films of Zr/Pt and Zr/Zr+Pt/Pt after 1 h annealing at 1200°C. The indicated time and temperature used for annealing the samples was chosen, since samples annealed for further time lost the surface percolation, especially in the case of the Zr/Pt and Zr/Zr+Pt/Pt films, but more profoundly in the former (see Figure 33-b and Figure 36-b). This annealing temperature was also aligned with the operational temperature for the perspective application (where the sensor operation is perceived to be <1200°C). The thin films must be further annealed above this temperature in order to stabilize the microstructure of the electrode and sensing material. In addition, the refractory sensing material (oxide in many cases) must be bonded to the substrate at temperatures >1000°C, and thus the electrodes must be stable to this additional processing step. Therefore, the 1 h at 1200°C annealing practice could be thought of as the final step before operational usage. Figure 38-c and –d show the aforementioned XPS depth profiling of the thin films of Zr/Pt and Zr/Zr+Pt/Pt, respectively. XPS spectra of the 28 different locations through the coating thicknesses from the surface to the substrate interface were taken in order to better understand the overall distribution and concentration of Zr across this depth. Three significant locations (near surface, middle zone and substrate interface) were analyzed in detail for the chemical state and identification of the Pt and Zr in both Zr/Pt and Zr/Zr+Pt/Pt thin films. The ZrO_2 phase was analyzed by using the Zr 3d core photoelectron line, which includes the doublet, positioned at the 185.5 eV and 183.1 eV for the $3d_{3/2}$ and $3d_{5/2}$. The intermetallic $ZrPt_3$ phase, which is significant in this work due to its low electrical resistivity [138], was analyzed by inspecting detailed scans of Pt 4f and Zr 3d photoelectron lines. The formation of $ZrPt_3$ shows its presence at the Pt 4f and Zr 3d spectra as shoulders on the high and low binding energy sites, respectively. The Pt main photoelectron lines are located at 72.5 eV ($4f_{7/2}$) and 75.8 eV ($4f_{5/2}$) for the intermetallic phases in both Zr/Pt and Zr/Zr+Pt/Pt thin film. These values for Zr and Pt are a good match with the reported literature values [103, 143, 144] .

As seen in the graph shown in Figure 38-c, the Zr distribution through the Zr/Pt thin film was restricted to the adhesion layer substrate interface. The 50-400 nm zones contain 5 % Zr in the form of ZrO_2 and $ZrPt_3$, while the latter is a minor contributor since it constitutes 15% of the total Zr phase. On the other hand, as seen in the Figure 38-d, the Zr/Zr+Pt/Pt thin film (which contains the defective adhesion layer) showed a well distributed and high amount of Zr phase in the form of ZrO_2 and $ZrPt_3$ starting from surface to the adhesion layer substrate interface. The $ZrPt_3$ consisted of nearly 30 % of the total Zr phase within this film. The high amount and overall distribution of the Zr through the Pt electrode is important to the microstructural stability identified for this film. The chemical state and concentrations analysis were conducted at three different depths; the depths were 0 nm (after surface cleaning with Ar^+, 2 minutes at 4 kV accelerating voltage), 225 nm (considered mid-depth) and 450 nm (considered the substrate-thin film interface). It was possible to conduct elemental concentration analysis, since the detailed spectra of the Zr 3d, Pt 4f and O 1s photoelectron lines were obtained at the same time. The surface of the Zr/Pt thin film contained 8% ZrO_2, whereas the Zr/Zr+Pt/Pt surface included 4.5% ZrO_2. In both of these thin films, the amount of $ZrPt_3$ intermetallic phase counted for less than 5% of the total Zr content at the surface. At the mid-depth (225 nm), the Zr/Zr+Pt/Pt thin film showed significant increase of Zr content (25% in total). This increase includes the increase in the total intermetallic phase percentage to 30 % of total, while the ZrO_2 phase was 70% of the total. At the same depth, the total amount of Zr in the Zr/Pt film was only 5%. At the substrate-thin film interface, the Zr content was about 10% of the total composition in the Zr/Pt thin film, while it showed 15% for the Zr/Zr+Pt/Pt.

3.6. Verification of Intermetallic Phases

Ficalora et *al.* reported the formation of intermetallic phases between fine particulate precursor mixtures of borides, carbides, nitrides and oxides of Zr, Hf, Nb and Ta reacted with elemental Pt at 1200-1300°C in quartz tubes purged with either hydrogen or nitrogen [137]. These experimental conditions were very similar to the annealing conditions in the current work for thin films. In order to verify the formation of intermetallics, XPS characterization was performed on the top surface of Hf/L-Zr+Pt and L-Zr+Pt samples annealed for 48 h. The 48 h annealing condition was chosen for the evaluation in order to increase the probability of reaching the lower detection limit of the XPS system. The XPS detailed spectra for Hf/L-Zr+Pt and L-Zr+Pt are shown in Figure 39-a and -b, respectively. The major peaks for Pt in the Hf/L-Zr+Pt and L-Zr+Pt multilayer coatings are present at 71.1 eV ($4f_{7/2}$) and 74.4 eV ($4f_{5/2}$). These values are comparable to the results obtained from the bilayer coatings for the Pt metal positions (seen in Figure 23-b and Figure 28).

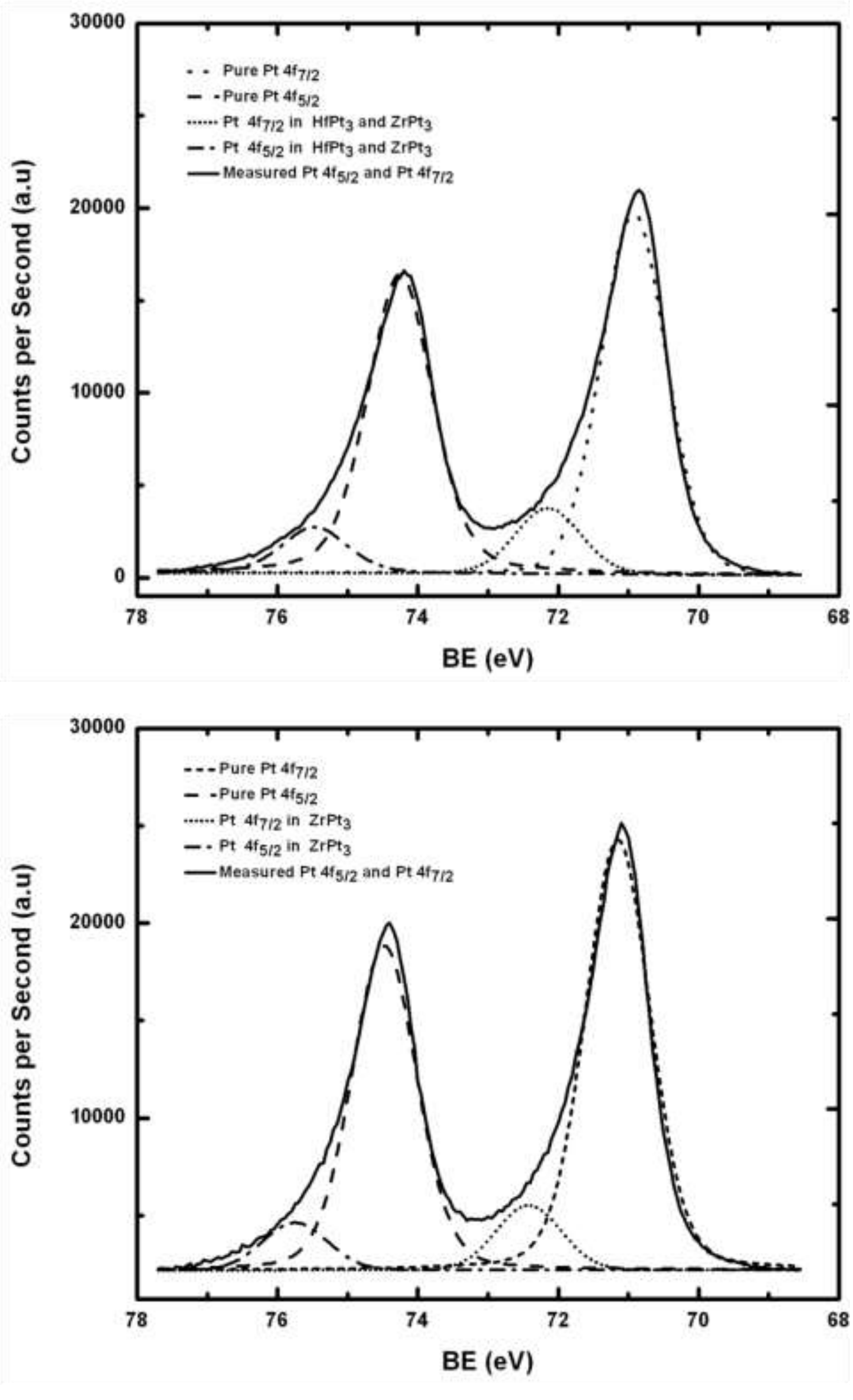

Figure 39 : Detailed XPS scan for the Pt 4f peaks positions in the **(a)** Hf/L-Zr+Pt sample and **(b)** L-Zr+Pt sample, both annealed at 1200°C for 48 h.

As displayed from the detailed XPS spectra (Figure 39-a and -b), Pt peaks showed broadening towards the high binding energy level indicated by data-fitting of the acquired doublet Pt 4f spectra. The broadening of these peaks is due to the formation of the intermetallic phases between Pt and Zr/Hf. The electron transfer from Pt d-orbitals to the Zr (and/or Hf) empty p- and d-orbitals contribute to the increase in the electron binding energy of Pt [145]. The peaks corresponding to $HfPt_3$ and $ZrPt_3$ were included below the metallic Pt peaks for comparison purposes. The Pt spectra from the bilayer structures (Hf+Pt and Zr+Pt) show a symmetric peak shape. The Pt spectra obtained from multilayer structures do not show the same symmetric shape due to broadening of the doublets. The intermetallic states ($HfPt_3$ and $ZrPt_3$) in the Hf/L-Zr+Pt composite coating were determined to reside at 72.1 eV ($4f_{7/2}$) and 75.4 eV ($4f_{5/2}$). The reported enthalpy values of formation (ΔH_{298}) for the $ZrPt_3$ and $HfPt_3$ intermetallics are -30±2.0 Kcal/(g·atom) and -33±2.5 Kcal/(g·atom), respectively [138]. The similarity in the formation enthalpies of these intermetallics indicates the equal formation probability of $HfPt_3$ and $ZrPt_3$. The Pt main photoelectron peaks at 72.4 eV ($4f_{7/2}$) and 75.7 eV ($4f_{5/2}$) were determined for the intermetallic state ($ZrPt_3$) in L-Zr+Pt coating. In both cases, the core photoelectron binding-energy of Pt 4f photo-electrons shifted towards higher energy levels. Wertheim et *al.l* reported the shift towards higher binding energy with a sligthly different energy value [143]. In the Wertheim et *al.* study, the $4f_{7/2}$ line for the pure Pt metal was given as 71.08 eV, which is roughly 0.029% less than the value found in this work. In the same study, the $4f_{7/2}$ binding energy for $HfPt_3$ was reported as 71.61 eV, which is 0.49 eV (~0.67%) less than the value found in the current work. It should be noted that the values reported by Wertheim *et al*. were related to the pure $HfPt_3$ phase, in contrast to our current work that consists of a mixed chemical state between $HfPt_3$-$ZrPt_3$ and pure Pt-metal. The higher binding energy for Pt in the mixed state within the $ZrPt_3$ structure also supports this reasonable difference.

The corresponding 3d and 4f photoelectron spectra of Zr and Hf metal also showed appreciable line broadening towards the lower binding energy level due to presence of the intermetallics. The detailed XPS spectrum of Hf 4f peak positions acquired from Hf/L-Zr+Pt multilayer coating are displayed in Figure 40-a. The shifting or broadening towards the lower energy levels of the Hf core electron binding energy peak is the result of intermetallic compound formation. The measured core-electron binding energies for Hf in the Hf/L-Zr+Pt composite multilayer film were 19.4 eV ($4f_{5/2}$) and 17.7 eV ($4f_{7/2}$). We report that the core-electron binding energies for Hf in the intermetallic phase ($HfPt_3$) were 17.9 eV ($4f_{5/2}$) and 16.2 eV ($4f_{7/2}$). These values are higher than that previously reported for pure Hf metal, as well as, lower than the Hf oxide state. Wertheim *et.al* also stated that the core electron binding energy shifts by 0.88 eV towards the higher binding energy for Hf $4f_{7/2}$ core-level electrons in $HfPt_3$ compared to that of the metallic Hf [143]. The same trend was also observed in the L-Zr+Pt multilayer structure for Zr (Figure 40-b). Fisher *et al.* showed that the core-electron peak position shift towards the higher energy for Zr 3d electrons in $ZrPt_3$ under high oxygen partial pressures [146, 103].

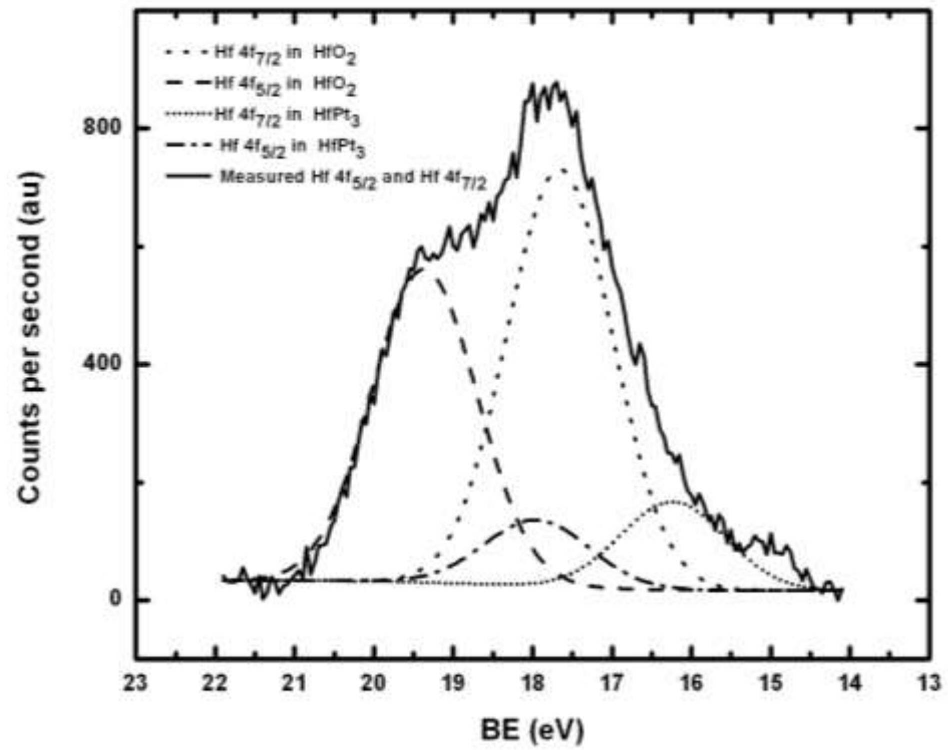

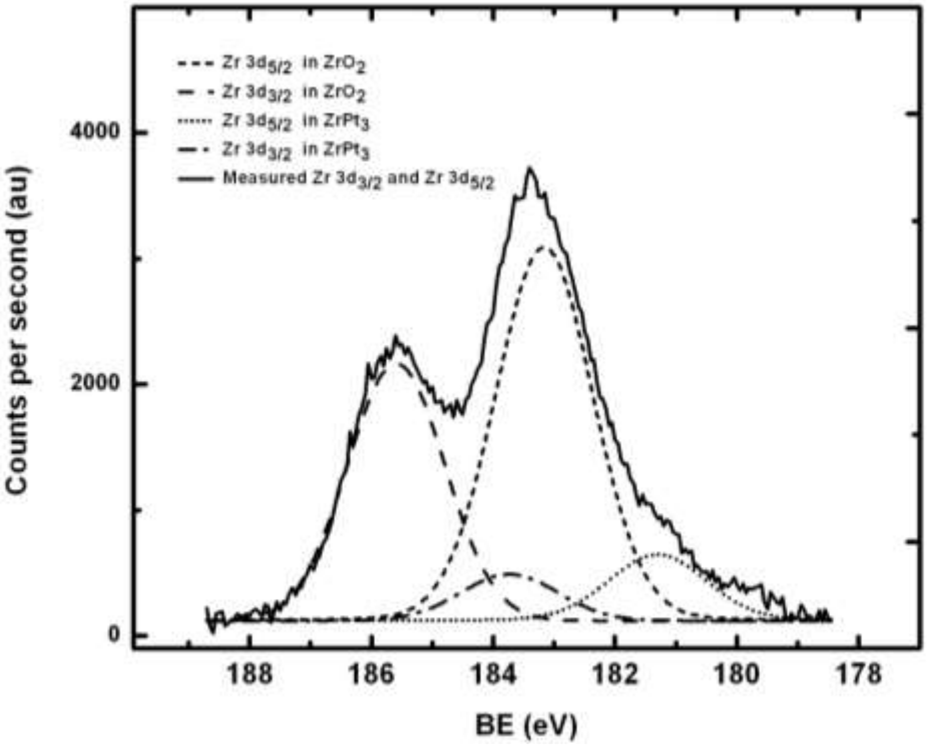

Figure 40 : Detailed XPS scan for the **(a)** Hf 4f peak positions in the Hf/L-Zr+Pt sample **(b)** Zr 3d peak positions in the L-Zr+Pt sample, both annealed at 1200°C for 48 h.

This result indicates that the core electron binding energy of Zr in ZrO_2 is higher than that shown in $ZrPt_3$. In the same study, the authors also reported that Zr $3d_{5/2}$ electrons in $ZrPt_3$ have higher binding energy than that of pure Zr metal. In our experiments, we report core level binding energies for Zr in the L-Zr+Pt structure as 185.5 eV ($3d_{3/2}$) and 183.1 eV ($3d_{5/2}$). These values are slightly lower (0.1%) than the values obtained from the bilayer structure (Zr+Pt). This result may indicate the transformation of ZrO_2 into $ZrPt_3$ which causes a shift in the spectrum peaks positions toward the lower energy levels. The values for $3d_{3/2}$ and $3d_{5/2}$ peaks in intermetallic $ZrPt_3$ phase were 183.7 and 181.3 eV, respectively.

3.7. Electrical Resistivity

The electrical resistivity of the platinum films with different adhesion layers were measured using van der Pauw technique [134]. The various composite films were annealed at 1200°C in N_2 atmosphere for 1-48 h. Table 3 displays the results of the resistivity tests performed at room temperature after the stated annealing procedures. The resistivity values for $ZrPt_3$ and $HfPt_3$ intermetallic phases at room temperature are reported as ~$80x10^{-9}$ Ω·m [104, 138], with the values for pure Pt being slightly higher at an average resistivity of ~$106x10^{-9}$ Ω·m [104]. The infinity symbol within the table indicates a complete loss of electrical conductivity of the coating after the annealing treatment. The as-deposited thin film resistivities for all type of coatings were higher than the reported values for bulk platinum. This higher resistivity is due to the thin film microstructure which contains significant defects, surface and interfacial roughness, oxide precipitates and grain boundaries. The incorporation of the lower conductive adhesion layers into the thin film composite structure also contributed to the electrical resistivity. The L-Zr+Pt and Hf/L-Zr+Pt multilayer composite coatings were the only coatings that showed continuous performance above the 5 h annealing time at 1200°C. The L-Zr+Pt coating sustained a lower relative resistivity with low degradation between 15 and 24 h annealing times; however after the 48 h annealing time, the film experienced a catastrophic failure of the percolated conductive network as seen in Figure 27-d.

The Hf/L-Zr+Pt multilayer coating also showed an increase in resistivity up to the 48 h annealing time, but the conductive network was preserved over the annealing period (see Figure 32-b). The initial (as-deposited) resistivity of the Hf/L-Zr+Pt multilayer coating was found to be higher than that for the 24 h annealed state. The potential cause of this temporary decrease in resistivity may be related to the formation of the lower resistive intermetallic phases ($ZrPt_3$ or $HfPt_3$), and the simultaneous decrease of porosity and grain boundaries due to the controlled sintering/coarsening processes. Similar chemical and microstructural changes also occurred for the L-Zr+Pt multilayer structure, but after the 1200°C annealing for 24 h, any improvements in conductivity due to the formation of the $ZrPt_3$ intermetallic phase was negated by the substantial increase in the level of porosity (as shown in Figure 27-c and -d).

Table 3 also provides the room temperature electrical resistivities of the Pt thin films with double adhesion layer (Zr/Zr+Pt/Pt) which were also processed at 1200°C for various times (in hours). The as-deposited thin film resistivities for all coatings were higher than the reported values for bulk Pt (106×10^{-9} Ω·m) as observed for all other coatings [104]. As observed in the bilayer thin films, the Zr/Zr+Pt/Pt thin film also showed high resistivity compared to the value of bulk Pt in the as-deposited state. However, the as-deposited electrical resistivity is a reasonable match to the values given in literature [144, 147].

Table 3 : Electrical Resistivity of Pt Composite Coatings (10^{-9} Ω.m)

Coating Type	As Deposited	1 h	5 h	15 h	24 h	48 h
Ti+Pt	210	561	∞	∞	∞	∞
Ta+Pt	192	442	3106	∞	∞	∞
Zr+Pt	201	234	684	∞	∞	∞
Hf+Pt	207	244	∞	∞	∞	∞
L-Zr+Pt	252	-	-	315	391	∞
Hf/L-Zr+Pt	247	-	-	-	211	624
Zr/Zr+Pt/Pt	219	257	289	508	∞	∞

Table 3 shows that the Zr/Pt thin film still possessed a conductive network after 5 h at 1200°C; however, the Ti/Pt lost conductivity after 5 h annealing at the same temperature. The Zr+Pt thin film lost electrical conductance after 15 h annealing at 1200°C. As can be shown from the SEM micrographs presented in Figure 36, the gradual microstructural deterioration of the thin film correlated well with the gradual increase in the measured resistivity values. After the 24 h annealing at 1200°C, the Pt granular network was destroyed for the Zr/Zr+Pt/Pt film which resulted in the loss of the conductive network across the film.

3.8. Stability of Microelectrodes

Micro-electrode fabrication was completed by optical lithography over highly-polished Al_2O_3 polycrystalline substrates with optimized coating architectures including Hf/L-Zr+Pt and Zr/Zr+Pt/Pt . The choice of photoresist was dictated by the deposition temperature. The positive resist AZ 3330-F, which is generally used for reactive-ion etching (RIE) procedures, was spin-coated over the alumina substrates to a thickness of 3.5 µm in order to have reasonable surface adhesion during the film deposition procedure at the elevated temperature (200°C). A conventional photolithography process was carried out to define the electrode pattern within the photo-resist. After the pattern was transferred, the wafers were given a post-bake at 120°C for 5 minutes to strengthen the photoresist. Different types of electrodes were deposited successfully by the previously described deposition processes at 200°C. Figure 41-a, -c and -d shows the micro-electrodes with a 1.5×5 mm and 50 µm finger spacing. As the micrographs reveal, the pattern quality was satisfactory with the desirable sharp image transfer.

To this point, the discussion on the stability of the Pt electrodes has been reserved for continuous thin films deposited over a ~5 cm^2 sample (without patterning). The continuous planar films represented the ideal case for the thermal stability of a patterned IDEs for micro-devices. However, the nature of the lift-process, which includes other processing variables, may inject processing factors that could affect the microstructure or architecture of the film (and thus limit the high temperature life-expectancy). These variables would be primarily aligned with the influence of the photoresist during deposition and the potential development stage, which may produce surface/edge defects or film under-cutting.

IDEs with the Hf/L-Zr+Pt multilayer and Zr+Pt bilayer coatings were annealed at 1200°C for 15 h. Figure 41-a and -b present the Zr+Pt bilayer electrode after annealing at 1200°C for 15 h. As seen from the micrographs, the micro-electrode microstructure was altered into isolated Pt grains and/or clusters of Pt grains. Figure 41-c shows the SEM micrograph of the as-deposited Hf/L-Zr+Pt microelectrode. Figure 41-d shows that the Hf/L-Zr+Pt micro-electrode after annealing at 1200°C for 15 h. As the micrograph reveals, the pattern quality was highly preserved, with even the corners and edges remaining distinct in shape; however, the percolation of the film deteriorated as expected from the previous thin film experiments, but the quality remained superior to the Zr+Pt bilayer micro-electrode. As seen from Figure 41-e, the edge of the Hf/L-Zr+Pt micro-electrode coarsened to a greater extent compared to the middle zone. The electrical resistivities of the IDEs were measured and the results were similar to that measured for the un-patterned electrodes which indicate no significant pattern or continuity loss.

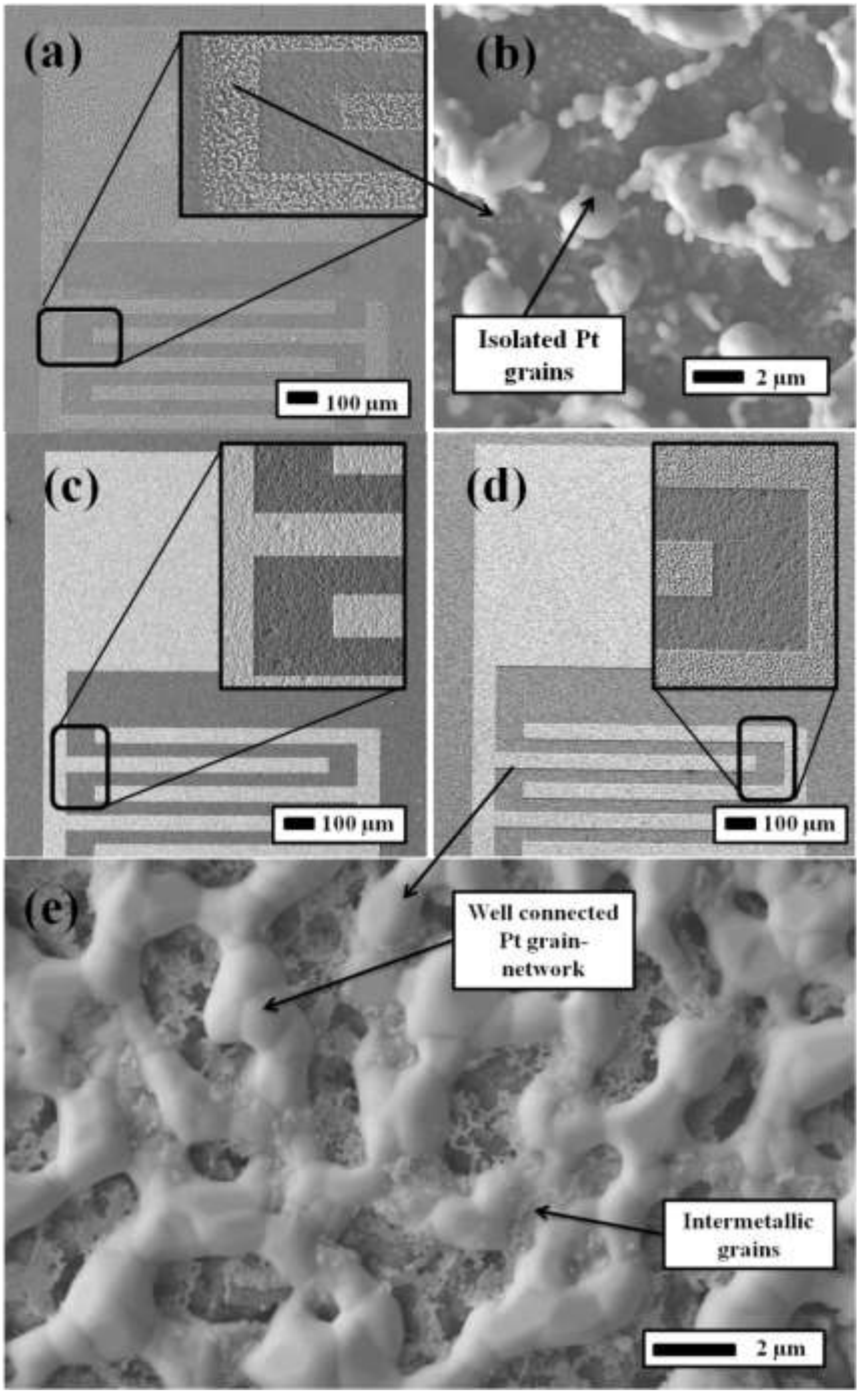

Figure 41 : (a) Zr+Pt bilayer electrode after annealing at 1200°C for 15 h, inset shows the edges closely (b) High magnification SEM image shows the edge of Zr+Pt electrode after annealing at 1200°C for 15 h. **(c)** As-deposited Hf/L-Zr+Pt multilayer electrode, inset shows the edges closely **(d)** High magnification SEM image shows the edge of 15 h 1200°C annealed electrode. **(e)** High magnification SEM image shows the edge of Hf/L-Zr+Pt electrode after annealing at 1200°C for 15 h.

Figure 42 shows SEM micrographs of the as-deposited micro-electrodes with Zr/Zr+Pt/Pt coating architecture. The general view of the Zr/Zr+Pt/Pt micro-electrode with 600 × 1350 µm and 20 µm finger spacing can be seen in Figure 42-a. Figure 42-b shows the higher magnification of the as-deposited microelectrode. As the SEM images reveal, the pattern quality was quite satisfactory where the pattern edges are sharply defined.

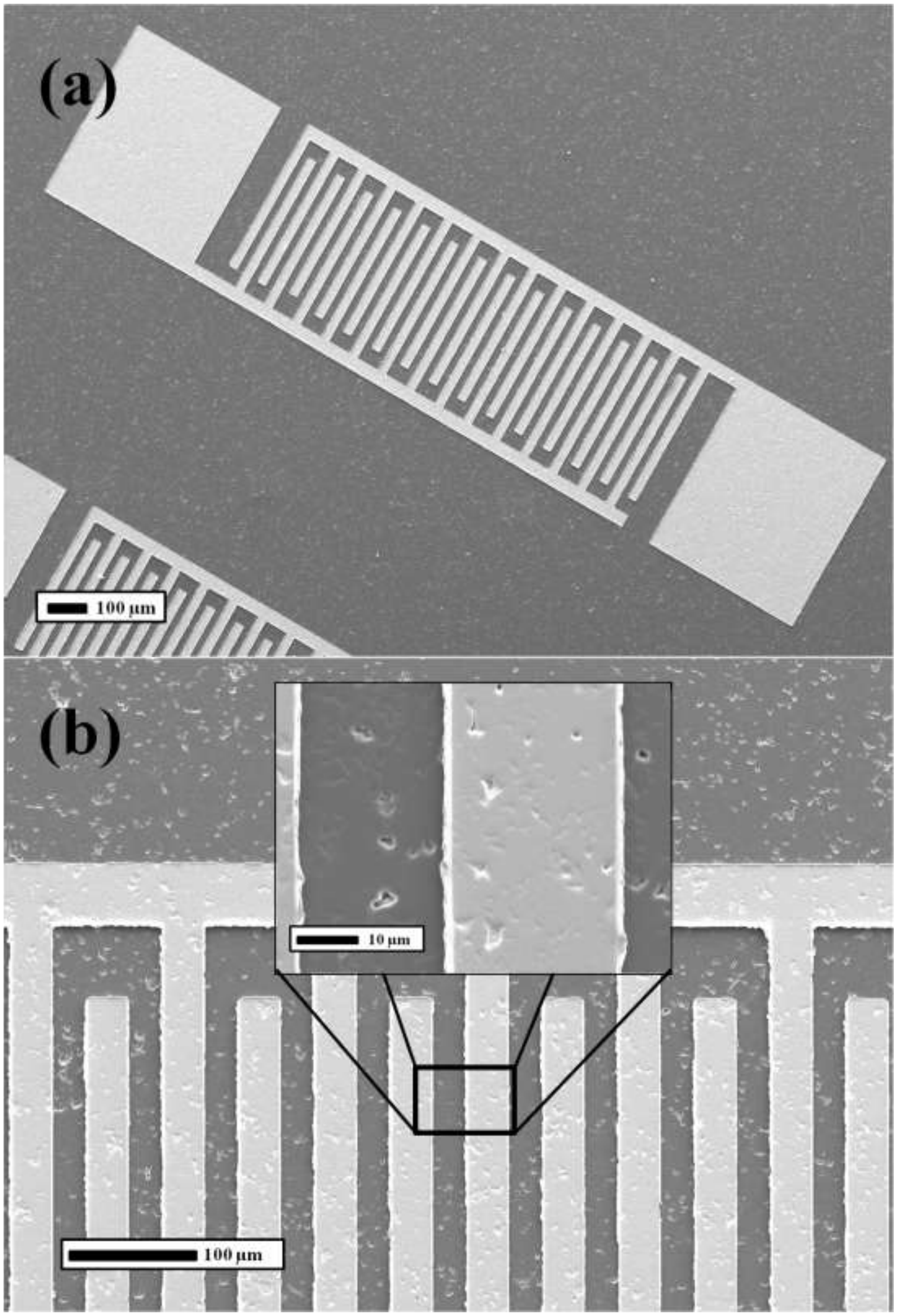

Figure 42 : SEM micrographs of as-deposited Zr/Zr+Pt/Pt microelectrodes, showing **(a)** general view and **(b)** high-magnification images (inset shows edges clearly defined).

Figure 43 shows SEM micrographs of the Zr/Zr+Pt/Pt microelectrodes after annealing 15 h at 1200°C. As seen in the Figure 43-a and -b, the IDE pattern, including adhesion layer, was preserved with even the most vulnerable part of the pattern (corners and edges) showing high definition. As seen from Figure 43-c, Pt microstructure coarsened to a greater extent at the edge of the electrode compared to the middle zone. In these regions, some disturbances of the Pt over Zr were observed. Although limited coarsening was seen for the Pt top layer (see Figure 43-b inset), the patterned Zr/Zr+Pt/Pt thin film retained a high level of percolation without isolation into discrete islands (see Figure 43-c), which is not valid for Ti/Pt and Zr/Pt. The conductive and continuous Pt top layer was not lost after the high temperature annealing, and the electrode pattern retained the high level of percolation leading to excellent electrical performance in Zr/Zr+Pt/Pt microelectrodes.

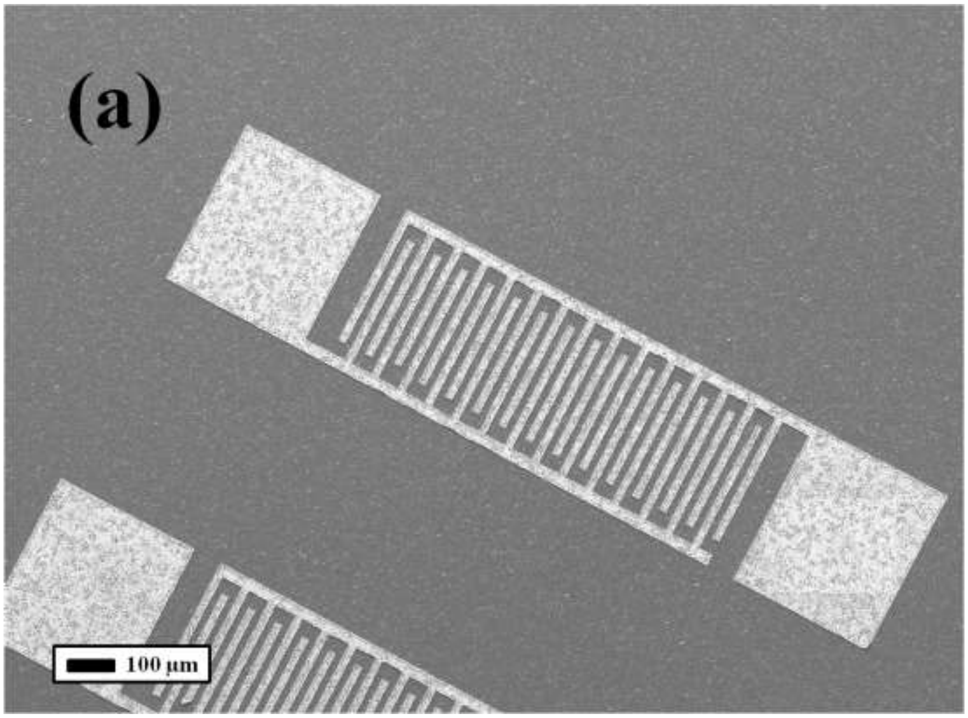
(a)
100 µm

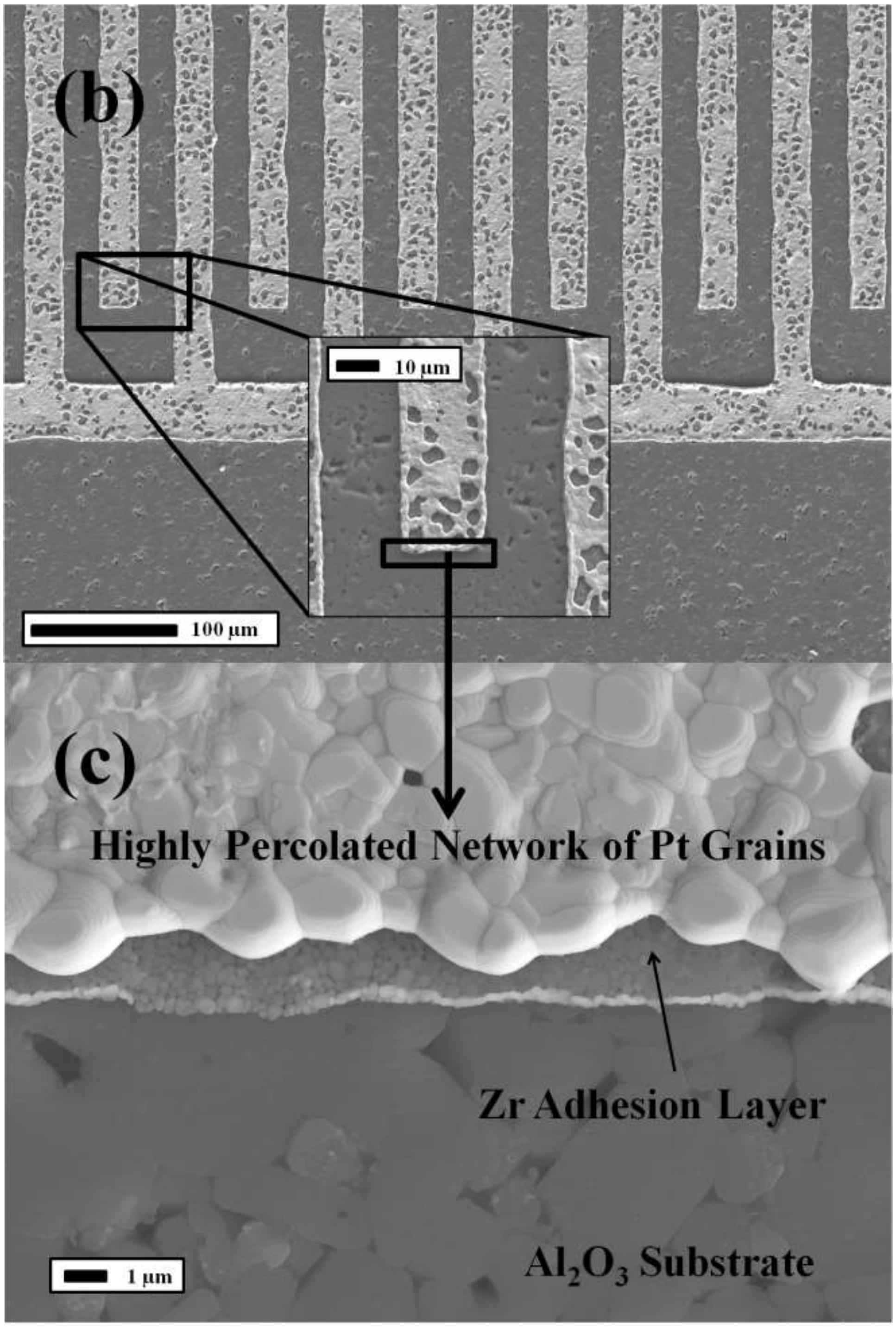

Figure 43 : SEM micrographs of the Zr/Zr+Pt/Pt microelectrodes after annealing at 1200°C for 15 h **(a)** general view **(b)** high-magnification close-ups for showing edges clearly **(c)** high-magnification taken form imminent edge of the microelectrode shows Pt top layer and adhesion layer over substrate

For comparison purposes, the Zr/Pt thin film micro-electrode was manufactured and annealed at 1200°C for 15 h. SEM micrograph of the Zr/Pt micro-electrode after annealing is presented in Figure 44-a. As seen in the image, the microstructure of the Zr/Pt micro-electrode presents non-conductive islands of Pt. The microstructure of the Zr/Pt microelectrode reveals a difference compared to Zr/Zr+Pt/Pt microelectrode which is annealed with same conditions (see Figure 43-c). For further comparison, screen-printed IDEs that are typically used for miniature sensor manufacturing in the mm- to cm-size range were prepared. The Pt ink used for screen-printing was made from Pt powder purchased from Technic Engineered Powders with particle sizes around 1 µm. The screen-printed electrodes had a total length of 10 mm with finger width and finger spacing of 400 µm and 10 µm in film thickness. The thick film (screen-printed) electrode with the large grain size Pt should resist the effect of coarsening/sintering at these high temperatures compared to thin film micro-electrodes. Figure 44-b shows the SEM micrograph of the screen-printed electrodes after annealing at 1200°C for 15 h. After annealing, the IDEs formed with the screen-printed Pt powder showed a highly disrupted microstructure. The microstructure displayed separate Pt islands in the size range of 5 µm with various size pores separating these islands. The microstructure is in far contrast to that shown for the Zr/Zr+Pt/Pt thin film micro-electrode structure processed at the same conditions (see Figure 43-b).

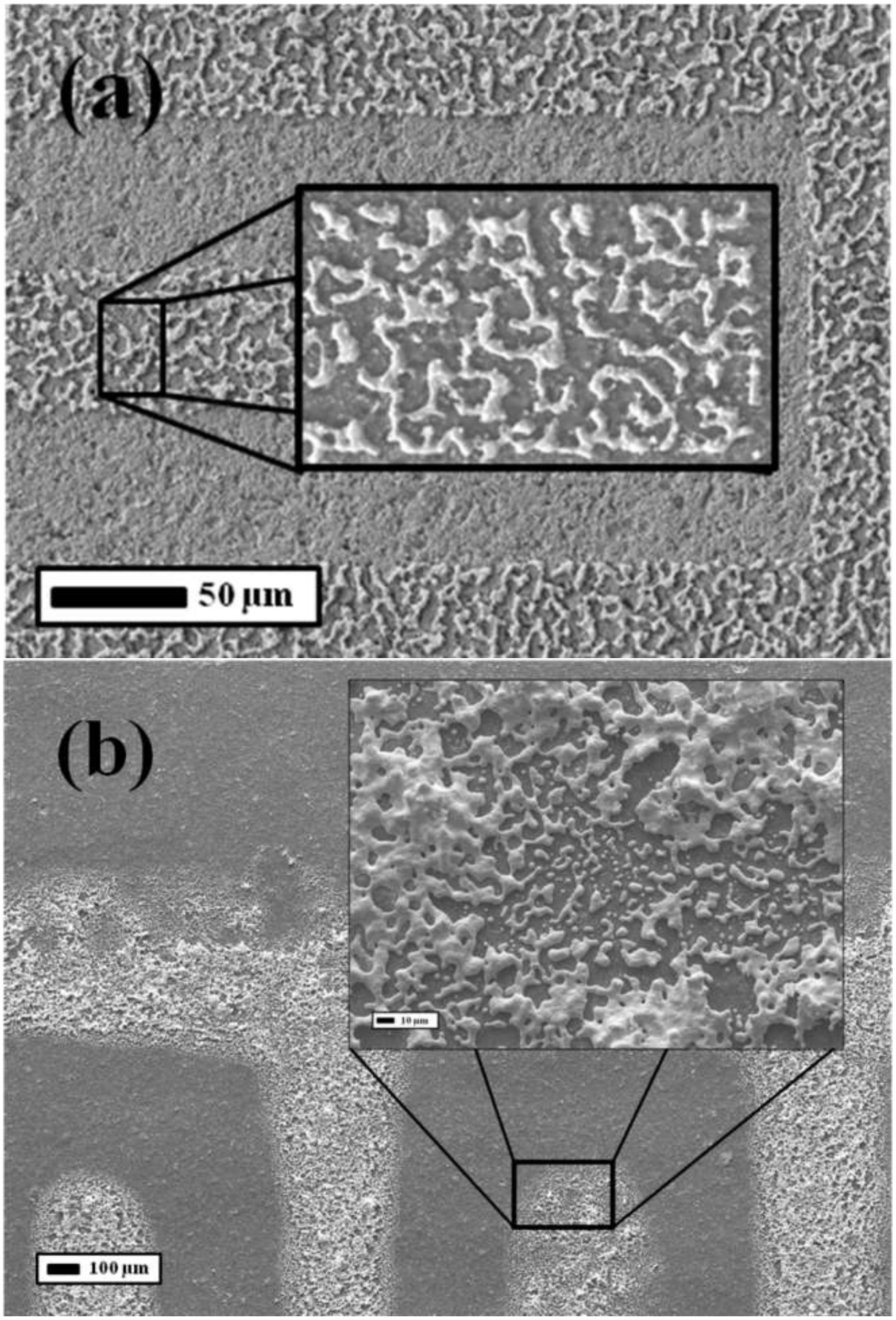

Figure 44 : SEM micrographs of **(a)** the partial view of Zr/Pt microelectrode and **(b)** the partial view of screen-printed Pt macroelectrode after annealing at 1200°C for 15 h

3.9. Conclusion

The thermal stability limitations of Pt films with various adhesion layers (Ti, Ta, Zr, and Hf) were characterized at 800 and 1200°C for various annealing times. The microstructural stability of the Pt thin films with the incorporation of Zr within the bulk was characterized by SEM, EDS and XPS, electrical resistivity measurements and stability tests after high temperature annealing procedures. The different migration behaviors of the refractory metals within Pt were shown to be the main variable that controlled wetting, sintering, and coarsening of the Pt films on alumina surfaces. The movement or chemical reaction of these adhesion layers, or lack thereof, dictated the formation of hillock formations and breaking of the percolated Pt conductive network. The deposition of the Hf adhesion layer showed a high level of microstructural stability (compared to the Ti, Ta, and Zr) to the highest operating temperature (1200°C). The Hf was also incorporated within the bulk Pt conductive layer by depositing an alternating layer structure of Hf and Pt metal. This conductive film was utilized in order to apply a Zener-pinning strategy to limit Pt grain boundary mobility. The incorporation of the Hf within the bulk Pt layer was found to be less successful in controlling the microstructural degradation at the highest annealing temperatures compared to that found with the use of Zr within the bulk Pt film. The combination of utilizing the Hf adhesion layer, as well as, the incorporation of Zr within the bulk Pt conductive layer resulted in a film with the greatest microstructural stability over a wide temperature range. This combination significantly hindered de-wetting and grain growth processes. The electrical resistivity measurements confirmed the retention of the percolated conductive network. In the end, a Pt composite multilayer film was developed that could withstand high-temperature exposure up to 1200°C for 48 h, which is beyond most reasonable, high-temperature chemical sensor applications or MEMS processing (and/or operation) conditions. Moreover, the stable films demonstrated in this work were sputtered at ≤200°C, which provided the opportunity to utilize a simple lift-off patterning process during device fabrication with a select photoresist composition. This is important since wet-etching processes of the bilayer/multilayer films may prove to be difficult due to the different chemical solubility of these metals in aqueous solutions. The final manufactured IDEs verified the compatibility of these complex electrode structures/compositions with basic lift-off patterning techniques.

It was further investigated that alternative a DC sputtering process for fabricating a functionally-gradient Pt and Zr composite microstructure with three deposition steps. The resultant microstructure of the composite electrode thin film was shown to be stable up to 1200°C. The microstructural stability of the Zr/Zr+Pt/Pt film architecture was attributed to the distribution of Zr throughout the bulk of the film during the three-step deposition process. The presence of the Zr deep within the Pt bulk microstructure resulted in the pinning of the Pt grain boundaries by the resultant ZrO_2 and $ZrPt_3$ phases, which in the end, impeded the sintering and coarsening of the Pt grains. Also, the presence of the Zr within the bulk Pt film decreased the migration of the Zr away from the adhesion layer at the oxide substrate surface. This migration of the metal/metal oxide adhesion layer film from this interface was previously shown to be a key characteristic leading to hillock formation (dewetting) of the precious metal electrode films (on oxide substrates) after high temperature processing (especially for Ti and Ta adhesion films). The four-point probe electrical resistivity measurements were also conducted in order to correlate the effect of microstructural alterations to the electrical conductance of the thin films after various annealing schedules. The electrical resistivity measurements agreed on the retention of the percolated conductive network for the Zr/Zr+Pt/Pt type thin film. The modified DC sputtering technique used to deposit the composite film in this work was proven to be an efficient method that did not require the use of various Pt solid solution targets and/or expensive dual-sputtering capabilities, layer by layer sequential deposition procedure. In addition, the methods used were compatible to typical lift-off techniques for producing micro-patterned electrodes consisting of the high temperature stable Pt films (Zr/Zr+Pt/Pt). The micro-electrodes formed with this technique performed similar to its thin film counterpart characterized throughout the work.

Chapter 4: Synthesis of Tungstate and Molybdate Nanomaterials

4.1 Introduction

Transition metal oxides (TMOs) have long been utilized as a fundamental contributor to many advanced functional materials and technological devices. Currently with the nanotechnology revolution, different transition metal oxides (such as TiO_2, ZrO_2, MoO_3, WO_3, ZnO, SnO_2, NiO, CrO_3, Co_3O_4, VO_2 and HfO_2) are of interest with controlled shapes, textures and ordered morphologies. All oxide compounds contain elements between titanium (Ti) and cupper (Cu) in the 3d series, zirconium (Zr) and silver (Ag) in the 4d series and finally hafnium (Hf) and gold (Au) are considered transition metal oxides (TMOs). The significant importance of those elements stem from their varying chemical and physical properties, which is dependent upon their crystal structure and bonding. The latter two for these elements are primarily dictated by the progressive filling of the energy levels of d orbitals by electrons. [7, 148, 149, 150]. Recently, the nanomaterials of these oxide compositions have shown exceptional and unexpected properties compared to their bulk counterparts. These enhancements in physical, electrical and magnetic properties have been attributed to: 1) the high surface to volume ratio, 2) varying surface energies, and 3) quantum confinement effects (which significantly affect the charge transport, electronic band structure as well as optical properties) [151, 152, 149, 153].

A tungstate is a chemical compound with an oxoanion of tungsten or is a mixed oxide containing tungsten. The orthotungstate (WO_4^{2-}) is the simplest tungstate ion. A molybdate is a compound containing an oxoanion with molybdenum in its highest oxidation state of 6, like orthotungstate, orthomolybdate is the simplest form of molybdates (MoO_4^{2-}). Molybdenum and tungsten can form a very large range of such oxoanions that is called polyoxometallates. Compounds ABO_4 stoichiometry can take different crystal structures such as scheelite ($CaWO_4$), rutile ($CrNbO_4$), wolframite ($CdMoO_4$), monazite ($CePO_4$) and zircon ($NdCrO_4$), however $CoWO_4$, $MnWO_4$ and $NiWO_4$ adopt monoclinic complex wolframite-type [154]. In these structures B site is occupied by high valence transition metal such as Cr, Nb, W or Mo, however alternatives for A site occupation range from earth metals to lanthanides [155]. The main difference between scheelite and zircon is the edge or corner sharing of the polyhedral. The difference between rutile and scheelite is based on the cation packing as well as size difference of the A site cation, bigger the size difference the more likely the scheelite formation. This conclusion is valid for wolframite and scheelite comparison as well. In rutile structure all cations packed in octahedral coordination, however in scheelite A site cation located in octahedral coordination while B site cations positioned in a distorted tetrahedral coordination. Scheelite structure can be thought as the distinct units of AO_8 and BO_4, while the latter isolated from each other and connected to alkaline earth dodecahedron via oxygen sharing. Scheelite structure ABO_4 stoichiometry can be defined as highly ionic with A site cations and BO_4 tetrahedra. The primitive cell has two units of ABO_4 units and crystal possess inversion center [156]. In scheelite structure all tetrahedral interstitial are occupied by oxygen ions, however octahedral interstitials are empty. For scheelite structure bigger the A site which is generally electropositive alkaline earth metal (Ca, Sr, Ba) cation smaller the crystal packing factor is achieved. In the case of smaller Mg cation as well as Ni and Fe for A site in the ABO_4 stoichiometry, the material crystallize in the α-$MnMoO_4$ structure. It should be noted that low pressure high temperature conditions favor the wolframite crystal structure for Ni, Co and Fe [155, 157, 158, 159, 160]. In recent years, oxide materials with a scheelite-type crystal structure, such as molybdates and tungstates with the general ABO_4 structure, have received great attention, because of their wide applications in optical devices, magnetic materials, catalysis and more recently potential anode material in SOCF, ion batteries as well. They potentially may be good choice as sensing material for sulfur compounds, especially in the nano form due to high surface to volume ratio. Moreover, binary oxide (WO_3) form of W has already utilized as an active sensing layer due to its well-known properties as reversible adsorbents of sulfur compounds, while Mo has appeared as a sensing material in a few papers [22, 32]. In addition to abovementioned technological fields, catalytically active nature of scheelite tungstates and molybdates is the subject of intense research recently [161] [162, 163] [164, 156, 153, 158, 165, 159, 166, 167, 168] .

There are many different methods for synthesizing nano-structures of TMOs using physical vapor deposition (PVD) and chemical vapor deposition (CVD) techniques. These include different sputtering, thermal evaporation, electron beam, pulsed laser deposition, arc-discharge, sol-gel templating, hydrothermal, electrochemical anodization and electrodeposition techniques and more recently a vapor diffusion sol-gel (VDGS) method [169]. These methods modified in a manner to tune the structural and electronic properties of the compounds of interest. Among those methods, sputtering, sol-gel and hydrothermal methods have received the most attention due to their relative simplicity. In sputtering, the process parameters can be carefully controlled in order to define the desired crystallinity, structure thickness, grain size and morphology. Sol-gel and hydrothermal routes are the most favorable deposition techniques due to their ability for mass production, low deposition temperature and good control of morphology as well as crystallinity [150, 164, 170].

The hydrothermal method is a well-established, facile and cost effective technique in contrast to solid-state synthesizing techniques for forming nano-structured oxides, sulfides, halides and zeolites [171, 172]. Solid-state reactions (mechanical mixing, stirring, shaking) are one of the simplest and well documented and established methods in order to prepare conventional size powders, but gives poor compositional and morphological control and usually results in low purity materials due to low diffusion rate of ions during synthesis. One of the best methods to synthesize complex chemistry oxides (such as ternary compositions) is through a solution method which results in an excellent control of both stoichiometry and morphology. The best are sol-gel and hydrothermal, but due to limited precursors and the need to thermally processes to higher temperatures (to form the complex chemistries) in sol-gel method, the hydrothermal process has shown to be the best. In comparison to others, co-precipitation is widely used method however must be accompanied by post processing steps such as calcinations to give rise to crystallinity and compositional homogeneity. In summary, the hydrothermal technique possesses homogeneous nucleation that produce homogeneous particle size with tunable of shape and satisfactory crystallinity, and stoichiometry [173, 17, 172].

The hydrothermal synthesis technique is based on the utilization of an aqueous or non-aqueous solution of precursor materials as a reaction medium in a sealed container accompanied by low (80°C) to intermediate (300°C) reaction temperature at high vapor pressures. The pressure inside the chamber is auto-generated; however it is strongly dependent upon the reactor fill volume (solid and liquid material), reaction temperature, reactant concentration, processing time, and pH of the parent solution. Other significant advantage of the hydrothermal method is its ability to increase dissolution of most inorganic reagents due to the increased pressure. The increase pressure and elevated temperature also enhances the rate of reaction compared to the solid state reaction to form the same compound [174]. Due to the aforementioned advantages, the hydrothermal technique has been utilized for synthesizing alkaline-earth ferrites, molybdates and tungstates with the general formula of MXO_4, where M and X represent the elements Co, Ni, Mn, Ba, Sr and Fe, Mo and W, respectively. The hydrothermal method was also used to form tungstates, such as that of the negative thermal expansion composition ZrW_2O_8. Xing et *al.* reported that a hydrothermal process could be used to synthesize nanorods by manipulating the reaction pH and temperature [175]. The general procedure for the hydrothermal synthesis of MXO_4 nano-structures starts with a salt solution of an alkaline-earth nitrate (nitrate, chlorate or carbonate) and ammoniate or sodium compound of a transition metal [151, 150, 176, 177, 178].

Among the metal molybdates, $SrMoO_4$ with a tetragonal scheelite structure has received considerable attention due to its ability to emit green and blue radiation at liquid nitrogen temperatures, and has been widely used in the fields of heterogeneous catalysis, photoluminescence, optical fibers, scintillating and laser materials. $SrMoO_4$ nanostructures have been investigated to a less extent compared to other molybdates in literature. The hydrothermal route with different initial ion concentrations, processing times and processing temperatures were used. The typical precursor materials used in literature to synthesize $SrMoO_4$ are $Sr(NO_3)_2$ (Strontium nitrate), $SrCl_2.6H_2O$ (Strontium chloride hexahydrate) or $Sr(CH_3CO_2)_2$ (Strontium acetate hemihydrate) for the Sr source and ammonium or sodium molybdates ($(NH_4)_6Mo_7O_{24}.4H_2O$ or Na_2MoO_4) as a source for the Mo. It was reported in the literature that various shaped particles could be formed using these starting source materials, such as donut, dumbbell, spherical, sheet and hollow morphologies of $SrMoO_4$ [179, 177, 178, 180].

The sensitivity of a gas sensor that utilizes a nanomaterial as the active material is largely based on the particle size and purity, crystallinity and microstructure of the sensing material; therefore attempts have been made in order to synthesize different morphologies as well as create different microstructural formations of the same compound. In this chapter, general hydrothermal methods will be presented for the synthesis of binary and ternary molybdates and tungstates as well as core structures for templates growth of aforementioned compounds. The hydrothermal method is preferred for this research due to its powerful control over powder size and morphology and ability to alter microstructure as well as high level of crystallinity at the final product. Different alkalineearths and transition metals will be used for the A-site of ABO_4 structure including Mg, Sr and Ni to increase sulfur and hydrogen sensing and coarsening resistant as well as chemical stability under reducing atmospheres. Precursor conditions (pH and ion concentration), hydrothermal processing temperature and time are main experimental parameters for different morphologies. Crystallinity, chemical state, stoichiometry and thermal stability of the materials will be presented for the choice of best material for hydrogen and sulfur sensing material.

4.2 Experimental

Tungstates and molybdates are the choice of sensing materials, due to their well-known properties as reversible adsorbents of sulfur compounds. Multiple hydrogen (H_2) and sulfur (SO_2) sensing materials were developed with different morphologies: those are tungsten trioxide (WO_3), molybdenum trioxide (MoO_3), and molybdates including $SrMoO_4$ and $MgMoO_4$. Double perovskites synthesized by solid state reactions such as strontium magnesium molybdates ($SrMgMoO_6$) and strontium magnesium tungstates ($SrMgWO_6$). Crystal structures of the as-synthesized powders were characterized by X-ray diffraction (XRD) at room temperature using a Panalytical X-Pert Pro diffractometer (PW 3040 Pro) with Cu Kα radiation with a scan rate of $2°min^{-1}$. Their morphologies were examined using a scanning electron microscope (JSM-7600F SEM) and a transmission electron microscope (JEM-2100 TEM) to confirm crystallinity and particle size. The EDS spectra were obtained using an Oxford INCA 350 connected to JEOL 7600F SEM. X-ray photoelectron spectroscopy (XPS) was also conducted to have deeper information regarding the weather or not secondary phase formation and/or chemical state analysis. The X-ray source was operated at 15 kV and 25 watts using Al Kα (1486.6 eV) radiation. The films were analyzed by a combination of 117.40 eV survey scan and 23.50 eV detailed scans of relevant peaks. A 0.5 eV step was used for the survey scan and a 0.05 eV step for the detailed scan. Prior to spectral analysis all coatings surfaces were cleaned to remove atmospheric and post-depositional contamination with Ar ion sputter cleaning at 2 kV accelerating voltage for 30 seconds. During measurement, the analysis chamber pressure was maintained at ($\sim 10^{-11}$ Torr). Gold (Au) is used as reference with the binding value 84.5 eV if it is possible; otherwise carbon (C) is used for reference at the value 284.5 eV.

4.3 Result and Discussion

4.3.1 Tungsten trioxide (WO_3)

The first composition from tungstates family is WO_3 due to it is the material of choice for SO_2 sensing in the literature [36]. A modified hydrothermal method was employed to synthesize the WO_3 nanorods [181]. Ammonium metatungstate ($(NH_4)_6W_{12}O_{39} \bullet xH_2O$, CAS# 12028-48-, Alfa Aesar) and acetic acid (Alpha Aesar) were used as starting materials. 1.59 g of ammonium metatungstate and 1.32 g of acetic acid were dissolved in 150 ml de-ionized and de-carbonized water in separate beakers. A clear solution was obtained after mixing the two solutions for 5 min with magnetic stirring bar. The pH of the final solution was 4. The 150 ml of the final solution was transferred into a 300 ml autoclave with PTFE (teflon) liner (401A-8336, Autoclave Engineers, PA)) and heated at a rate of 3°C heating to 180°C and held constant for 8 h. The reactor was cooled at the same rate described. After the autoclave hold, the pH of the obtained solution was 4.5. The as-synthesized light blue powder was washed with de-ionized and de-carbonized water buffered to a pH of 4.5, therefore it was prevented that the as-synthesized powder dissolving back into solution. The washing procedure was repeated until the conductivity (σ) of the solution measured less than 10 $mScm^{-1}$.

Figure 45-a and -b show the SEM micrographs of the dried nano-WO_3 powder. WO_3 nanorods are 5 to 150 nm in size a modified procedure in comparison to original work completed by Liu et *al.* [181] resulted in more anisotropic growth rather than assembles of low length nanorods. A SEM micrograph of the commercial grade WO_3 (Tungsten (VI) oxide, 99.8% (metals basis, CAS# 1314-35-8, Alpha Aaser) is presented in Figure 45-c. The grain size of the commercial grade powder is in the range of 500 nm to 2 µm. The nano-WO_3 not only has a smaller grain size compared to commercial grade WO_3, but also possesses a higher porous network. It other words, it means that the commercial grade powder packed better due to isotropic shapes of the powder, however nanosize anisometric-shaped WO_3 particles do not pack efficiently and create porous network.

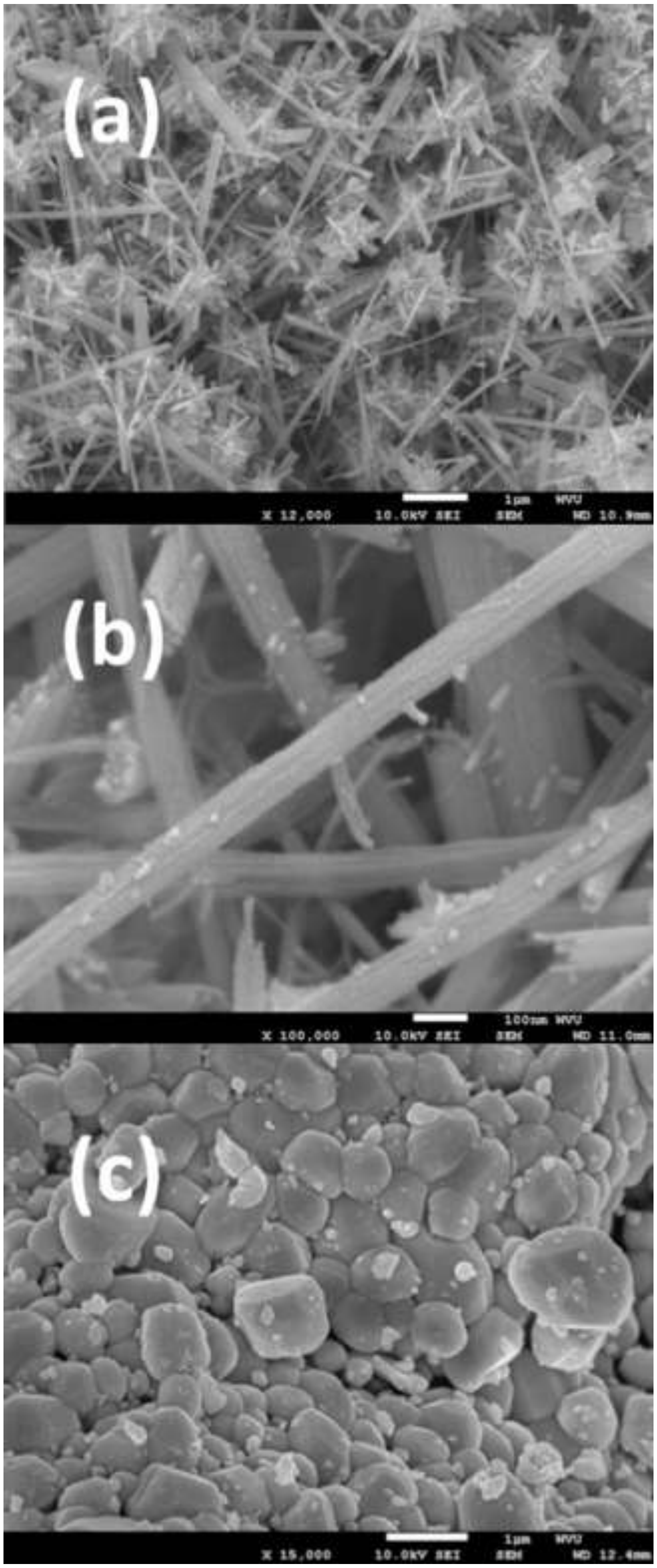

Figure 45: SEM micrograph of the as-synthesized nano-WO_3 **(a)** general view **(b)** high magnification **(c)** commercial grade WO_3.

The powder X-ray diffraction pattern (XRD) of WO_3 nanorods was obtained by running from a 2θ of 20°to 70°. Figure 46 shows the XRD powder diffraction graph of the as-synthesized WO_3 nano powder. All reflections are indexed based on a hexagonal WO_3 cell with a = 7.3242 Å, c = 7.66 Å cell parameters. The JCPDS card used to reference the pattern was 01-085-2460. XPS analysis was also completed over the as-synthesized nano-WO_3, as well as, the commercial grade powder and the results are presented in Figure 47.

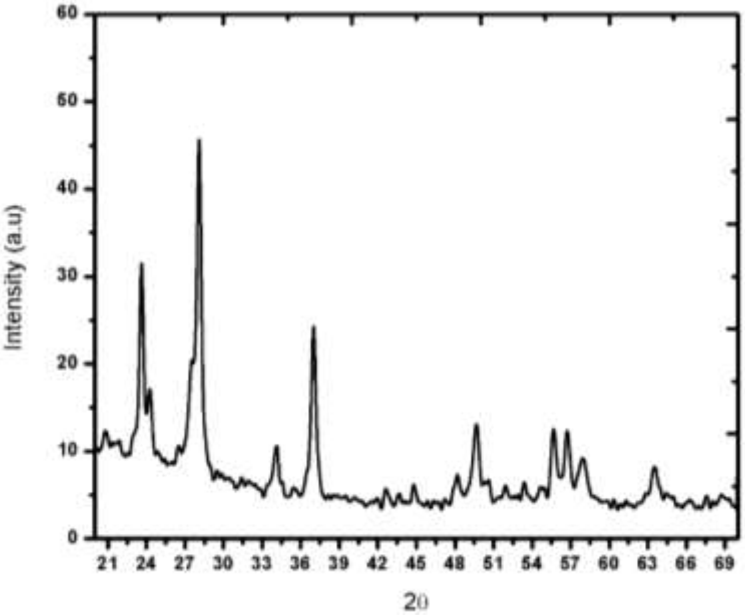

Figure 46 : XRD powder diffraction graph of the as-synthesized nano-WO_3

As seen in Figure 47-a, the XPS peak positions for the nano-WO_3 are 35.67 and 37.85 eV and 34.46 and 36.84 eV for W^{+6} and W^{+5}, respectively. The XPS quantitative analysis showed 14.02% W^{+5} and 85.98% W^{+6} in the nano-WO_3. The XPS analysis of the commercial grade WO_3 is presented in Figure 47-b. The quantitative analysis showed that W^{+5} is less than 5% and remaining is W^{6+}, peak positions located at 35.56 and 37.74 eV for W_{4f} doublet. This difference is important to note, since the sensing testing in the Chapter 5 will discuss the difference in potential sensing mechanism due to these differences in the chemical state of the two abovementioned powders.

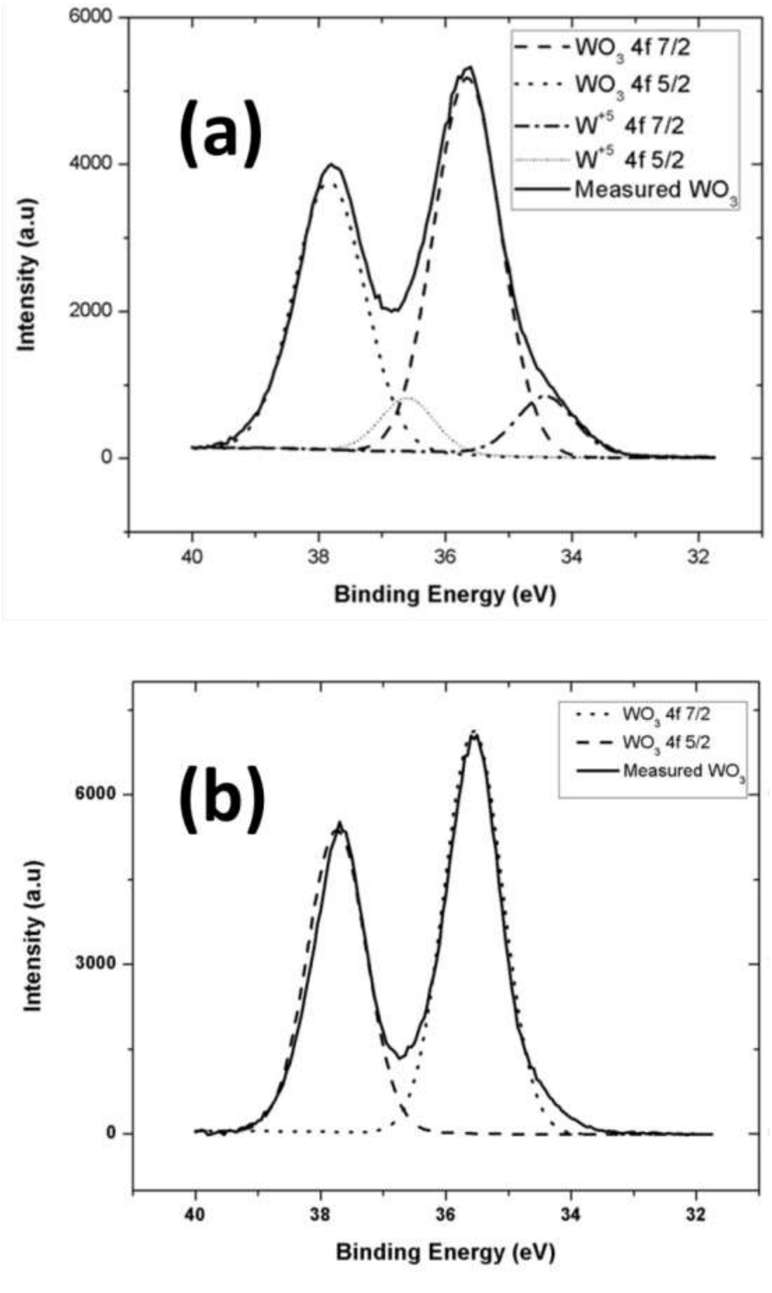

Figure 47 : XPS analysis of **(a)** as-synthesized nano-WO_3 powder and **(b)** commercial grade WO_3.

4.3.2 Molybdates

4.3.2.1 Magnesium Molybdate ($MgMoO_4$)

$MgMoO_4$ is the first ternary material that was synthesized in this work by the hydrothermal method. The results of the procedures that will be described resulted in various morphologies; the variations were primarily controlled by the slight manipulation of the hydrothermal processing parameters. Due to extremely scarce literature regarding the liquid-based synthesis of molybdate compounds, different dwell time, starting compositions and hydrothermal processing temperatures were included as into experimental parameters investigated. In the only available source in the literature synthesis of the $MgMoO_4 \cdot H_20$ and the $MgWO_4 \cdot H_2O$ was realized by mild hydrothermal conditions by transferring the equal volumes of Na_2MoO_4, and $MgCl_2$ and Na_2WO_4 and $Mg(NO_3)_2$ into Pyrex tubes and keeping at 155°C for three days. Although authors conducted detailed crystal structure analysis there was no morphological data available [182]. The first experiments included the combination of 1.48 g of magnesium nitrate hexahydrate ($Mg(NO_3)$, ACS, 98.0-102.0%, CAS# 13446-18-9, Alfa Aesar) and 1.23 g of ammonium molybdate tetrahydrate ($(NH_4)_6.Mo_7O_{24}$, ACS, 81-83% as MoO_3, CAS# 12054-85-2, Alfa Aesar) were dissolved in deionized and decarbonized water in separate beakers. After mixing the two solutions, the pH of the final mixture was adjusted to 7 by drop wise addition of ammonium hydroxide. The final mixture was transferred to an autoclave lined with teflon and processed at 80°C for 8 h; however, the final product was mixture of MgO and MoO_3. SEM micrographs presented in Figure 48 show the microstructure and morphology of the as-synthesized powder, as well as, the EDS analysis of the powder surface. The as-synthesized material showed neither nano-crystalline structure nor stoichiometry of the desired powder.

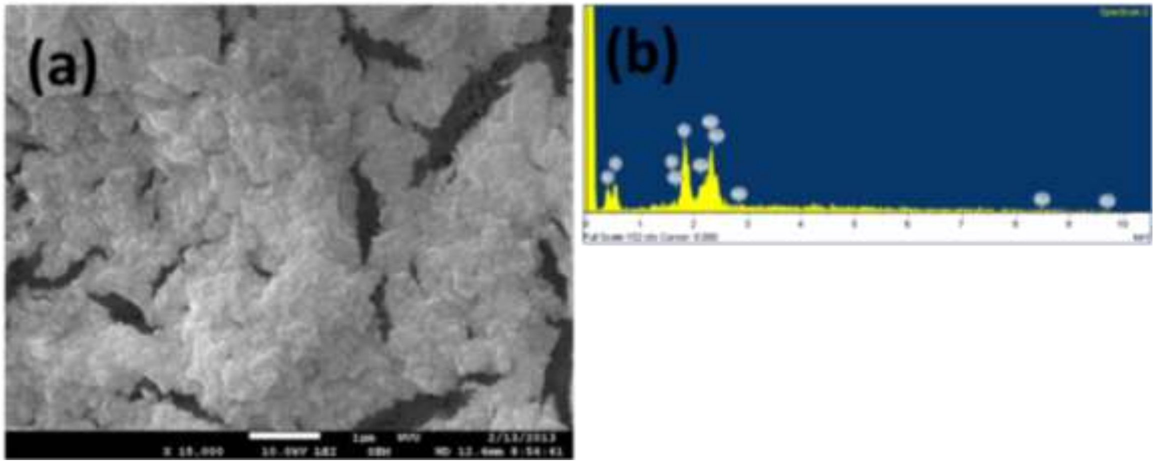

Figure 48 : (a) SEM micrograph of $MgMoO_4$ **(b)** EDS analysis of the as-synthesized powder.

Due to the unsuccessful results obtained in the first experiments, the magnesium nitrate ((Mg(NO_3), magnesium nitrate hexahydrate, ACS, 98.0-102.0%, CAS# 13446-18-9, Alfa Aesar) and ammonium molybdate (($(NH_4)_6.Mo_7O_{24}$) were replaced with magnesium chloride ($MgCl_2$, magnesium chloride hexahydrate, ACS, 99.0-102.0%, CAS# 7791-18-6, Alfa Aesar)) and sodium molybdate (Na_2MoO_4), respectively. In the second set of experiments, 1.02 g of $MgCl_2$ and 1.21 g of Na_2MoO_4 were dissolved in 30 ml of deionized and decarbonized water in separate beakers. After mixing the two solutions, the final pH of the 60 ml solution was adjusted to 11 by drop addition of ammonium hydroxide. The final product was transferred to autoclave with PTFE liner and processed at 160°C for 12h under auto-generated pressure.

The as-synthesized white powder was washed with de-ionized and de-carbonized water as the pH adjusted to a pH of 10.5 in order to hinder un-wanted agglomeration. The washing procedure repeated until the conductivity (σ) of the solution measured less than 10 $mS.cm^{-1}$. Figure 49 shows the microstructure of the as-synthesized powder after drying at 80°C. The SEM micrograph shows that the material is composed of loosely agglomerated particles with a thickness of 20 nm. The material showed very poor crystallinity as can be seen from Figure 49-c that presents the XRD powder diffraction data together with reference JCPDS card numbers of 01-072-2153 for $MgMoO_4$ and 01-047-0457 for hydrogen molybdenum oxide hydrate ($HMoO_3.H_2O$) with for comparison purposes and identification of the obtained powder. As the XRD peak analysis indicates, the material has poor crystallinity and materials contains hydrated molybdenum oxide rather than the desired $MgMoO_4$ phase.

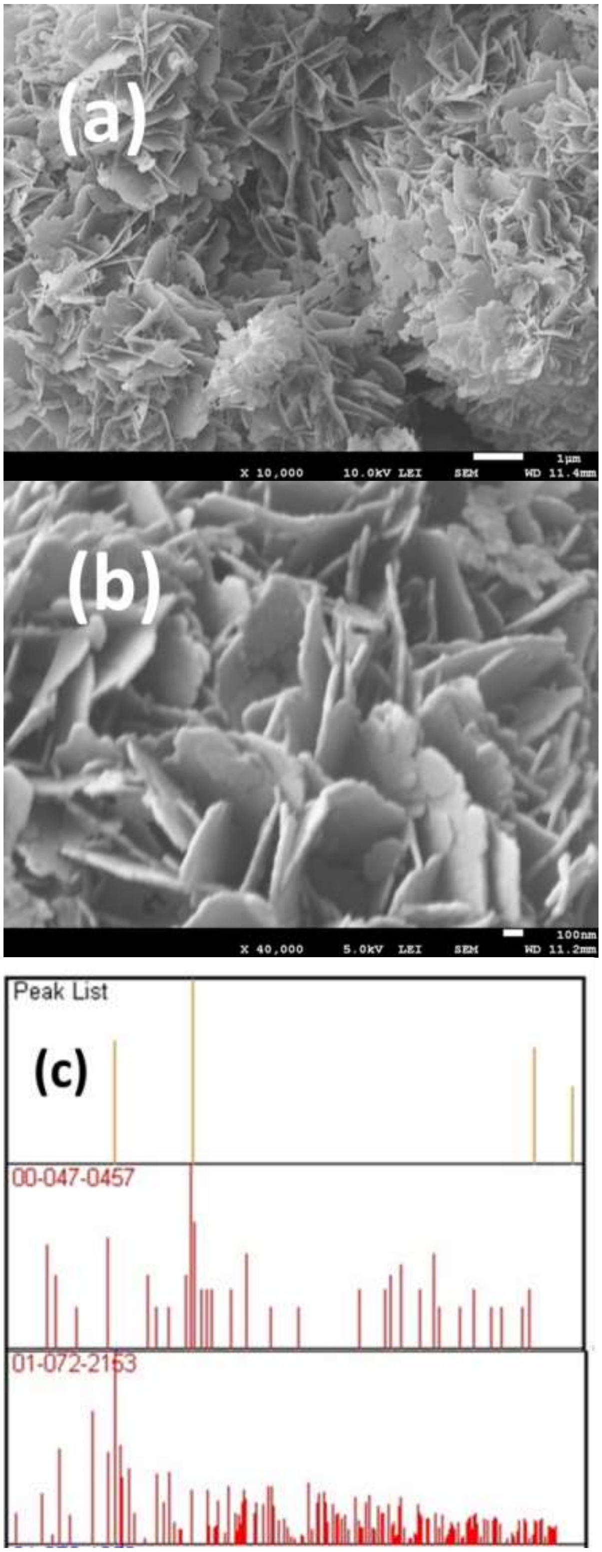

Figure 49 : SEM micrographs of the as-synthesized $MgMoO_4$ **(a)** general view **(b)** high magnification **(c)** XRD of the as-synthesized powder.

Another set of experiments was made by increasing the ion concentration to double the previous level. 2.04 g of $MgCl_2$ and 2.420 g of Na_2MoO_4 were dissolved in 30 ml of deionized and decarbonized water in separate beakers. After mixing the two solutions together, the final pH of the 60 ml solution was adjusted to 11 by drop wise addition of addition of ammonia. The final product was transferred to autoclave with PTFE liner and processed at 160°C for 12h under auto-generated pressure. Figure 50-a, -b and –c show the micrographs of the as-synthesized powder. As can be seen, the as-synthesized material does not have a homogeneous morphology. Two distinct microstructures were shown in the micrographs. The particles had a flake-like morphology with a wall thickness of ~50 nm. The other morphology was spherical with an average size of 50 to 100 nm. Figure 50-d shows the XRD powder scan of the as-synthesized material together with reference JCPDS card numbers of MoO_3 and $MgMoO_4$, 01-076-1003 and 01-072-2153, respectively. As the XRD pattern reveals, the material might be interpreted as either MoO_3 or $MgMoO_4$ due to the lack of observed distinguishable $MgMoO_4$ peaks especially located between 2θ values of 10° and 20°. The EDS analysis of the nano-flakes presented in Figure 50-e showed that nano-flakes contain Mg; however, the spherical particles did not. Therefore, it can be concluded that the as-synthesized material consisted of segregated MoO_3 and Mg deficient $MgMoO_4$ compounds.

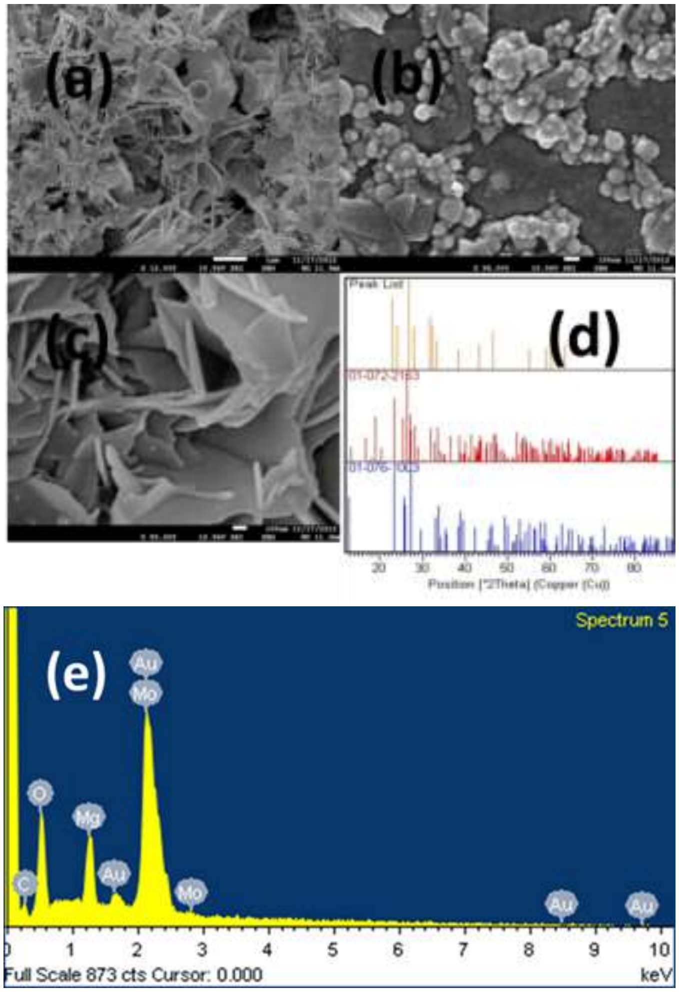

Figure 50 : SEM micrographs of the as-synthesized $MgMoO_4$ **(a-b)** general view **(c)** high magnification **(d)** XRD of the as-synthesized powder with reference MoO_3 and $MgMoO_4$ patterns **(e)** EDS analysis of the as-synthesized nano flakes.

Further experiments were conducted by decreasing the pH concentration of the final solution. Similar solutions were synthesized using 2.04 g of $MgCl_2$ and 2.420 g of Na_2MoO_4 dissolved in 30 ml of deionized and decarbonized water in separate beakers. After mixing the two solutions, the final pH of the 60 ml solution was adjusted to 9 by drop wise addition of ammonia hydroxide. The final product was transferred to the autoclave and processed at 160°C for 12 h under auto-generated pressure. The SEM micrograph of the as-synthesized product presented in Figure 51 reveals that the morphology of the particles were not homogeneous. It can be concluded that lowering the pH increases the material packing, as well as, the amount of the spherical shaped particles. The crystallinity of the nano size flakes must have deteriorated.

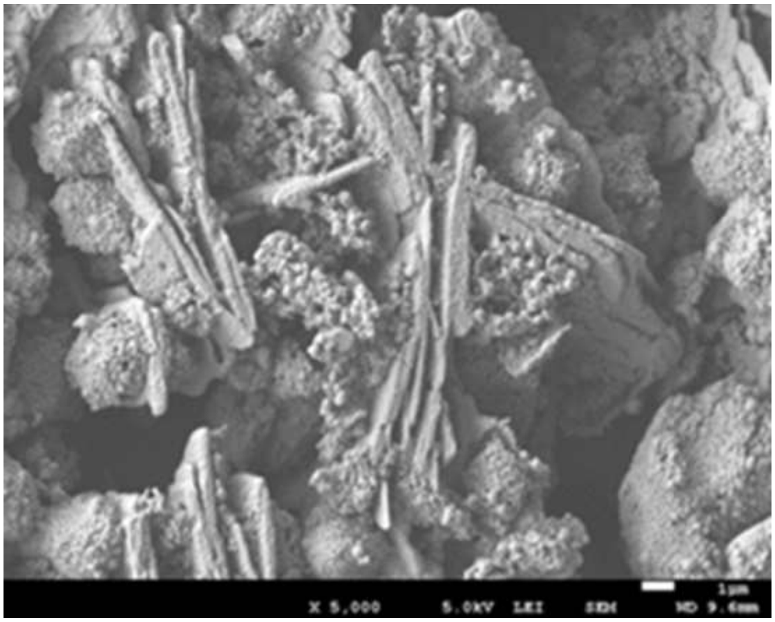

Figure 51 : SEM micrographs of the as-synthesized $MgMoO_4$ (4th).

Further experiments investigated the effect of the ion concentration and pH of the solution on the final product. 2.72 g of $MgCl_2$ and 3.22 g of Na_2MoO_4 were dissolved in 30 ml of deionized and decarbonized water in separate beakers. After mixing two solutions in another beaker, the final pH of the 60 ml solution was adjusted to 11.5 with the addition of ammonium hydroxide. The final mixed product was transferred to the autoclave and treated at 160°C for 12 h under auto-generated pressure. Figure 52-a and –b show the microstructure of the as-synthesized material. As the micrographs reveals, the as-synthesized material displays a blade-like morphology with a 10-20 nm thickness and 50-500 nm width and 2000-3000 nm length. XRD scan of the as-synthesized product was compared against the JCPDS 01-084-1686 reference pattern, which is the only reference pattern available in the literature for Magnesium Molybdenum Oxide Hydrate ($MgMoO_4$ (H_2O)). The XRD spectra is shown in Figure 52-c. The data shows that the material has excellent crystallinity without any further heat treatment. Figure 52-d shows the EDS spectrum of the as-synthesized product. As the spectrum reveals, Mg and Mo co-exist and almost have same intensity when the blades are targeted at various locations.

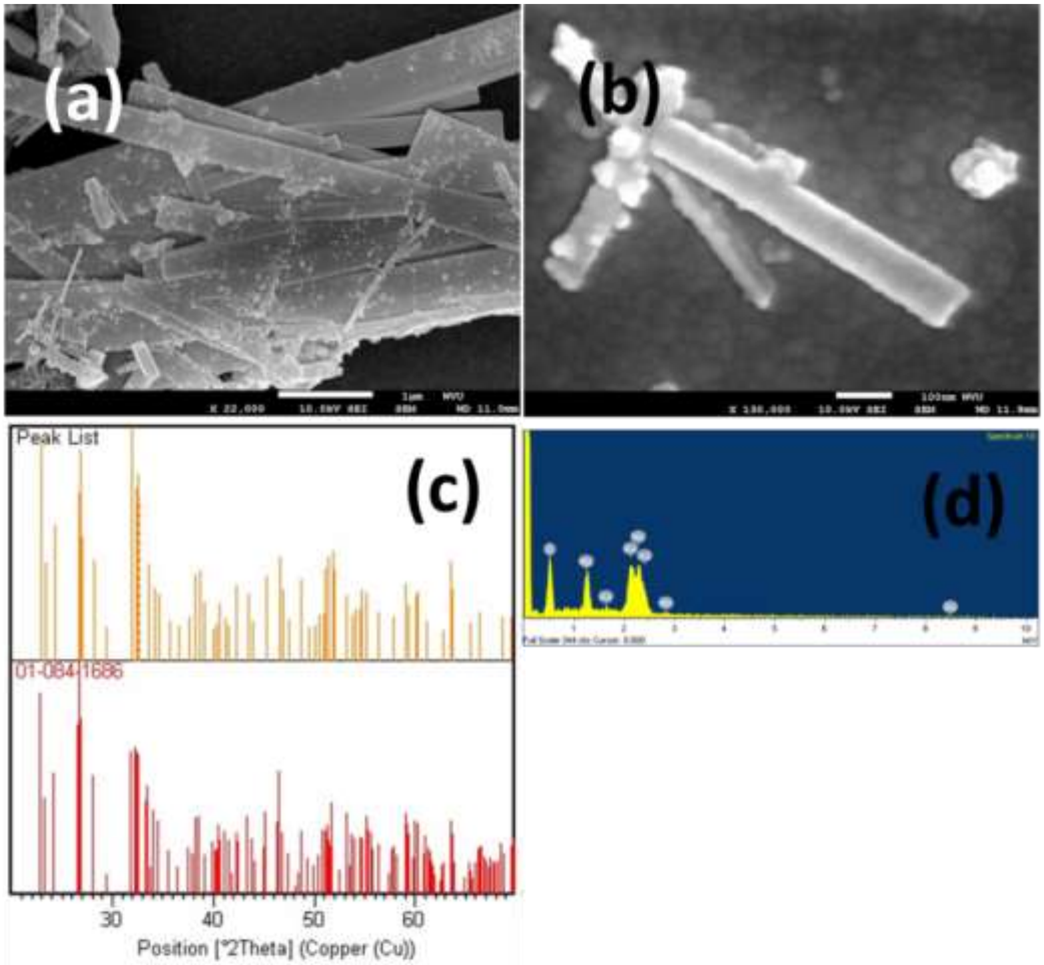

Figure 52 : (a-b) SEM micrographs of the as-synthesized $MgMoO_4$ (5th). **(c)** XRD of the as-synthesized powder with reference $MgMoO_4$ pattern **(d)** EDS analysis of the as-synthesized nano bundles.

4.3.2.2 Strontium Molybdate ($SrMoO_4$)

$SrMoO_4$ is a promising material for wide range of applications [177, 178]. Figure 53 shows the results of the different hydrothermal routes use to synthesize $SrMoO_4$ nanomaterials. There are two main reasons behind allocation time and effort for different morphological formation of the same compound with the same level of crystallinity and stoichiometry. The first reason was to optimize the surface to volume ratio and reduce the packing density as much as possible by creating anisotropic microstructure, which is desirable for gas sensing applications. The second reason is to define the potential material microstructure possesses low diffusional kinetics in order word high temperature sintering resistive morphology. Liu et *al.* used a simple approach to synthesize $SrMoO_4$ by precipitating it out of ammonium molybdate and strontium nitrate over an aluminum (Al) substrate as a dense thick film over a 24 h reaction time without any surfactants. It was reported that controlling the thickness of the sheets was possible via changing the concentrations of the solutes. Another point should be emphasized in this work is that a very simple deposition/synthesis technique was realized however in all cases the general view of microstructure was densely packed leaves/sheets of material covered over a metal substrate [183]. A facile, low temperatre and novel hydrothermal method was developed and employed to synthesize the $SrMoO_4$ nanomaterial in this work. In all of the synthesis processes, the same precursor materials were utilized; strontium nitrate ($Sr(NO_3)_2$, (Strontium nitrate, ACS, 99.0% min, CAS# 10042-76-9, Alfa Aaser)) and ammonium molybdate ($((NH_4)_6{\cdot}Mo_7O_{24}){\cdot}4H_2O$, Ammonium molybdate (para) tetrahydrate, 99%, CAS #12054-85-2, Alfa Aaser). In all cases, 1.48 g of strontium nitrate and 1.23 g of $((NH_4)_6{\cdot}Mo_7O_{24}){\cdot}4H_2O$ were dissolved in de-ionized and de-carbonized water in separate beakers. A clear solution was obtained after magnetic stirring the two solutions for 15 min. The pH of the final solution ranged from 4.5 to 5.5. The final product was transferred into a 300 ml PTFE sealed autoclave and kept at 180°C, 120°C and 80°C for 12 and 8 h, respectively with 3°C heating and cooling rate in all cases. After mixing the two solutions, the final pH of the solution was adjusted to the corresponding values indicated in Table 4 through the addition of ammonia hydroxide. The as-synthesized white powder was washed with de-ionized and de-carbonized water in order to hinder the un-wanted agglomeration. The washing procedure was repeated until the conductivity (σ) of the solution measured less than 10 $mScm^{-1}$.

Table 4 provides the details of the hydrothermal synthesis parameters. Figure 53 shows the micrographs of the as-synthesized $SrMoO_4$ nanomaterials for the nano-teeth, nano-sheet, nano-flowers and nano-rice. Distinctly different morphologies of the same compound were obtained by modifying the hydrothermal reaction temperature, precursor concentration, and pH. The isothermal hold time for the autoclave reaction during the synthesis of the nano-teeth, nano-sheets, nano-flowers and nano-rice were the same (12 h); however, the reaction temperatures were 180°C, 120°C and 80°C, respectively. The decrease in the temperature and increase in the ion concentration affected the growth rate of the co-precipitated $Sr^{2+}$and MO_4^{2-} ions and decrease in feature size and packing density was observed as a general trend. As can be seen from Figure 53-c and –d, at the same pH, higher ion concentration and lower hydrothermal processing and time and temperature resulted in more anisotropic powder morphology in addition to reduction in packing density. This can be attributed to hydrothermal processing time and temperature since it is not likely to see that increase in ion density lead loosely packed microstructure. Liu et *al.* reported that increase in the ion concentration resulted in further increase in the thickness of the sheets and density of the structure as well [183].

Table 4 : Process parameters for hydrothermal synthesis of $SrMoO_4$ with different morphologies

Morphology	**Precursor Materials**	**Processing Time (h) and Temperature (C°)**	**Precursor ion concentration (M)**		**pH**
			Anion ($\mathbf{MO_4^{2-}}$)	**Cation (Sr^{2+})**	
Nano-teeth	$Sr(NO_3)_2$ $((NH_4)_6.Mo_7O_{24})\cdot 4H_2O$	12 & 180	0.0134	0.0934	8
Nano-sheet	$Sr(NO_3)_2$ $((NH_4)_6.Mo_7O_{24})\cdot 4H_2O$	12 & 120	0.025	0.175	8
Nano-flowers	$Sr(NO_3)_2$ $((NH_4)_6.Mo_7O_{24})\cdot 4H_2O$	8 & 80	0.05	0.35	8
Nano-rice	$Sr(NO_3)_2$ $((NH_4)_6.Mo_7O_{24})\cdot 4H_2O$	8 & 80	0.05	0.35	10

Decreasing hydrothermal processing temperature from 180°C to 120°C and doubling the anion and cation concentration from 0.0134 to 0.025 and from 0.094 to 0.175, respectively lead to more isotropic growth as the morphology changed from nano-teeth instead nano-sheet with highly symmetrical spatial growth. It should be noted that the same hydrothermal processing time and temperature, yet different pH level caused drastic change in growth mode and rate. The morphology of the powder has evolved from nano-flower like loosely packed anisotropic structure to densely packed and isotropic rice shaped morphology.

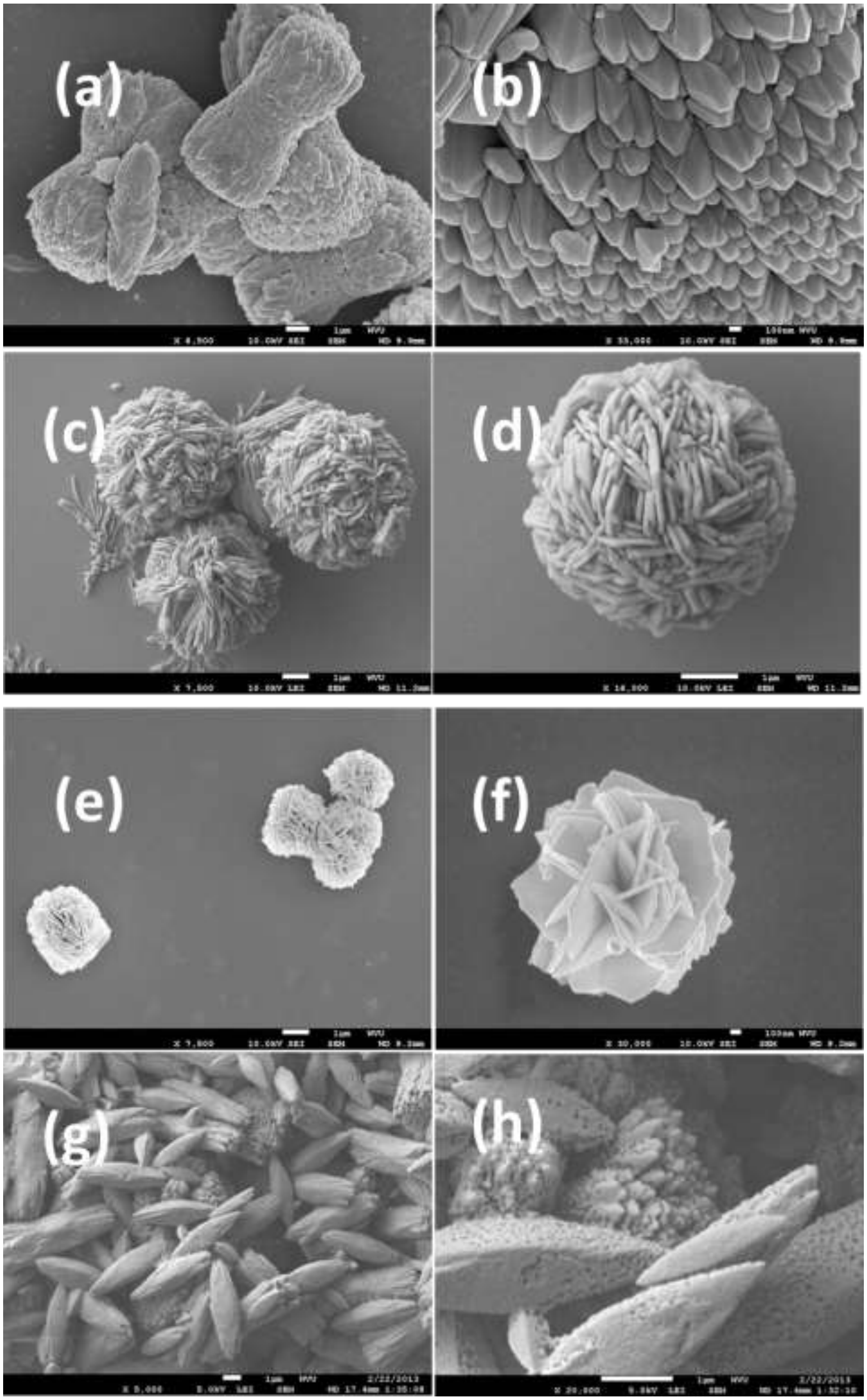

Figure 53 : SEM micrographs of **(a-b)** nano-teeth **(c-d)** nano-sheet **(e-f)** nano-flowers and **(g-h)** nano-rice.

Figure 54 shows the unit cell of the tetragonal scheelite-type structure of the strontium molybdate. The scheelite structure was originally termed after the $CaWO_4$ mineral. For the structure, the Mo is surrounded by 4 O^{2-} in tetrahedral system; on the other hand, the Sr is surrounded by 8 O^{2-} octahedral symmetry. The scheelite structure is mainly made of MoO_4^{2-} and Sr^{2+} as a charge compensator. It can be concluded that oxygen vacancies have important consequences over the electronic and chemical behavior of the compound. The missing oxygen is most likely coming from the c-directions within the structure, since the Sr-O bonds are weaker than that of Mo-O bonds.

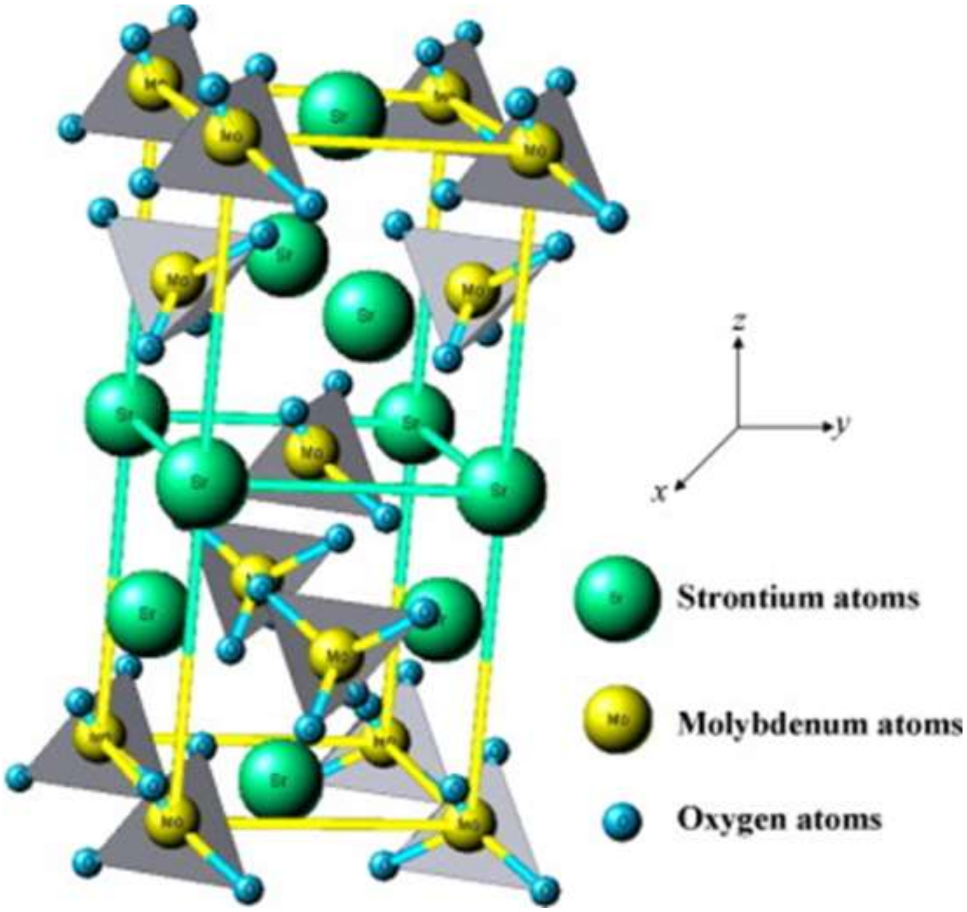

Figure 54 : Schematic presentation of Scheelite tetragonal $SrMoO_4$ unit cell **[184]**.

All of the as-synthesized nano-structures were subjected to XRD analysis to investigate the for crystal structure of each powder. Figure 55 presents the XRD graph of the as-synthesized $SrMoO_4$ nano-flower, and the JCPDS reference pattern (00-008-0482) for the $SrMoO_4$ was also included in the figure. As can be seen in the Figure 55-a, the measured peaks show an excellent match with the reference peaks. All of the diffraction peaks can be indexed with the JCPDS card number 00-008-

0482. The sharp and high intensity diffraction peaks of the as-synthesized nano-flower powder showed good crystallinity with no secondary phases present. In all other cases (nano-sheets, nano-teeth and nano-rice), such an excellent match between the measured and reference XRD data were also obtained.

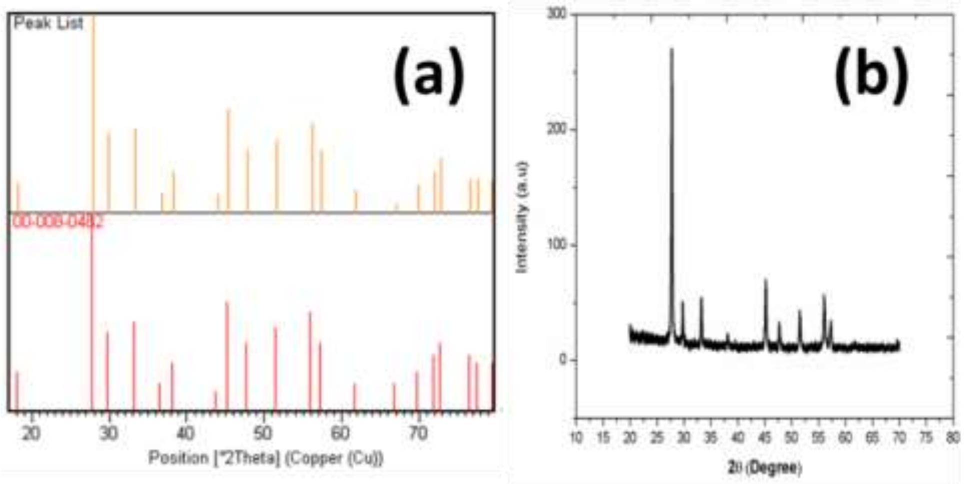

Figure 55 : **(a)** Comparative XRD graph of $SrMoO_4$ nano-flowers with the reference *XRD* JCPDS card number 01-085-0586 **(b)** Measured XRD spectrum of the $SrMoO_4$ nano-flowers.

The XRD pattern was interpreted and specified as the highly anisotropic tetragonal structure of $SrMoO_4$ (JCPDS 00-008-0482). The pattern matches the pattern perfectly with the lattice parameters a=b=5.3944 and c=12.0200. Using the plane spacing and Bragg`s law for diffraction, the lattice parameters were calculated and given in Table 5. As compared to the position given in the JCPDS 00-008-0482, the calculated a- and c- parameters of the as-synthesized nanomaterial show residual stress, which can be attributed to the oxygen vacancies, charge compensation and cation columbic interactions.

Table 5 : Comparison of calculated cell parameters and reference data (00-008-0482).

In this study	**In JCPDS no. 00-008-0482**
Crystal system: Tetragonal unit cell, a=b≠c, α=ß=γ=90°, Space group: I41/a, Space Group number: 88, Scheelite	
(112) plane, peak position; 27.892°, $d_{(112)}$ = 3.1988 Å	(112) plane, peak position; 27.664°, $d_{(112)}$ = 3.2220 Å
(204) plane, peak position; 45.302°, $d_{(204)}$ = 2.0008 Å	(204) plane, peak position; 45.116°, $d_{(204)}$ = 2.0080 Å
(004) plane, position; 29.907°, $d_{(004)}$ = 2.9989 Å	(004) plane, position; 29.696°, $d_{(004)}$ = 3.0060 Å
a=b=5.3236 Å, c= 12.123 Å, a/c= 0.4391 Å	a=b=5.3944 Å, c= 12.020 Å, a/c= 0.4487 Å
Crystalline Size with Scherrer formula: 35 nm	NA

Figure 56 presents the TEM and SEM images of the as-synthesized $SrMoO_4$ nano-flowers including selected area electron diffraction (SAED) pattern and high-resolution transmission electron microscopy (HRTEM) micrograph of (112) plane with interplanar spacing. HRTEM image shows that the $SrMoO_4$ as-synthesized powder shows high crystallinity. Nano-flowers are composed of nanoparticles as seen in the SEM micrograph shown in Figure 56-a. The SEM image shows the morphology of an individual flower. The HRTEM images and SAED patterns further proved that as-synthesized material well crystallized. The SAED pattern shows regular diffraction spots which suggest their good crystallinity. From the HRTEM image, it can also be concluded that the as-synthesized powder is structurally uniform with an inter-planar spacing of about 3.20 Å, which corresponds to the (112) plane spacing of the $SrMoO_4$. The calculated interplanar spacing from the XRD measurements for this plane was 3.1988 Å. TEM images show that due to extensive sonication during sample preparation step (that was also proved by SEM), the as-synthesized nanomaterials consisted of a number of dispersive, fractured nano-size particles with different orientations, which is the result of the fracturing of the flower-like shape. According to the TEM data, the particle size of the powder should be around 50 nm (Figure 56-c); however, that does not reflect the true morphology and grain size of the as-synthesized powder. The TEM data clearly concludes that the building blocks of the as-synthesized powder is poly-crystalline that is consisted of single crystalline leaves.

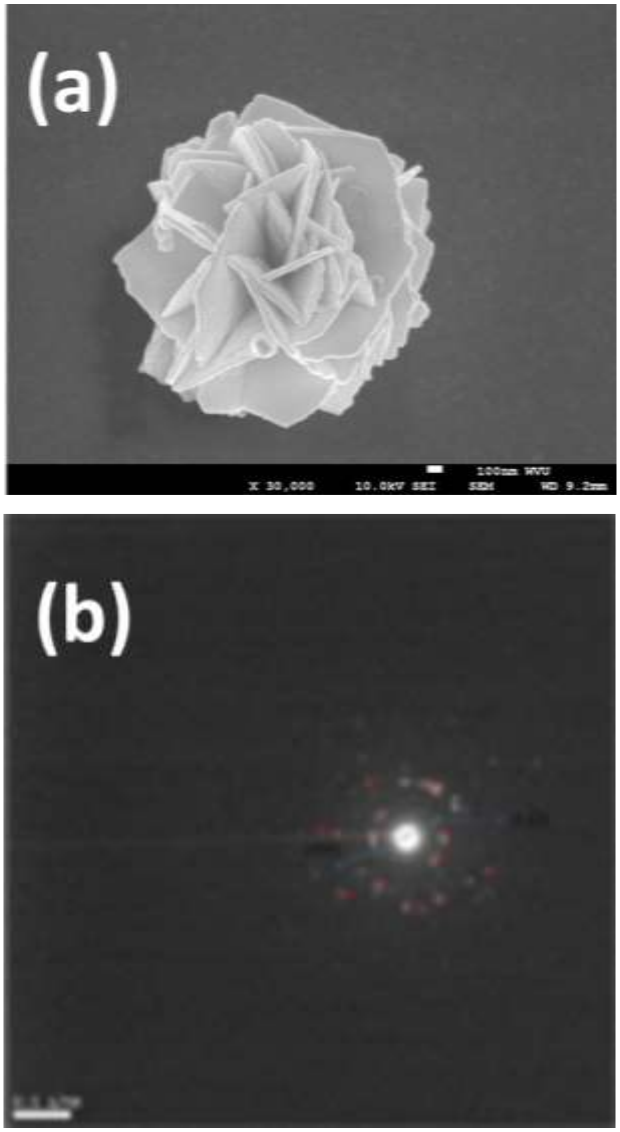
(a)
100nm WVU
X 30,000 10.0KV SEI SEM WD 9.2mm
(b)

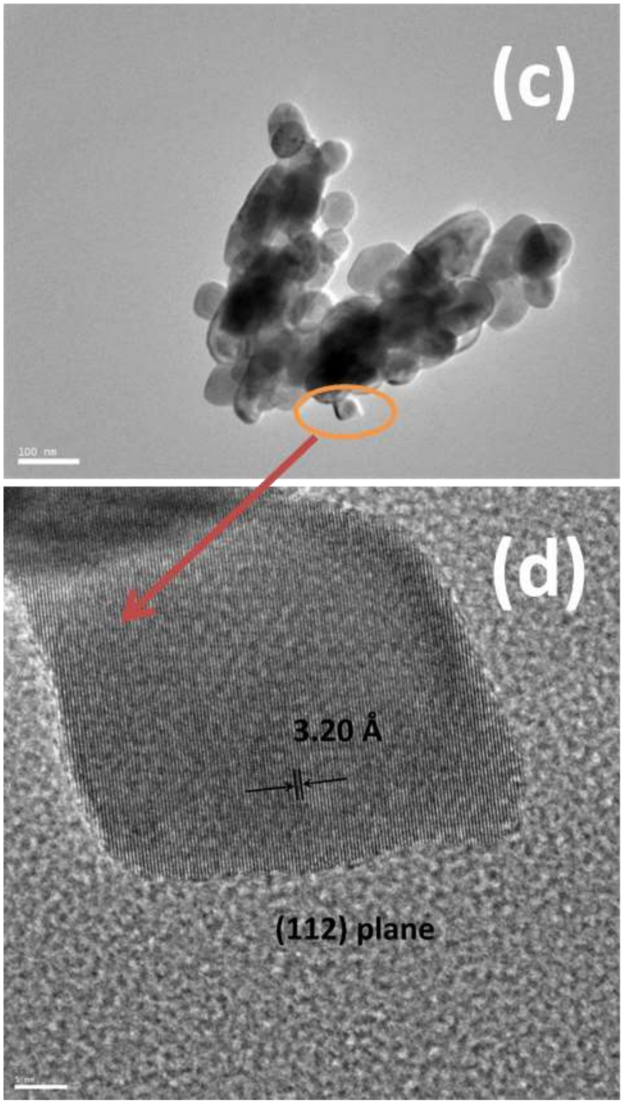

Figure 56: (a) SEM micrograph of $SrMoO_4$ nanoflowers **(b)** selected area electron diffraction (SAED) **pattern (c-d)** TEM image of the as-synthesized $SrMoO_4$ nano-flowers

The quantification of the missing oxygen as well as unlattice/interstitial oxygen are completed by XPS analysis. It was proved that material contains Mo^{5+} up to 5%. It can be concluded that as-synthesized product showed oxygen vacancies and interstitial oxygen to large extent. XPS analysis was conducted in order to quantify the amount of interstitial and/or unlattice oxygen as well as, the amount of Mo in the Mo^{+5} chemical state. The XPS would also assist in determining the level of glassy secondary-phase formation that cannot be detected by XRD. Varhegyi et *al.* stated that the oxygen adsorption to the stoichiometric surface would be very difficult to compare to the non-stoichiometric counterpart [60]. Another point to be deserved before interpreting the photoelectron spectra of the O, Mo and Sr in $SrMoO_4$ nano-flowers is the stability of adsorbed (chemically or physically) oxygen on the transition metal oxide surface. Not only is the bulk structure important, but also the surface chemistry in the end will be important, especially for gas sensor applications. The oxygen ion and vacancy content on the surface will dictate much of the functionality of a gas sensor. As stated by Hirschwald, $\mathrm{O}^-_{2\,\mathrm{ads}}$to $\mathrm{O}^-_{\mathrm{ads}}$ transformation occurs at about 200°C and desorption of the latter occurs at 250°C [185, 12]. According to this data, the functionality of the semiconducting oxides terminated after 300°C, however although the sensitivity decreases to great extent after 300°C, there many semi conducting metal oxide type sensor in the literature function after 300°C. Therefore, due to functionality of the sensors equipped with the semiconducting sensing material, it might be concluded that the amount of the adsorbed oxygen is less compared to the low temperature regime, and/or involvement of the lattice oxygen and interstitials oxygen. Azad et *al.* [12] concluded that oxygen cannot be chemisorbed onto an undoped and/or stoichiometric oxide surface since oxygen ions cannot be adsorbed unless their negative charge is compensated by varying density of states on the surface. A similar discussion was stated by Varhegyi et *al.* In addition; Korotcenkov [16] approved of this conclusion, but also discussed the possibility of a small fraction of monolayer chemisorption for an n-type semiconductor surface. Abraham et *al.* concluded that relatively stable and large amount of interstitial oxygen formation between isolated cation (Mo or W) tetrahedrals in $PbWO_4$ and $CaMoO_4$ tetragonal scheelite structures [186, 155]. In addition to that Esaka reported that scheelites containing interstitials oxygen would be more reducing resistant (compositionally stabile) under low oxygen partial pressure environments [187]. From the point of thermodynamic considerations, a defect structure containing of missing oxygen ions and interstitials oxygen can allow the semiconducting metal oxide to function upon exposure to reducing gas atmospheres at elevated temperatures.

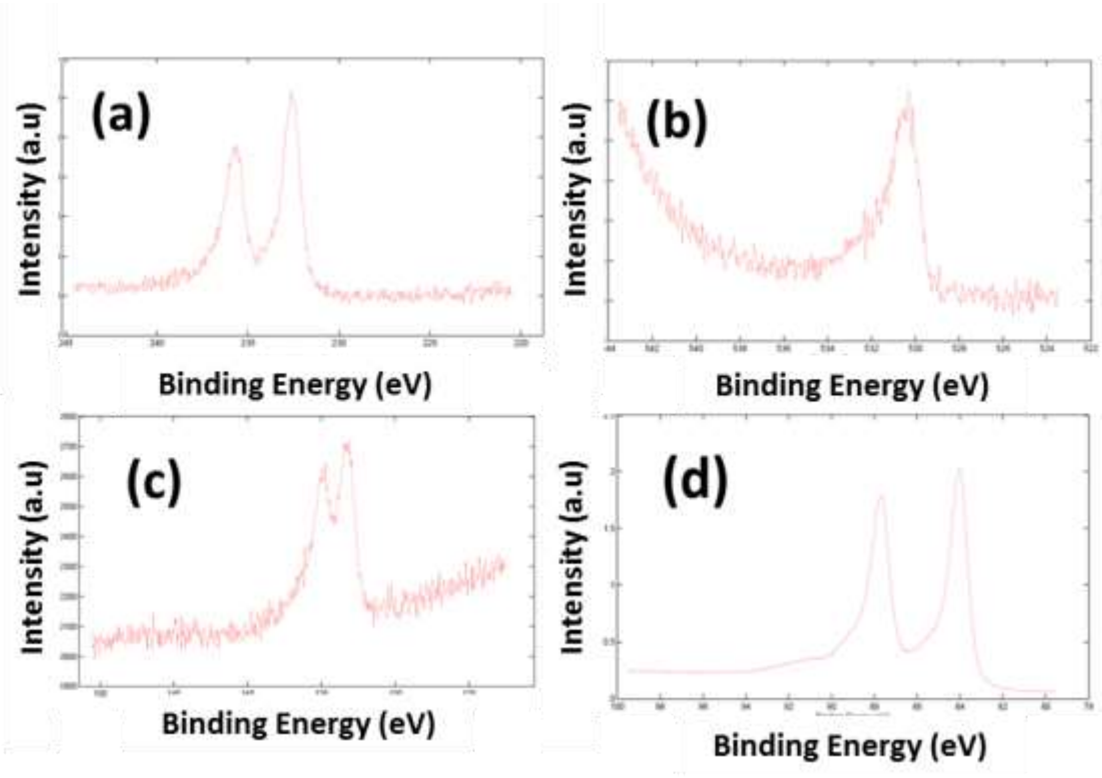

Figure 57: XPS core spectrum of Mo **(a)** and **(b)** O^{2-} **(c)** Sr in as-synthesized $SrMoO_4$ nano-flowers and **(d)** Au 4f photoelectron line as a reference.

Figure 57 presents the photoelectron spectrum of the Mo, O and Sr in $SrMoO_4$ nano-flowers, as well as, the Au 4f spectrum as a reference. Figure 57-b shows the core photoelectron line of the O^{2-}. After deconvolution of the O 1s spectrum, two main chemical states of the oxygen were determined. Those are located at 529.82 and 531.24 eV. The former is in a good match with the literature for $SrMoO_4$, while the latter for interstitial/adsorbed (un-lattice) oxygen [188, 189]. Sr $3d_{5/2}$ and $3d_{3/2}$ photoelectron lines are located at 132.60 and 132.40 eV, respectively. Figure 57-a shows the XPS spectrum of Mo 3d doublet. For molybdenum (Mo), the main photoelectron lines were positioned at 232.92 and 236.02 eV. The convolution of the Mo doublets proved that Mo^{5+} chemical state exists in the as-synthesized material and located at 231.9 and 234.96 eV. The deconvolution of the O and Mo main photoelectron lines made it possible to quantify the relative amount of the corresponding chemical states. Approximately 20% of the O^{2-} was located on un-lattice (adsorbed/interstitial) locations. Un-lattice oxygen can be thought of as adsorbed O^{2-} down to 10 nm from surface, which is a characteristic sampling depth of the XPS.

4.3.3 Core structure approach

Constructing porous networks of 1-D materials such as, nanowires and nanorods have attracted much attention recently due to their intriguing electronic, optical and mechanical properties. The construction of porous network made of nanomaterials is of great importance to sensor designers due to its theoretical extraordinary gas permeability capability and high surface area. A limited number of reports appeared on synthesize of transition metal oxide structures such as ZrO_2 in 1-D structures. Wang et *al.* synthesized ZrO_2 nanorods by using $ZrNO_3$ and NH_4F, but the material synthesized was 25 in length and 5-10 nm in width, looks more like beans not nanorods. Another attempt made by Pei *et al.* The ZrO_2 was hydrothermally synthesized by zirconium hydroxide, however material showed non-homogeneous morphology changing form nanorods to spherical particles, however Xia et al made successful attempt and synthesized ZrO2 nanowires by using electrospinning. [190, 153, 191, 192, 193]. Ogihara et *al.* tried to use carbon nanofibers as template for synthesizing Al_2O_3, SiO_2 and ZrO_2 nanotubes, wall thicknesses of them were 30, and 10-20 nm [194]. Unfortunately nano scales materials succumb to coarsening and sintering effects at high temeoarture, therefore it is the challenge to keep the nanomaterials nano at elevated temperatures (>800°C). There are two possible solutions to hinder/stop coarsening, those are Zener pinning by benefiting from the influence of fine-refractory-stabile particles on the movement of low and high angle grain boundaries by exerting a pinning pressure. The second technique is growth/deposite of the nanoscale material over a a core refractory-oxide structure preferentially with epitaxial match. İn current study both both technques were used in order to stop/hinder the coarsening of the nanomaterial for sensor applications.

4.3.3.1 MgO nanorods

MgO nano-rods were synthesized via a hydrothermal method by repeating the procedure described by Ghamdi et *al.* [195]. The hydrothermal process begins with the synthesis of a gel which was initiated synthesized by dissolving 6.44 g of magnesium acetate (Magnesium acetate tetrahydrate, ACS, 98.0-102.0%, CAS 16674-78-5, Alfa Aesar) into 75 deionized and decarbonized water and magnetically stirred 30 min. 1.2 gram urea (ACS, 99.0-100.5%, CAS 57-13-6, Alfa Aesar) first dissolved in again deionized and decarbonized water**.** The urea was added drop-wised added to the previously prepared magnesium acetate solution, and after stirring the total 100 ml solution for 10 min, the solution was added into autoclave sealed with teflon for 2 h at 180°C. The measured pH before the autoclave hydrothermal process was 7.5; after the hydrothermal run the pH was 9. The washing procedure repeated until the conductivity (σ) of the solution measured less than 10 mScm^{-1}. Figure 58-a, -b and -c show the SEM micrograph of the as-synthesized MgO nanorods with different magnifications. In order to evaluate the high temperature sintering/coarsening resistance of the compound, the powder was held for 5 h at 1000°C. The final microstructure is shown in the Figure 58-d. As can be seen from the SEM micrograph, the MgO nano-rods did not coarsen and retained their needle-like morphology at the temperature regime of interest.

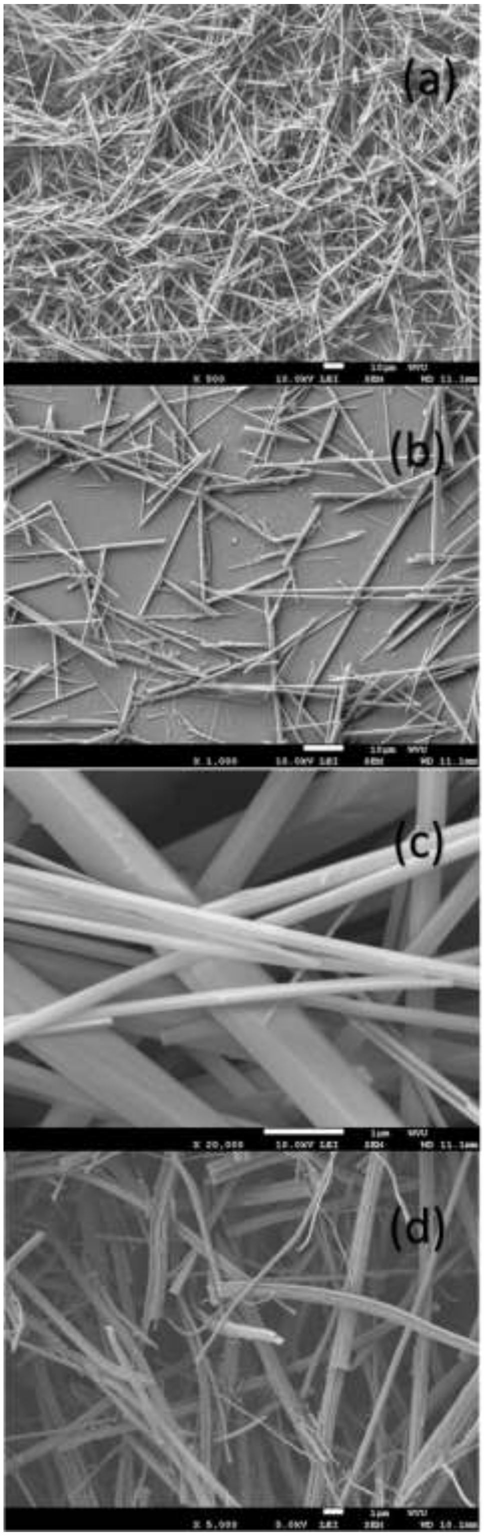

Figure 58 : MgO nanorods as-synthesized **(a-c)** and **(b)** heat treatment after 5 h at 1000°C.

Figure 59 shows the EDS spectrum of the as-synthesize powder. The detected Au in the spectrum originated from the sputtered coating needed to eliminate charging effects during the SEM investigation of the surface. The EDS data shows nearly a 1 to 1 ratio, which is what would be expected for the stoichiometry of the MgO. The XRD data showed the material has very good crystallinity (not included).

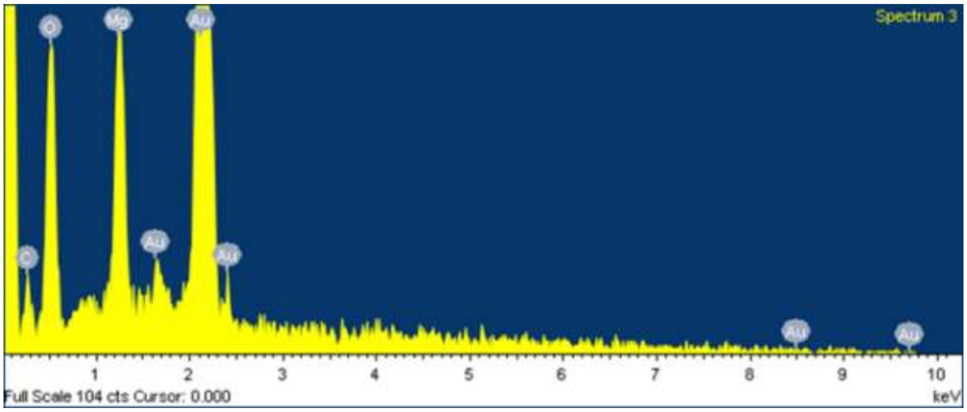

Figure 59: EDS spectrum of as-synthesized MgO nanorods.

4.3.3.2 ZrO_2 nanorods

Due to the well-known refractory properties of ZrO_2, various hydrothermal experiments were completed in an attempt to synthesize ZrO_2 nanorods similar to the MgO nanorods. The procedures explained in the beginning of the section were followed in order to obtain nano-rod like formations. As a precursor material, zirconium hydroxide ($Zr(OH)_4$, CAS 14475-63-9, Sigma-Aldrich) was in dissolved in 100 ml of deionized and decarbonized water and magnetically stirred for 10 min in a beaker. The final solution was transferred into a PTFE sealed autoclave for 24 h at 120°C, 150°C and 180°C. Figure 60 shows the SEM micrographs as the morphological formation of the as-synthesized powders vary with the different processing temperatures. There were nanorods or nanorods like formation in any treatment temperature. Therefore this ZrO_2 totally abandoned as a core material for templated growth of the sensing material.

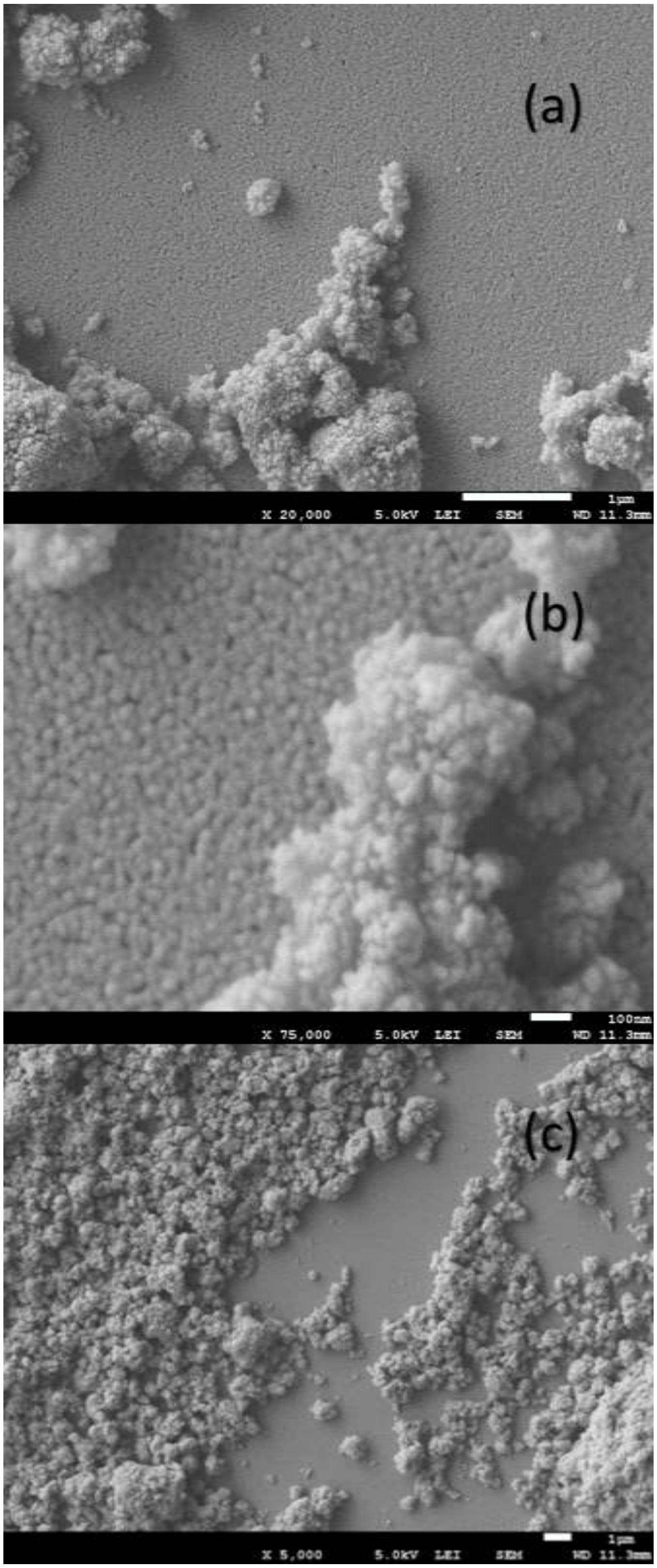

Figure 60 : ZrO_2 after autoclave treatments at different temperatures (°C) **(a)** 180 **(b)** 150 **(c)** 120.

Chapter 5: Sensing Characteristics of Various Tungstate and Molybdate Nanomaterials for H_2, H_2S and SO_2

5.1 Introduction

Transition metal oxides (TMOs) range from electrically insulating to semiconducting to metallic compounds. Due to the ability to modify the of the electronic and ionic conduction mechanisms through the control of their defect type and concentration, tungstates and molybdates are also used in many other electrochemical applications such as fuel cells, batteries, heterogeneous catalysis, optical applications, photo-catalysis, photoluminescence medium, antibacterial materials and polymeric electronics (as an electronic filler) [158, 196, 165, 183, 153, 197]. Tungstates and molybdates type TMOs are one of the prime choice sensing materials for hydrogen and sulfur compounds. Many are sensitive to H_2, but not many are sensitive to sulfur compounds such as SO_2 and H_2S. In the perovskite structure $BaTiO_3$, $SrTiO_3$, La doped $BaTiO_3$ were utilized as a CO, CO_2 and humidity sensor in the form of thick film or bulk pressed powder compact at the temperature regime 25-600°C [5]. The most common metal oxide used for sulfur compounds are SnO_2, WO_3 and TiO_2, due to their specific electronic state and. Unfortunately, these compositions have shown to be unstable at elevated temperatures [36, 58]. In this chapter, we will look at different compounds of W and Mo, which are known to show such sulfur activity and are stable to higher temperatures. In addition to compositional instability, nanomaterials of those families succumb to coarsening regardless of compound type as practice other nano materials. The goal is to find a method to control the defect structure of the W and Mo, so that the selectivity of the sulfur compositions and hydrogen can be controlled specifically. More recently Sabolsky et *al.* for the first time utilized and characterized the nickel tungstate ($NiWO_4$) as a solid oxide fuel cell (SOFC) anode by making use of the material`s reduction to metallic nickel (Ni) and different tungsten oxides (WO_3, WO_2 and W_2O_5) [166].

Propensity for surface interactions on TMOs is result of non-stoichiometry, multiple oxidation states (mixed-valence states) and crystal defects. The characteristic features dictate the chemical-electronic-physical properties of the TMO is typically achieved by modifying the crystal structure, band gap, work function and surface electronic states [7, 8, 6]. Wide band gap oxide semiconductors (4-5 eV), such as tungstates and molybdates, are chosen in order to secure microstructural, chemical and morphological stability at high temperatures for preliminary examination for sensitivity and selectivity. In this work, we will look at ternary compounds of W and Mo, which are known to show such sulfur activity and are stable to higher temperatures.

The selective detection of SO_2, CO, and H_2S or other reducing gases in the presence of H_2, is formidable task for sensor designer, because the working mechanism of the chemiresistive sensor is based on the catalytic oxidation of gas molecules. H_2 goes through oxidation as other reducing gases do; therefore, most types of surface conducting sensors are sensitive to H_2. WO_3, WO_3 nano, MoO_3, MoO_3nano, $MgMoO_4$, $NiMoO_4$, $NiWO_4$, Sr_2MgWO_6 (SMW), Sr_2MgMoO_6 (SMM), $SrMoO_4$, $SrMoO_4$ nano, $SrWO_4$ are among the materials that were tested for H_2S, SO_2, H_2, and syngas composition (H_2S, CO, N_2, O_2, CO_2, H_2O).

Among the alkaline earth metals Ca, Sr and Ba crystallized to ABO_4 stoichiometry with scheelite structure, however small Mg cation is isotypic with α-$MnMoO_4$ [160, 155]. Alkaline earth molybdates with ABO_3 stoichiometry show perovskite crystal structure. ABO_3 perovskite is not stabile phase [198] in the case of occupation of B site by W and Mo due to low oxidation state of those transition metals, the perovskite structure tend to accommodate more oxygen and transform to scheelite (ABO_4, $SrWO_4$, $SrMoO_4$) even under room temperature [199, 198]. Another drawback of type is not availability of the direct synthesis method. In general perovskite type of alkaline earth molybdates (ABO_3) synthesized by reducing of ABO_4 structure under high temperature reducing atmospheres or some cases thin film growth method was utilized with the very narrow oxygen partial pressure and temperature window due to possible ABO_4 structure formation [198, 200, 201]. Moreover in the case of Sr, ABO_3 structure shows metallic conductor behavior [202, 198]. Each material was be tested for sensitivity, stability (at 1000°C), response and recovery time, and cross sensitivity (to CO). Figure 61 shows the sulfur uptake capabilities of simple oxide of Mo and different binary molybdates. X-ray absorption near edge structure (XANES) data proves that chemical reactivity of the binary molybdate and some other ABO_4 stoichiometry ternary molybdate toward

H_2S increases from MoO_3 to $NiMoO_4$ [203]. The goal is to find a method to control the defect structure of the W and Mo, so that the selectivity of the sulfur compositions and hydrogen can be controlled specifically. In addition to this, ECR will be utilize to better estimate the adsorption and diffusion kinetics of sulfur species on the most successful composition. Before synthesizing nanomaterials, candidate compositions will be tested, if possible, in micro-scale due to their sulfur uptake capabilities, and suitable ones synthesized in nano-scale for further sensor tests. In addition evaluation of abovementioned compositions, ECR will be utilize to better estimate the adsorption and diffusion kinetics of sulfur species on the most successful composition. The chemical composition, and nano- and micro-structure of the developed nanomaterial films, as well as sensing mechanism, were characterized by means of scanning electron microscopy (SEM), energy dispersive X-ray spectroscopy (EDS), X-ray and ultraviolet photoelectron spectroscopies (XPS and UPS), atomic absorption spectroscopy (AAS), X-ray diffraction (XRD), temperature programmed reduction (TPR), Raman spectroscopy and transmission electron microscopy (TEM).

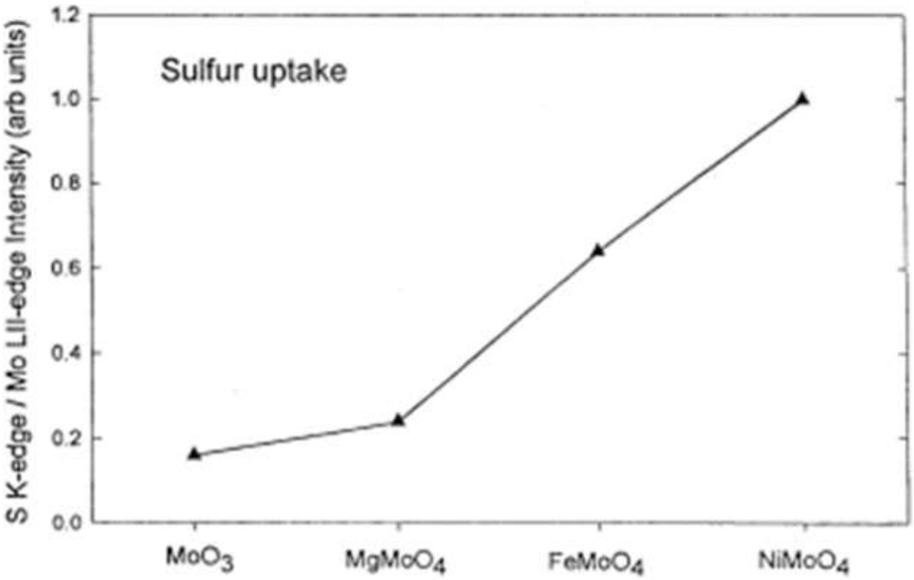

Figure 61 : Sulfur uptake capabilities of different binary and ternary TMO **[203]**.

5.2 Experimental

A schematic of the resistive-type sensor design used in this work to evaluate the sensitivity of each composition is illustrated in Figure 62. The sensors consisted of an insulating (Al_2O_3) substrate, a metallic interdigitized electrode (IDE), and an oxide semiconductor that serves as the sensing material on the outermost layer.

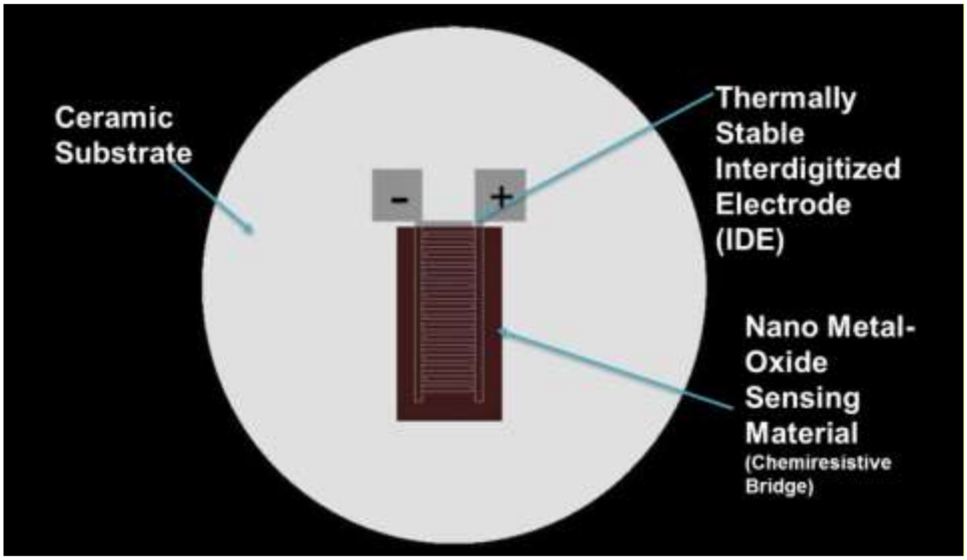

Figure 62: Schematic of gas sensor showing different integral parts.

The sensor platform was composed of highly polished in-house made alumina (Al_2O_3) substrates. Pt-based IDEs were screen-printed through 100 µm mesh silk screen and annealed at 1200˚C for stabilization. Figure 63 shows the schematic of the dimensions used for the sensor structure used to evaluate the performance of the various sensing molybdate and tungstate sensing nanomaterials. The Pt ink was made from Pt powder (Technic Engineered Powders) with average particle sizes around 1 µm. The electrodes have a total length of 10 mm with finger width and finger spacing of 0.25 mm.

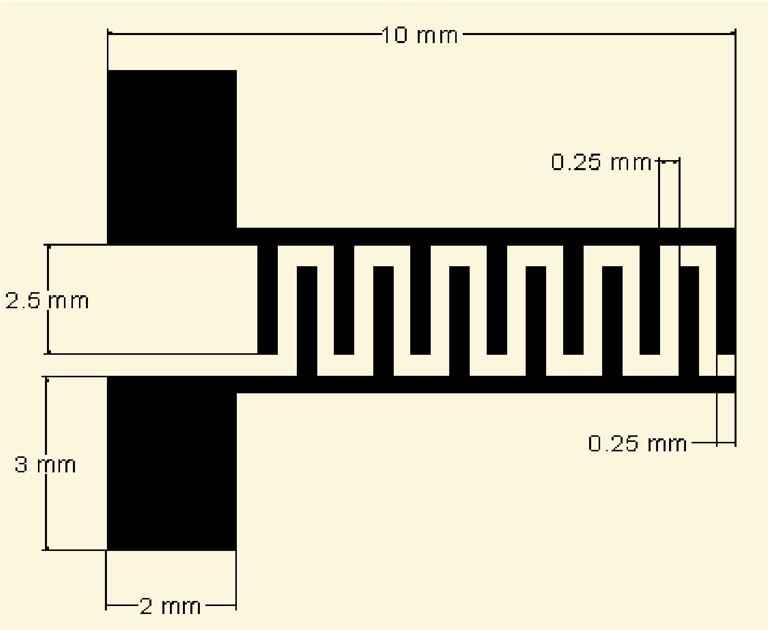

Figure 63 : Schematic of the screen printed IDE **[17]**.

The test unit consists of the target gas tubes, mass flow controllers (for each gas), an alumina (Al_2O_3) testing tube, a digital multimeter (DMM) for resistance measurements and computer. The resistance measurements were made with a Keithley 2700 Multimeter/Data Acquisition System set to 2-point resistance mode which supplied a 5-10 µA DC current to obtain the measurement. Computer-controlled testing was used to change the gas flow rate and record the resistance measurement of the temperature and resistance of the sensor during testing.

Parameters such as selectivity, sensitivity, cross-sensitivity, response and recovery time were characterized. In the literature, sensitivity of a sensor is usually represented by equation given in Eq. 5.1., where R_a is the resistance in dry air and R_g is the resistance in the target gas. The response time is defined by the sensor to reach 90% of the total resistance variation due to the change in concentration of the target gas.

$$\boldsymbol{S = R_a - \frac{R_g}{R_a} = \frac{\Delta R}{R_a}} \qquad \textbf{(Eq. 5.1)}$$

The sensing material was printed to a thickness of ~300 µm onto platinum (Pt) electrodes and sintered at 1200˚C. In order to promote the adhesion between the substrate and printed sensing material (and to reduce cracking in the sensing material), the sensors were placed on a hotplate at 90˚C for half an hour to dry and then heat treated in a box-furnace with a heating rate of 2˚min^{-1} to 600˚C and then 4˚/min to 1200˚C, and held for 1 hour at that temperature.

Figure 64 shows the total heat cycle that each sensor was exposed to during the test. During these tests, the sensors were heated and held at 600˚C, 800˚C, and 1000˚C for 8.5 hours, and then the sensors were cooled down to room temperature under atmospheric conditions unless otherwise indicated. In a few situations, the sensor was cooled down under N_2 flow in order to conduct chemical analysis of the final sensing material.

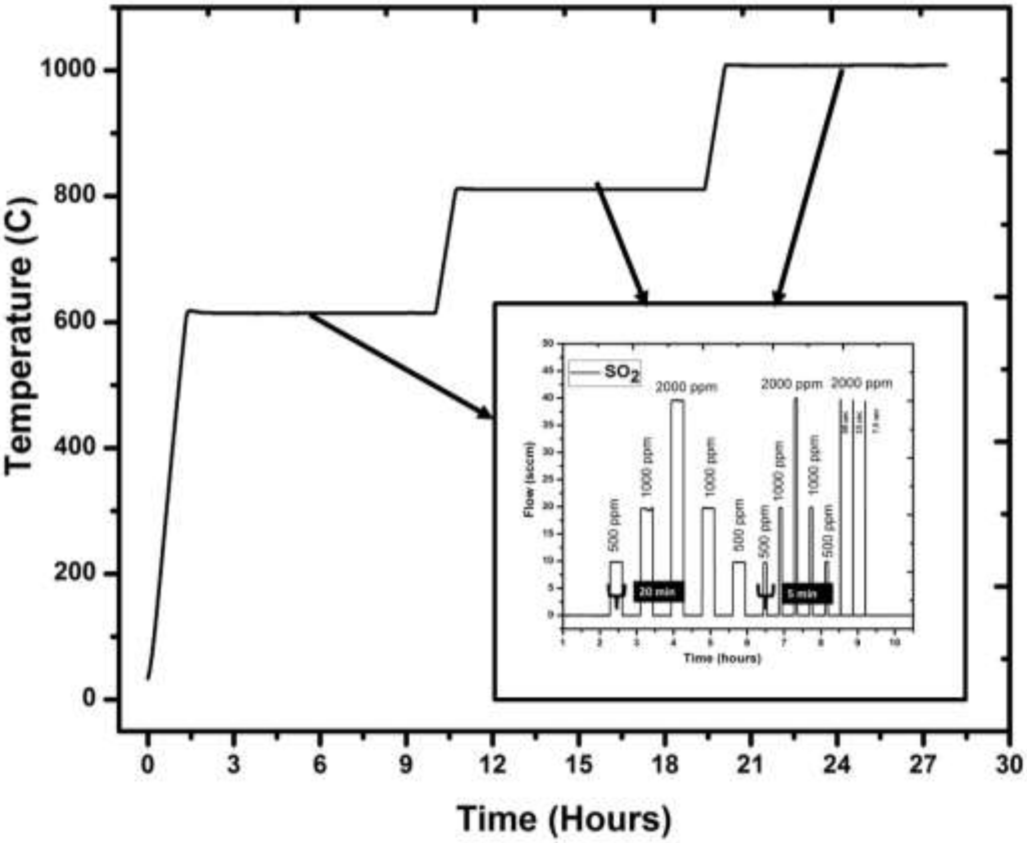

Figure 64: Thermal cycle for sensor testing.

Figure 65 shows the concentration of the target gas and time of exposure during holds at the designated temperatures. In every case, the total flow was adjusted to 50 sccm by adjusting the flow of hydrogen (H_2), nitrogen (N_2) and oxygen (O_2) via the digital mass flow controllers (MFCs). Three different concentration levels of target gas balanced with a pure nitrogen (N_2, 99.99%, Matheson

Ultra High Purity grade) were tested at three different exposure times (at three different temperature regimes, 600, 800, 1000°C). Three different ultra-high purity O_2 (Matheson research Grade 99.998%) partial pressures (1, 5 and 20 %) were further tested for the selected compounds in order to understand the contribution of ionic conduction to the total electrical conduction. The exposure cycle presented in Figure 65 increased the ppm level of SO_2 from 500 to 1000, and then to 2000 ppm, and then decreased back down to 500 ppm. Each of these gas concentrations were held for 20 min and then the pyramid was repeated with a hold time of 5 min. A final pulse of the maximum concentration was placed on the sensors for 30 sec, 15 sec, and 7.5 seconds in order to test the response and recovery time. Each of these pulses balanced with pure N_2 and 1% O_2 (05 sccm) was kept present during the entire hold at designated temperature. A 30 min holding time in pure N_2 was placed on the sensors between each pulse in order to allow the sensors to recover before further exposure testing.

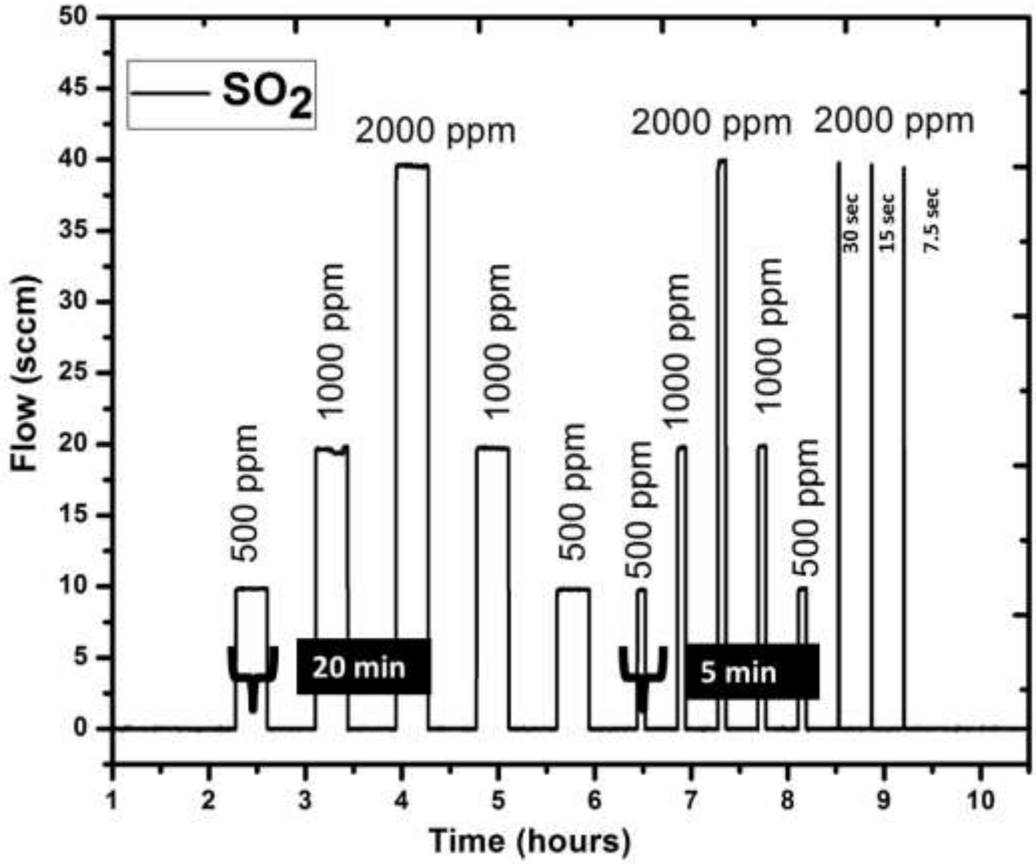

Figure 65: Flowrate of target gases for sensor tests.

The select sensing materials were also tested in the presence of 1000, 2000 and 4000 ppm for H_2 and CO. The successful compounds that showed high sensitivity toward SO_2 were further tested for 50-100 ppm H_2S as well as syngas composition. The syngas is consist of %32 H_2, %40 CO, %20 CO_2, 1% O_2, 1% Steam (H_2O), 1 % H_2S, 5% N_2. The detailed testing conditions regarding to H_2S and syngas are covered in Chapter 5.3.4. Table 6 presents the material systems tested.

Table 6 : Material systems tested for H_2S, SO_2 and H_2 sensing.

Target Gas	Molybdates				Tungstates			
	MoO_3	$SrMoO_4$	$SrMgMoO_6$	$NiMoO_4$	WO_3	$SrWO_4$	$SrMgWO_6$	$NiWO_4$
SO_2	X	X	X	X	X	X	X	X
H_2		X	X	X		X	X	X
H_2S		X						X
CO		X	X	X		X	X	X
Syngas		X						

5.3 Results and Discussion

5.3.1 Baseline Tests

5.3.1.2 Micron size WO_3 and MoO_3 testing

The first composition to be tested was tungsten trioxide (WO_3) due to it is wide range applications for SO_2 sensing in the literature. Investigation over both commercially available micron-WO_3 and nano-WO_3 were completed. Figure 66 shows characterization and testing results of the micron size WO_3 (Alpha-Easer, 99.8% metals basis, CAS 1314-35-8) powder. Particle size of the Alfa Aesar WO_3 powder was around 1 µm and the powder showed a mixture of sizes ranging from 300 nm to 1 µm (Figure 66-a). The SEM micrograph showed that the particle morphology was spherical, without any other shape of particle within the micrograph (indicate a low probability of alterative phases present). The XPS analysis of the same powder is shown in Figure 47-b. The figure shows that the WO_3 material does not have any other W chemical state, but the W^{+6}. The W 4f doublet peak positions for this state are located at 35.56 and 37.74 eV. Figure 66-b and -c show the chemiresistive response of the WO_3 towards SO_2 under 1% O_2 partial pressure. The maximum sensor response was 20% decrease in the resistivity towards 2000 ppm of SO_2; however, the signal was not smooth and fluctuations and drift were observed at 600°C. The given powder exhibited reasonable sensitivity and response recovery. The main shortcoming of this composition is its compositional/chemical instability at elevated temperature, such as that of 1000°C (see Figure 66-c). At 1000°C, the sensor did not show any response towards SO_2. In addition, the baseline resistance decreased drastically down to ~17 ohms. This indicates that particles were necking, and more profoundly, the compound was reducing.

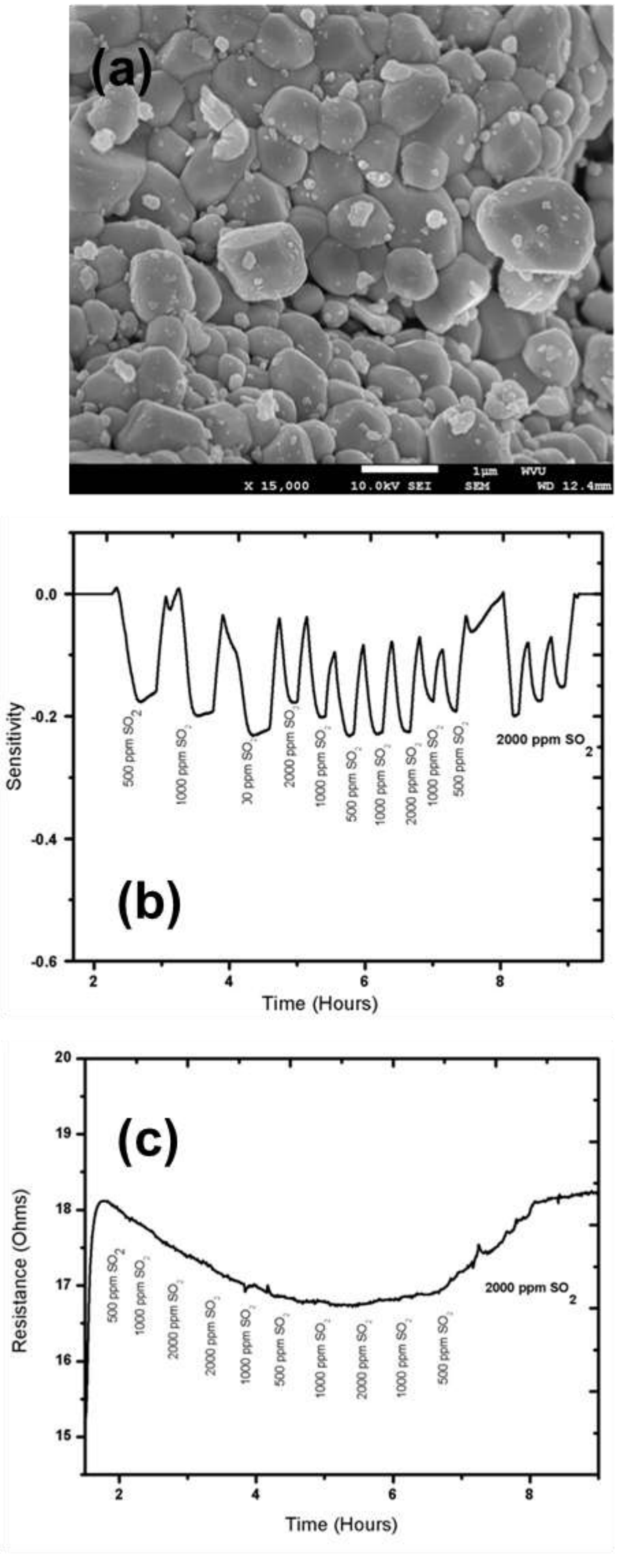

Figure 66 : (a) SEM micrograph of WO_3 micro powder and sensor response to SO_2 at 1% O_2 **(b)** 600 °C **(c)** 1000°C.

Molybdenum trioxide (MoO_3) has not been studied to a large extent for gas sensing applications. The melting point of MoO_3 is 795°C and this material is prone to evaporate rapidly; however, in order to gain a baseline understanding regarding more complicated molybdate compositions for H_2, H_2S and SO_2 sensing, MoO_3 (Alpha-Easer, molybdenum(VI) oxide, 99.5%, CAS 1313-27-5) was also subject to similar testing. This work was completed in parallel to the testing of the baseline WO_3 from Alfa Aesar. At 600°C, the sensor initially showed a large p-type response, as seen in Figure 67-a. The figure shows that the sensitivity decreased significantly and almost disappeared afterwards. The p-type response was also accompanied by a resistance increase, which is unusual for the n-type semiconductor MoO_3. It is not clear the reason behind the p-type response and no literature information could be found in order to clarify the reason at 600°C. However, it is well-known for WO_3 that a change in response behavior (from n-type to p-type or opposite) has occurred upon expose to different level of target gas at different temperatures under various partial pressures of oxygen. The same characteristic can also attributed to MoO3 in order to explain unexpected p-type response. Figure 67-b shows the sensor response in the resistance versus time graph during the exposure to SO_2 at 1000°C. Visual examination the sensor surface after the test revealed that as expected almost all of the MoO_3 sensing material evaporated, and the IDEs were the only remaining material on the sensor platform.

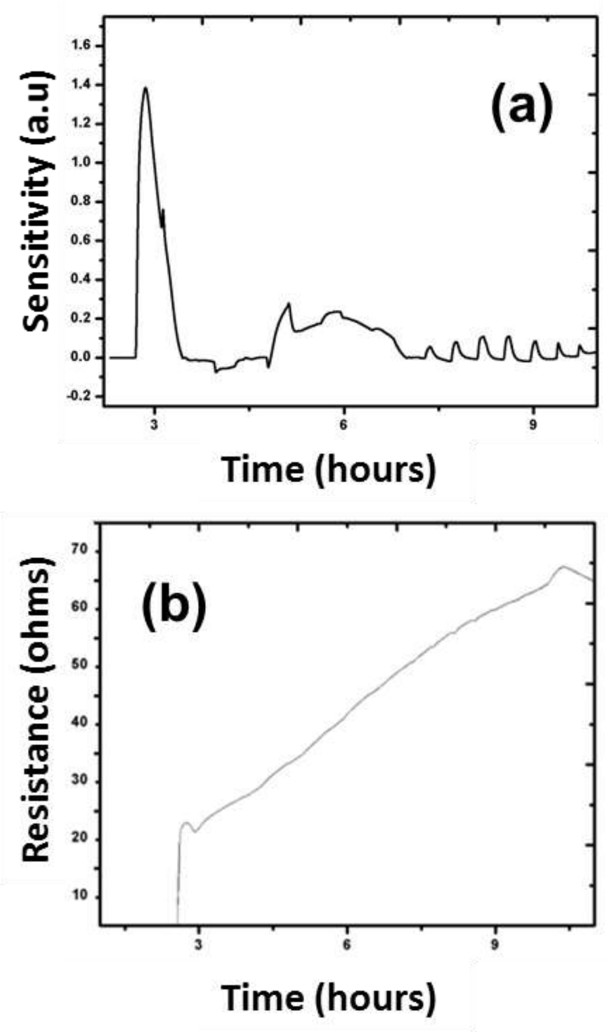

Figure 67 : MoO_3 sensor response to SO_2 at 1% O_2 **(a)** 600°C **(b)** 1000°C.

5.3.1.3 Nano size WO_3 testing

Surface modification of oxide semiconductor sensing materials by incorporation of noble metals (Pt, Pd, and Ag) is the prime way to increase the sensitivity and response/recovery time in gas sensors [5, 32]. In addition to this, recently efforts to decrease particle size has gained significant attention in the scientific community in order to increase sensitivity [17, 54]. Therefore, nano-WO_3 was also tested in this work. Figure 45-a and -b show WO_3 nanorods which are 5-100 nm in size. XPS analysis given in Figure 47-c showed that ~15% of the material contained the W^{+5} chemical state in the as-synthesized compound. The sensor test of the WO_3 nanorods at 600°C (under 1% O_2 partial pressure) is displayed in Figure 68-a. The nanorods showed a 60% decrease in the resistance towards 2000 ppm of SO_2. For 2000 ppm of SO_2, 200% increase in sensitivity obtained by using WO_3 nano in comparison to micron size counterpart. Although the sensing nanomaterial showed a very high sensitivity, the signal drifted due to coarsening of the nanomaterial during the test. Figure 68-c shows the SEM micrograph of the nanomaterial after testing at 600°C. Under the 1000°C testing condition, the sensor did not show any response towards SO_2 (as seen in Figure 68-b). The SEM micrograph of this material is shown in Figure 68-d. As can be seen in this micrograph, the WO_3 nanorods displayed a large level of grain growth in addition to a reduction problem.

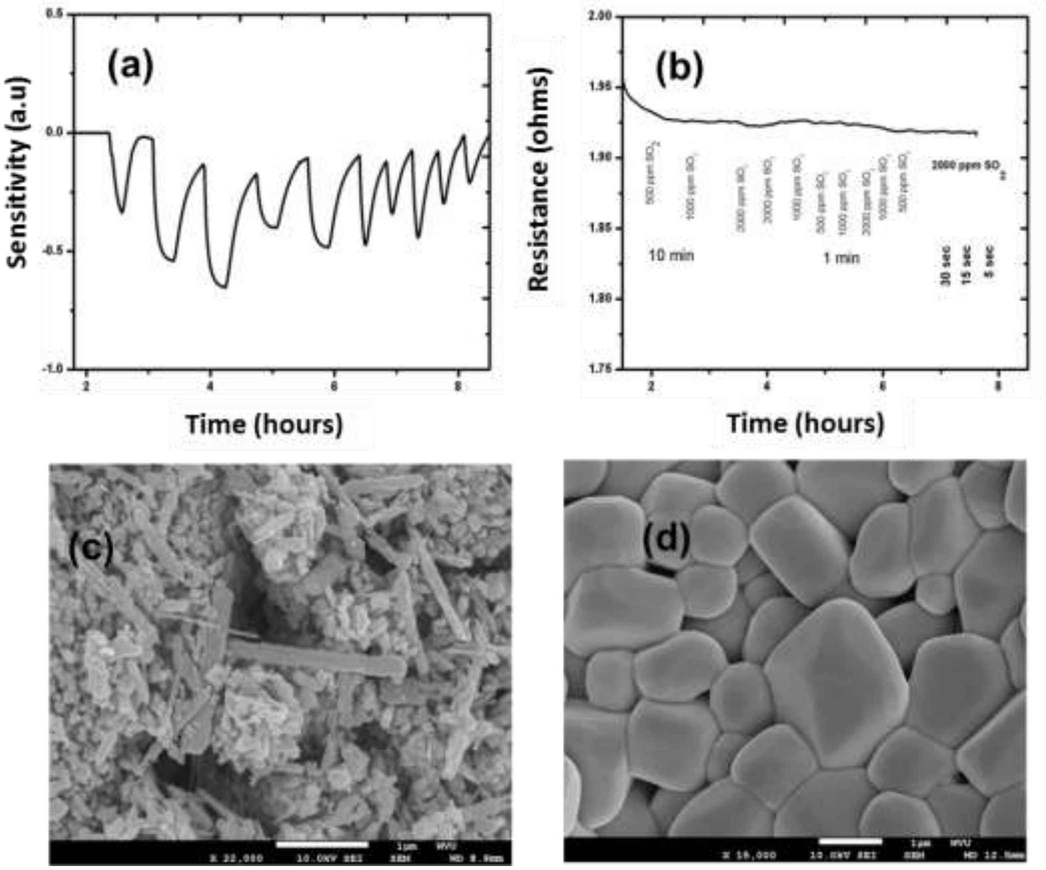

Figure 68: SO_2 testing results under 1%O_2 at **(a)** 600°C **(b)** 1000°C and SEM micrographs of WO_3-nano after **(c)** 600°C **(d)** 1000°C testing.

WO_3 nanorods showed an increase in sensitivity towards SO_2 at 600°C; however, at elevated temperatures (800°C and 1000°C), the sensitivity decreased and eventually diminished. Grain coarsening and chemical reduction of oxide semiconductor are the reasons behind the insensitivity.

Grain coarsening cannot solely explain the insensitivity of the material at high temperature, yet it explains the reduction in the sensitivity. Therefore, XPS analysis was conducted in order to clarify the final chemical state of the nano-WO_3 after the complete sensor test protocol. Figure 69 shows the post-mortem XPS surface analysis of the tested sensor. The XPS data shows the core photoelectron line of tungsten (W). In the Figure 69-a, the red and blue colored graphs represent the data collected from air and N_2 cooled sensor surfaces, respectively. In the red colored graph, the binding energies of W correspond to the WO_3 compound perfectly. The WO_3 4f peak positions were determined to be at 35.6 and 37.7 eV. These determined binding energies are in a good agreement with the literature values. The reason behind this is that during the cool down from 1000°C to room temperature under atmospheric conditions, the previously reduced compound had opportunity to obtain enough oxygen in the testing unit together with suitable thermodynamic conditions for its re-oxidation process from metallic W to WO_3 to occur. Cooling down WO_3 in N_2 atmosphere further clarified the situation by showing that WO_3 reduced to metallic tungsten (W) in a large extent during testing. The main photoelectron spectra of the W in this case showed that a large portion of the surface is reduced to the metallic state (W metallic phase 4f peaks were observed at 31.6 and 33.7 eV with 2.1 eV spin-orbital splitting).

Figure 69-b and -c show that the electrical resistance changes during the heat up to 1000°C and the cool down to 25°C periods under 1% O_2 balanced in N_2. This result was found without any expose to a reducing gas. As seen in the XPS data in Figure 69-b, the semiconductor-metallic transition occurred around 150°C. As seen in the XPS graphs presented in Figure 69-b and –c, the resistance was not able to recover back to the initial value. This can be interpreted as a permanent reduction event that occurred and the amount of oxygen present during the actual sensor testing was not high enough to both hinder the reduction of the semiconductor to the metallic phase and assist in the recovery. The WO_3 commercial powder also showed a similar reduction behavior under the same testing conditions. The final chemical state of the W had a strong effect on the sensing performance of the sensor made of WO_3, regardless of its microstructure and grain size.

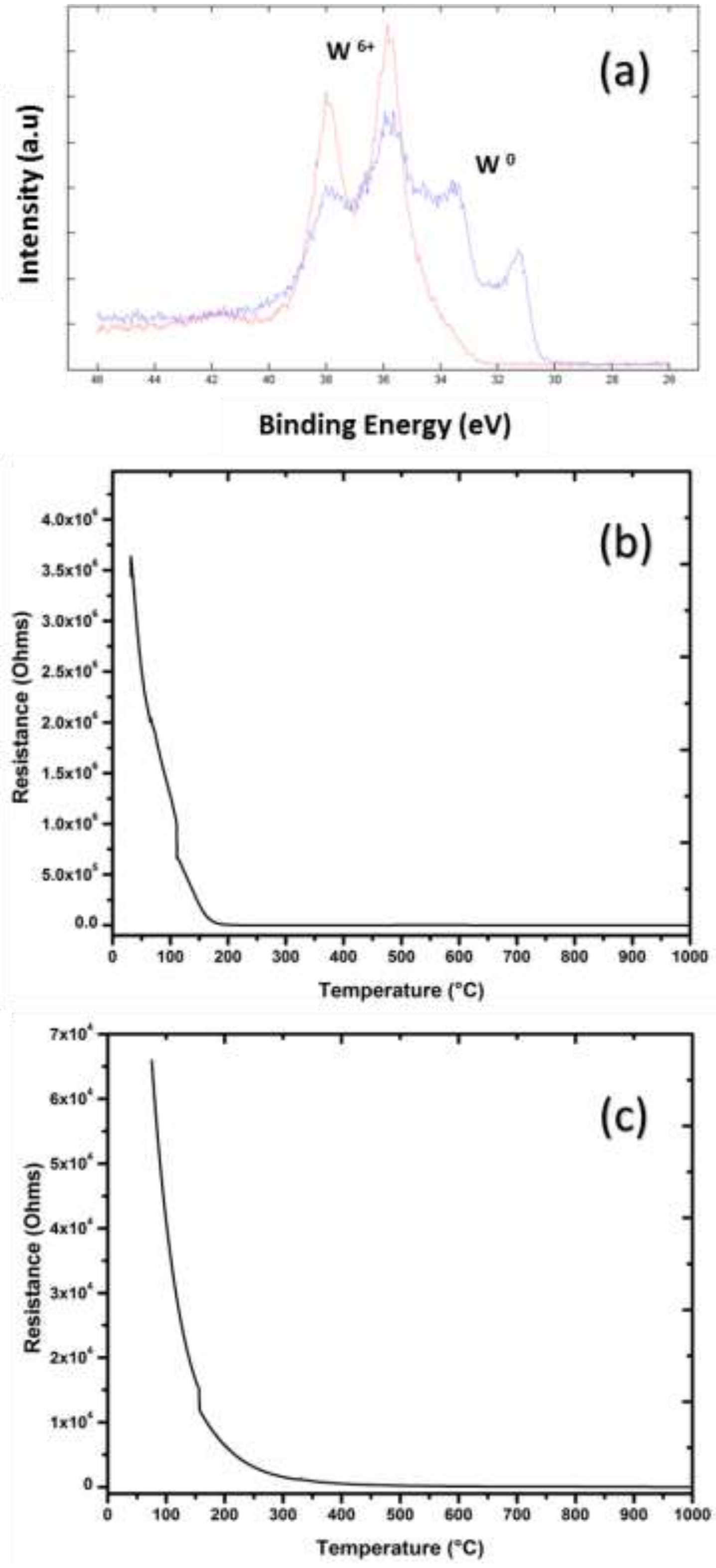
(a)
W 6+
W 0
Intensity (a.u)
46
44
42
40
38
36
34
32
30
28
26
Binding Energy (eV)
(b)
Resistance (Ohms)
4.0x10^6
3.5x10^6
3.0x10^6
2.5x10^6
2.0x10^6
1.5x10^6
1.0x10^6
5.0x10^5
0.0
0
100
200
300
400
500
600
700
800
900
1000
Temperature (°C)
(c)
Resistance (Ohms)
7x10^4
6x10^4
5x10^4
4x10^4
3x10^4
2x10^4
1x10^4
0
0
100
200
300
400
500
600
700
800
900
1000
Temperature (°C)

Figure 69: (a) XPS analysis of the sensor surface after SO_2 testing, sensor cooled down in air (red) cooled down in N_2 (blue), electrical resistance of the sensor during **(b)** heating up **(c)** cooling-up without exposing reducing gas atmosphere.

5.3.3 Tungstates and molybdates

5.3.3.1 $NiMoO_4$

$NiMoO_4$ was the third sensing material to be tested for SO_2 on the resistive-type sensing platform. The melting point of $NiMoO_4$ is 970°C [204]. As previously indicated, the material was first tested in with micron-size commercial powder (Alpha Easer, Nickel molybdenum oxide, 99%, CAS 14177-55-0). Figure 70 shows the resistance versus time results of the $NiMoO_4$ sensor under 1% O_2 partial pressure for various SO_2 exposures at three different temperatures. For this compound it was not possible to present the sensor output in sensitivity scale due to high noise to signal ratio. As can be seen from the graph presented in Figure 70-a, the material showed n-type response at 600°C with great sensitivity upon the exposure to SO_2; however, repeatability was very poor afterwards at this temperature. At 800°C, the sensing material experienced a reduction to large extent. At 1000°C, as can be seen from Figure 70-c, the recorded resistance value (5 ohms) was comparable to the metallic state of Ni. Due to this complete reduction event, the material was not further subjected to the investigation and experiments were not completed to produce a nanomaterial version of this composition (as discussed in the previous chapter).

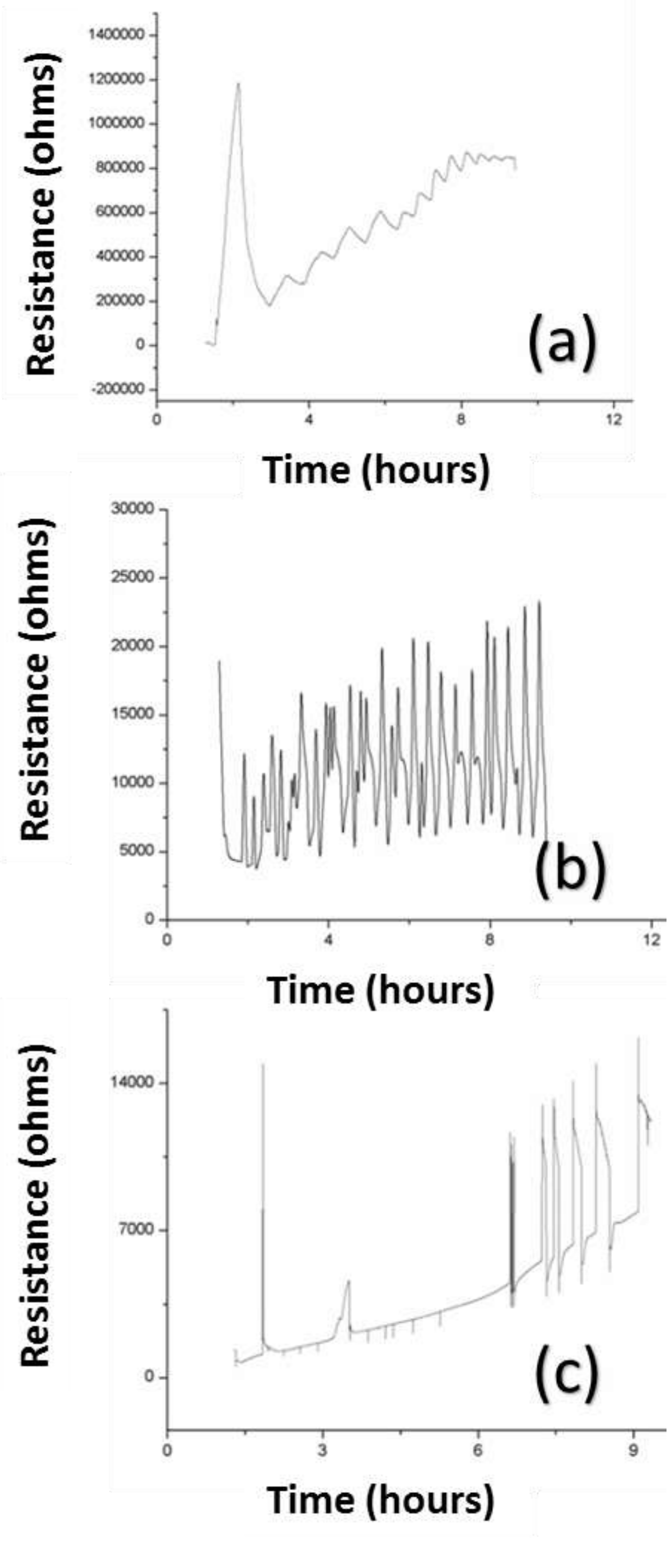

Figure 70: Micron size $NiMoO_4$ response to SO_2 under 1%O_2 at **(a)** 600°C **(b)** 800°C and **(c)** 1000°C.

Figure 71 shows the XPS surface data of the tested sensor for Ni main photoelectron line. Analyzing the peak position makes it clear that Ni was in a mixed chemical state. The tested sensor surface was composed of Ni metal and different suboxides of Ni such as Ni_2O_3 and NiO. As it is quite known, the sampling depth of the XPS is in a close range to the active surface depth of the metal oxide surfaces. From this point, it can be concluded that reduction and accumulation of the metallic Ni phase over the senor surface dictates the response behavior; therefore, the material becomes insensitive to the target gas.

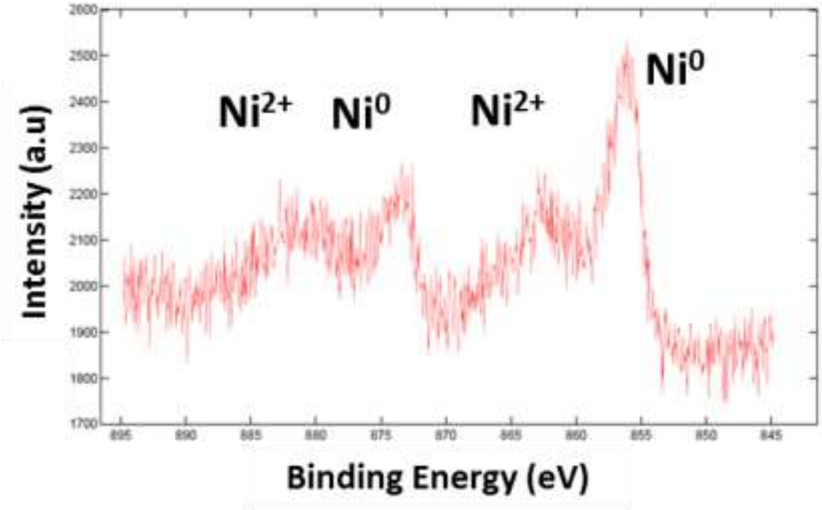

Figure 71 : XPS surface analysis for Ni main photoelectron lines of the tested $NiMoO_4$ sensor.

5.3.3.2 $SrMoO_4$ nano-flowers and commercial grade powder

$SrMoO_4$ adopts tetragonal scheelite crystal structure and reported to be stabile up 1000°C under 15% H_2/Ar [198]. Figure 72 shows the testing results of the commercial grade micron size $SrMoO_4$ (Alfa Easer, Strontium molybdenum oxide, 99.9%, CAS 13470-04-7). The material showed very good sensitivity and accurate output, and excellent repeatability at especially 1000°C. It was not observed that sensor signal output switch from n-type to p-type or opposite as it was observed for WO_3, MoO_3 and $NiMoO_4$. The sensitivity at 1000°C was 20% decreased in resistance, which has not been observed so far any of the materials tested for 2000 ppm of SO_2. For these reasons, the material was subjected to further investigation by synthesizing various nanomaterial morphologies of this composition (as discussed in Chapter 4). The specific nanomaterial synthesis procedure of the compound was explained in detail in the chapter 4.3.2.2.

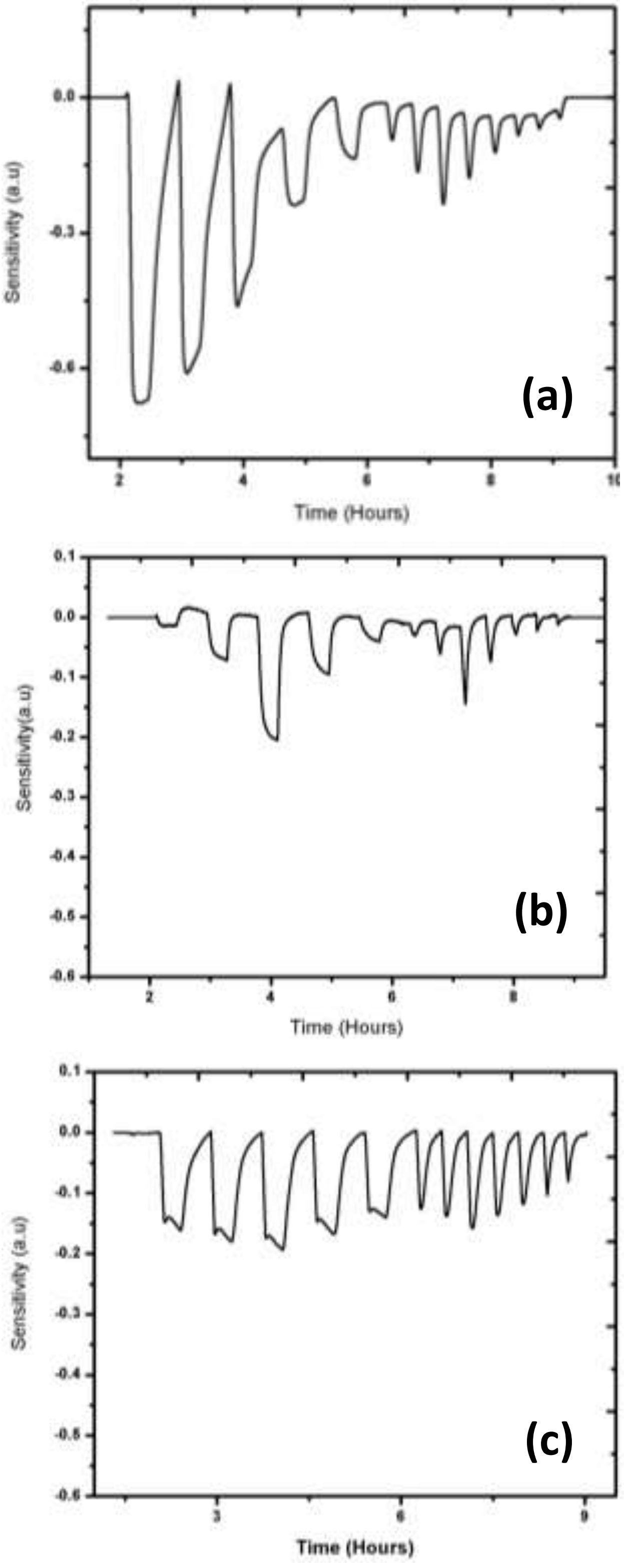

Figure 72 : $SrMoO_4$ micron response to SO_2 under 1% O_2 partial pressure **(a)** 600°C and (**b**) 800°C and **(c)** 1000°C.

Different $SrMoO_4$ nanomaterials (Figure 53) were tested at the same conditions with the previous compounds. In comparison to other morphologies of $SrMoO_{4,}$ the nanoflowers showed the highest sensitivity at all three temperatures. Therefore; only testing results of $SrMoO_4$ nanoflowers were shown in Figure 73. The results revealed that the sensitivity at 600°C for the $SrMoO_4$ was 90%, with the resistivity decreasing upon exposure to SO_2 at the first exposure. The following exposures in the testing procedure showed that sensitivity was up to 40%. At the 800°C and 1000°C testing temperatures, the sensitivities of $SrMoO_4$ nanoflowers was almost 50% higher compared to the $SrMoO_4$ commercial powder. The change in resistance is defined as the percent drift in the data. The sensor signal also was smooth and drift was not observed. In other words material recovered to its initial resistance once the target gas removed from testing chamber. Another significant point is that nano strontium molybdate was more accurate to distinguish different concentrations of the target gas. It is noteworthy to indicate that the $SrMoO_4$ was tested for the first time for SO_2 in the literature. Figure 73-c shows sensitivity versus time graph at 1000°C. As can be seen from the graph, the material not only demonstrates reasonable repeatability, but also the sensing material permits the ability to distinguish between different concentration levels of the target gas.

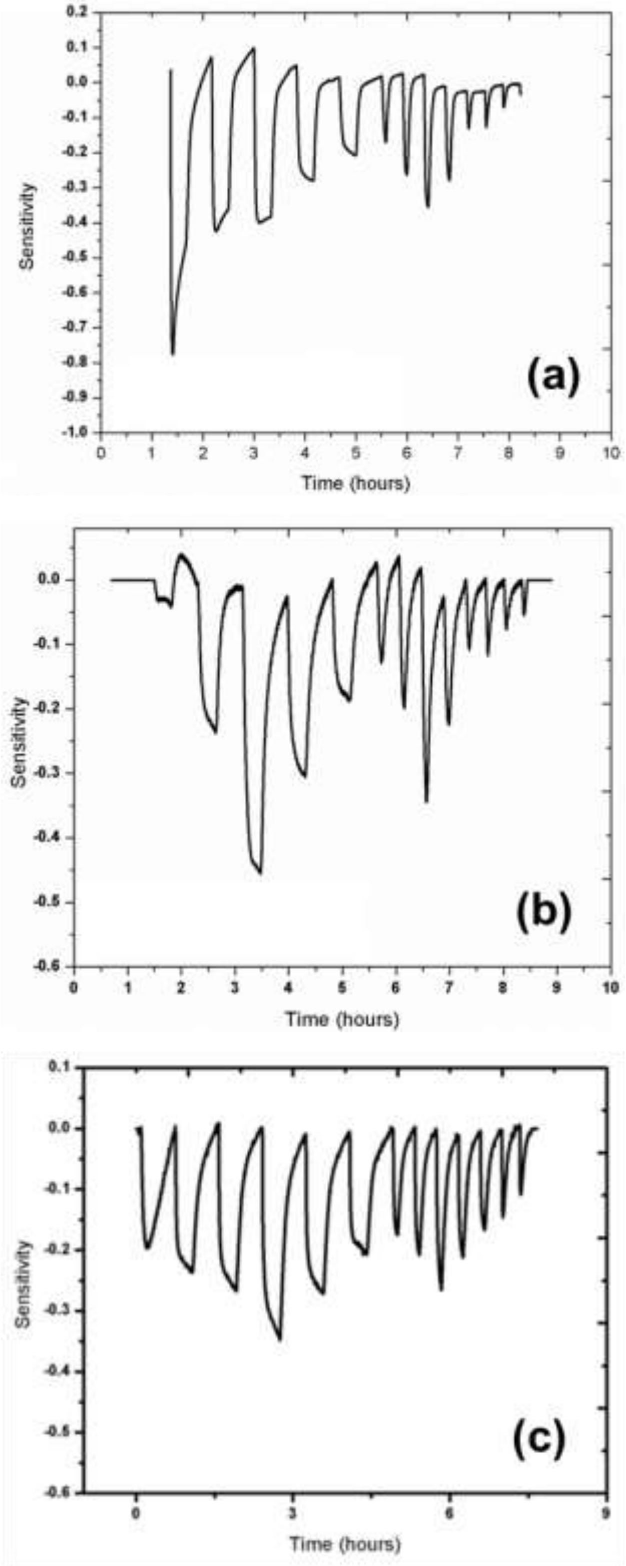

Figure 73 : $SrMoO_4$ nanoflowers sensor response to SO_2 under 1% O_2 partial pressure **(a)** 600°C **(b)** 800°C and **(c)** 1000°C.

The $SrMoO_4$ nanoflowers were also tested for H_2 cross-sensitivity under 1% O_2 partial pressure and the results were very promising. The concentration of H_2 (4000 ppm at maximum) was twice as much as SO_2 (2000 ppm at maximum). The sensitivity was much smaller for the H_2 sensing compared to SO_2, and there was even no sensitivity at 600°C against H_2, at this temperature the sensing material was not even electrically conductive. It can be summarized from Figure 74 that at 1000°C, the sensitivity towards SO_2 was 10 times that of H_2.

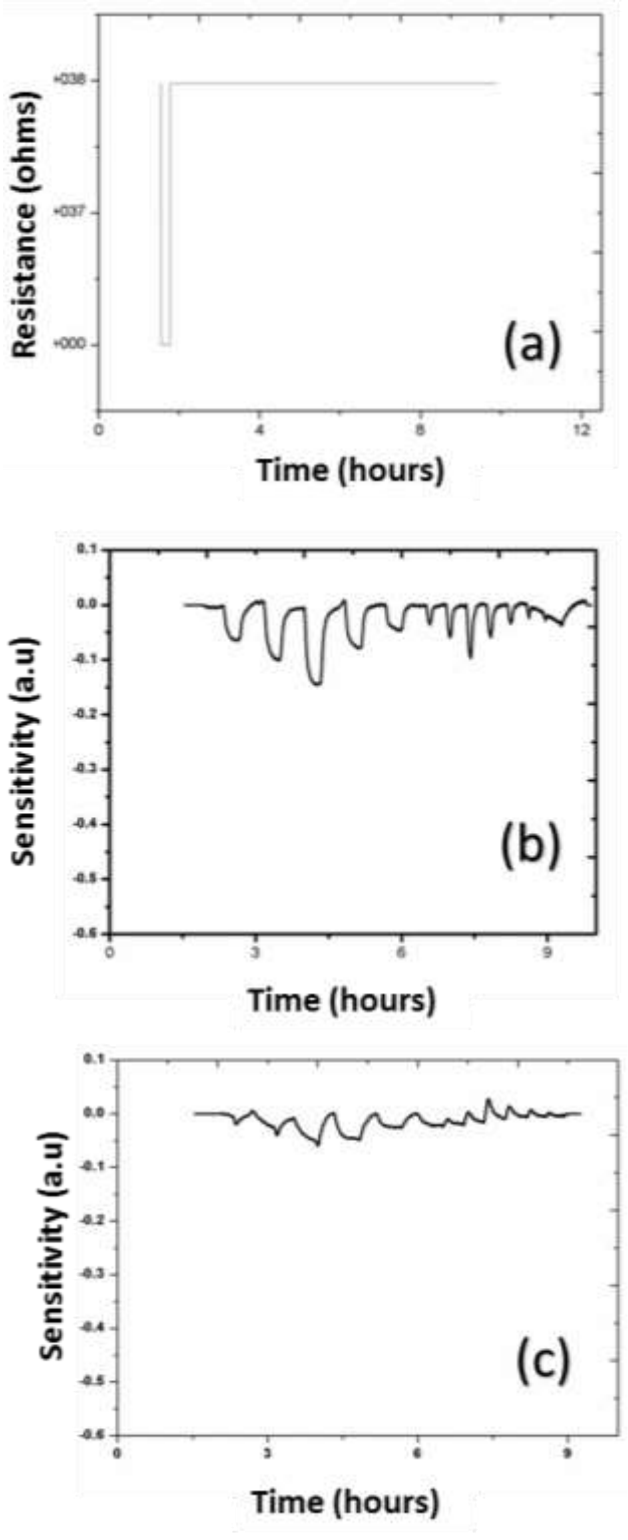

Figure 74 : $SrMoO_4$ nanoflowers sensor response to H_2 under 1% O_2 partial pressure **(a)** 600°C **(b)** 800°C and **(c)** 1000°C.

As a brief summary, it can be concluded that micro-WO_3, WO_3 nanorods, micro-MoO_3, and micro-$SrMoO_4$ were evaluated for SO_2 sensing at three different high temperatures (600, 800 and 1000°C). XPS analysis was completed for WO_3 nanorods to better understand the sensing mechanism. Even though MoO_3 itself did not show reasonable sensitivity towards SO_2, the $SrMoO_4$ composition showed highly reliable sensitivity and repeatability without drift at 1000°C. The reason behind the failure of the WO_3 nano-rods at high temperature was investigated, and it can be concluded that both coarsening and reduction of the sensing semiconducting oxides were the prime causes of the sensing failure. Nano-$SrMoO_4$ was synthesized with different microstructures and the SO_2 testing results for best material was presented. $SrMoO_4$ nano-flowers showed the highest SO_2 sensitivity and lowest H_2 cross sensitivity at 1000°C.

5.3.3.3 $SrMgMoO_6$ (SMM)

Sr_2MgMoO_6 (SMM) with a particle size of ~0.5 µm was synthesized via a solid-state method by using $SrCO_3$ (Alfa Aesar, Strontium carbonate, 99%, CAS 1633-05-2), MgO (Magnesium oxide, ACS, 95.0% min, CAS 1309-48-4), and MoO_3 (Molybdenum (VI) oxide, ACS, 99.5% min, CAS 1313-27-5) as raw starting materials. Calcination was completed at 1200°C for 4 hours. Figure 75 shows the SEM micrograph of the SMM powder after calcination.

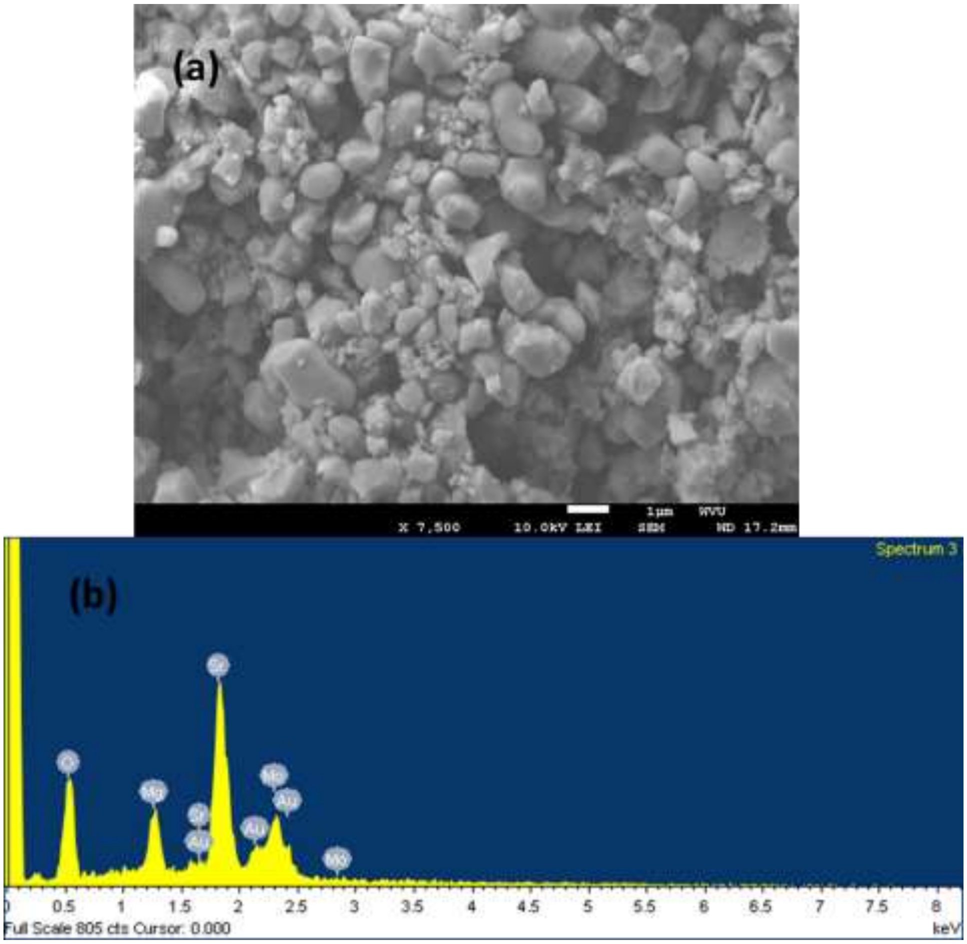

Figure 75 : The SEM micrograph **(a)** and EDS spectrum **(b)** as-synthesized calcined SMM.

Figure 76-a and –b displays the sensitivity versus time data for testing the SMM against SO_2 and H_2 exposure (with 1% O_2), respectively, at 1000°C. The SMM did not sense SO_2 or H_2 at 600°C and 800°C. Surprisingly, the material showed a p-type response to both the SO_2 and H_2 at 1000°C. The sensitivity was far less compare to that showed by nano-$SrMoO_4$ and was neither accurate at the distinguishing different levels of the target gas. However, it was seen that the material showed a lower cross-sensitivity towards H_2. SMM was not further investigated at the nano-scale due its lack of repeatability and lower sensitivity, compared to that of the nano $SrMoO_4$.

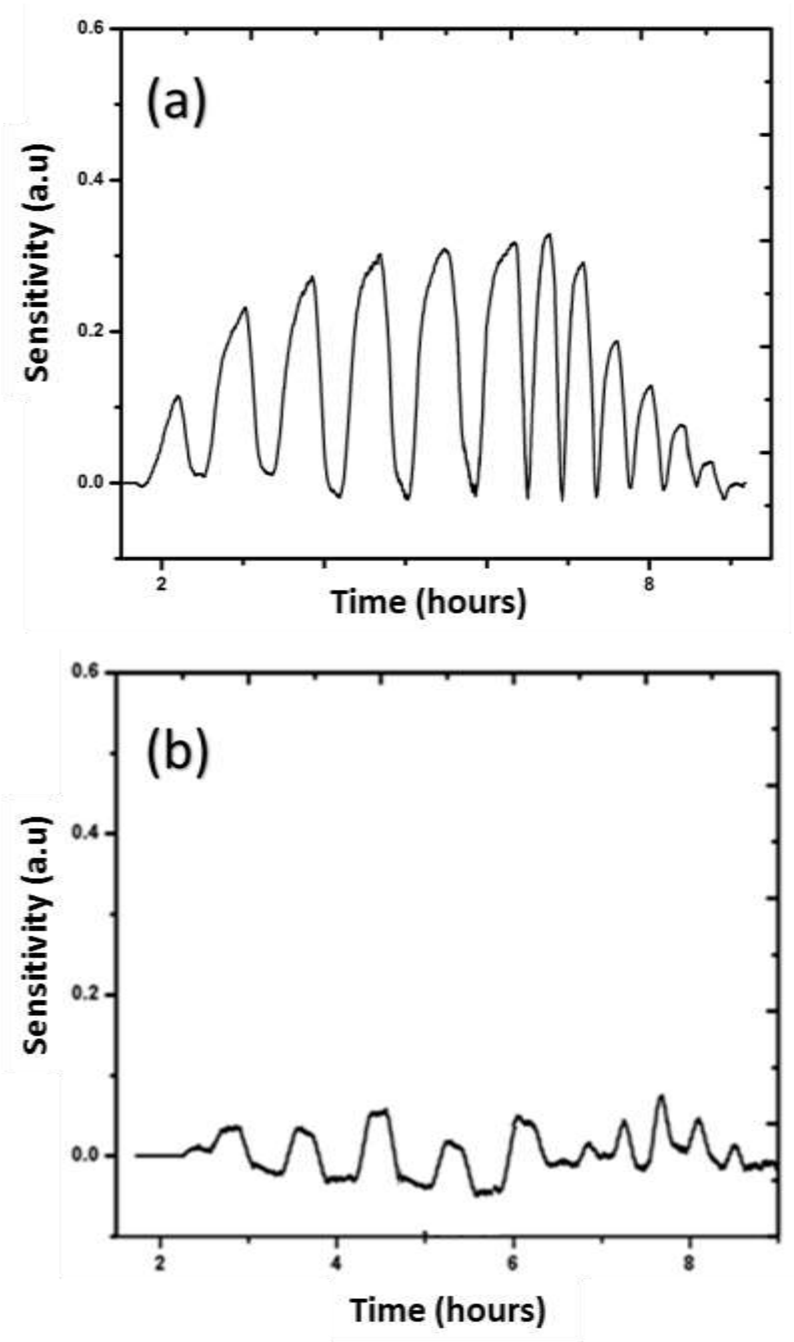

Figure 76 : SO_2 **(a)** and H_2 **(b)** testing results of SMM (Sr_2MgMoO_6) composition at 1000°C under 1% O_2.

5.3.3.4 $MgMoO_4$

Nano-$MgMoO_4$ was another nanomaterial tested for SO_2 sensitivity on the previously described platform. Figure 77 shows the testing results of the compound against SO_2 at three different temperatures. The micron-size and nano-size $MgMoO_4$ powder both did not show any sensor signal output at 600°C. At 800°C, the nano-$MgMoO_4$ showed 10% higher sensitivity compared to the micron-size commercial powder; however, the sensor response of the nano-size powder diminished at 1000°C, and both powders showed similar insensitivity. Figure 77-c shows the sensitivity versus time graph of the nano-powder at 1000°C. As can be seen from the graph, the sensor was totally insensitive to SO_2. Due to low sensitivity at 800°C, and the insensitivity at 1000°C; this material was not subject of further H_2 and CO cross-sensitivity tests. This has particular importance since for a H_2 sensor for potential coal gasification and/or petrochemical applications must possess sustain operational capability in gas streams containing sulfur compounds as well as hydrocarbons and CO [26].

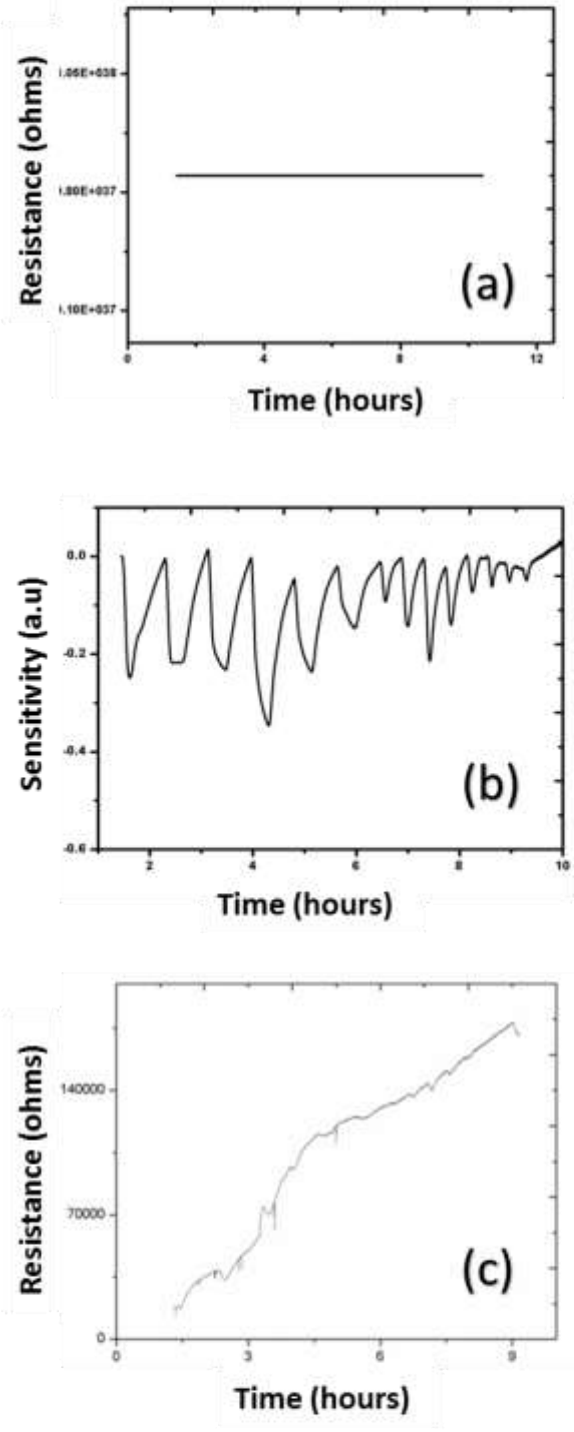

Figure 77: $MgMoO_4$-nano response to SO_2 under 1% O_2 partial pressure **(a)** 600°C **(b)** 800°C and **(c)** 1000°C.

5.3.3.5 NiWO$_4$

Commercial grade micron size NiWO$_4$ powder (Nickel tungsten oxide, 99.9%, CAS 14177-51-6) was tested for SO$_2$ sensitivity on the previous described resistive-type sensor platform. Figure 78 displays the testing results for SO$_2$ exposure of the material. It showed good sensitivity and repeatability at 800°C, but not at 600 and 1000°C. Therefore, the same composition was not investigated at the nano-scale. The sensor showed 0.05% resistance decrease upon exposure to 2000 ppm of SO$_2$ at 600°C. At 1000°C it was observed that the sensitivity was around 0.025% resistance decrease at the same level of gas concentration; however at this temperature the signal was not reliable and diminished toward the end of the testing.

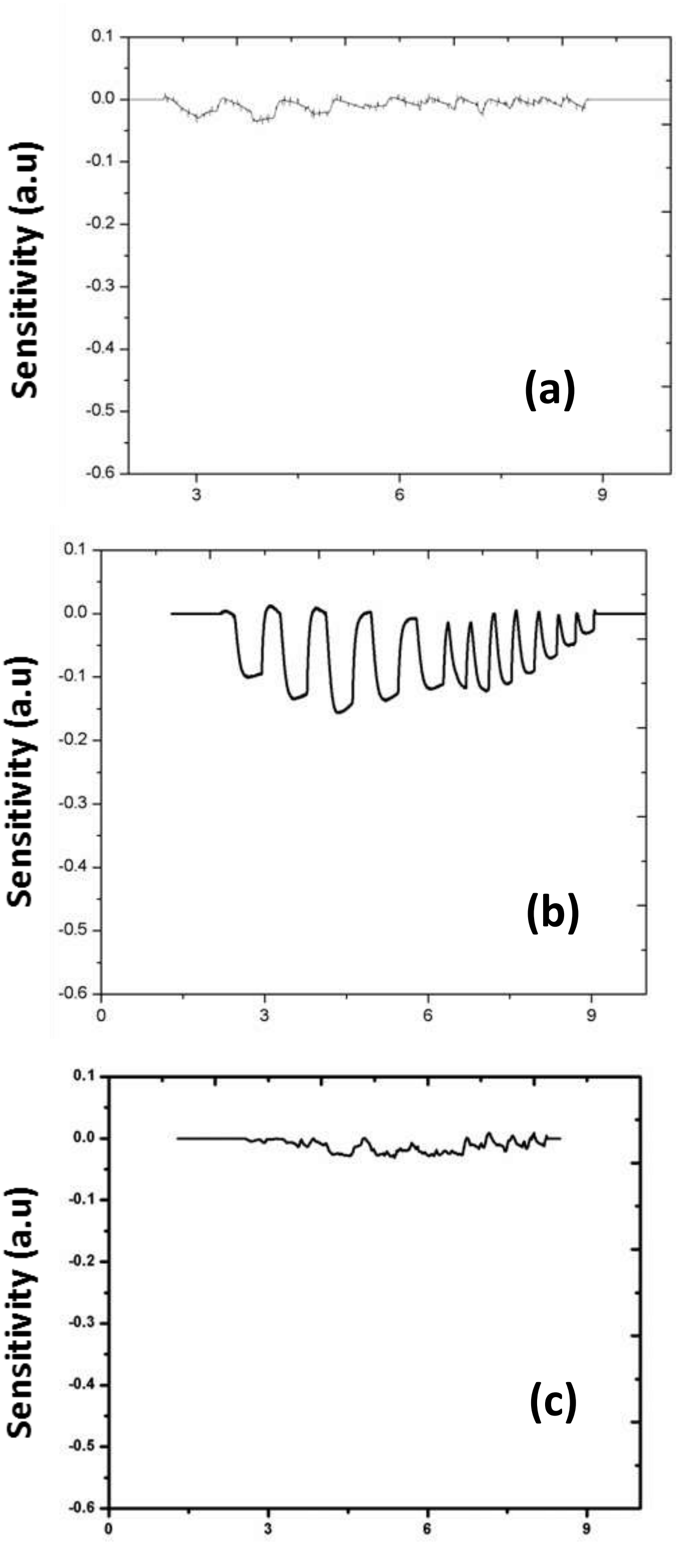

Figure 78 : Micron size $NiWO_4$ composition at against SO_2 600°C **(a)** 800°C **(b)** 1000°C **(c)** at 1% O_2.

The SEM micrograph and XPS data for the Ni main photoelectron positions of the tested sensor are shown in Figure 79-a and –b, respectively. The SEM micrograph shows that the materials is composed of small grains lie over larger $NiWO_4$. The XPS characterization (seen in Figure 79-b) showed the presence of metallic Ni on the surface. The detailed spectra from the data presented for the Ni $2p_{3/2}$ and $2p_{1/2}$ doublets, which are positioned at 852.8 (and 870.1) eV. The binding energy values agree well with chemical state values for metallic Ni at 852.7±0.1 and 869.9±0.1 eV [136]. Another chemical state detected was the NiO (Ni^{2+}), yet was less compare to metallic Ni. It is most likely due to the reduction of the Ni-W-O structure at 1000°C in the reducing atmosphere. Ni migrated and subsequently agglomerated on the surface of the grains. This accumulation of Ni grains on the surface was also observed by other researchers [166]. Basically, it can be summarized for $NiWO_4$ that the sensitivity improved at 800°C due to the decreased reduction rate of the W by using the $NiWO_4$ compound instead of WO_3. After conducting EDS-SEM and XPS analysis, the characterization showed that the Ni was released from the lattice and was accumulated on the surface as a metal. This metallic phase drastically decreased the sensor response to the reducing gas. Ni is good choice for SO_2 adsorption but is not good cation due to its multiple oxidation state and tendency to reduction at especially beyond 800°C under insufficient oxygen background concentration.

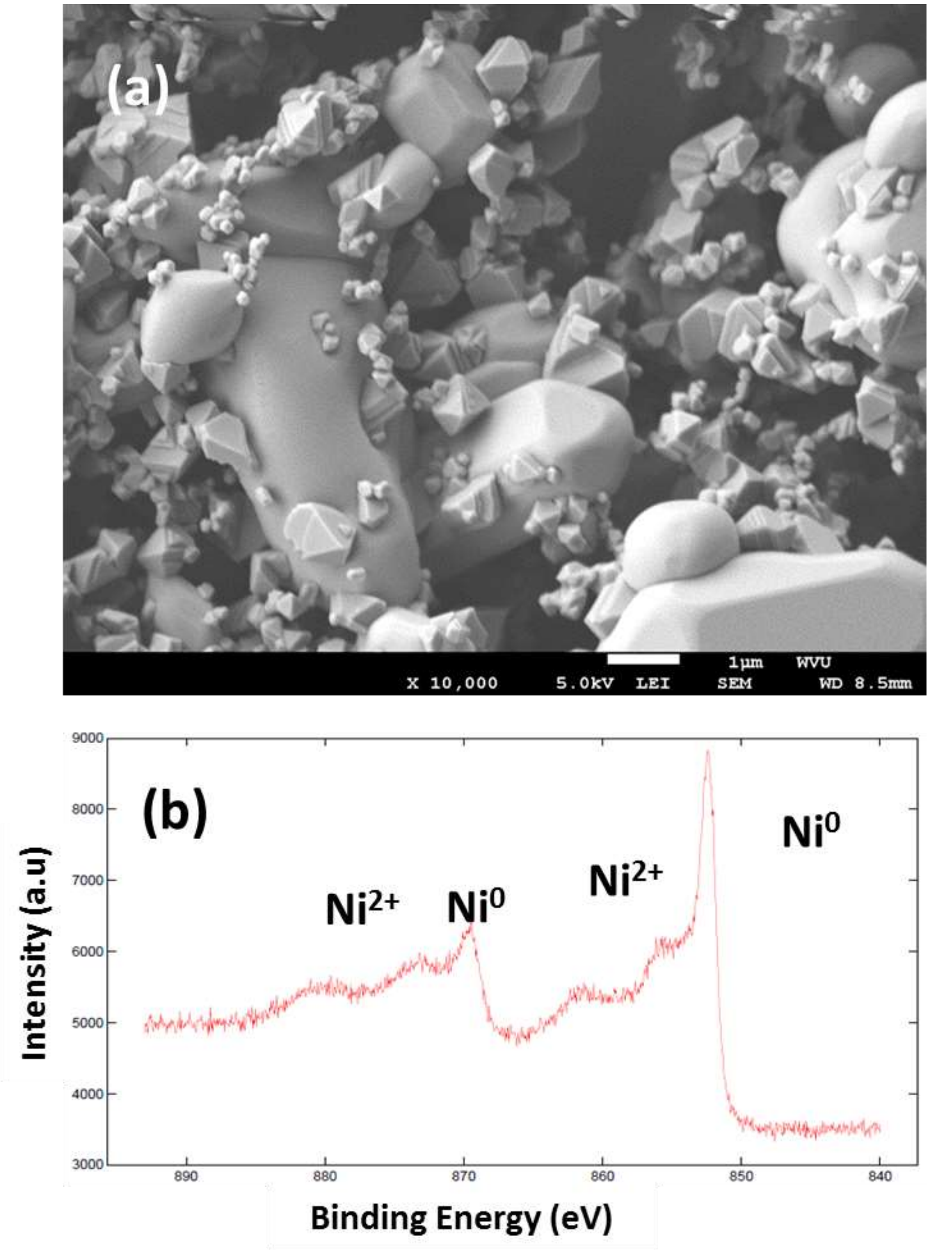

Figure 79 : (a) SEM micrograph of the $NiWO_4$ sensor surface after full scale SO_2 testing **(b)** XPS analysis for Ni main photoelectron line.

5.3.3.6 SrWO$_4$

The SrWO$_4$ composition was also tested using the same sensor platform. Figure 80 shows the SrWO$_4$ sensor response to SO$_2$ under 1% O$_2$ partial pressure. As known from initial experiments and literature, WO$_3$ showed reasonable sensitivity towards SO$_2$. At 600°C under 1% O$_2$ (mix N$_2$), the sensor response was accompanied by a resistivity increase upon exposure to SO$_2$ for SrWO$_4$ in contrast to what observed in WO$_3$. The SrWO$_4$ sensitivity toward SO$_2$ was higher than that of the nano-WO$_3$ at 600°C by showing 90% chance in the resistance, which was 20% change in WO$_3$ case. At 800°C, the sensing behavior of SrWO$_4$ (see Figure 80-b) was not reliable and large drift was also observed. In addition, the sensor did not recover totally and could not sense 70% of the gas pulses. Figure 80-c shows the sensor response at 1000°C. The SrWO$_4$ showed good and smooth response to SO$_2$ characterized by a resistance decrease up to 20% decrease in resistance upon exposure to 2000 ppm of SO$_2$ balanced with N$_2$ and 1% O$_2$. SrWO$_4$ was tested for the first time as a gas sensing material; therefore the switch from p-type to n-type behavior cannot be compared with the literature. However, the sensing response change upon an alteration in the testing environment oxygen content and/or temperature (p-type to n-type or opposite) is typical characteristic of WO$_3$.

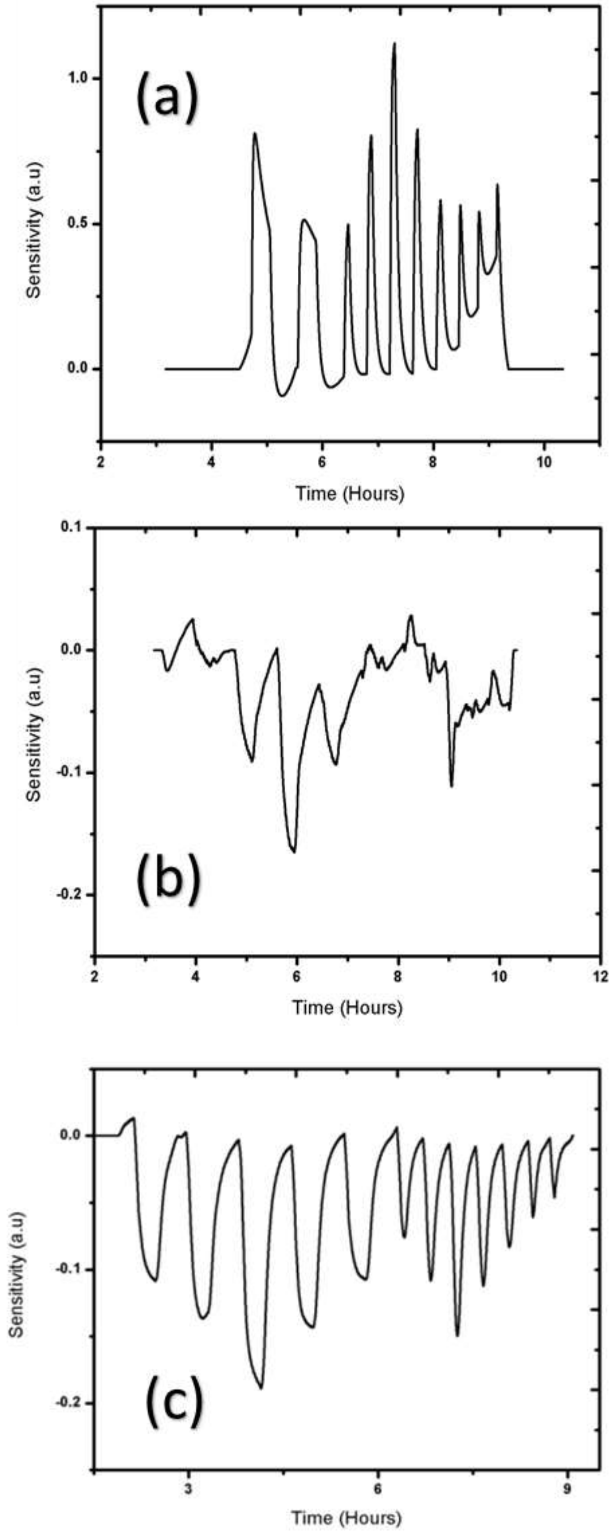

Figure 80 : Micron size $SrWO_4$ sensor response to SO_2 under 1% O_2 partial pressure **(a)** 600°C **(b)** 800°C and **(c)** 1000°C.

5.3.3.7 $SrMgWO_6$ (SMW)

The SMW powder was made via a solid-state synthesis method. $SrCO_3$ (Alfa Aesar, Strontium carbonate, 99%, CAS 1633-05-2), MgO (Magnesium oxide, ACS, 95.0% min, CAS 1309-48-4), WO_3 (Alpha-Easer, 99.8% metals basis, CAS 1314-35-8) was used as the raw materials. Calcination was completed at 1200^0C for 4 hours. SEM micrograph presented in Figure 81 shows the as-calcined powder with particle size~1 µm.

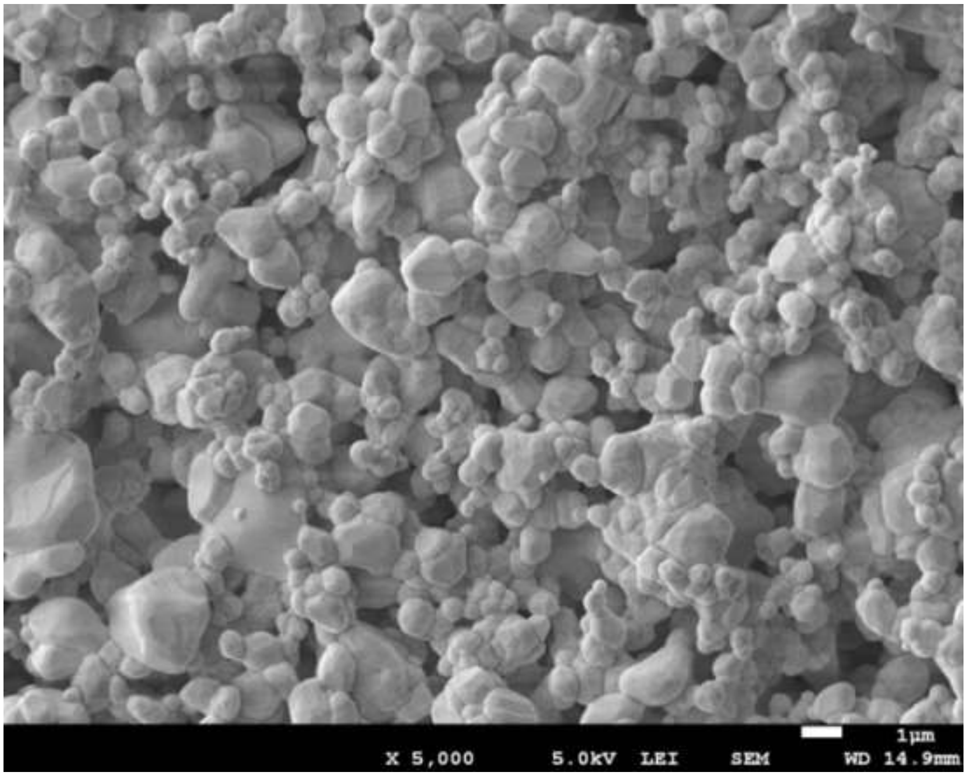

Figure 81 : The SEM micrograph of the as-synthesized and calcined SMW powder was made via a solid-state synthesis method.

The synthesized SMW micron-size was tested in the previously described resistive-type sensor platform towards SO_2 at levels of 500, 1000 and 2000 ppm at three different temperature regime (600, 800 and 1000°C). Figure 82-a and -b show the measured sensitivities the SMW micron-size under 1% O_2 partial pressure against SO_2 and H_2, respectively. The material showed an n-type response to the SO_2 and H_2 exposure at 1000°C. The sensitivity was less compared to nano-$SrMoO_4$, but comparable to SMM. The response was not accurate in distinguishing the different levels of the target gas like SMM; however, it was seen that the material showed high cross-sensitivity toward H_2 similar to that of SMM. In addition to that sensitivity was suddenly diminished after 7 hours of testing due to drift in baseline resistance of the compound. The sensing capabilities of SMW was not investigated at the nano-scale due its lack of sensing repeatability and less sensitivity compare to other systems tested (such as the $SrMoO_4$ nanoflowers).

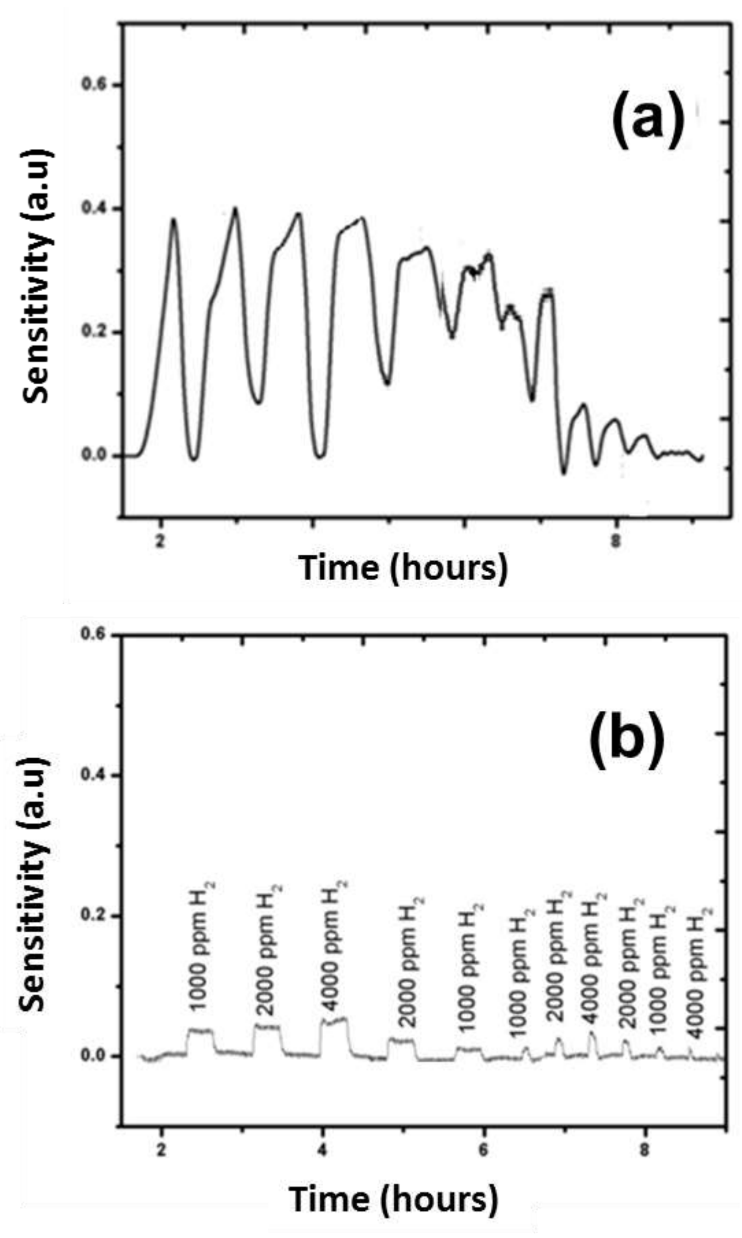

Figure 82 : SMW at 1000°C under 1% oxygen atmospheres testing results for **(a)** SO_2 and **(b)** H_2.

Both SMM and SMW showed superior high temperature sensitivity compared to micro- and nano-scale simple oxides of tungsten and molybdenum. SMM showed less drift and less cross-sensitivity towards H_2, however, the SMW showed higher sensor sensitivity at 1000°C.

5.3.4 Hydrogen sulfide (H_2S) testing of selected compounds

The materials showed high sensitivity toward SO_2 and low cross sensitivity to H_2 tested against hydrogen sulfide (H_2S). Two different approaches were employed to have better understanding over sensing mechanism and evaluate the successful implementation of potential sensor material under real service environment. The H_2S tests were completed at the commercial partners testing facilities and following testing procedure was developed and carried out for all H_2S testing. The sensors for H_2S were heated to 800°C at 5°C/min in N_2 and then held near 800°C overnight with data collection the entire time. The total flow of all gases into the oven was set at 100 sccm. In first type of test, the H_2S was derived from a gas blend with 200 ppm of H_2S and a balance with H_2 and select of sensing material was tested for 5, 50 and 100 ppms of H_2S. In the second type of test, the sensing material was exposed to 4, 34 and 64 ppms of H_2S balanced in syngas is consist of %32 H_2, %40 CO, %20 CO_2, 1% O_2, 1% Steam (H_2O), 5% N_2. Once the magnitudes of the flows were established, the balance of the total 100 sccm flow was made up of N_2 from a tank. Figure 83-a and -b shows the testing results of the micron size $NiWO_4$. $NiWO_4$ showed a p-type sensing behavior at 800°C that switched to an n-type behavior at 1000°C. At both temperatures, abovementioned compound underwent reduction to the metallic state as observed in the WO_3 case. Sensitivity of the $NiWO_4$ was found to be not reliable, since it is not able to distinguish between 50 and 100 ppm concentration levels of H_2S.

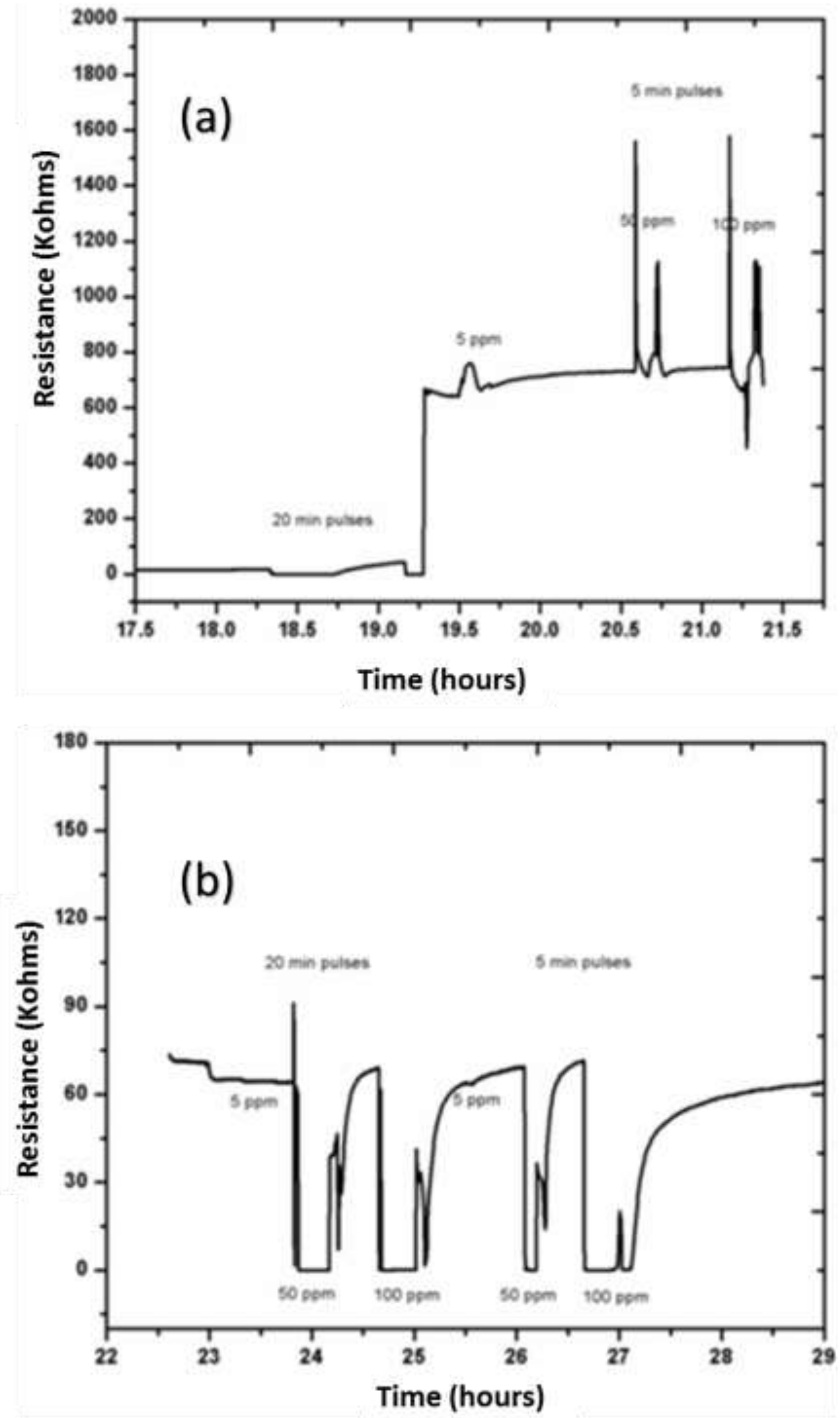

Figure 83 : H_2S testing of $NiWO_4$ **(a)** 800 and **(b)** 1000°C.

The second composition tested was $SrWO_4$. As expected, the sensing material showed better high temperature behavior and showed better sensing and sensitivity behavior. The results are shown in Figure 84-a and –b. The compound showed a p-type response to 5 ppm H_2S at 800°C; however, the rest of the responses were n-type in behavior. The material showed high sensitivity toward the H_2S compared to $NiWO_4$ which can be attributed to highly stable 2+ state of the Sr in the $SrWO_4$ lattice Even though $SrWO_4$ showed reasonable sensitivity, the compound was not able to distinguish between different levels of H_2S. As seen in the Figure 83-c and-d, there is no distinguishable difference between 50 ppm and 100 ppm of H_2S exposure.

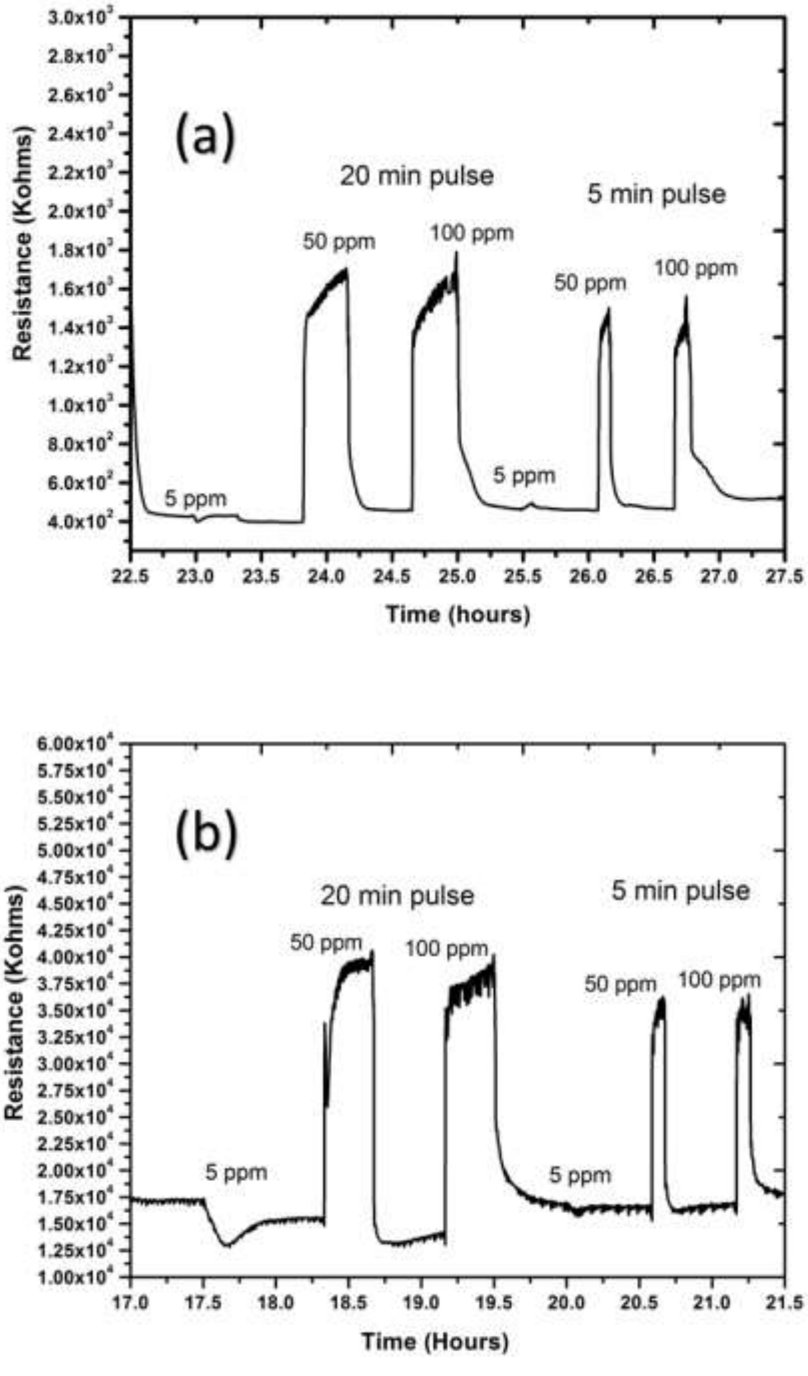

Figure 84 : H_2S testing of $SrWO_4$ **(a)** 800 and **(b)** 1000°C.

The third compound tested for the H_2S was the $SrMoO_4$ nanoflowers. Figure 85-a and –b shows the results of the compound against H_2S. The compound showed n-type sensing response to the target gas at all concentration levels and testing temperatures. The responses at 800°C showed a difference between the exposure to 50 and 100 ppm concentration levels of the target gas. Moreover, the difference in the gain of the sensor response increased at 1000°C. The compound showed stable electrical conductivity at high temperature like $SrWO_4$ that can be seen on the graphs presented in the Figure 85-c and –e. $SrMoO_4$ adopts tetragonal scheelite crystal structure which has low symmetry, inversion center in the middle of the unit cell and relatively open crystal structure. The early study by Hayashi et *al.* stated that $SrMoO_4$ transfers from scheelite to perovskite after 1200°C under very low oxygen partial pressure (log P (O_2)=-12.45). Another study reported that $SrMoO_4$ can be reduced under 15%H_2/Ar conditions at temperatures higher than 1000°C. Another point is to be deserved is that ABO_3 ($SrMoO_3$) is not stabile phase, even under room conditions with the help of humidity it's tend to oxidize to scheelite structure [202]. It was also shown that ABO_3 (A=Sr, Ba B=Mo) oxidation starts at 250°C. [198].

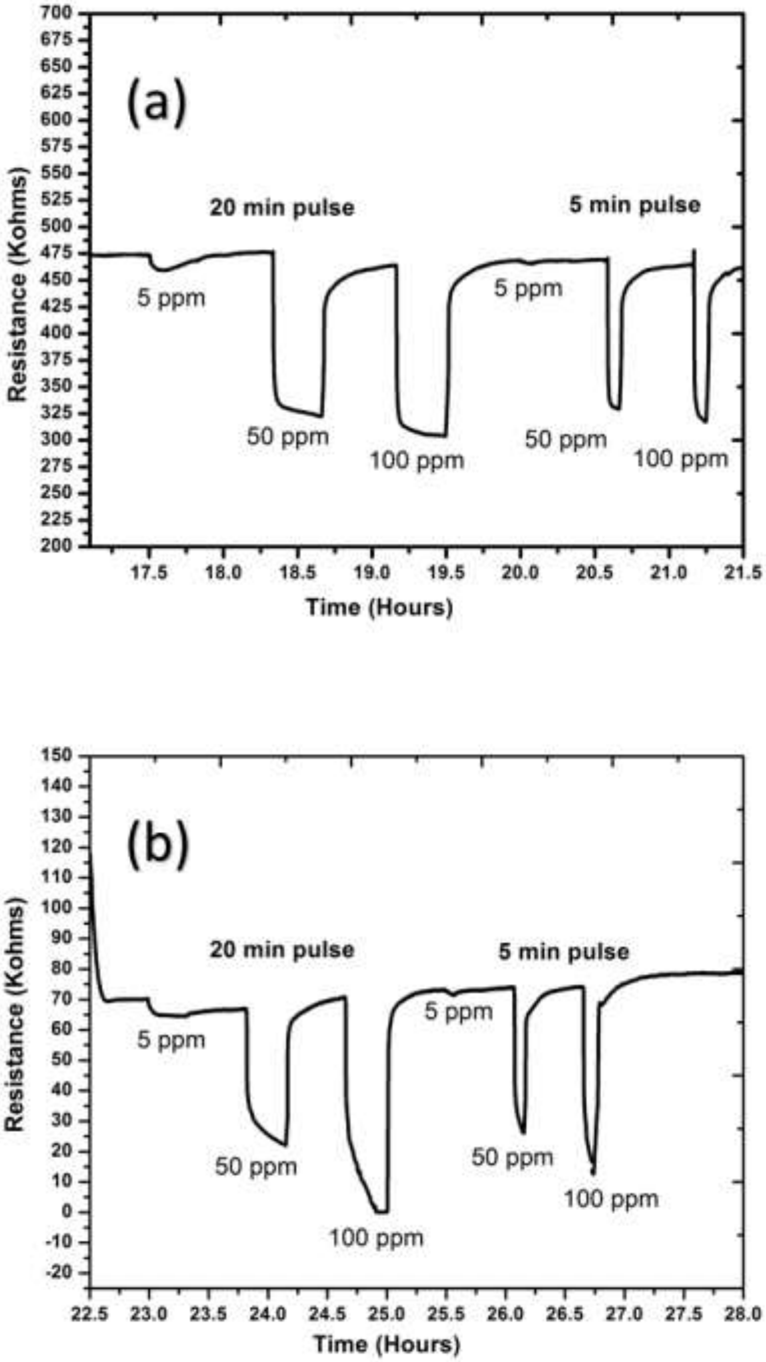

Figure 85 : H_2S testing of $SrMoO_4$ **(a)** 800 and **(b)** 1000°C.

The testing results for syngas composition is given in the Figure 86-a and –b. Syngas is consist of %32 H_2, %40 CO, %20 CO_2, 1% O_2, 1% Steam (H_2O) and 5% N_2 and sensor exposed the different levels of H_2S at 800 and 1000°C for 5 and 20 minutes. During steady stead conditions 4, 34 and 68 ppm of H_2S introduced the testing chamber and the $SrMoO_4$ nano showed p-type sensing behavior. The missing signal at the 1000°C is 68 ppm exposure. It is not sensing material malfunction, most likely at that point the contact/connection between sensor pad and DMM was disturbed. Sensor unexpectedly showed p-type sensing behavior. This is the first time $SrMoO_4$-nano showed n/p type switch in terms of sensing behavior. Apart from this sensor showed up to 60% resistance change upon exposure to different levels of H_2S.

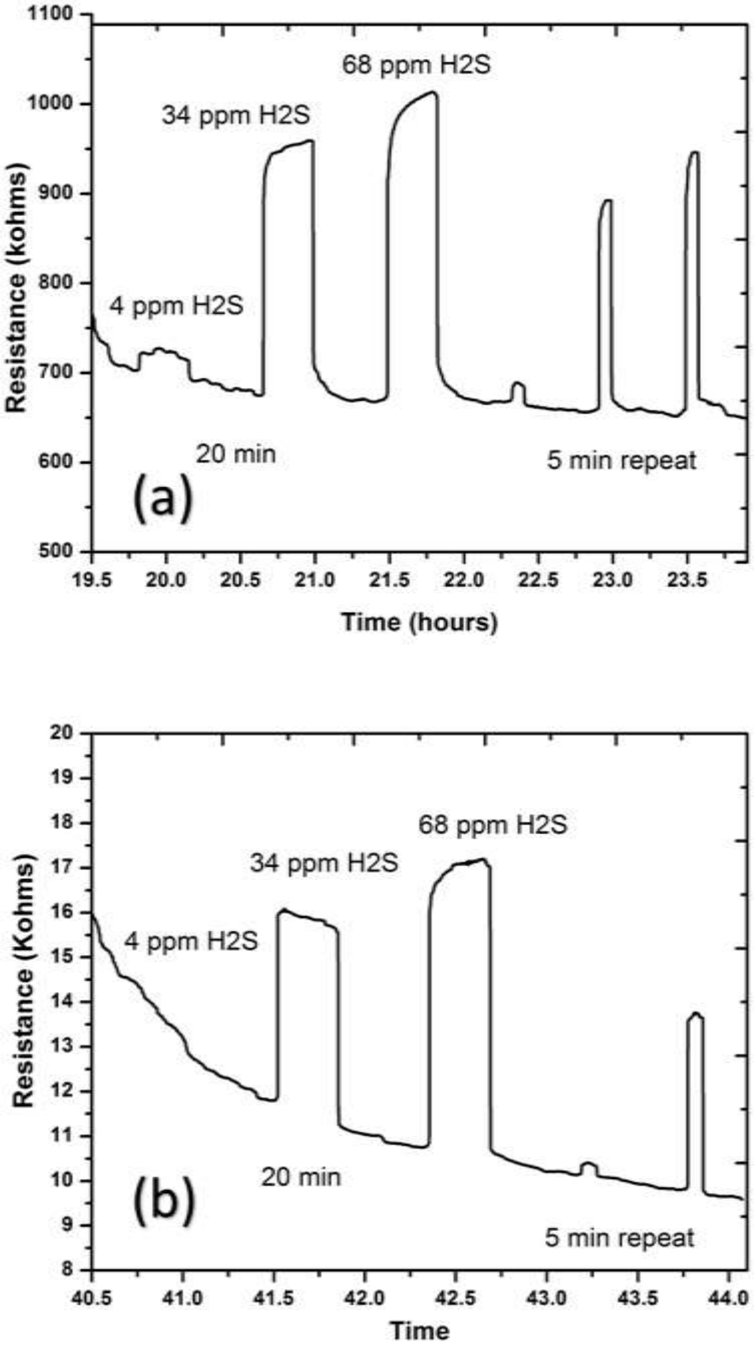

Figure 86 : Syngas testing results of $SrMoO_4$-nano at 800°C **(a)** and 1000°C **(b)** upon exposure to 4, 34 and 68 ppm levels of H_2S.

5.3.5 Summary and nanomaterial stabilization efforts

Figure 87 shows the comparison of the sensitivies of the different sensing materials at 1000°C against SO_2 under 1% O_2 partial pressure condition. $SrMoO_4$ nano-flowers showed the highest sensitivity toward SO_2 at 800°C and 1000°C among all other compounds tested. However, at an elevated temperature of 1000°C, the sensitivity of the compound decreased compared to the low testing temperatures. In addition, the $SrMoO_4$ nano-flowers possessed the highest sensitivity against H_2S exposure among the other materials tested (see Figure 83). Moreover, the material showed very stability and sensitivity toward H_2S in syngas stream as well.

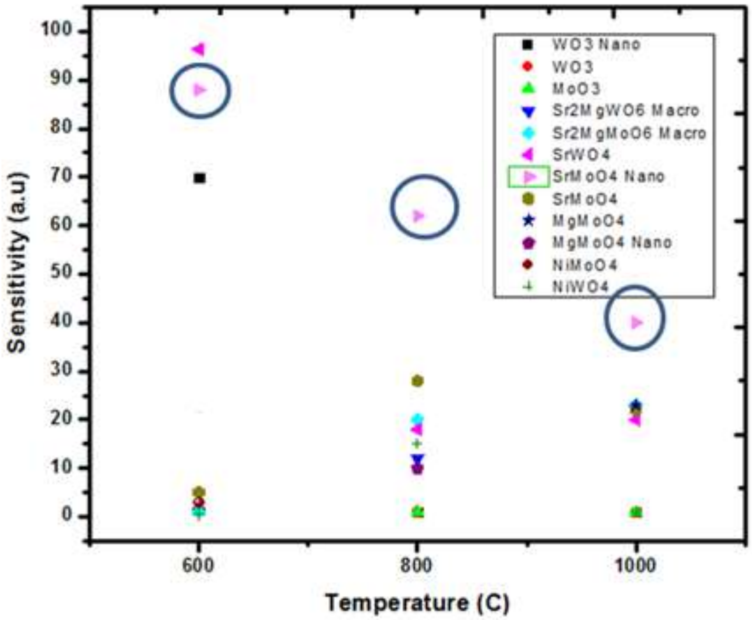

Figure 87 : Testing results of different oxides in nano and macro scale at 1000°C for 2000 ppm SO_2 balanced in N_2 at 1% O_2.

After evaluation all of the material systems (considering SO_2 and H_2S sensitivity and cross-sensitivity toward CO and H_2), the $SrMoO_4$ emerged as a choice sensing material for SO_2 and H_2S. The compound was synthesized in four different morphologies; although all of them showed sensing behavior towards the sulfur compounds at high temperature, they succumbed to coarsening and lost the high sensitivity. The coarsening issue can be seen clearly in the SEM micrographs presented in Figure 88-a and –b. The $SrMoO_4$ nanostructures turned into 5-10 micron particles that were densely packed regardless of the initial morphology.

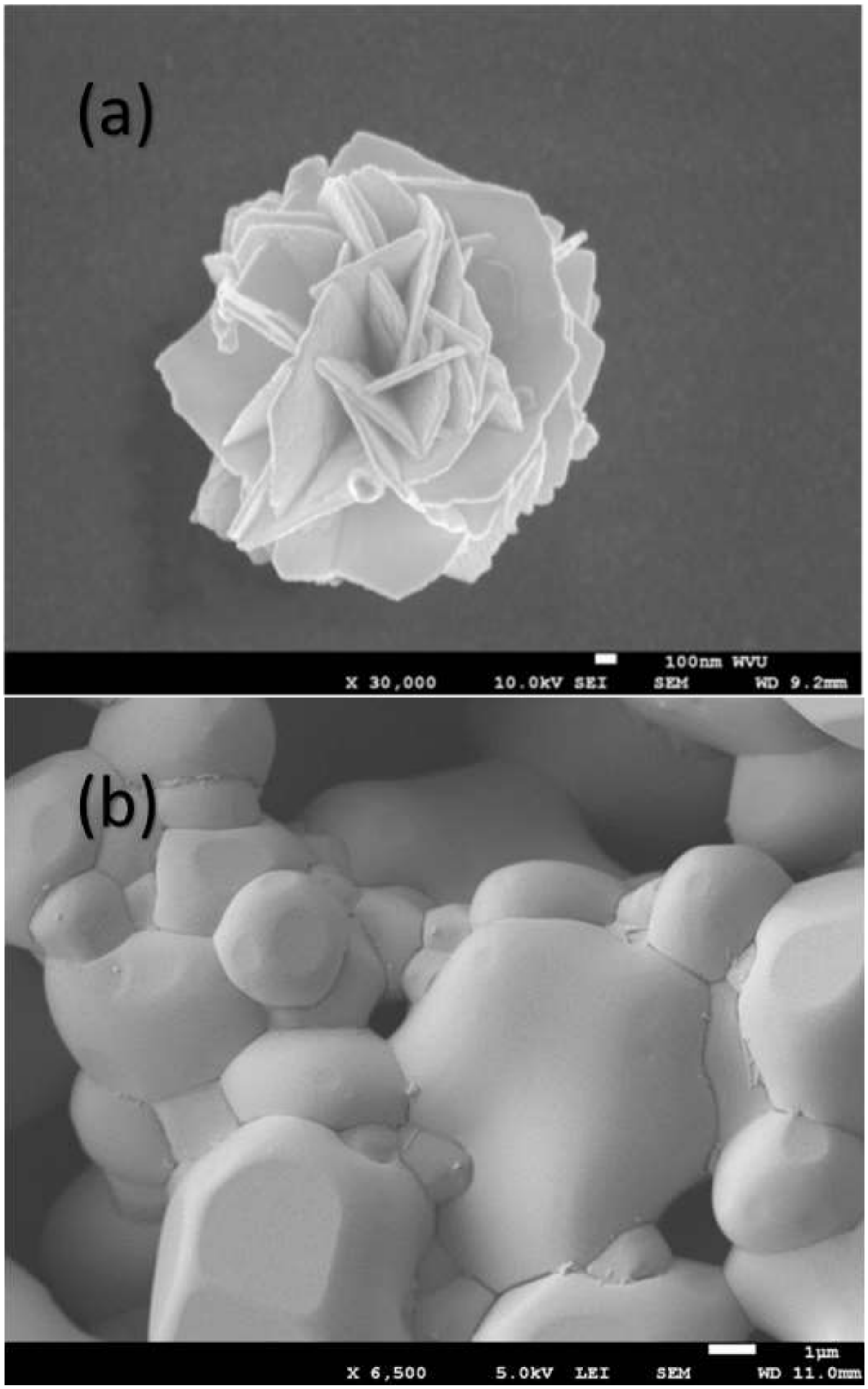

Figure 88 : SEM micrographs of the $SrMoO_4$ nano-flowers **(a)** as-synthesized and after full scale testing **(b)**.

Nanomaterials are known to be unstable at elevated temperatures due to sintering and coarsening mechanisms, and these issues drawback their prospective utilization within advanced sensors at high temperature. In order to retain the high surface area of the synthesized $SrMoO_4$ nanomaterials, strategies were required to limit the sintering and grain growth processes of this material. In order to retain the high surface area of the synthesized nanomaterials, this work focused on strategies to limit the sintering and grain growth processes. Two different strategies with different stabilizing mechanisms were proposed in order to hinder/stop the coarsening/sintering process. The strategies chosen were grain and substrate pinning of the chosen nanomaterial through the distribution of coarsening resistant secondary phase among nanomaterial grains and the bonding of nano-granular microstructure over a stable refractory substrate where thin film grains are usually pinned to their 2 D substrates at low thicknesses, and the grains cannot grow. Also, if the substrate is refractory then the substrate will be stable to high temperatures. If it is in fiber form, then the refractory fiber will only have a few connections to permit transport that would significantly hinder the coarsening and sintering related diffusion.

Grain pinning strategy was realized by dispersing 10% wt. in-house made CeO_2 nano-particles by solvent exchange method to $SrMoO_4$. In order to evaluate the temperature resistivity of the mixture, 5 h heat treatment at 1000°C was conducted. Figure 89 shows the SEM micrograph of the $SrMoO_4$ with the secondary phase CeO_2 after heat treatment. As seen in the SEM micrograph, partial success was obtained through this method, where the grain growth was hindered to some extent. However, the densely packed grain morphology would not result in an increase in the sensitivity. Because of that this composition was not used as a sensing material and this strategy abandoned.

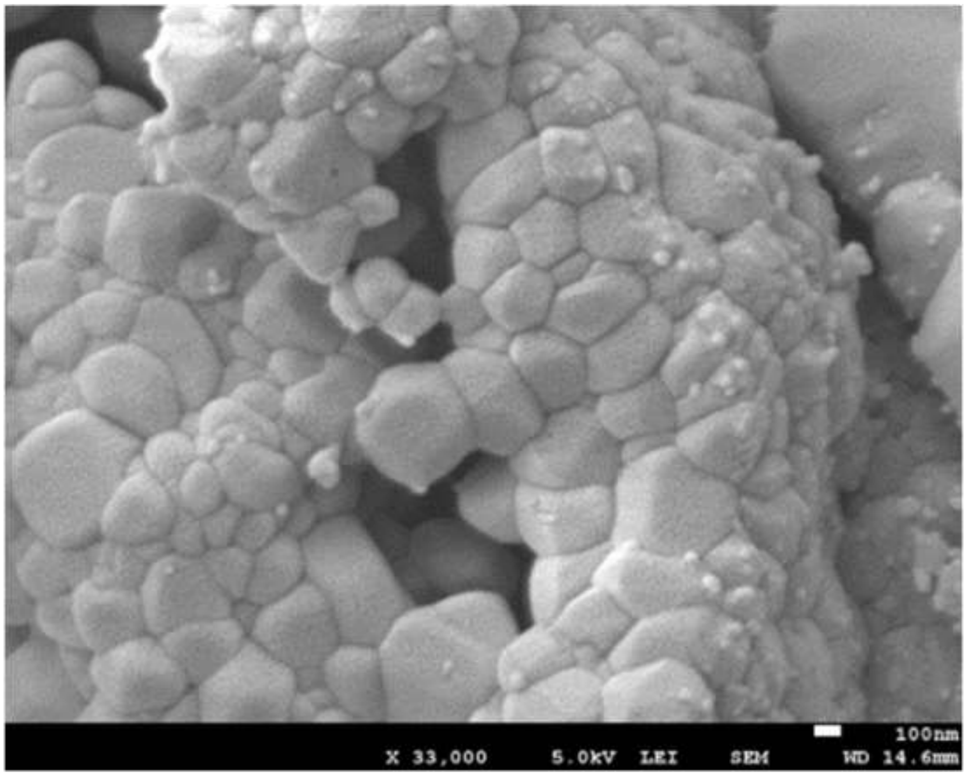

Figure 89 : SEM micrograph of 10% wt. CeO_2 mixed with $SrMoO_4$ by solvent exchange after annealing at 1000°C for 5 h.

In order to realize second strategy, MgO nano-rods were synthesized via hydrothermal route (see chapter 4.3.3). Figure 90-a shows the SEM micrograph of the as-synthesized MgO nanorods. In order to evaluate the high temperature coarsening resistance of the compound, the fibers were heat treated to 1000°C for 5 h. The final microstructure of the MgO fibers are shown in the Figure 90-b. As can be seen from the SEM micrograph, the MgO nano-rods did not coarsen and retained their microstructural formation at the temperature of interest.

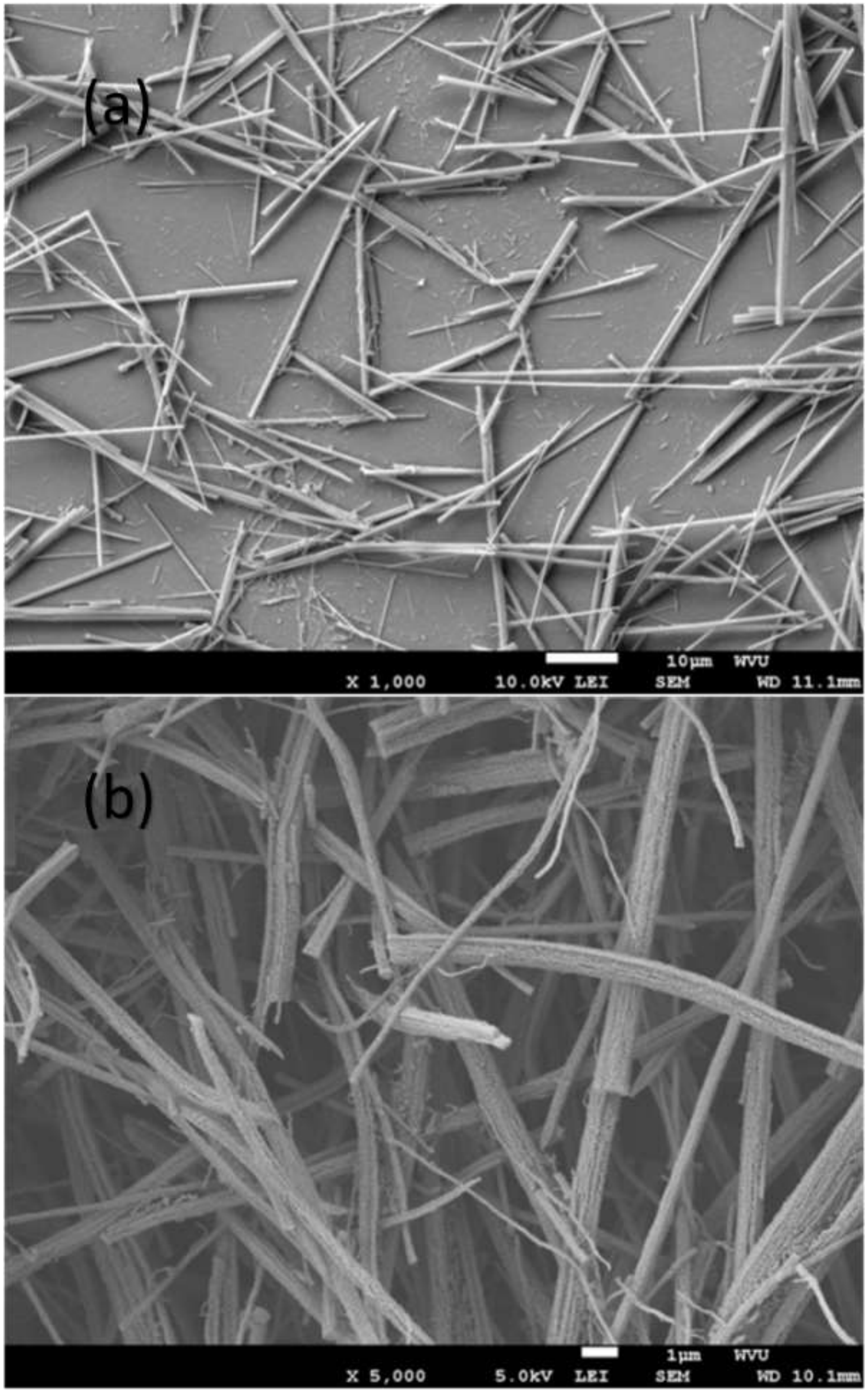

Figure 90 : SEM micrograph of the MgO nanorods **(a)** as-synthesized and **(b)** heat treatment after 5 h at 1000°C.

$SrMoO_4$ nanoflowers showed superior sensing behavior against SO_2 compare to other compounds and low cross-sensitivity toward H_2 and CO. Figure 91-a and -b shows the sensitivity results of the tested compounds against SO_2. Figure 91-c shows testing result of the $SrMoO_4$ nano structures against H_2. As seen in the sensitivity graph, the material showed very low cross-sensitivity toward H_2. The sensitivity was ~0.5% reduction in resistance upon exposure to 4000 ppm of H_2. That low level of cross-sensitivity further increases the usability of the material as a SO_2 sensor. The $SrMoO_4$ showed n-type sensing response to target gas at all concentration levels and testing temperatures. Post-exposure characterizations were completed on this compound which included XPS and SEM-EDS, in order to better establish an understanding of the sensing mechanism and the final chemical state of the compound after exposure to a reducing atmosphere. Figure 91-a shows comparison of the sensitivies against SO_2 at 1000°C under 1%O_2 partial pressure. High sensitivity of the $SrMoO_4$ nano-flowers diminishes as the temperature increases. Therefore, the $SrMoO_4$ nano-flowers were grown over MgO core structure via hydrothermal route.

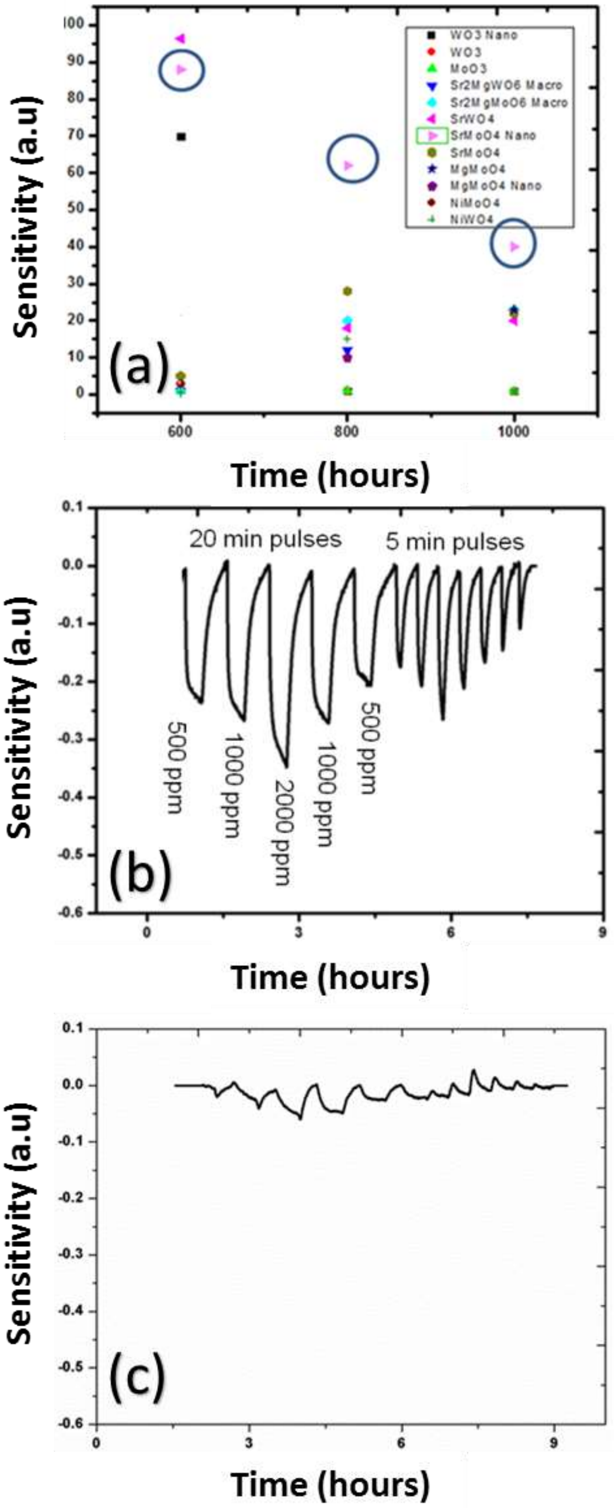

Figure 91: (a) Testing results of different oxides in nano and macro scale at 1000°C for 2000 ppm SO_2 balanced in N_2 with 1% O_2 Sensor signal of $SrMoO_4$ nano-flowers in response to **(b)** SO_2 **(c)** H_2.

There was no modification to the hydrothermal processing route parameters that were presented in Chapter 4 for the synthesis of $SrMoO_4$ nanoflowers. Figure 92-a and -b presents the SEM micrograph of the $SrMoO_4$ decorated over MgO core structure at low and high magnifications, respectively. In order to evaluate high temperature resistance of the templated growth material, the materials were heated to 1000°C and held for 5 h. The resulting microstructure is presented in the SEM micrograph shown in the Figure 92-c. The microstructure of the nano-$SrMoO_4$ decorated over the MgO fiber was highly resistant to effects of the high temperature conditions. The highly porous microstructure was preserved after preliminary annealing practice at 1000°C for 5 h. The nano-$SrMoO_4$ decorated over MgO will be termed as $SrMoO_4$/MgO in the rest of the work.

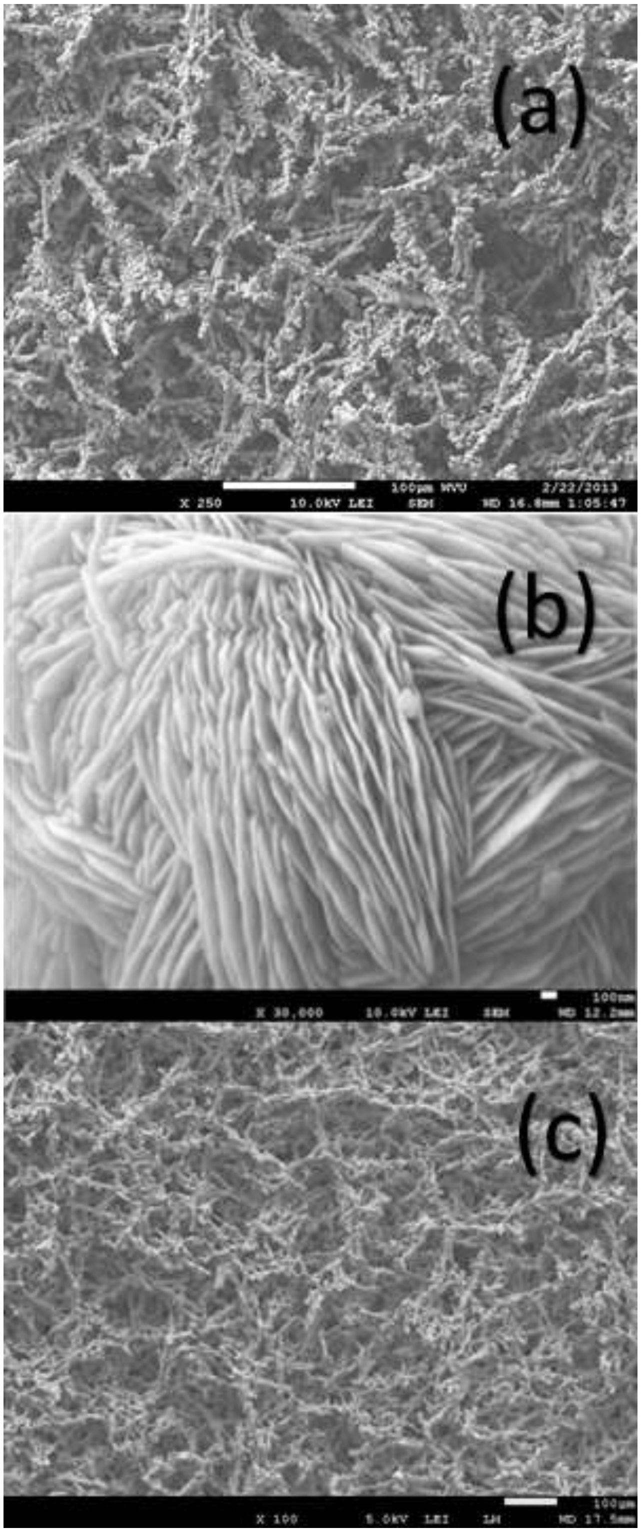

Figure 92 : (a-b) As-synthesized $SrMoO_4$ nanoflowers growth over MgO nanorods ($SrMoO_4$/MgO) low and high magnification **(c)** after 5 h at 1000°C heat treatment**.**

$SrMoO_4$/MgO was tested against exposure of H_2S, SO_2, H_2 and CO on the previously described sensing platform. The H_2S testing was completed at the facilities of the commercial partner (NexTech Materials, Ltd., Lewis Center, OH, USA) with the same testing parameters described in the section 5.3.4. Figure 93 shows the testing results of $SrMoO_4$/MgO for SO_2 at 600, 800 and 1000°C. $SrMoO_4$/MgO engineered material unexpectedly showed very low sensitivity toward SO_2 at all of the testing temperatures. Further tests were conducted over different sensors of same material and similar results were obtained. The reasons behind the $SrMoO_4$/MgO`s different selectivity against SO_2 was the subject of intensive investigation by utilizing various advanced characterization methods, which included TEM, Raman, XPS-UPS, TPR and mass spectroscopy. This work was completed in order to better understand whether or not Mg incorporation into the parent compound lattice and caused changes in the electronic properties of the $SrMoO_4$. These changes would include the band-gap/work function (Φ), density of states in the band-gap and/or MgO target surface/gas interactions that also may change the characteristics of the sensor output.

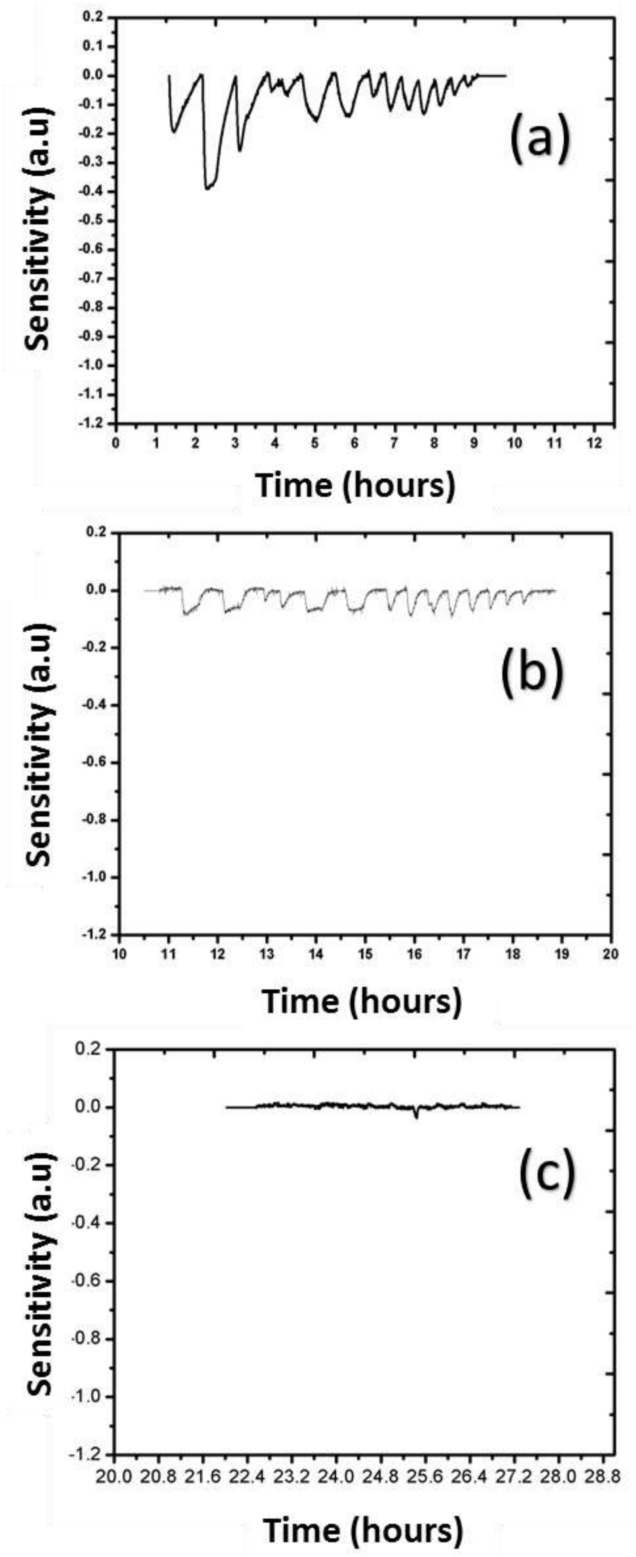

Figure 93 : Sensor signal of $SrMoO_4$/MgO core structure in response to different levels of SO_2 with different time of exposure **(a)** 600°C **(b)** 800°C **(c)** 1000°C.

Figure 94 shows the CO cross-sensitivity tests of the $SrMoO_4$/MgO at three different temperature regimes (600, 800 and 1000°C). In this case, the results are not drawn in sensitivity scale since the material did not show any reasonable sensor response to target gas (CO). Therefore, the y-axes in those graphs are drawn in resistance values (Ohms). This behavior of material was already estimated due to $SrMoO_4$`s preliminary tests. As can clearly be seen from the graphs, the compound did not sense the CO at all temperatures.

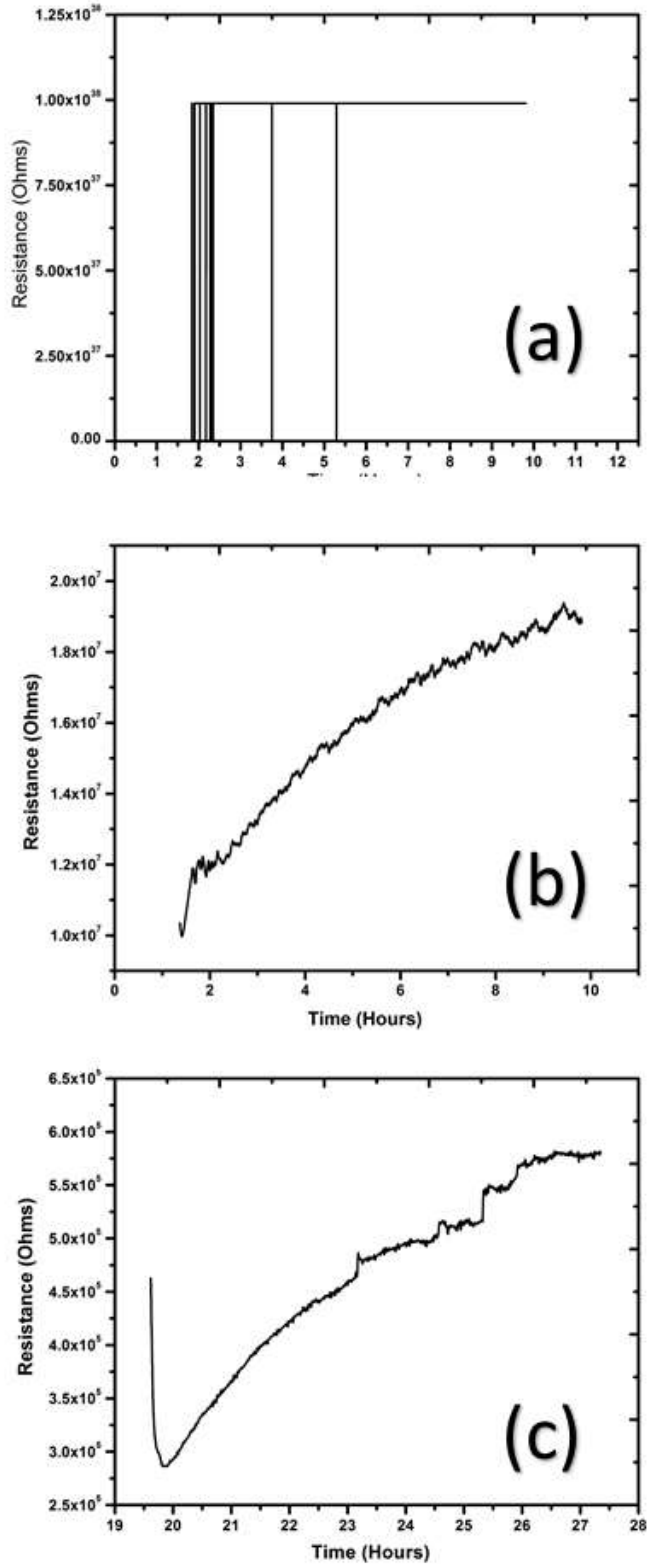

Figure 94 : Sensor signal of $SrMoO_4$ /MgO core structure in response to different levels of CO at **(a)** 800°C and **(b)** 1000°C.

Figure 95 shows the H_2 cross-sensitivity tests of the $SrMoO_4$/MgO at three different temperature regimes 600, 800 and 1000°C in accordance to testing procedure given in Figure 64 and Figure 65. The $SrMoO_4$/MgO sensor did not give any output signal and electrically not conductive at 600°C. The material unexpectedly showed a very good sensing behavior against H_2 at 800 and 1000°C. The opposite occurred for the $SrMoO_4$ nano-flowers structure. At especially 1000°C, almost 85% change in resistance was observed and the sensor showed similar behavior even after 5 successive tests that covered almost 150 hours of operation at 1000°C. Again, the different sensors were tested and similar sensing capabilities observed for this material and target gas composition.

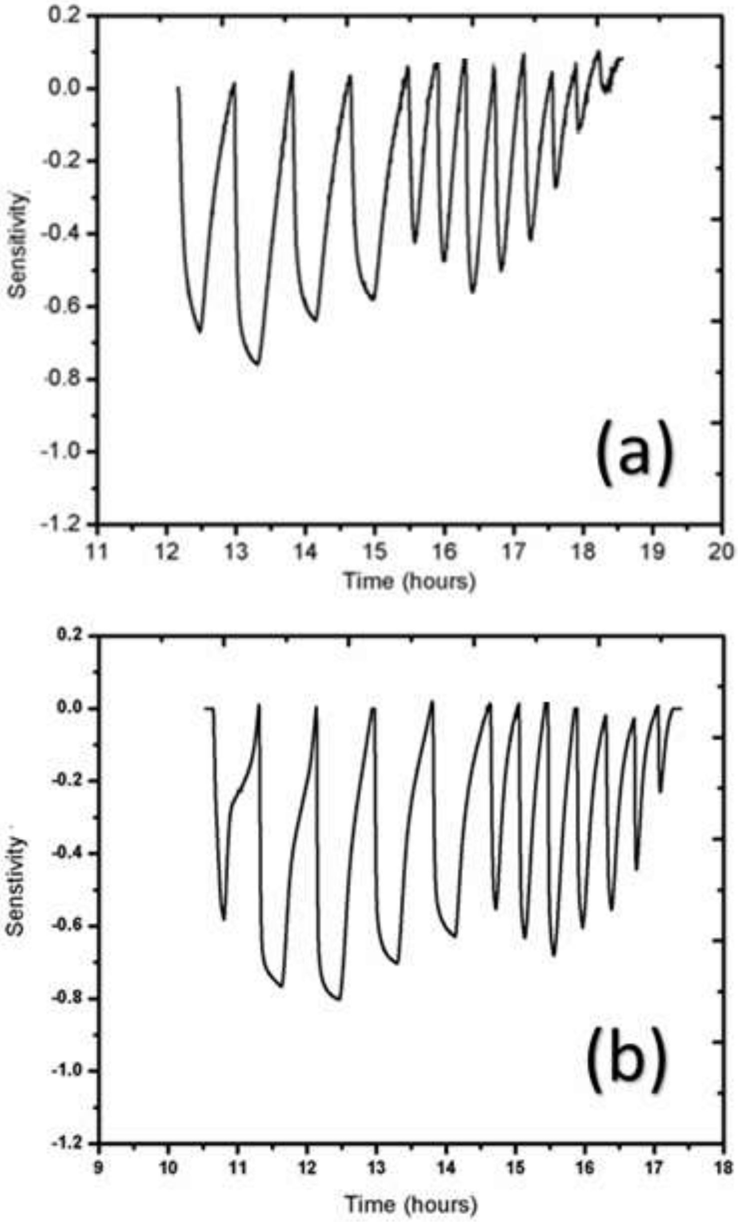

Figure 95 : Sensor signal of $SrMoO_4$/MgO core structure in response to different levels of H_2 with different time of exposure **(a)** 800°C **(b)** 1000°C at 1% O_2 partial pressure.

As a first step in order to explain the difference in sensing behavior of the materials ($SrMoO_4$ nano and $SrMoO_4$/MgO), the MgO core structure itself was extensively characterized by Raman, XRD, XPS, TPR and SEM-EDS. It is known that MgO nanorods are stable at the temperature regime of interest; however, they are not stable during wet chemical processing. In order to synthesize the $SrMoO_4$ nano-flowers via hydrothermal method, the pH must be adjusted to ~7-8 and at that pH surface of the MgO core structure fist starts to amorphousization and dissolve to the solution at the same time leaving behind a precipitation area for MoO_4^{2-} and Sr^{2+} ions.

Figure 96-a and-b shows the as-deposited state of the nano/micro rods. The as-deposited state of the powders showed very good level of crystallinity (XRD spectrum not included showed single phased highly crystallized material). Figure 96-c shows the Raman spectrum of the MgO after treating at the desired level of pH ~8. The Raman spectrum of the crystallized MgO should have a peak around 3600 cm^{1-}. However, the treated sample did not possess that vibrational mode, or indeed, any vibrational modes. This clearly shows that material lost the crystallinity not from surface, but also at least 1 µm depth, which is typical penetration depth of the utilized laser during measurement. Figure 96-d and –e show the morphological evolution of the powders during the pH treatment that mimics the synthesis conditions. After observing this morphological alteration during deposition, it was decided to conduct further analysis over this core structure and $SrMoO_4$/MgO particles alone in order to help clarify the material composition, electronic and chemical structure. These areas are thought to all contribute to the changed sensing behavior of the compounds against H_2 and SO_2 exposure. Most of the attention was focused on the difference between the $SrMoO_4$ nano-flowers and $SrMoO_4$/MgO structure through extensive characterization for chemical, electronic, structural and phase analysis of aforementioned materials by means of X-ray photoelectron spectroscopy (XPS), Raman, ultraviolet photoelectron spectroscopy (UPS) and ultraviolet-visible light absorption spectrum (Uv-Vis), temperature programmed reduction (TPR) and atomic absorption spectrum (AAS).

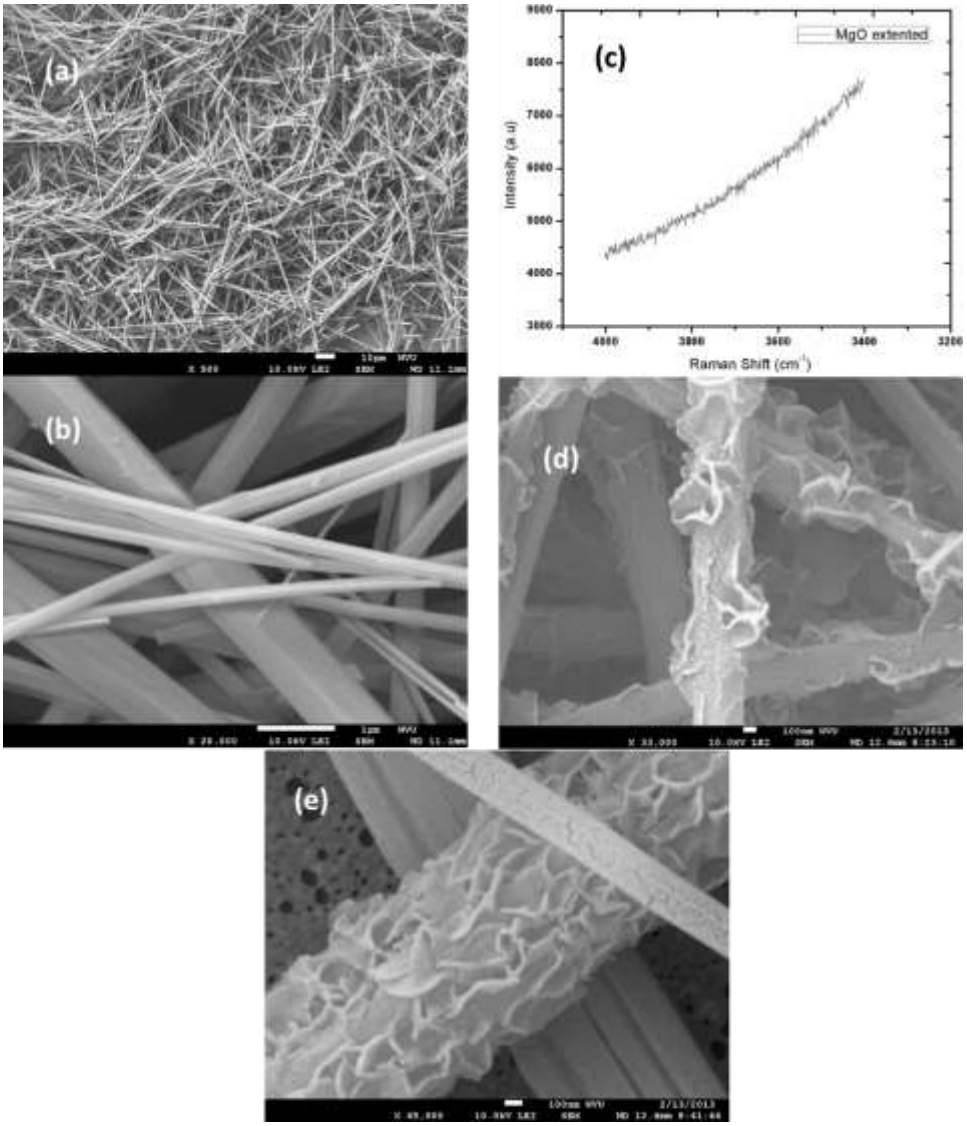

Figure 96 : (a-b) As-synthesized MgO core structure **(c)** Raman spectrum of pH 8 treated MgO **(d)** SEM image of pH 8 treated MgO **(e)** higher magnification of pH 8 treated MgO**.**

The TPR technique is used to characterize the reduction behavior of the oxides as well as catalytic activity of the surfaces toward H_2. Kubo et *al.* conducted TPR analysis for scheelite $SrMoO_4$ and perovskite $SrMoO_3$ in the 25-800°C temperature window with 10% H_2/Ar gas mixture. Authors concluded that reduction of $SrMoO_4$ to $SrMoO_3$ starts at 650°C under hydrogen flow without any oxygen background. In the same study it was also reported $BaMoO_4$ and $SrMoO_4$ have two H_2 consumption peaks located around 600 and 725°C, however $SrMoO_4$`s $H_2$ consumption was almost twice as much as $BaMoO_4$`s H_2 consumption. Authors also concluded over the stability of the $SrMoO_4$ and $SrMoO_3$ by taking TG profiles of them. $SrMoO_3$ weight gain started around 300C until

725°C, after this point there was no further weight gain. And it was confirmed with calculations that $SrMoO_3$ transformed in to $SrMoO_4$ [198, 205]. In this work, the technique was utilized in order to shed light over different H_2 adsorption/consumption behavior of the $SrMoO_4$-nano and $SrMoO_4$/MgO. Figure 97 shows the measurements results of the $SrMoO_4$-nano and $SrMoO_4$/MgO. The temperature increased from room temperature to 900°C with the 5°C/min heating rate. As can be seen from the Figure 97-a $SrMoO_4$-nano showed two consumption peaks. They were located at 580 and 825°C. Those values were close to reported in the Kubo et *al.`s* work, however it should be noted that firs adsorption occurs at around 25°C lower than that of the reported value in Kubo et *al.*`s work [198], however the second absorption peak located around 125°C higher compare to their work. Figure 97-b provide the result of the TPR measurement of $SrMoO_4$/MgO. As seen in the figure it showed totally different absorption/consumption behavior in terms of peak position, number and intensity. First of all $SrMoO_4$/MgO showed a sole maxima around 540°C and the signal output which is proportional to the consumption of H_2 was almost 10 times of $SrMoO_4$-nano. This difference in H_2 consumption could axiomatically attributed to incorporation of MgO into the $SrMoO_4$-nano lattice as well as surface and modify the electronic and catalytic behavior of the compound.

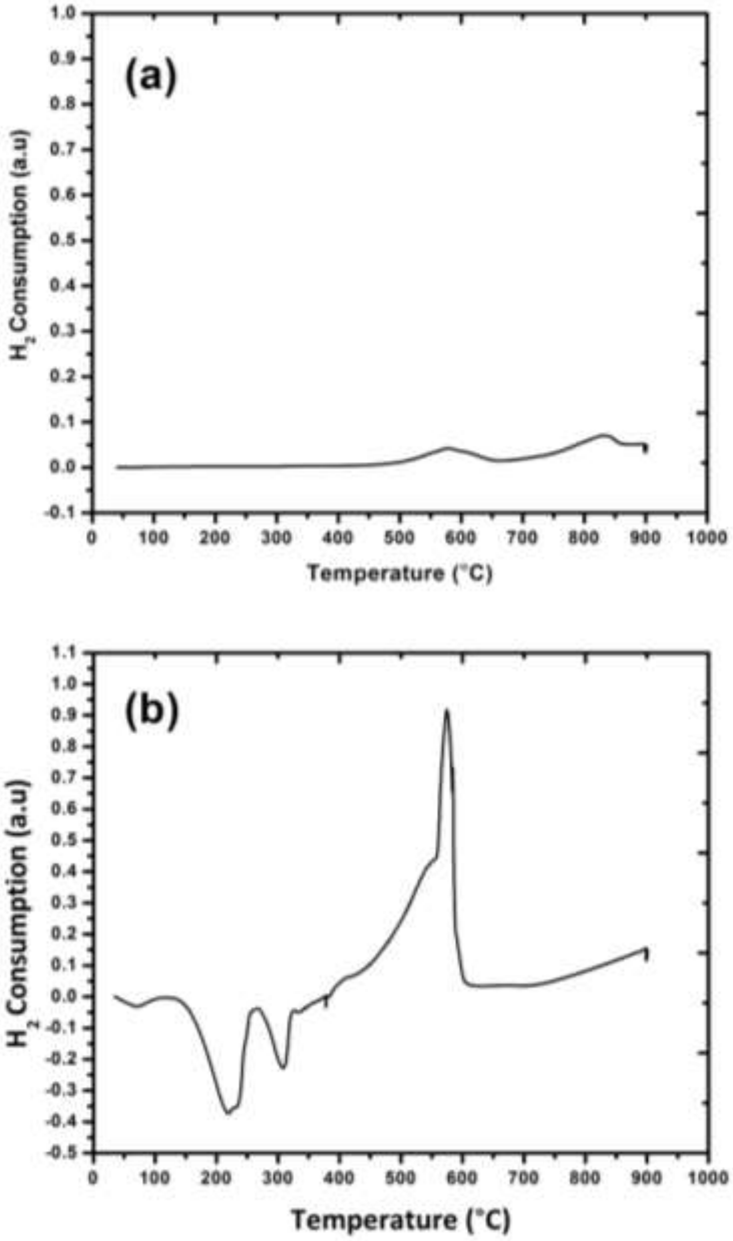

Figure 97 : TPR measurements of $SrMoO_4$-nano **(a)** and $SrMoO_4$/MgO **(b)** heating rate 5C°/min.

In order to shed light over the difference in sensing behavior of the aforementioned compounds, the first step was to quantify the mount of Mg that was incorporated into the $SrMoO_4$ nanoflowers ($SrMoO_4$/MgO) by atomic absorption spectrum (AAS). Before AAS examination of the $SrMoO_4$/MgO material, XRD analysis was conducted, however it was not possible to determine the MgO. The AAS technique is known for its high certainty for the quantitative determination of chemical elements by employing the absorption and subsequent emission of visible light despite lacking of providing information regarding to chemical, structural and electronic structure of the material of interest. According to AAS analysis of the $SrMoO_4$/MgO, the material contained 3.1% (atomic unit) Mg. After calculation of the atomic concentration of the Mg incorporation into $SrMoO_4$ matrix, it was focused on the chemical and electronic aspect of the integration**.** For this purpose, as well as determination of the chemical state condition of supposedly remaining core structure, the compositional depth profiling maps of the synthesized material were obtained via XPS and are presented in Figure 98. The thickness of the depletion layer is shown in Eq. 2.10, which corresponds to approximately 10 nm, which makes photoelectron spectroscopy (XPS) very useful technique.

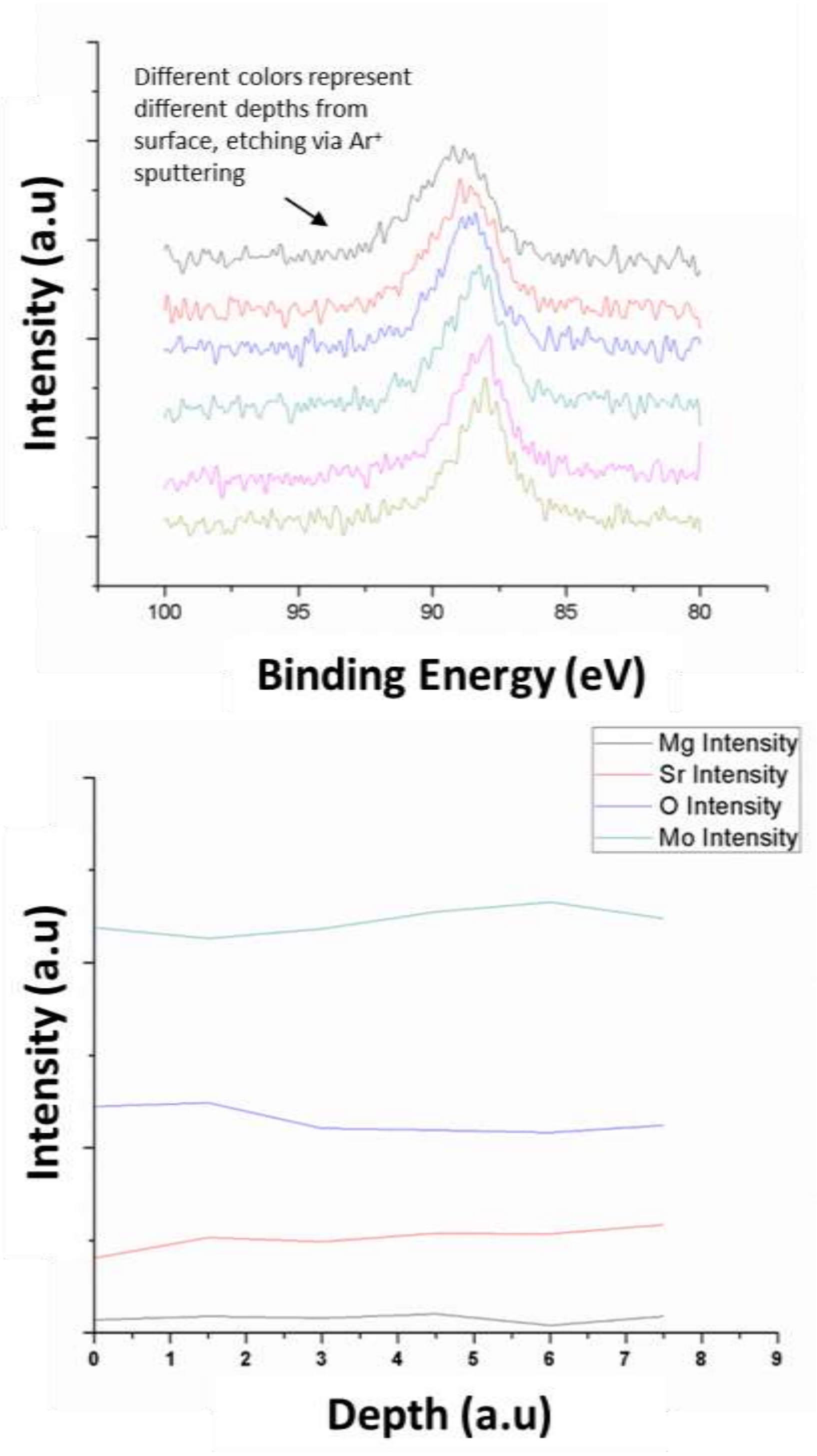

Figure 98: (a) Mg 2p photo-electron line at different depths **(b)** concentration of the Mo, O, Mg and Sr thorough the $SrMoO_4$/MgO template growth structure.

Figure 98-a represents the chemical state of the Mg throughout the different depths of the as-synthesized $SrMoO_4$/MgO structure. As can be observed form the graph, Mg changes its chemical state through the depth profile. At the surface of the as-synthesized powder, the material contained Mg in two different compounds (MgO and $Mg(OH)_2$). As the analysis depth increased, a shift in the main photoelectron line occurred towards lower binding energy. This shift can be attributed to the decrease in the amount of $Mg(OH)_2$ and the increase in MgO phases. Another point to mention is that despite the fact that the $Mg(OH)_2$ phase diminished, a shoulder on the high energy binding site still existed. The deconvolution of the peak fits very well to the reported binding values of the Mg in the SMM ($SrMgMoO_{6-\delta}$). It could be argued that the binding energy of the Mg in $SrMoO_4$ and SMM would be different; however, it should be noted that Mo has the decisive effect on the chemical environment of the compound. The most important result of the XPS analysis is shown in Figure 98-b. The figure provides atomic concentrations of the Sr, Mg, O and Mo in different colors through the depth of the as-synthesized material. A significant change in the concentration of the aforementioned elements was not observed. In other words, (as expected) the core structure of the MgO was totally lost, with it forming a secondary phase (MgO and/or $Mg(OH)_2$ or it going into the $SrMoO_4$ lattice as a substitutional solid solution formation discussed above. While the latter was the focus of the Raman investigation, in order to further confirm and determine the amount of the phase precisely. Yet, it should be noted that substitution of Mg with Sr is not likely due to different size of these cations and $MgMoO_4$ as discussed previously has different crystal structure than that of $SrMoO_4$. Figure 99 shows the Raman spectra of the micron, nano, templated and SMM powders, respectively. The Raman technique is sensitive to vibrational modes [206, 207] which can be altered by changes in bond lengths and coordination geometries in the crystal structure, allowing it to characterize any substitutional solid solution formation, such as $SrMg_xMo_{1-x}O_4$ and/or Mg incorporation into the $SrMoO_4$ lattice. This substation would cause the peak to broaden, as observed in the Raman data of the SMM ($SrMgMoO_{6-\delta}$) powder. Raman is capable of detecting down to 0.5% substitution in $SrMoO_4$ lattice as main peaks get broad; however, this was not observed in the case of $SrMoO_4$/MgO powder. It should be considered that Raman is not a surface sensitive technique, therefore presented results represent the bulk of the material. In the case of substitutional solution formation, the corresponding amount of it would be less than 0.5%.

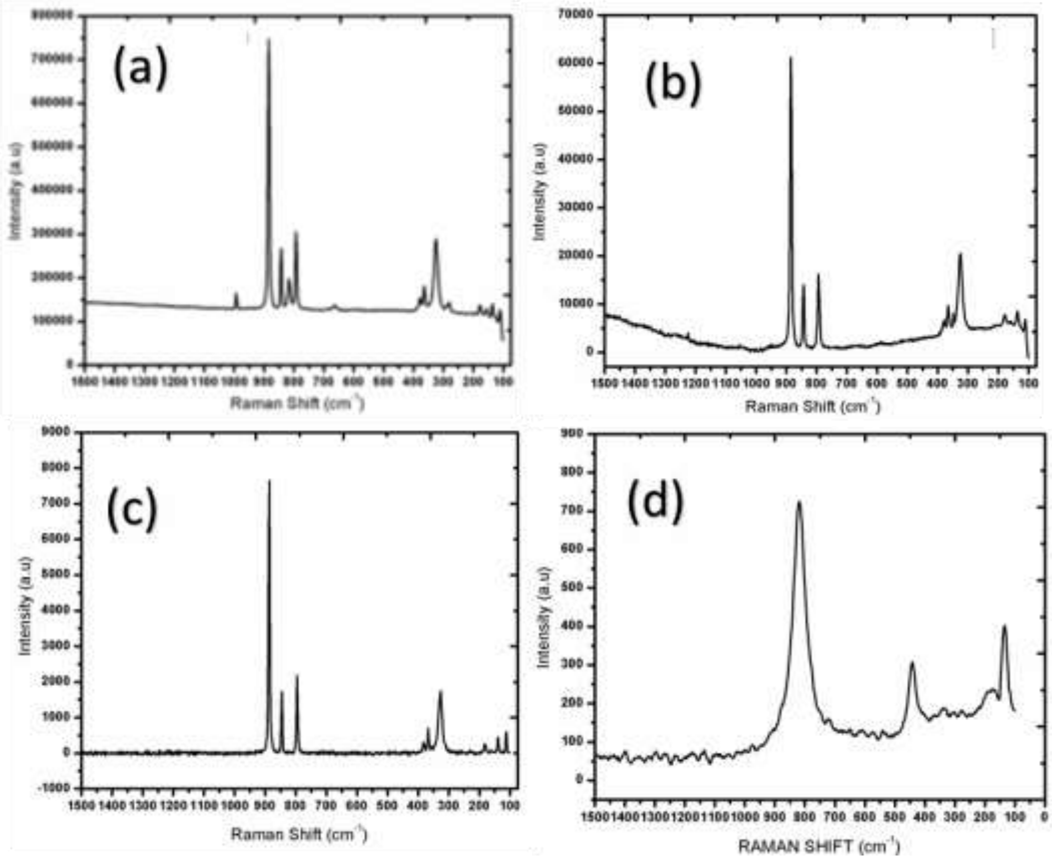

Figure 99: Raman spectrum of the as-synthesized **(a)** $SrMoO_4$-micron **(b)** $SrMoO_4$-nano **(c)** $SrMoO_4/MgO$ **(d)** SMM powders.

Other important consequences of Mg incorporation can be observed in electronic aspects; therefore, the work function and band-gap measurements were conducted via ultraviolet photoelectron spectroscopy (UPS) and ultraviolet-visible light absorption spectrum (Uv-Vis), respectively.

The surface of the sensing material ($SrMoO_4$-nano and $SrMoO_4/MgO$) engages in charge exchange (e^-) with the absorbed and/or approaching gaseous material. Charge exchange between the solid surface and absorbed species depends on the solid surfaces`s work function, which further depends on chemical environment, defect structure, vacancy concentration and cation oxidation state. In order to explain observed reduction in the band gap in $SrMoO_4$ nano compare to $SrMoO_4$+MgO work functions were determined. Average cation oxidation state proportional to work function (ϕ_m). In other words, oxygen deficiency is disproportional to work function (ϕ_m). Work-function measurements showed that the measured values for the nano-$SrMoO_4$, $SrMoO_4$-micron and

$SrMoO_4$/MgO are 9.3, 8.2 and 7.7 eV, respectively. Regarding the band gap, possible Mg will change the band gap and will create defects related to the bands in the main gap. Figure 100 shows the band-gap measurements of the micron-$SrMoO_4$, nano-$SrMoO_4$ and $SrMoO_4$/MgO. Oxygen deficiency (δ) in $SrMoO_4$/MgO is higher in comparison $SrMoO_4$ nano [8]. XPS analysis was conducted on the as-synthesized on the surface of $SrMoO_4$/MgO powder. It was concluded that 17% of the O^{2-} was located on unlattice (interstitial) locations. This is also further supports the lower working value measured in the case of $SrMoO_4$/MgO.

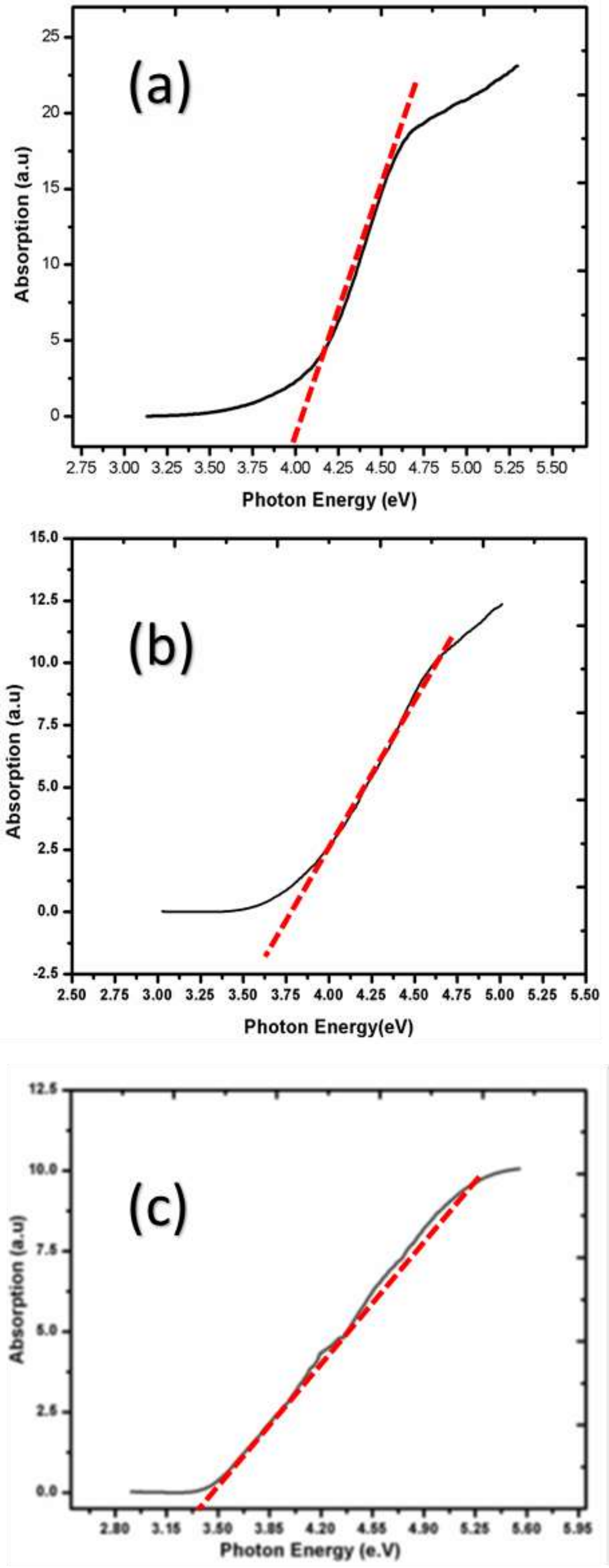

Figure 100: Band-gap measurements of **(a)** $SrMoO_4$-micron **(b)** $SrMoO_4$-nano **(c)** $SrMoO_4$/MgO.

The measured values for the band-gaps are 3.9, 3.6 and 3.2 eV for abovementioned compounds, respectively. The band-gap values for the micron- and nano-sized powder are in a good match with literature [184, 176]. Vidya et *al.* synthesized nano $SrMoO_4$ with the average crystalline size 20 nm by modified combustion process and reported 3.7 eV for optical band-gap of the compound [208]. The reason for the reduction in band-gap value of $SrMoO_4$/MgO compared to that of nano-$SrMoO_4$ can be axiomatically attributed to two reasons. One reason is that Mo atoms may be missing from the $SrMoO_4$ during the deposition process and/or reduction in the un-lattice (interstitial) oxygen sites. The substitution of Mg into Mo would result in opposite effect regarding to the band-gap height. It is known that quantum confinement and structural disorder and stress results in a decrease in the band gap, which may explain the decrease in the band gap $SrMoO_4$-nano compare to $SrMoO_4$-micron [180]. However it should be noted that the band gap value (3.9 eV) determined for micron size $SrMoO_4$ powder may not reflect the real optical band gap of the compound due to secondary SrO phase formation which was determined by XRD and further confirmed by Raman spectrum.

Beside the chemical and electronic effect of the Mg incorporation into $SrMoO_4$, the structural formation of the secondary phase on the surface has an important consequences regarding to the catalytic action of the MgO against H_2. Incorporation of Mg into the $SrMoO_4$ is shown and quantified by AAS and further proved by XPS. The unexpected sensing behavior of the $SrMoO_4$/MgO can be attributed to modification of the electronic/chemical structure and catalytic effect of the Mg, as was detected by XPS on the surface of $SrMoO_4$/MgO. The difference in the electronic structure of the nano-$SrMoO_4$ and $SrMoO_4$/MgO was observed both in band-gap and work function values. Incorporation of MgO into $SrMoO_4$, as well as a secondary phase and/or surface layer, are both possible as describe by the above characterization. As small as <0.5% substituted into the structure may have occurred, as is the detection limitation o Raman technique. In order to have better understanding over sensing mechanism, the exactly same amount of MgO that was determined by AAS and XPS was incorporated into $SrMoO_4$ nanoflowers by mechanically mixing and stirring. The first and second tests of the mechanical mix are presented in Figure 101-a and-b, respectively. As seen from the graphs, mechanical mixing does not permit the sensing of SO_2 at 1000°C as its templated counterpart ($SrMoO_4$/MgO) does not either at 1% O_2.

In summary, there are two Schottky barriers in sensor, first between the grains and the second one is located between sensing material and Pt (platinum) electrode due to work function difference of Pt and sensing material. Pt is known to behave like Schottky contacts rather than Ohmic at high temperature [209]. Work function of Pt is 5.7 eV [210], basically it becomes decisive at high temperature due to its barrier effect for flowing electrons. Less the difference more the electron flow. In other words the high sensor signal output. Lower work function the SrMoO4/MgO (7.6 eV) in comparison to the $SrMoO_4$ Nano (9.3 eV) increases its sensitivity, apart from its catalytic action against H_2 and lower band gap, porous micro-structure as well.

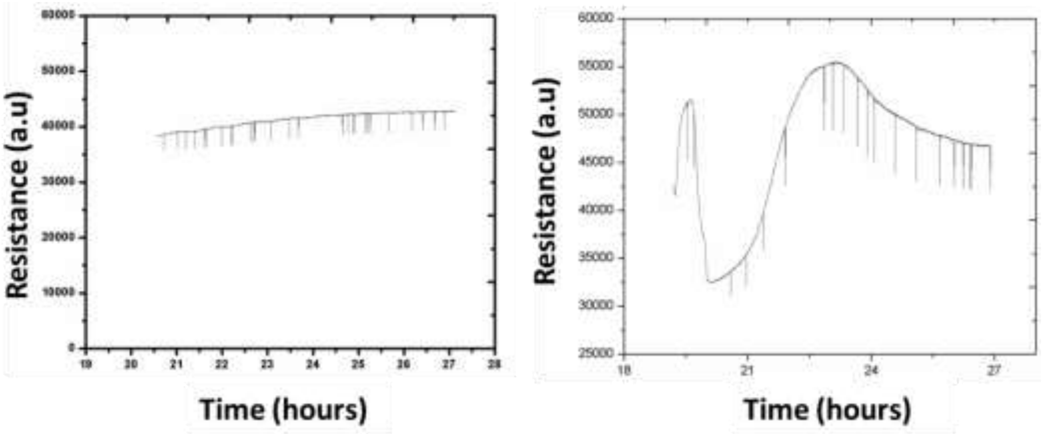

Figure 101 : $SrMoO_4$ and MgO mechanically mixed and tested for SO_2 at 1000°C under 1%O_2 partial pressure **(a)** first **(b)** second repeat.

$SrMoO_4$/MgO growth introduced O^{2-} intersitials all the way through the material so this also has positive effect over H_2 sensing together with its porous structure (see Figure 92) and the MgO catalysis effect. As the $SrMoO_4$ crystallized during autoclave procedure and MgO dissolves and forms $Mg(OH)_2$ during this oxygen can be trapped in the relatively large scheelite structure. Despite the ccp cation packing in the tetragonal scheelite due to corner sharing and isolation of the B site cation tetrahedra, the tetragonal structure has relatively lower packing density and further compressible to orthorhombic and monoclinic phases [211, 158, 155]. In addition to this, octahedral interstitials are not occupied in the tetragonal scheelite [155]. At this point it should be noted that scheelite structure has more prone to formation of interstitial oxygen as well as transportation of oxygen vacancy while the former is not likely in perovskite structure (ABO_3) [212]. This discussion supports the XPS data showed that up to 17% of the O^{2-} was located on unlattice (interstitial) locations. However it is not clear the reason behind formation of high amount of interstitial oxygen in $SrMoO_4$-

nano in comparison to $SrMoO_4/MgO$. Both the work function and band gap measurements showed that MgO incorporation into $SrMoO_4$-nanolattice affected the both amount of interstitials oxygen as well as cation oxidation state.

The reason behind this insensitivity toward SO_2 is that the stable compound formation between Mg and S. After the formation of metastable MgS phase fomation on the surface; it reacts with oxygen to form the corresponding sulfate ($MgSO_4$), and/or $MgSO_4$ can form from, MgO, SO_2 and O_2. $MgSO_4$ is impermeable to further SO_2 diffusion and that is the reason behind insentisivty of the $SrMoO_4/MgO$ toward SO_2 [213]. Compound formation between Mg and S are well reported in literature for MgO with the increasing temperature beyond the 500°C. Above this temperature, the surface sulfur starts to accumulate in the form of $MgSO_4$ and /or MgS. It was also reported by Lee *et al.* that the exposure of MgO to SO_2, in order to promote SO_2 transformation to SO_3, the formation of a very stable compound of Mg and S was formed ($MgSO_4$) and even could not even removed from surface during regenerative cracking conditions [214]. The same authors also reported that SO_2 exposed MgO could not recover after 500°C [63].

The XPS spectrum $SrMoO_4/MgO$ sensor material after testing to SO_2 and cooled down to room temperature (under constant N_2 flow) is presented in Figure 102. As seen in the graph presented, the sulfur (S) was detected on the surface in the form of $MgSO_4$ and to small extent MgS (Figure 102-a). The binding energies of sulfur in $MgSO_4$ and MgS are 168.9 and 165.0 eV, respectively. The values are in an excellent match with the literature [215]. The further examination conducted over the O peak position in order to confirm the sulfate and/or sulfide formations. The Figure 102-b shows that the oxygen XPS spectrum taken from the SO_2 tested sample surface. Sugiyama et *al.* also reported the O^{2-} peak position in magnesium sulfate ($MgSO_4$) and reported that the value is 532.3 eV, which is higher than ordinary peak position of the O found in oxides.

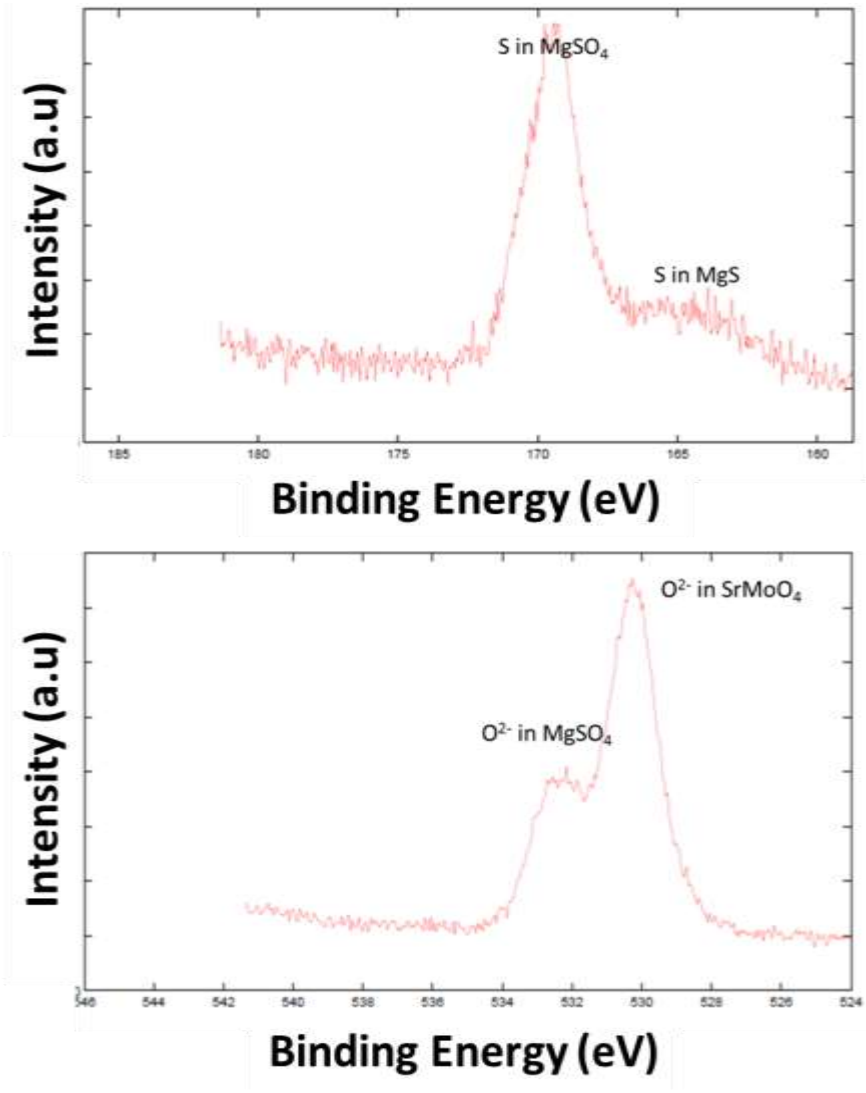

Figure 102 : XPS analysis of S **(a)** and O 2p **(b)** positions from full scale SO_2 tested $SrMoO_4$/MgO sensor.

The (111) surface of MgO is particularly reactive to H_2. The unique catalytic properties of the defective MgO surfaces also depend on steps, kinks, and point defects (ion vacancies and substitutions). On the (100) MgO surface, H_2 has a small adsorption energy and does not dissociate [216, 217]. In order to explain the excellent sensing properties of $SrMoO_4$/MgO against H_2, the mechanical mixture of $SrMoO_4$ and MgO was further tested for H_2, and the resulting sensitivity graph is given in Figure 103. The figure shows better response than SMM, but worse than $SrMoO_4$/MgO. So, the catalytic activity of the Mg is important but also electronic modification of the Mg created on the surface of the nano-$SrMoO_4$ is also important. The differences can be observed by the work function and band gap, as well as, the highly porous structure of $SrMoO_4$/MgO makes the difference compared to nano-$SrMoO_4$ and MgO mechanical mixture.

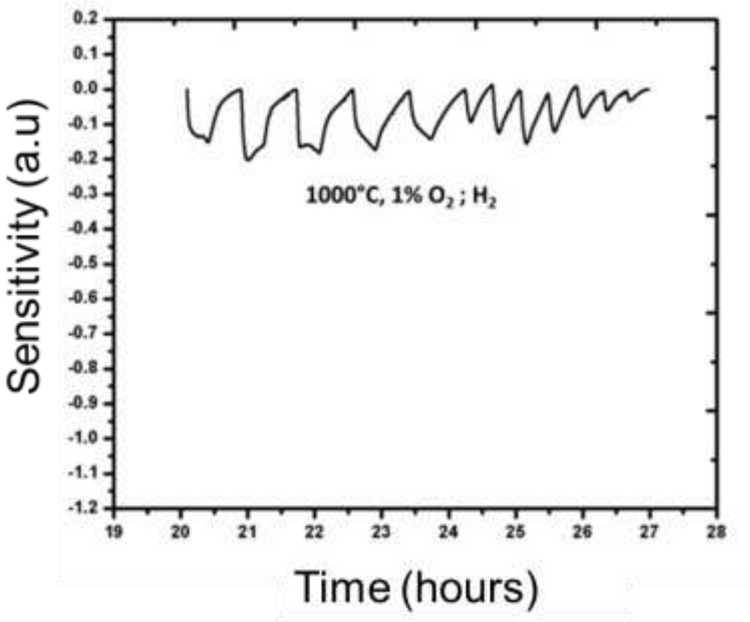

Figure 103 : $SrMoO_4$ and MgO mechanically mixed and tested for H_2.

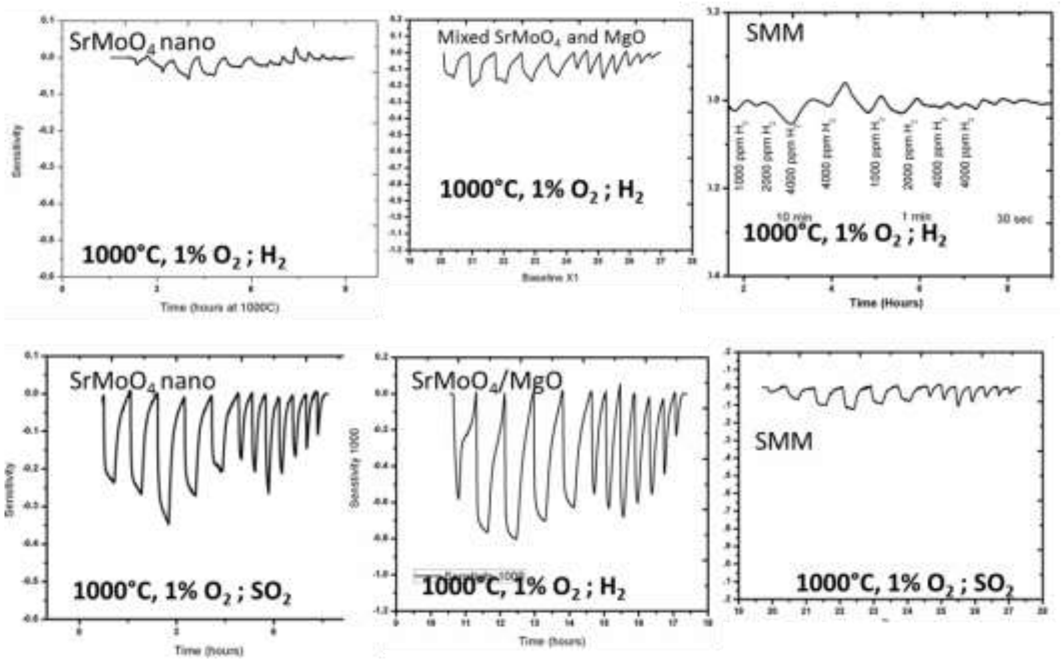

Figure 104 : Summary of the sensing capabilities of different compounds towards SO_2 and H_2 at 1000°C under 1%O_2.

5.4 Surface diffusive kinetics of SO_2 over $SrMoO_4$ nanoflowers

Model regarding the surface interaction kinetics of SO_2 with $SrMoO_4$ nanoflowers was developed over the measurements taken at 1000°C for $SrMoO_4$ nanoflowers tested against 500, 1000 and 2000 ppm concentrations of SO_2, at three different partial pressure of 1,5 and 20% O_2. The interaction kinetics model used considers the interaction of adsorbed of SO_2 with defect, vacancy, electronically modified interstitial sites, lattice oxygen on the surface of sensing element, $SrMoO_4$ nanoflowers. This phenomenon will be called surface adsorption and/or etching like interaction. It is anticipated that once an active site (vacancy, electronically modified interstitial sites, lattice oxygen) is occupied/consumed by SO_2, it is not available for other SO_2 molecules, until the final product of this interaction, SO_3 is released from the occupied location. The sites that are exposed to SO_2 do not form any type of compound with the cations and/or remain on the surface, it was assumed the final product, SO_3 release from the surface immediately in accordance with the literature findings.

The electrical conductivity relaxation (ECR) technique was utilized in order to characterization of the SO_2 - $SrMoO_4$ nanoflowers surface interactions. In this technique (ECR), a change in the electrical conductivity of a sample is recorded as the ambient oxygen concentration is gradually changed in order to determine the oxygen surface exchange (k, mass transfer coefficient) and bulk diffusion coefficients (D) of oxygen over designated surface, as well as correlation between conductivity and non-stoichiometry of the oxide material is established. Σ and δ show the electrical conductivity and oxygen non- stoichiometry, respectively. Σ (0), σ (∞) and σ (t) are conductivities and correspond to δ(0), δ(∞) and δ(t), respectively and since the non-stoichiometry (δ), interstitial sites occupancy by oxygen and chemi and/or physic adsorbed oxygen can be counted as concentration on the surface. From this point it also can be established and correlate that, consumption of abovementioned oxygen during interaction with the approaching SO_2 molecules will change conductivity and this can be correlated to SO_2-$SrMoO_4$ nano material surface interactions: in this case C(0), C(∞) and C(t) will represent the conductivities corresponding to σ(0), σ(∞) and σ(t), respectively. Based on this boundary condition and Fick's second law given in Eq. 5.1 can be solved in order to obtain solution for the k_{chem} and D_{chem} for SO_2 over $SrMoO_4$ nanoflowers` surface. It should be noteworthy to indicate that there has been no reports application of numerical approach in order to solve Fick`s second law for electrical conductivity relaxation. Three dimensional fitting according solution used in the literature developed by I. Yasuda`s, the analytic solution that is published in early 1990s is given in Eq. 5.2, 5.3 and 5.4 [218, 219, 220].

$$\frac{\partial \theta_i}{\partial t} = D_\theta \frac{\partial^2 \theta_i}{\partial z^2} + \omega_{\theta_i}$$

(Eq. 5.1)

Gardner at the University of Warwick in U.K. stated that semiconducting metal oxide sensor response is predominantly limited by diffusion and suggested that improvements in the sensor field would be achieved by modifying the film properties such as porosity and indeed indicated underlying chemical kinetics would not provide a path for progress. Considering a porous semiconducting thick film into which as gas diffuses slowly and can be rapidly immobilized at surface sites with the assumption semiconducting layer is macroscopically homogeneous [221]. Figure 105 presents H_2 gas testing results of the $SrMoO_4$/MgO at 1000°C for three different O_2 partial pressures. In order to develop a model, it must be known whether or not material change its resistance via ionic conduction in addition to its natural electron conduction. It can be seen from the graphs change in the oxygen partial pressure did not affect sensitivity more than 0.5%.

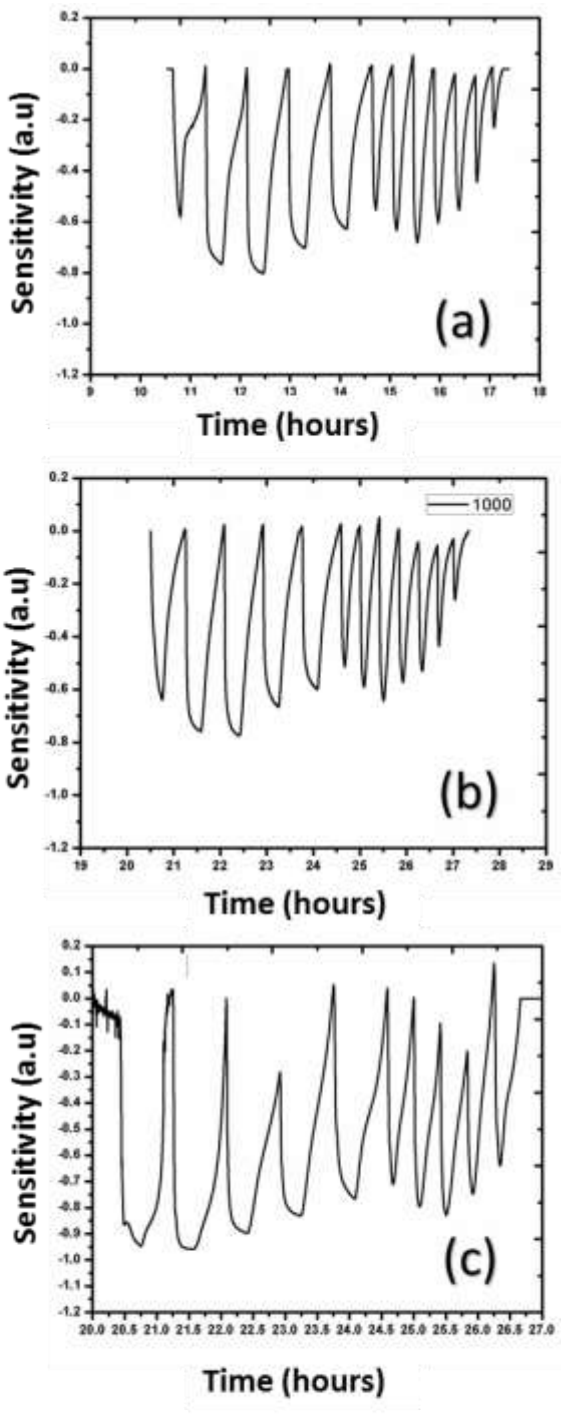

Figure 105 : Sensor signal of $SrMoO_4$ nano-flowers decorated over MgO core structure in response to different levels of H_2 with different time of exposure at 1000°C under **(a)** 1**(b)** 5 **(c)** 20% O_2 partial pressure.

The same (oxygen partial pressure dependence) valid for $SrMoO_4$ nano`s SO_2 sensitivity, oxygen partial pressure independency is important, negligible ionic conductance. ECR is generally used to determine the oxygen surface exchange coefficient (mass transfer coefficient), k_{chem} and bulk diffusion coefficient, D_{chem} of mixed oxygen anion and electronic conductors.

As shown in the Figure 105 the material tested did not change its sensing response type (pure n-type, electron conduction) it was decided on the deconvolution the data two regions, as described in the conductivity graphs presented in Figure 106, Figure 107 and Figure 108 and precisely calculate the D_{chem} and $k_{chem.}$ D_{chem} and K_{chem} values are good match with literature with discrete approach. The rate determining reaction in the sequence determined by many is the chemical interaction of the reducing gas and the chemisorbed oxygen which is followed by thermal adsorption of the final compound from surface otherwise is defined as poisoning of the surface. For each different concentration of the SO_2 continuous and discrete approached utilize and aforementioned constants extracted. The following assumptions are made in order to proceed to calculate D_{chem} and K_{chem} values of SO_2 over $SrMoO_4$ nanoflowers. SO_2 is a bidentate molecule, with a permanent dipole moment, which can interact in several different ways with the surface of an ionic crystal like. The five assumptions are made in order to develop the model are given below [64] [65] [66] [84].

- Not considerable SO_3 formation in the test chamber volume between background O_2 and SO_2.
- No adsorption of SO_3 at 1000°C.
- Not considerable SO_4 formation.
- Surface interaction is diffusion like process, amount of interstitials are determined by XPS, and the first part of interacting is etching-like process.
- Second part is diffusion related.

Figure 106, Figure 107 and Figure 108 show the extracted D_{chem} and K_{chem} values for 500, 1000 and 2000 ppm of SO_2 over $SrMoO_4$ nano. In discrete approach as can be seen at first part sudden increase in the conductivity is related to pure surface interaction of the approaching SO_2 molecules and interstitial and/or chemically physically adsorbed oxygen. The second side of the given graphs, the conductivity increase is related to diffusion of the SO_2 and its interaction with the lattice oxygen.

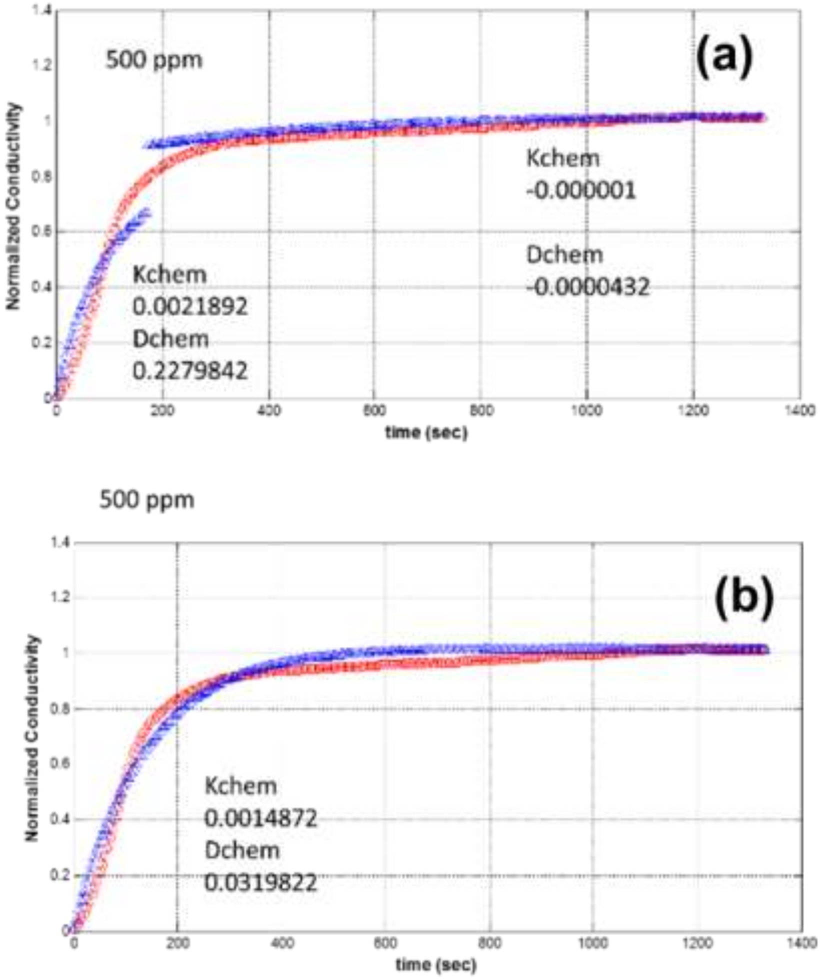

Figure 106 : 500 ppm SO_2 **(a)** discrete **(b)** continuous approaches.

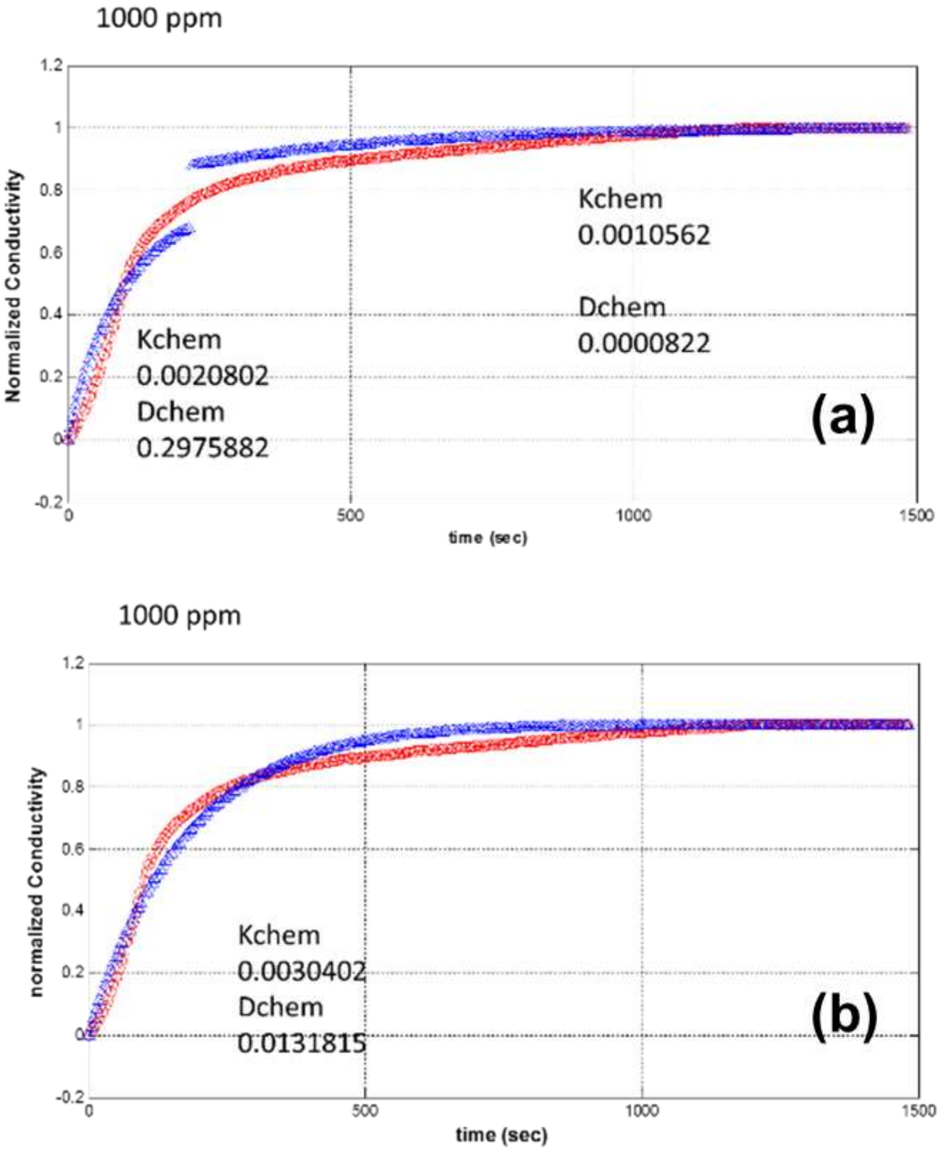

Figure 107 : 1000 ppm SO_2 **(a)** discrete **(b)** continuous approaches.

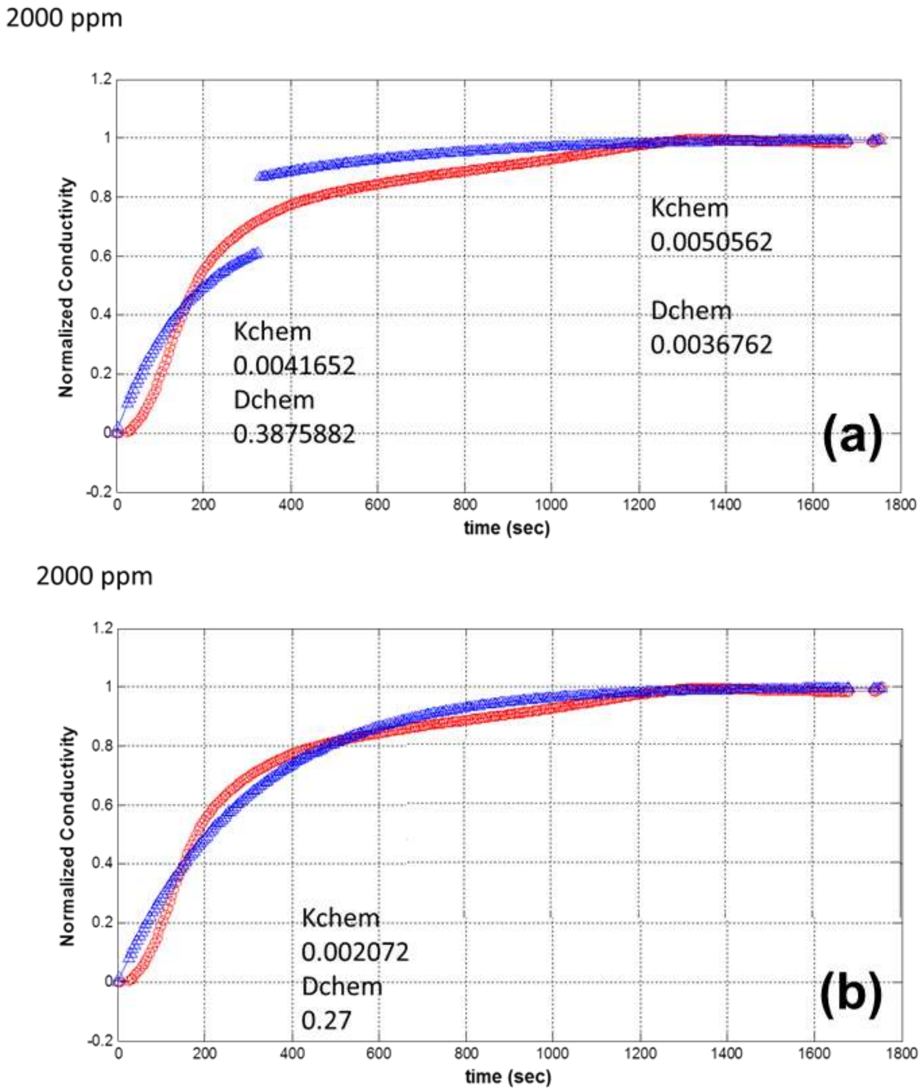

Figure 108 : 2000 ppm SO_2 **(a)** discrete **(b)** continuous approaches

That can easily be concluded that discrete approach is suitable approach since SO_2 extracts the surface adsorbed O_2 (interstitial) and moves away because of the high temperature conditions after removal of all physi or chemi absorbed and/or interstitial O_2 (first part). The second side of the normalized conductance curve can be attributed to both extraction of lattice oxygen by diffusing SO_2 species an or $SrMoO_4$ nanoflowers lattice may lose oxygen and that oxygen can diffuse upwards and interact with approaching SO_2 and after formation of SO_3 species cannot interact with atmospheric O_2 and or stay on the surface as it's known desorption of the SO_3 at this temperature is very high and almost and formation of SO_4 is also very since that reaction requires two electrons on where e^- deficiency high.

5.5 Conclusion

Evaluation of sensing behavior of binary and ternary tungstates and molybdates (WO_3, MoO_3, $SrWO_4$, $SrMoO_4$, $NiWO_4$, $NiMoO_4$, $MgMoO_4$, Sr_2MgWO_6, and Sr_2MgMoO_6) were completed for SO_2, and H_2S. The CO and H_2 cross-sensitivity tests were also completed for abovementioned compounds. The tests were conducted at three different temperatures (600, 800 and 1000°C) in the presence of 500, 1000 and 2000 ppm of the testing gas (SO_2 primarily). The successful compounds ($SrWO_4$, $SrMoO_4$, $NiWO_4$) that demonstrated high sensitivity towards SO_2 were further tested for 4-100 ppm H_2S diluted in both H_2 and syngas composition. After all evaluation considering SO_2 and H_2S sensitivity and cross-sensitivity toward CO and H_2, the $SrMoO_4$ composition emerged as an excellent sensing material for SO_2 and H_2S. The compound was synthesized in four different morphologies; although, all of them showed superior sensing behavior at high temperature, they succumbed to coarsening and lost the high sensitivity.

Two different strategies were focused upon to limit coarsening process for the synthesized nanomaterials. The strategies centered on grain pinning mechanism using either a second phase or an inert substrate. In order to utilize a surface or substrate pinning mechanism, the $SrMoO_4$ composition was grown onto a MgO substrate through a templated growth process. In this case, the $SrMoO_4$ was grown by the hydrothermal template growth process on a coarsening resistant (refractory) core structure. In order to realize the second strategy, MgO nano-rods were synthesized via hydrothermal route, as well as, the $SrMoO_4$ nano-flowers were grown over MgO core structure using a similar process (where the MgO was used as seed or template particles for the growth process). The $SrMoO_4$/MgO coarsening resistant structure unexpectedly showed superior sensing behavior and chemical stability for H_2 up to 150 hours of operation at 1000°C; however, the $SrMoO_4$ nano-flowers showed high sensitivity towards SO_2 and H_2S. Extensive surface, bulk and interface characterization for chemical, electronic, structural and phase analysis of aforementioned materials were completed in order to clarify the sensing behavior difference. And it was concluded that incorporation of Mg into $SrMoO_4$ nano as an MgO is the reason behind drastic change in sensitivity by stabile compound formation between Mg and S in addition to change in electronic properties.

Chapter 6: Microsensor Fabrication and Testing

6.1 Introduction

Many publications have shown that reducing the dimensions of sensing materials, as well as, reducing the scale of the sensor architecture affect the overall performance of the gas sensing device**.** Further demand from industrial applications is the reliable implementation of select of semiconducting nanomaterials onto a single platform and enable simultaneous detection of different gases under harsh environmental conductions. Sensor array demands have diverted the scientific interest more toward miniaturizing sensor architecture. Both sensor material and metallizations, either electrode or lead must be compatible with micromachining in order to satisfy the aforementioned demands. For resistive-type sensors, the sensing material creates an electrical contact between the fingers of the electrodes allowing a signal produced by releasing electrons as a result of redox reactions on the sensor material surface to be sent to the data collector. By reducing the finger spacing, as well as, increasing the number of fingers have significant importance to the sensor designer. The most crucial factors for the electrode design is the gap between the fingers, where the length and width of the fingers must be optimized in order to have large network of electrode materials to be in contact with the sensing material in order to maximize by increasing the effective electrode size while decreasing the electron mean path distance. In this chapter, the miniaturizing effort will be presented by using the developed nanomaterial systems optimized in the Chapter 5 for H_2 and SO_2 sensing, and these sensing materials were deposited over the drift-free Zr/Pt (Zr/Zr+Pt/Pt) composite electrodes that were developed and discussed in Chapter 3 [17, 54, 222, 223, 224] [225] [226] [227].

6.2 Experimental

6.2.1 Substrate fabrication and Planarizing

In order to manufacture chemiresistive type sensor, at first the in-house made alumina substrates were subject of planarizing in order to increase the quality of the pattern transfer during metallization and sensor material deposition. Surface roughness of the in-house made Al_2O_3 substrates is a significant obstruction for homogeneous spin coating of photoresist, which is a crucial step in obtaining a well-defined micro-electrode structure. The fluctuations in substrate thickness affect the overall performance of the sensors by its possible modifications over the thickness of the deposited electrode as well as pattern quality. To overcome this problem, the substrates were glued onto stainless steel substrate holders using a high-strength thermoset plastics, as seen in the optical micrograph in Figure 109-a. The substrates were then polished by mounting on automated polishing machine (MTI 2000s) with various grit levels of diamond materials. The entire procedure performed in this work is described in Table 7 in detail.

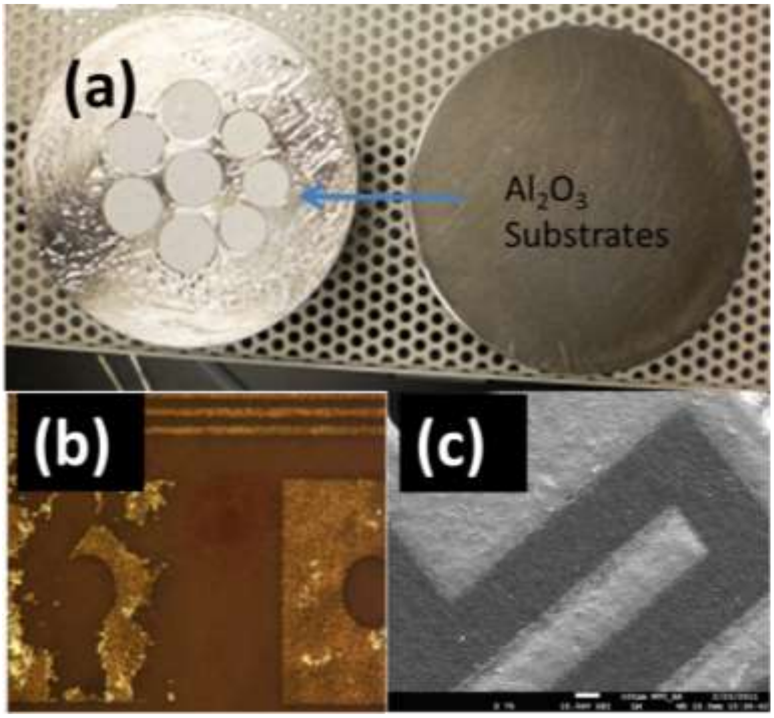

Figure 109 : a) Photograph of the Al_2O_3 samples on substrate holder **b)** SEM micrograph of the electrode deposited on unpolished Al_2O_3-surface **c)** SEM micrograph of the electrode deposited on polished Al_2O_3 substrate.

After the plane grinding, coarse polishing and subsequent cleaning, samples were polished on napless polishing cloths loaded with lubricant and 7.5, 1, and 0.5 µm diamond paste, respectively. AFM surface analyses of the polished and un-polished Al_2O_3 substrates are represented in Figure 110. Surface roughness of the in-house made alumina substrates was reduced from 173 nm to 46.3 nm by using the polishing procedure described in Table 7.

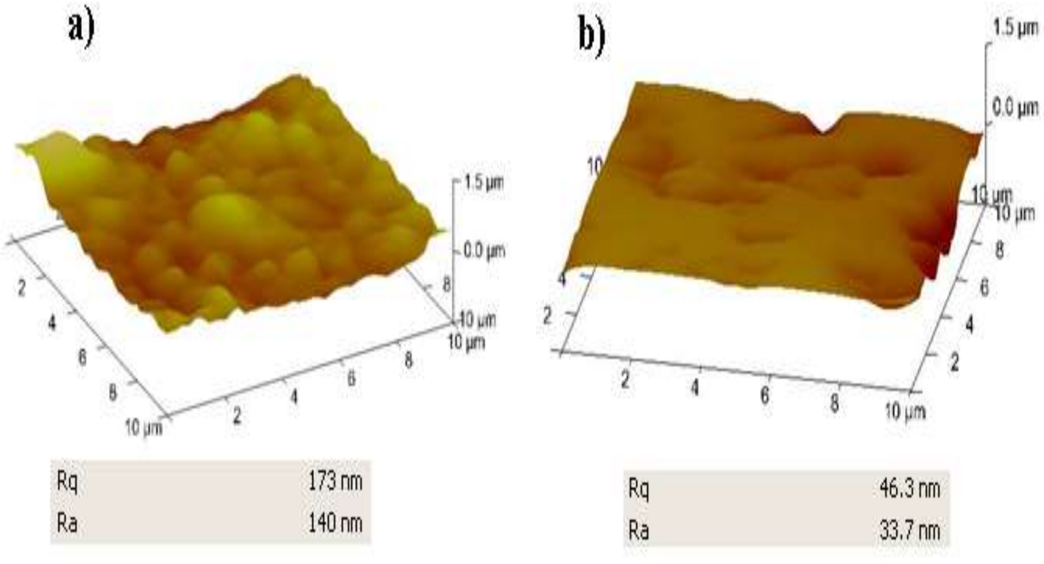

Figure 110 : AFM surface analysis of Al_2O_3 substrates **a)** before polishing **b)** after polishing.

The hardnesses of the commonly used abrasives are 2500 HV (silicon carbide), 2000 HV (Al_2O_3), and 8000 HV (diamond) [228]. In practice for example, very little material can be removed by silicon carbide from materials with a hardness of about 1000-2000 HV, such as Al_2O_3. Abrasives should be at least two times, and preferably three times, harder than the specimen material. Diamond abrasives clearly are desirable for all stages of the preparation of Al_2O_3 surfaces. The preparation of the sensor substrates appeared to be crucial, since the quality of the pattern transfer during lift-off process were affected by the surface roughness. SEM micrographs presented in Figure 109-b and –c show the quality difference in pattern transfer over un-polished and polished substrates after lift-off. It has been concluded that the flatness and thickness control of these substrates are valuable to the formation of sub-millimeter sized sensors.

Table 7 : Grinding and polishing procedure for an automatic polishing of Al_2O_3

Step	**Abrasive and lubricant**	**Time, min**	**Rotation frequency, rpm**
Plane grinding	600-grit diamond disc	0.5–1 (or until specimen is flat)	300
Coarse polishing	1200-grit diamond disc	15-20	300
Coarse polishing	7.5 µm diamond paste refresh lubricant every 10 min. on napless cloth	15-20	400
Polishing	1 µm diamond paste refresh lubricant every 10 min. on napless cloth	15-20	400
Fine polishing	0.5 µm diamond paste refresh lubricant every 10 min. on napless cloth	15-20	120–150

6.2.2 Microsensor fabrication

6.2.2.1 Electrode fabrication

Microelectrodes for sensor fabrication were completed by optical lithography over highly-polished Al_2O_3 polycrystalline substrates with the optimized coating architectures for Zr/Zr+Pt/Pt. This architecture was used due to its highly reliable microstructure and cost (which includes the amount labor needed for patterning and deposition). A conventional photolithography process was carried out to define the microelectrode pattern within the photo-resist. AZ 3300-F (AZ Electronic

Materials) photoresist was deposited on a polished alumina substrate in a spin-coater (Laurell Technologies, 400 spinner) to a thickness of 3.5 µm and was baked at 110°C for 5 min before exposure. The substrates were placed in a mask aligner (Suss Microtech, MA6), exposed, and baked at 120°C for 5 min. The substrate was then developed in an ultrasonic bath of AZ 917 developer until the pattern was fully etched away. After the pattern was transferred, the wafers were given a post-bake at 120°C for 5 min to strengthen the photoresist. The patterned substrate was located in a sputtering station (Magnetron Sputtering, CVC 610 DC) and the deposition of two layers of zirconium (Zr) as an adhesion promoter and grain pinning phase was followed by a 425 nm thick layer of platinum. The details of microelectrode fabrication are provided in section 3.5. The electrodes were annealed at 1200°C for 1 h to stabilize the microstructure for high temperature testing. Figure 111 shows the microelectrodes with a 1.5 ×5 mm and 50 µm finger spacing. As the micrographs reveal, the pattern quality was very good with the desirable sharp image transfer. The microelectrode was further heat treated at 1000°C for 10 h in 1% O_2 balanced with N_2 atmosphere in order to quantify the drift in the resistance. It was seen that the resistance of the as-deposited microelectrode was 1.5 ohms and after heat treatment it increased to 2.1 ohms. It can be concluded that microelectrode architecture is drift-free once considering the typical resistance value of optimized sensing material is in the range of mega ohms.

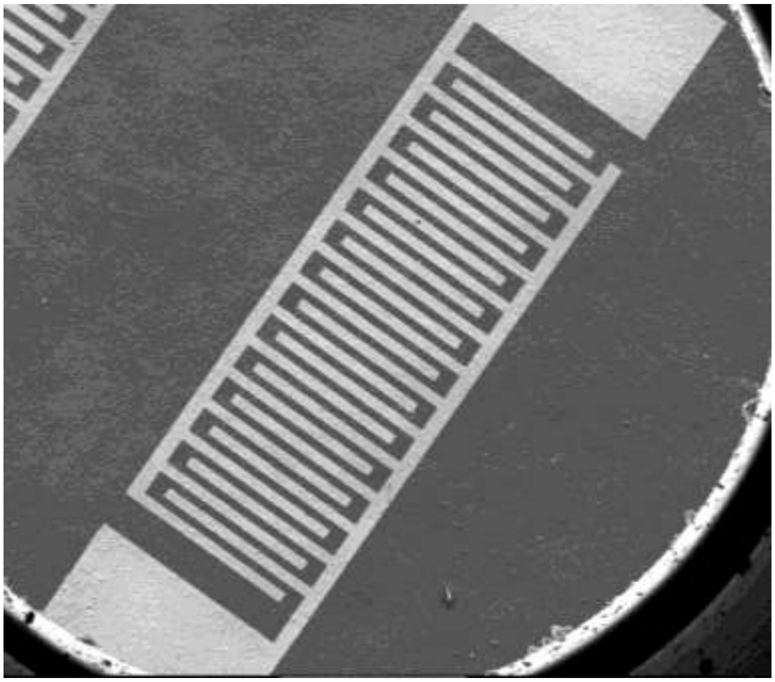

Figure 111 : SEM micrograph of the Zr/Zr+Pt/Pt type microelectrode seen in as-deposited state.

6.2.2.2 Microsensor fabrication via lost molding technique

In order to deposit the sensing material over electrode, a lost-mold microcasting process was used which was optimized by Wildfire et *al.* [17]. Figure 112 shows a schematic cross-section of the microsensor through the manufacturing steps. The process starts with the deposition of the high temperature compatible electrode pattern onto highly polished Al_2O_3 substrate as described in 6.2.2.1. STEP 1 through STEP 5 show electrode deposition schematically. STEP 6 through 11 summarize the application of SU-8 25 (MicroChem Corp. MA) negative photoresist over patterned electrodes as well as casting of sensing material into the molds [17].

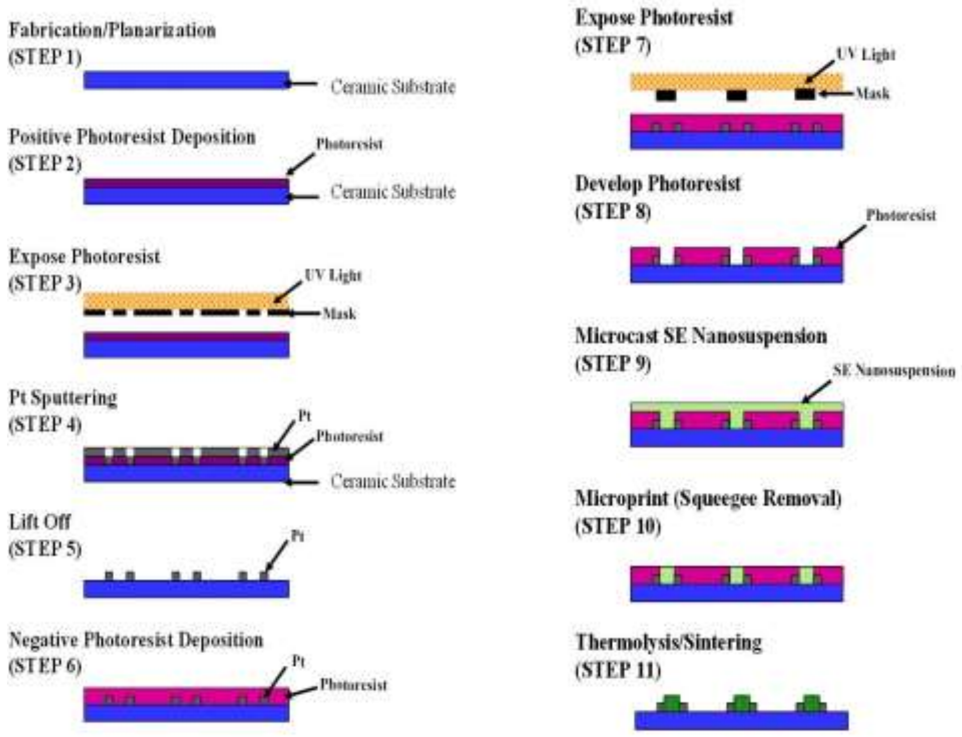

Figure 112: Schematic of the microcasting process microsensor **[17]**.

Once the micromold fabrication was completed, the depth of the channels were measured by profilometer precisely. The thickness profile of the molds is given in the Figure 113. An optimized microcasting system developed by Wildfire et *al.* used and a thick film photolithography methode that was able to produced molds up to 50 and 100 µm depth with good lateral resolution [17].

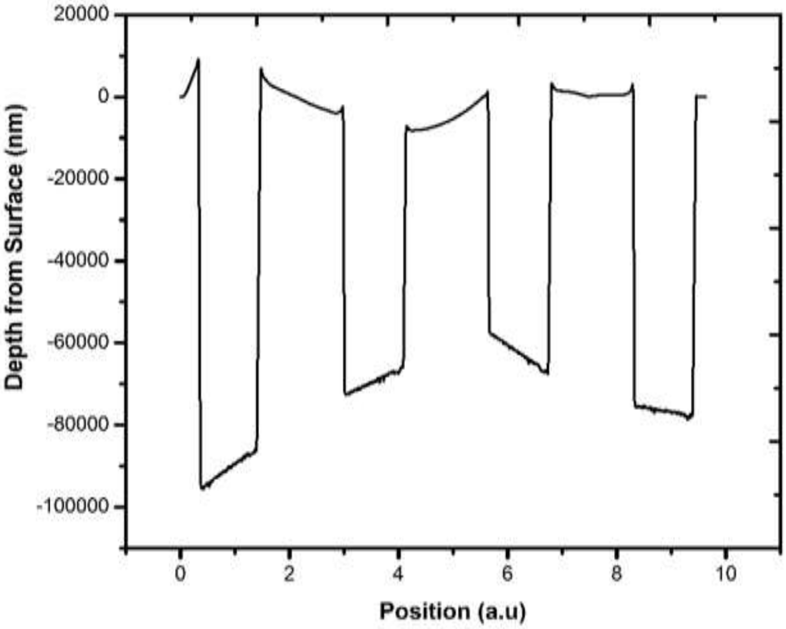

Figure 113 : The thickness profiles of the molds made of SU-8.

Microcasting was completed with non-aqueous inks of previously optimized and determined choices of sensing materials; $SrMoO_4$ nanoflowers and $SrMoO_4/MgO$ for H_2S/SO_2 and H_2, respectively. Each of the material systems was casted on the IDEs with an approximate film thickness of 50 µm by using two channels located in the middle of the pattern. The two other channels also could be used, but were not the chosen due to their large depth. The inks consisted of 70 wt% of nano but agglomerated hydrothermally produced ceramic powder and a terpineol/ethyl cellulose ink vehicle, J2M, (Johnson Matthey, UK) that was sonicated in order to break agglomerates and increase the dispersion. The microcasting process was accomplished via a stenciling process using a screenprinter (DEK, Weymouth, UK) in order to have repeatable deposition thicknesses. Upon compilation of casting the substrate was placed in a high-temperature box-furnace and burned out, sintered and stabilized in a two-step process with heating rates of 1˚/min to 600˚C and form that temperature to 1200˚C with 5˚/min with a one hour dwell time at 1200˚C. Figure 114 shows the SEM micrograph of the microsensor after sintering and the stabilization heat treatment.

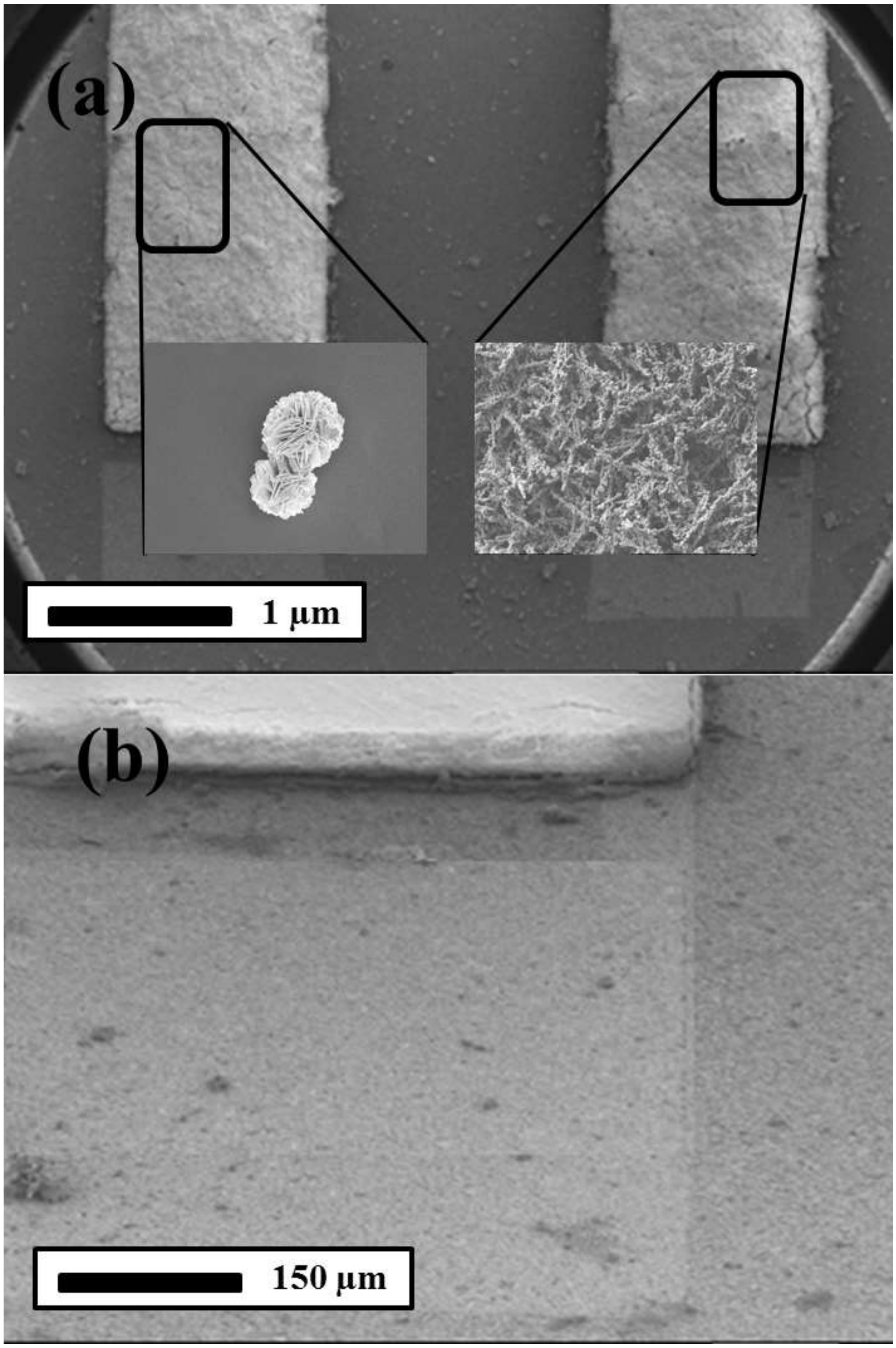

Figure 114 : SEM micrographs of **(a)** $SrMoO_4/MgO$ and $SrMoO_4$ nanoflowers sensing material deposited over Zr/Zr+Pt/Pt type microelectrode **(b)** close-up of edge.

6.3 Results and Discussion

The spacing between the fingers is what significantly affected the response rate of the sensor. Figure 115-a and -c presents the testing results of the $SrMoO_4$ nano-flowers for SO_2 in the micro- and macro-scale chemi-resistive sensor architecture. Figure 115-b and -d shows the testing results of the $SrMoO_4$/MgO for H_2 in micro- and macro-scale chemi-resistive sensor architecture at 1000°C under 1%O_2 partial pressure against different levels of SO_2 and H_2. It is known that the sensitivity and response time can be increased and decreased for designated target gas, respectively by including nanomaterials on a macrosensor platform or by reducing the size of the electrode system for the sensors [17, 54]. As seen in the Figure 115-b, the 1000, 2000, and 4000 ppm H_2 exposures resulted in sensitivities of ~67%, ~81%, and ~87% in the $SrMoO_4$/MgO microsensor, respectively. These responses are up to 30% increase in comparison to performance of the macrosensor (see Figure 115-d). As seen in the Figure 115-a and –c, the sensitivity data for different concentration levels of SO_2 for the $SrMoO_4$ nanoflowers tested on the micro and macrosensor platforms at 1000°C are remarkably different as also observed in the $SrMoO_4$/MgO case. The average measured sensitivities were ~24%, ~29%, and ~37% for the 500, 1000, and 2000 ppm of SO_2, respectively for macro sensor platform, however for microsensor platform these values almost doubled and were ~55%, ~63%, and ~67% for the 500, 1000, and 2000 ppm of SO_2, respectively. As seen from the results, the microsensors not just only increased the sensitivity, but also decreased the response and recovery times. The difference in performance for the $SrMoO_4$ nanoflowers and $SrMoO_4$/MgO in the micro platform can be attributed to nature of the materials. The highly porous network of the later, in which H_2 molecules can easily diffuse through and reach more surface are of the sensing material.

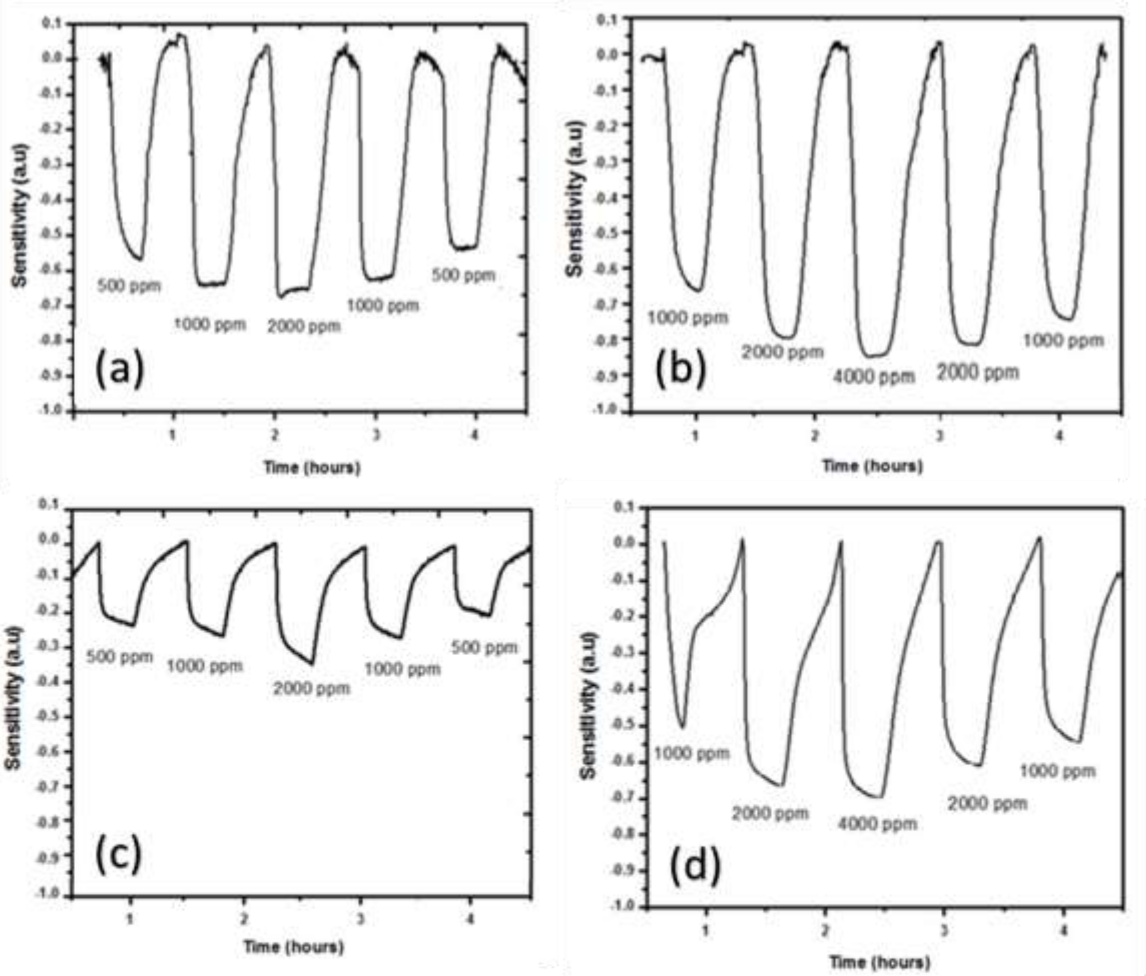

Figure 115 : Response of microsensor equipped with **(a)** $SrMoO_4$ nano-flowers tested for SO_2 **(b)** $SrMoO_4$/MgO tested for H_2. Response of macrosensor **(c)** $SrMoO_4$ nano-flowers tested for SO_2 **(d)** $SrMoO_4$/MgO tested for H_2.

Chapter 7: Conclusions and Future Work

The thermal stability limitations of Pt films with various adhesion layers (Ti, Ta, Zr, and Hf) were characterized at 800 and 1200°C for various annealing times. The deposition of the Hf adhesion layer showed a high level of microstructural stability (compared to the Ti, Ta, and Zr) to the highest operating temperature (1200°C). The Hf was also incorporated within the bulk Pt conductive layer by depositing an alternating layer structure of Hf and Pt metal. The electrical resistivity measurements confirmed the retention of the percolated conductive network. In the end, a Pt composite multilayer film was developed that could withstand high-temperature exposure up to 1200°C for 48 h, which is beyond most reasonable, high-temperature chemical sensor applications or MEMS processing (and/or operation) conditions. It was further investigated that alternative a DC sputtering process for fabricating a functionally-gradient Pt and Zr composite microstructure with three deposition steps. The resultant microstructure of the composite electrode thin film was shown to be stable up to 1200°C. The microstructural stability of the Zr/Zr+Pt/Pt film architecture was attributed to the distribution of Zr throughout the bulk of the film during the three-step deposition process. Co-deposition of Hf and Pt would result high microstructural stability due to high stability of Hf compare to Zr.

Baseline testing of current SO_2 and H_2S sensing materials were completed. Nanomaterials as an active sensing layer that are stable at high temperatures are completed by templated growth of $SrMoO_4$ over MgO ($SrMoO_4$/MgO). This material showed high resistance to sintering and high accuracy, stability, and sensitivity toward H_2 due to MgO incorporation into $SrMoO_4$ matrix. Although the sintering of the $SrMoO_4$ nanoflowers could not hinder, the material performed very good sensitivity, stability, accuracy and long term stability against SO_2. The chosen material system ($SrMoO_4$ nanoflowers) was further tested for up to 100 pmm of H_2S diluted in H_2 as well as syngas composition and showed very promising sensing capabilities as well as accuracy in order to determine the different level of the target gas under extremely reducing atmosphere. The reasons behind sensitivity of the chosen two material systems for H_2 and SO_2 were characterized by Raman, XPS-UPS, XRD, EDS-SEM, AAS, TPR and TEM. The compound formation between Mg and S is the reason behind insensitivity of the $SrMoO_4$/MgO against SO_2, while its high sensitivity toward H_2 can be attributed to its highly porous microstructure and catalytic action of the surface. ECR was utilized for exploring the surface kinetics of the SO_2 over $SrMoO_4$ nanoflowers and it was concluded that interacting can be distinguished to discrete sections, etching like surface interacting and subsequent diffusive part.

The microsensors utilized with the nano compositions of the optimized sensing material systems not just only increased the sensitivity, but also decreased the response and recovery times. In the case of microsensor platform, the $SrMoO_4$/MgO reported a sensitivity increase of 40% compared to the macro platform. However, in the case of usage of micro platform of $SrMoO_4$ nanoflowers, compared to the macro platform of $SrMoO_4$ nanoflowers, the increase in sensitivity was up to 65%. The process regarding the synthesis of MgO nanorods can be optimized toward reducing the diameter of the as-synthesized products. This would result in more surface area after templated growth of sensing material.

References Cited

[1] C. Powell and B. Morreale, "Materials challenges in advanced coal conversion technologies," *MRS Bull,* vol. 33, pp. 309-315, 2008.

[2] "Annual Energy Outlook 2007 With Projections to 2030," U.S. Department of Energy, Washington, DC, 2007.

[3] D. L. West, F. C. Montgomery and B. L. Armstrong, "Compact, DC-electrical biased sulfur dioxide sensing elements for use at high temperatures," *Sensors and Actuators B: Chemical,* vol. 162, no. 1, pp. 409-417, 2012.

[4] M. J. Madou and S. R. Morrison, Chemical sensing with Solid State Devices, San Diego: Academic Press, INC, 1989.

[5] G. Eranna, B. C. Joshi, D. P. Runthala and R. P. Gupta, "Oxide Materials for Development of Integrated Gas Sensors-A Comprehensive Review," *Critical Reviews in Solid State and Materials Sciences,* vol. 29, no. 3-4, pp. 111-188, 2010.

[6] A. Mandelis and C. Christofides, Physics, Chemistry and Technolgy of Solid State Gas Sensor Devices, Toronto and Nicosia: Joh Wiley & Sons. Inc., 1993.

[7] P. A. Cox, Tarnsition Metal Oxides, An Introduction to Their Electronic Structure and Properties, Oxford: Clarendon Press, 1995.

[8] M. T. Greiner, L. Chai, M. G. Helander, W. M. Tang and Z. H. Lu, "Transition Metal Oxide

Work Functions: The Influence of Cation Oxidation State and Oxygen Vacancies," *Advanced Functional Materials,* vol. 7, no. 11, pp. 4557-4568, 2012.

[9] A. A. Saaman and P. Bergveld, "A Classification of Chemically Sensitivr Semiconductor Devices," *Sensors and Actuators,* vol. 7, pp. 75-87, 1985.

[10] T. E. Sullivan, R. B. Childs, J. M. Ruths and S. J. Fonash, "Phys. SiO2 and Its Interfaces,," *Proc. Int. Top. Conf.,* p. 454, 1978.

[11] F. Maximilian and H. Meixner, "Selectivity in High-temperature Operated Semiconductor Gas-sensors," *Sensors and Actuators B: Chemical,* vol. 52, no. 1-2, pp. 179-187, 1998.

[12] A. M. Azad, S. A. Akbar, S. G. Mhaisalkar, L. D. Birkefeld and K. S. Goto, "Solid State Gas Sensors A review," *J. Electrochem. Soc.,* vol. 139, no. 12, pp. 3690-3701, 1992.

[13] J. F. Marucco, J. Gautron and P. Lemasson, *J. Phys. Chem. Solids,* vol. 42, p. 363, 1981.

[14] D. E. Williams, In Solid State Gas Sensors, Chapter 5, Bristol, 1987.

[15] G. Korotcenkov, "The role of morphology and crystallographic structure of metal oxides in response of conductometric-type gas sensors," *Materials Science and Engineering R: Reports,* vol. 61, pp. 1-39, 2008.

[16] G. Korotcentov, "Metal oxides for solid-state gas sensors: What determines our choice?," *Material Science and Engineering B,* vol. 139, no. 1, pp. 1-23, 2007.

[17] C. Wildfire, "Investigation of Gadolinium Based Pyrochlores for their use in High-Temperature Nano Derived H2 Gas Sensors," West Virginia University, Morgantown, 2012.

[18] D. X, "Understanding and optimization of gas sensors based on metal oxide semiconductors," Chemical Engineering Department, University of Colorado, USA, Ph.D. Thesis Dissertation, 2007.

[19] E. B. Varhegyi, J. Gerblinger, F. Reti, I. V. Perczel and H. Meixner, "Study of the behaviour of CeO2 in SO2-containing atmosphere," *Sensors and Actuators B,* Vols. 24-25, pp. 631-635, 1995.

[20] H. Windischmann and P. Mark, "A model for the Operation of a Thin film SnOx Conductance Modulation Carbon Monoxide Sensor," *J. Electrochem Soc.,* vol. 126, 1979.

[21] P. Mark, *J. Chem. Phys. Solids. ,* vol. 25, no. 911, 1964.

[22] A. M. Azad, S. G. Mhaisalkar, L. D. Birkefeld, S. A. Akbar and K. S. Goto, "Behaviour of a New ZrO2-MoO3 Sensor for Carbon Monoxide Detection," *J. Electrochern. Soc,* vol. 139, no. 10, pp. 2913-2920, 1992.

[23] L. D. Birkefeld, A. M. Azad and S. A. Akbar, "Carbon Monoxide and Hydrogen Detection by Anatase Modification of Titanium Dioxide," *J. Am. Ceram. Soc.,* vol. 75, no. 11, p. 2964, 1992.

[24] B. Chiou, J. Li and J. Duh, "Characteristics of Pd-doped tin oxide ceramics in response to CO gas," *J. Electron. Mater.,* vol. 17, no. 485, 1988.

[25] V. Aroutiounian, "Metal Oxide hydrogen, oxygen and carbon monoxide sensors for hydrogen setups and cells," *International Journal of Hydrogen Energy,* vol. 32, pp. 1145-1158, 2007.

[26] P. Soundarrajan and F. Schweighardt, "Hydrogen Sensing and Detection," in *Hydrogen*

Fuel, Taylor & Francis Group, LLC, 2009, pp. 496-518.

[27] G. J. Li and s. Kawi, "High-surface area SnO2: a novel semiconductor oxide gas sensor," *Materials Letters,* vol. 34, pp. 99-102, 1998.

[28] J. P. Ahn, J. H. Kim, J. k. Park and M. Y. Huh, "Microstructure and gas-sensing properties of thick film sensor using nanophase SnO2 powder," *Sensors and Actuators B: Chemical,* vol. 99, pp. 18-24, 2004.

[29] N. Yamazoe and N. Miura, "Some basic aspects of semiconductor gas sensors," in *Chemical Sensor Technology, Volume 4*, vol. 4, Tokyo, Chemical Sensor Technology, 1992, p. 19.

[30] M. Hayashi, T. Hyodo, Y. Shimizu and M. Egashira, "Effects of microstructure of mesoporous SnO2 powders on their H2 sesing properties," *Sensors and Actuators B: Chemical,* vol. 141, no. 2, pp. 465-470, 2009.

[31] C. Xu, J. Takaki, N. Miura and N. Yamazoe, "Grain size effects on gas sensitivity of porous SnO2-based elements," *Sensors and Actuators B: Chemical,* vol. 3, pp. 147-155, 1991.

[32] Y. Shimizu, N. Nakamura and M. Egashira, "Effects of diffusivity of hydrogen and oxygen through pores of thick film SnO2-based sensors on their sensing properties," *Sensors and Actuators B: Chemical,* vol. 13/14, pp. 128-131, 1993.

[33] Y. Shimizu, T. Maekawa, Y. Nakamura and M. Egashira, "Effects of gas diffusivity and reactivity on sensing properties of thick film SnO2-based sensors," *Sensors and Actuators B: Chemical,* vol. 46, pp. 163-168, 1998.

[34] N. Yamazoe, G. Sakai and K. Shimanoe, "Oxide semiconductor gas sensors," *Catalysis Surveys form Asia,* vol. 7, no. 1, pp. 63-75, 2003.

[35] D. Davazoglou and K. Georgouleas, "Low Pressure Chemically Vapor Deposited WO3 Thin Films for Integrated Gas Sensor Applications," *J.Electrochemical Society,* vol. 145, pp. 1346-1350, 1998.

[36] Y. Shimizu, N. Matsunaga, T. Hyodo and M. Egashira, "Improvement of SO2 sensing properties of WO3 by noble metal loading," *Sensors and Actuators B: Chemical,* vol. 77, pp. 35-40, 2001.

[37] I. Kim, S. Han, J. Gwak, D. Hong, D. Jakhar, K. Singh and J. Wang, "Development of micro hydrogen gas sensor with SnO2-Ag2O-PtOx composite using MEMs process," *Sensors and Actuators B: Chemical,* vol. 127, no. 2, pp. 441-446, 2007.

[38] Y. Lee, K. Lee, D. Lee, Y. Jeong, H. Lee and Y. Choa, "Preperation and gas sensitivity of SnO2 nanopowder homogenously doped with Pt nanoparticles," *Current Applied Physics, Nano Korea 2007 Symposium,* vol. 9, no. 1, pp. S79-S81, 2009.

[39] B. Guo, A. Bermak, P. C. Chan and G. Yan, "Characterization of intergrated in oxide gas sensors with metal additives and ion implantations," *IEEE Sensors Journal,* vol. 8, no. 8, pp. 1397-1398, 2008.

[40] P. Manjula, L. Satyanarayana, Y. Swarnalatha and S. V. Manorama, "Raman and MASNMR studies to support the mechanisms of low temperature hydrogen sensing by Pd doped mesoporous SnO2," *Sensors and Actuators B: Chemical,* vol. 138, no. 1, pp. 28-34, 2009.

[41] A. Galdikas, V. Jasutis, S. Kaciulis, G. Mattogno, A. Mironas, V. Olevano, D. Senuliena and A. Setkus, "Peculiarities of Surface Doping with Cu in SnO2 Thin Film Gas Sensors," *Sensors and Actuatros B: Chemical,* vol. 43, pp. 140-146, 1997.

[42] M. Radecka, K. Zakrzewska and M. Rckas, "Solid Solutions for Gas Sensors," *Sensors and*

Actuators B : Chemical, vol. 47, pp. 194-204, 1998.

[43] U. S. Choi, G. Sakai, K. Shimanoe and N. Yamazoe, "Sensing properties of Au-loaded SnO2–Co3O4 composites to CO and H2," *Sensors and Actuators B: Chemical,* vol. 107, no. 1, pp. 397-401, 2005.

[44] O. Safonova, T. Neisiua, A. Ryzhikov, B. Chenevier, A. Gaaskov and M. Labeau, "Characterization of the H2 sensing mechanism of Pd-promoted SnO2 by XAS in operando conditions," *Chemical Communications,* pp. 5202-5204, 2005.

[45] I. P. Matusko, V. K. Yatsimirskii, N. P. Maksimovich, N. V. Nikitina, P. M. Silenko, V. P. Ruchko and V. B. Ishchenko, "Sensitivity to hydrogen of sensor materials based on SnO2 promoted with 3d metals," *Theoretical and Experimental Chemistry,* vol. 442, no. 2, pp. 128-133, 2008.

[46] N. Yamazoe, Y. Kurokawa and T. Seiyama, "Effects of additives on semiconductor gas sensors," *Sensors and Actuators,* vol. 174, p. 283–289, 1983.

[47] R. K. Sharma, P. H. Chan, Z. Tang, G. Yan, I. M. Hsing and J. K. Sin, "Sensitive, Selective and Stable Tin Dioxide Thin-films for Carbon Monoxide and Hydrogen Sensing in Integrated Gas Sensor Array Applications," *Sensors and Actuators B : Chemical,* vol. 72, pp. 160-166, 2001.

[48] A. Salehi and M. Gholizade, "Gas-sensing properties of indium-doped SnO2 thin films with variations in indium concentration," *Sensors and Actuators B: Chemical,* vol. 89, pp. 173-181, 2003.

[49] J. Xu, Y. Shun, Q. Pan and J. Qin, "Sensing characteristics of double layer film of ZnO," *Sensors Actuators B: Chemical,* vol. 66, pp. 161-163, 2000.

[50] M. Franke, U. Simon and T. Koplin, "Metal and Metal Oxide Nanoparticles in Chemiresistors: Does the Nanoscale Matter?," *Small,* vol. 2, no. 1, pp. 36-50, 2006.

[51] H. Zhang, Z. Li, L. Liu, X. Xu, Z. Wang, W. Wang, W. Zheng, C. Wang and B. Dong, "Enhancement of hydrogen monitoring properties based on Pd-SnO2 composite nanofibers," *Sensors and Actuators B: Chemical,* vol. 147, no. 1, pp. 111-115, 2010.

[52] R. Huck, U. Bottger, D. Kohl and G. Heiland, "Effects in the Detection of H2 and CH4 by Sputtered SnO2 Films with Pd and PdO Deposites," *Sensors and Actuators B: Chemical,* vol. 17, pp. 355-359, 1989.

[53] Y. Li, W. Wlodarski, K. Galatsis, S. H. Moslih, J. Cole and S. Russo, "Gas sensing properties of p-type semiconducting Cr-doped TiO2 thin films," *Sensors and Actuators B: Chemical,* vol. 83, no. 1-3, pp. 160-163, 2002.

[54] C. Wildfire, E. Çiftyürek, K. Sabolsky and E. M. Sabolsky, "Fabrication and Testing of High-Temperature Nano-Derived Resistive-Type Microsensors for Hydrogen Sensing," *Journal of The Electrochemical Society,* vol. 161, no. 2, pp. B3094-B3102, 2014.

[55] S. M. Kanan, O. M. El-Kadri, I. A. Abu-Yousef and M. C. Kanan, "Semiconducting metal oxide based sensors for selective gas pollutant detection," *Sensors,* vol. 9, no. doi:10.3390/s91008158, pp. 8159-8196, 2009.

[56] D. L. West, F. C. Montgomery and B. L. Armstrong, "Compact, DC-electrical biased sulfur dioxide sensing elements for use at high," *Sensors and Actuators B : Chemical,* vol. 162, pp. 409-417, 2012.

[57] D. Shin, T. M. Besmann and B. L. Armstrong, "Phase stability of noble metal loaded WO3 for SO2," *Sensors and Actuators B,* 2012.

[58] D. Morris and R. G. Egdell, "Application of V-doped TiO2 as a sensor for detection of SO2," *Journal of Materials Chemistry,* vol. 11, pp. 3207-3210, 2001.

[59] X. Liang, T. Zhong, B. Quan, B. Wang and H. Guan, "Solid-state potentiometric SO2 sensor combining NASICON with V2O5-doped TiO2 electrode," *Sensors and Actuators B : Chemical,* vol. 134, pp. 25-30, 2008.

[60] E. B. Varhegyi, J. Gerblinger, F. Reti, I. V. Perczel and H. Meixner, "Study of the behaviour of Ce02 in S02-containing environment," *Sensors and Actuators B: Chemical,* Vols. 24-25, pp. 631-635, 1995.

[61] A. Neubecker, T. Pompl, T. Doll, W. Hansch and I. Eisele, "Ozone Enhanced Molecular Beam Deposition of Nickel Oxide (NiO) for Sensor Applications," *Thin Solid Films,* vol. 310, pp. 19-23, 1197.

[62] C. Fujimoto, Y. Hayakawa and A. Ono, "Evaluation of the efficiency of deodorants by semiconductor gas sensors," *Sensors and Actuators B : Chemical,* pp. 191-194, 1996.

[63] S. C. Lee, B. W. Hwang, S. J. Lee, H. Y. Choi, S. Y. Kim, S. Y. Jung, D. Ragupathy and D. D. Lee, "A novel tin oxide-based recoverable thick film SO2 gas sensor promoted with magnesium and vanadium oxides," *Sensors and Actuators B: Chemical,* vol. 160, no. 1, pp. 1328-1334, 2011.

[64] D. Girardin, F. Berger, A. Chambaudet and R. Planade, "Modelling of SO2 detection by tin dioxide gas sensor," *Sensors and Actuators B: Chemical,* vol. 43, p. 147–153, 1997.

[65] F. Berger, M. Fromm, A. Chambaudet and R. Planade, "Tin dioxide-based gas sensors for SO2 Detection," *Sensor and Actuators B,* vol. 45, pp. 175-181, 1997.

[66] N. Bukun, A. Vinokurov, M. Vinokurova, L. Derlyukova, Y. Dobrovolsky and A. Levchenko, "Chemisorption and electrochemical reactions of SO2 on modified SnO2 elctrodes," *Sensors and Actuators B: Chemical,* vol. 106, pp. 153-157, 2005.

[67] M. Egashira , Y. Shimizu and Y. Takao, "Trimethylamine Sensor based on Semiconductive Metal Oxides for Detection of Fish Freshness,," *Sensors and Actuators B : Chemical,* vol. 1, pp. 108-112, 1990.

[68] T. Akamatsu, T. Itoh, N. Izu and W. Shin, "NO and NO2 Sensing Properties of WO3 and Co3O4 Based Gas Sensors," *Sensors,* vol. 13, pp. 12467-12481, 2013.

[69] J. Leng, X. Xu, N. Lv, H. Fan and T. Zhang, "Synthesis and gas-sensing characteristics of WO3 nanofibers via electrospinning," *Journal of Colloid and Interface Science,* vol. 356, pp. 54-57, 2011.

[70] N. Izu, G. Hagen, D. Schonauer, U. Roder-Roith and R. Moos, "Application of V2O5, WO3, TiO2 for Resistive-Type SO2 Sensors," *Sensors,* vol. 11, pp. 2982-2991, 2011.

[71] M. Stankova, X. Vilanova, J. Calderer, E. Llobet, P. Ivanov, I. Gracia, C. Cane and X. Correig, "Detection of SO2 and H2S in CO2 stream by means of WO3-based micro-hotplate sensors," *Sensors and Actuators B: Chemical,* vol. 102, pp. 219-225, 2004.

[72] S. Dongwon, T. M. Bessman and B. L. Armstrong, "Phase stability of noble metal loaded WO3 for SO2," *Sensors and Actuators B : Chemical,* vol. 176, pp. 75-80, 2013.

[73] C. Imawan, H. Steffes, F. Solzbacher and E. Obermeier, "A new preparation method for sputtered MoO3 multilayers for the application in gas sensors," *Sensors and Actuators B: Chemical,* vol. 78, no. 1-3, pp. 119-125, 2001.

[74] C. Imawan, H. Steffes, F. Solzbacher and E. Obermeir, "Structural and gas-sensing properties of V2O5-MoO3 thin films for H2 detection," *Sensor and Actuators B: Chemical,* vol. 77, no. 1-2, pp. 346-351, 2001.

[75] M. Ferroni, V. Guidi, G. Martinelli, P. Nelli, M. Sacerdoti and G. Sberveglieri, "Characterization of a molybdenum oxide sputtered thin film as a gas sensor," *Thin Solid Films,* vol. 307, no. 1-2, pp. 148-151, 1997.

[76] K. Galatsis, Y. X. Li, W. Wlodarski, E. Comini, G. Faglia and G. Sberveglieri, "Semiconductor MoO3–TiO2 thin film gas sensors," *Sensors and Actuators B: Chemical,* vol. 77, no. 1-2, pp. 472-477, 2001.

[77] A. K. Prasad and P. I. Gouma, "MoO3 and WO3 based thin film conductimetric sensors for automotive applications," *Journal of Material Science,* vol. 38, no. 21, pp. 4347-4352, 2003.

[78] J. F. Currie, A. Essalik and J. C. Marusic, "Micromachined thin film solid state electrochemical CO2 , NO2 and SO2," *Sensors and Actuators B: Chemical,* vol. 59, no. 2-3, pp. 235-241, 1999.

[79] C. H. Foulkes, “GAS!” The Story of the Special Brigade, N&M Press, 2001.

[80] S. K. Pandey, K. H. Kim and K. T. Tang, "A review of sensor-based methods for monitoring hydrogen sulfide," *Trends in Analytical Chemistry,* vol. 32, pp. 87-99, 2012.

[81] G. Fang, Z. Liu, C. Liu and K. Yao, "Room Temperature H2S Sensing Properties and Mechanism of CeO2-SnO2 Sol-gel Thin Films," *Sensors and Actuators B: Chemical,* vol. 66, no. 1-3, pp. 46-48, 2000.

[82] S. C. Lee, S. Y. Kim, B. W. Hwang, S. Y. Jung, D. Ragupathy, I. S. Son, D. D. Lee and J. C. Kim, "Improvement of H2S Sensing Properties of SnO2-Based Thick Film Gas Sensors Promoted with MoO3 and NiO," *Sensors,* vol. 13, pp. 3889-3901, 2013.

[83] Z. Sun, H. Yuan, Z. Liu, B. Han and X. Zhang, "A Highly Efficient Chemical Sensor Material for H2S: Fe2O3 Nanotubes Fabricated Using Carbon Nanotube Templates," *Advanced Materials ,* vol. 17, pp. 2993-2997, 2005.

[84] D. H. Dawson, G. S. Henshaw and D. E. Williams, "Description and characterization of a hydrogen sulfide gas sensor based on Cr2-yTiyO3+x," *Sensor and Actuators B: Chemical,* Vols. 26-27, pp. 76-80, 1995.

[85] E. P. Barret, G. C. Georgiades and P. A. Sermon, "The mechanism of operation of WO3-based H2S sensors," *Sensors and Actuators B: Chemical,* vol. 1, pp. 116-120, 1990.

[86] B. Fruhberger, M. Grunze and D. J. Dwyer, "Surface chemistry of H2S sensitive tungsten oxide films," *Sensors and Actuators B: Chemical,* vol. 31, pp. 167-174, 1995.

[87] R. M. Ferrizz, R. J. Gorte and J. M. Vohs, "TPD and XPS investigation of the interaction of SO2 with model ceria catalysts," *Catalysis Letters,* vol. 82, no. 1-2, pp. 123-129, 2002.

[88] B. J. Lindberg, K. Hamrin, G. Johansson, U. Gelius, C. Nordling and K. Siegbahn, "Molecular Spectroscopy by Means of ESCA II. Sulfur compounds. Correlation of electron binding energy with structure," *Phys. Scripta 1,* vol. 286, 1970.

[89] C. D. Wagner and J. A. Taylor, "Contributions to screening in the solid state by electron systems of remote atoms: Effects to photoelectron and Auger transitions," *J. Electron Spectrosc. Relat. Phenom.,* vol. 28, p. 211, 1982.

[90] M. D. Antonik, J. E. Schneider, E. L. Wittman, K. Snow, J. F. Vetelino and R. J. Lad, "Microstructural effects in WO3 gas sensing films," *Thin Solid Films,* vol. 256, no. 1-2, pp. 247-252, 1995.

[91] X. Niu, W. Du and W. Du, "Preparation, characterization and gas-sensing properties of rare earth mixed oxides," *Sensors and Actuators B: Chemical,* vol. 99, p. 399–404, 2004.

[92] C. Liewhiran, N. Tamaekong, A. Wisitsora and S. Phanichphant, "The Monitoring of H2S and SO2 Noxious Gases from Industrial Environment with Sensors Based on Flame-spray-made SnO2 Nanoparticles," *Engineering Journal,* vol. 16, no. 3, pp. 123-134, 2012.

[93] C. V. Gopal, S. V. Reddy, S. V. Manorama and V. J. Rao, "Preparation and Characterization of Ferrites as Gas Sensor Materials," *Journal of Material Science Letter,* vol. 19, no. 9, pp. 775-778, 200.

[94] G. N. Chaudhari, M. A. Alvi, H. G. Wankhadea, A. B. Bodade and S. V. Manorama, "Nanocrystalline chemically modified CdIn2O4 thick films for H2S gas sensor," *Thin Solid Films,* vol. 520, no. 11, p. 4057–4062, 2012.

[95] S. V. Jagtab, V. Kadu A, V. S. Sangawar, s. V. Manorama and G. N. Chaudhari, "H2S sensing characteristics of La0.7Pb0.3Fe0.4Ni0.6O3 based nanocrystalline thick film gas sensor," *Sensors and Actuators B: Chemical,* vol. 131, no. 1, pp. 290-294, 2008.

[96] U. Kersen and L. Holappa, "Surface Characterization and H2S sensing potential of iron molybdate particles produced by supercritical solvothermal method and subsequent oxidation," *Appl. Phys. A ,* vol. 85, pp. 431-436, 2006.

[97] E. P. Schneeberg, "Sulfur Fugacity Measurements with the Electrochemical Cell AgAgIAg (sub 2+x) S,f s," *Economic Geology,* vol. 68, pp. 507-517, 1973.

[98] J. Vangrunderbeek, F. Vandecruys and R. V. Kumar, "Sensing Mechanism of high temperature hydrogen sulphide sensor based on sodium ß-alumina," *Sensors and Actuators B : Chemical,* vol. 56, pp. 129-135, 1999.

[99] R. S. Falconer, I. F. Vetelino, D. J. Smith and M. J. Osborn, "An Activation Process for Increased Sensitivity of a SAW Gas Microsensor," *IEEE Ultrasonic Sympososium,* 1990.

[100] W. Luo, q. Fu, D. Zhou, J. Deng, H. Liu and G. Yan, "A surface acoustic wave H2S gas sensor employing nanocrystalline SnO2 thin film," *Sensors and Actuators B: Chemical,* vol. 176, pp. 746-752, 2013.

[101] G. N. Chaudhari, D. R. Bambole, A. B. Bodade and P. R. Padole, "Characterization of nanosized TiO2 H2S gas sensor," *J. Mater. Sci. ,* vol. 41, pp. 4860-4864, 2006.

[102] M. D. Shirsat, M. A. Bangar, M. A. Deshusses, N. V. Myung and A. Mulchandani, "Polyaniline nanowires-gold nanoparticles hybrid network based chemiresistive hydrogen sulfide sensor," *Appl. Phys. Lett.,* vol. 94, 2009.

[103] E. Çiftyürek, K. Sabolsky and E. M. Sabolsky, "Platinum thin film electrodes for high-temperature chemical sensor applications," *Sensors and Actuators B:Chemical,* vol. 181, p. 702–714, 2013.

[104] J. K. Howard and K. V. Srikrishnan, "Thin film capacitor with a dual bottom electrode structure". U.S. Patent, Patent 4 423 087, 27 Dec. 1981.

[105] S. L. Firebaugh, K. F. Jensen and M. A. Schmidt, "Investigation of high-temperature degradation of platinum thin films with an in situ resistance measurement apparatus," *J. of Microelectromech. Syst., .,* vol. 7, pp. 128-135, 1998.

[106] D. Briand, F. Beaudin, N. F. de Rooij, R. Desplats and P. Perdu, "Failure analysis of micro-heating elements suspended on thin membranes," *Microelectron. Reliab.,* vol. 45, no. 9-11, p. 1786–1789, 2005.

[107] M. P. da Cunha, T. Moonlight, R. Lad, D. Frankel and G. Bernhardt, "High Temperature Sensing Technology for Applications Up To 1000°C," in *IEEE SENSORS Conference*, Lecce, 2008.

[108] S. V. Patel, M. di Battista, J. L. Gland and J. W. Schwank, "Survivability of a silicon-based microelectronic gas-detector structure for high-temperature flow applications," *Sensors and Actuators B: Chemical,* vol. 37, pp. 27-35, 1996.

[109] S. P. Beeby, A. Blackburn and N. M. White, *J. Micromech. Microeng.,* vol. 9, pp. 218-229, 1999.

[110] M. N. Hamidon, V. Skarda, N. M. White, F. Krispel, P. Krempl, M. Binhack and W. Buff, "Fabrication of high temperature surface acoustic wave devices for sensor applications," *Sens. Actuator A: Phys,* Vols. 123-124, pp. 403-407, Sep. 2005.

[111] C. Y. Lee, S. J. Lee and C. L. Hsieh, *Proc. NEMS-IEEE International Conference,* pp. 434-437, 2007.

[112] S. A. Wright and Y. B. Gianchandani, "Discharge-Based Pressure Sensors for High Temperature Applications Using Three-Dimensional and Planar Microstructures," *in Proc. MEMS, IEEE 20th International Conference,* pp. 115-118, 2007.

[113] L. C. Martin and R. Holanda, "NASA Technical Memorandum, NASA-IM- 106714," National Aeronautics and Space Administration, Cleveland, Ohio, 1994.

[114] J. D. Wrbanek and K. H. Laster, "NASA/TM-2005-213433,," National Aeronautics and Space Administration, Cleveland, Ohio, Jan. 2005.

[115] D. Bonfert, H. Gieser, K. Bock, P. Svasta and C. Ionescu, *In Proc. SIITME-IEEE,* pp. 83-88, 2010.

[116] J.-F. Lei, C. L. Martin and H. A. Will, "NASA Technical Memorandum 107418," National Aeronautics and Space Administration, Lewis Res. Center, Cleveland, Ohio, Jun. 1997.

[117] R. C. Budhani, S. Prakash, H. J. Doerr and R. F. Bunshah, "Thin-film temperature sensors for gas turbine engines: Problems and prospects," *J. Vac. Sci. Technol., A 4,* vol. 6, p. 3023–3024, Nov/Dec. 1986.

[118] M. Sreemany, S. Sen, M. Sreemany and S. Sen, *Appl. Surf. Sci,* vol. 253, pp. 2739-2746, Dec. 2006.

[119] C. C. Mardare, E. Joanni, A. Mardera, J. R. Fernandes, C. M. De sa and P. B. Traves, "Effects of adhesion layer (Ti or Zr) and Pt deposition temperature on the properties of PZT thin films deposited by RF magnetron sputtering," *Appl. Surf. Sci,* vol. 243, pp. 113-124, 2005.

[120] J. Puigcorbe, D. Vogel, B. Michel, A. Vila, I. Gracia, C. Cane and J. R. Morante, "Thermal and mechanical analysis of micromachined gas sensors," *J. Micromech. Microeng.,* vol. 13, pp. 548-556, 2003.

[121] H. Esch, G. Huyberechts, G. Maes, J. manca and W. d. Ceuninck, "The stability of Pt heater and temperature sensing elements for silicon integrated tin oxide gas sensors," *Sensors and Actuators B: Chemical,* vol. 65, pp. 190-192, 2000.

[122] H. C. Kim, N. D. Theodore and T. L. Alford, "Comparison of texture evolution in Ag and

Ag(Al) alloy thin films on amorphous SiO2," *J. Appl. Phys,* pp. 5180-5188, May 2004.

[123] K. Sieraddzki, K. Bailey and T. L. Alford, "Agglomeration and percolation conductivity," *Appl. Phys. Lett.,* vol. 79, pp. 3401-3403, Nov. 2001..

[124] D. J. Srolovitz and M. G. Goldiner, "The thermodynamics and kinetics of film agglomeration," *JOM-J. Miner. Met. Mater. Soc,* vol. 47, pp. 31-36, Mar. 1995.

[125] K. Sreenivas, I. Reaney, T. Maeder, N. Setter, C. Jagadish and R. G. Elliman, "Investigation of Pt/Ti bilayer metallization on silicon for ferroelectric thin film integration," *J. Appl. Phys.,* vol. 75, pp. 232-239, 1993.

[126] K. F. McCarty, J. C. Hamilton, Y. S. Angela, S. R. Stumpf, J. Figuera, K. Thurmer, F. Jones, A. K. Schmid, A. A. Talin and N. C. bartelt, "How metal films de-wet substrates—identifying the kinetic pathways and energetic driving forces," *New J. Phys.,* vol. 11, April 2009.

[127] C. Dong, J. W. Ha, H. M. Kim, S. D. Lee, Y. D. Park, J. H. Woo and E. J. Yoon, "Method for depositing a platinum layer on a silicon wafer". U.S. Patent Patent 5.736,422, 7 April 1998.

[128] R. M. Tiggelaar, R. P. Sanders, A. W. Groenland and J. G. Gardeniers, "Stability of thin platinum films implemented in high-temperature microdevices," *Sens. Actuator A: Physical,* vol. 152, pp. 39-47, May 2009.

[129] T. Maeder, L. Sagalowicz and P. Muralt, "Stabilized Platinum Electrodes for Ferroelectric Film Deposition using Ti, Ta and Zr Adhesion Layers," *Jpn. J. Appl. Phys.,* vol. 37, pp. 2007-2012, 1998.

[130] M. P. d. Cunha, T. Moonlight, R. Lad, G. Bernhardt and D. J. Frankel, "“Enabling Very High Temperature Acoustic Wave Devices for Sensor & Frequency Control Applications," in *IEEE*

2007 International Ultrasonics Symposium Proceedings, New YorK, 2007.

[131] G. L. Selman, J. G. Day and A. A. Bourne, "Dispersion Strengthened Platinum," *Platinum Metals Rev,* vol. 18, pp. 46-57, 1974.

[132] R. B. McGrath and G. C. Badcock, "New Dispersion Strengthened Platinum Alloy," *Platinum Metals Rev.,* vol. 31, no. 1, pp. 8-11, 1987.

[133] D. J. Frankel, G. P. Bernhardt, B. T. Sturtevant, T. Moonlight, M. P. Cunha and R. J. Lad, "Stable Electrodes and Ultrathin Passivation Coatings for High Temperature Sensors in Harsh Environments," in *Sensors, IEEE*, Lecce, 2008.

[134] L. J. van der Pauw, "A method of measuring specific resistivity and Hall effect of discs of arbitrary shape," Philip Res. Rep. , Eindhoven, Netherlands, Feb. 1958..

[135] T. C. Tsone and J. Drobek, "Diffusion in Thin Film Ti–Au, Ti–Pd, and Ti–Pt Couples," *J. Vac. Sci. Technol.,* vol. 9, pp. 271-275, July 1972.

[136] J. F. Moulder, W. F. Stickle, P. E. Sobol and K. D. Bomben, Handbook of X-Ray Photoelectron Spectroscopy, Chigasaki, Japan: ULVAC-PHI. Inc., 1992-1995.

[137] P. Ficalora, J. Wu, V. Srikrishnan and J. Carloni, "Department of the Navy," Naval Ordnance Systems Command, Washington, D.C., Mar. 1971..

[138] L. M. Pecora and P. J. Ficalora, "Some bulk and thin film properties of ZrPt3 and HfPt3," *J. Elec. Mat.,,* vol. 6, pp. 531-540, Feb. 1977..

[139] J. Puigcorbe, D. Vogel, B. Michael, A. Vila, I. Gracia, C. Cane and J. R. Morante, "High temperature degradation of Pt/Ti electrodes in micro-hotplate gas sensors," *Journal of*

Micromechanics and Microengineering, p. 119–124, 13 (June) (2003.

[140] J. Courbat, D. Briand and N. F. de Rooij, "Reliability improvement of suspended platinum-based micro-heating elements," *Sensors and Actuators A: Physical,* vol. 142, pp. 284-291, 2008.

[141] T. Ryll, H. Galinski, L. Schlagenhauf, P. Elser, J. L. Rupp, A. Bieberle-Hutter and L. J. Gauckler, "Thin-Film Electrodes: Microscopic and Nanoscopic Three-Phase-Boundaries of Platinum Thin Film Electrodes on YSZ Electrolyte," *Advanced Functional materials,* vol. 21, no. 3, pp. 565-572, 2011.

[142] M. Ohring, Material Science of Thin Films, ISBN: 978-0-12-524975-1,.

[143] G. K. Wertheim and D. N. Buchanan, "Charge transfer in intermetallics: HfPt3," *Physical Review B,* vol. 40, p. 5319–5324., 1989.

[144] U. Seidel and H. Schmid, "Effect of high temperature annealing on the electrical performance of titanium/platinum thin film," *Thin Solid Films,* vol. 516, pp. 898-906, 2008.

[145] W. l. Worrell and P. J. Meschter, *Met. Trans. A.,* vol. 8A, pp. 503-509, Mar. 1977.

[146] P. M. Georgea, M. D. Alvey and R. F. Fisher, *J. Vac. Sci. Technol. A,* vol. 10, pp. 2253-2260, 1991.

[147] J. M. Lee, S. K. Hong, C. S. Hwang and H. J. Kim, *Journal of the Korean Physical Society,* vol. 33, pp. 148-151, 1998.

[148] J. B. Goodenough, "Perspective on Engineering Transition-Metal Oxides," *Chemistry of Materials,* vol. 26, pp. 820-829, 20136.

[149] R. Marschall and L. Wang, "Non-metal doping of transition metal oxides for visible-light photocatalysis," *Catalysis Today,* vol. 225, pp. 111-135, 2014.

[150] H. Zhenk, J. Z. Ou, M. S. Strona, R. B. Kaner, A. Mitchell and K. Kalantar-zadeh, "Nanostructured Tungsten Oxide properties, Synthesis, and Applications," *Advanced Functional Materials,* vol. 21, pp. 2175-2196, 2011.

[151] W. T. Yao and S. H. Yu, "Recent advances in hydrothermal synthesis of low dimensional nanoarchitectures," *International Journal of Nanotechnology,* vol. 4, no. 1/2, pp. 129-141, 2007.

[152] S. Walia, S. Balendhran, H. NILI, S. Zhuiykov, G. Rosengarten, Q. H. Wang, M. Bhaskaran, S. Sriram, M. S. Strano and K. Kalantar-zadeh, "Transition metal oxides – Thermoelectric," *Progress in Materials Science,* vol. 58, pp. 1443-1489, 2013.

[153] X. Li, Z. Song and B. Qu, "Shape-controlled electrochemical synthesis of SrWO4 crystallites and their optical properties," *Ceramics International,* vol. 40, no. 1, pp. 1205-1208, 2013.

[154] A. Kuzmin, A. Kalinko and R. A. Evarestov, "First principles LCAO study of phonons in NiWO4," *Central Europian Journal of Physics,* vol. 9, no. 2, pp. 502-509, 2011.

[155] G. S. Rohrer, Structure and Bonding in Crysatlline Materials, Cambridge: Cambridge University Press, 2004.

[156] B. Y. Zhang, A. W. Holzwarth and R. T. Williams, "Electronic band structures of the scheelite materials CaMoO4, CaWO4, PbMoO4, and PbWO4," *PHYSICAL REVIEW B ,* vol. 50, no. 20, pp. 57-69, 1998.

[157] B. J. Macey, "Crystal Chemistry of MTO4 Compounds with the Zircon, Scheelite and

Monazite Structure Types," Virginia Polytechnique Institute and State University, Blacksburg, 1995.

[158] Z. Shan, Y. Wang, D. H. and F. Huang, "Structure-dependent photocatalytic activities of MWO4 (M = Ca, Sr, Ba)," *Journal of Molecular Catalysis A: Chemical,* vol. 302, no. 1-3, pp. 54-58, 2009.

[159] F. a. Rabuffetti, S. P. Culver, L. Suescun and R. L. Brutchey, "Structural Disorder in AMoO4 (A = Ca, Sr, Ba) Scheelite Nanocrystals," *Inorganic Chemistry,* vol. 53, pp. 1056-1061, 2013.

[160] W. Oganowskil, J. Hanuza, B. Jezowska, J. Trzebiatowska and J. Wrzyszcz, "Physicochemical properties and structure of MgMoO4-MoO3 catalysis," *Journal of catalysis,* vol. 39, no. 2, pp. 161-172, 1975.

[161] Y. Hu, Z. Gao, W. Sun and X. Liu, "Anisotropic surface energies and adsorption behaviors of scheelite crystal," *Colloids and Surfaces A: Physicochemical and Engineering Aspects,* vol. 415, pp. 439-448, 2012.

[162] E. Alan and N. Greenwood, Chemistry of the Elements, 2nd ed., Butterworth-Heinemann, 1997.

[163] D. A. Spasskii, V. N. Kolobanov, V. V. Mikhailin, L. Y. Berezovskaya, L. I. Ivleva and I. S. Voronina, "Luminescence peculiarities and optical properties of MgMoO4 and MgMoO4:Yb crystals," *Optics and Spectroscopy,* vol. 106, no. 4, pp. 556-563, 2009 , V. N. Kolobanov, V. V. Mikhaĭlin, L. Yu. Berezovskaya, L. I. Ivleva, I. S. Voronina.

[164] L. Zhou, W. wang, H. Xu and S. Sun, "Template-Free Fabrication of CdMoO4 Hollow Spheres and Their Morphology-Dependent Photocatalytic Property," *Crystal Growth Design,* vol. 8, no. 10, pp. 3595-3601, 2008.

[165] L. Tang, J. Zhai, H. Zhang and X. Yao, "Microwave dielectric properties of tunable Ba0.5Sr0.5TiO3 and scheelite AMoO4 (A = Ba, Sr) composite ceramics," *Journal of Alloys and Compounds,* vol. 551, pp. 556-561, 2013.

[166] E. M. Sabolsky, P. Gansor, E. Çiftyürek, K. Sabolsky, C. Xu and J. W. Zondlo, "In-situ formation of a solid oxide fuel cell cermet anode by NiWO4 reduction," *Journal of Power Sources,* 2013.

[167] M. V. Reddy, G. V. Subba and B. R. Chowdari, "Metal Oxides and Oxysalts as Anode Materials for Li Ion Batteries," *Chemical Rewievs,* vol. 113, no. 7, p. 5364–5457, 2013.

[168] E. Lassner, W. D. Schuber, E. Lüderitz and H. U. Wolf, "Tungsten, Tungsten Alloys, and Tungsten Compounds," *Ullmann's Encyclopedia of Industrial Chemistry,* 2000.

[169] S. P. Culver, F. A. Rabuffetti, S. Zhou, M. Mecklenburg, Y. Song, B. C. Melot and R. L. Brutchey, "Low-Temperature Synthesis of AMoO4 (A = Ca, Sr, Ba) Scheelite Nanocrystals," *Chemistry of Materials ,* vol. 25, p. 4129−4134, 2013.

[170] C. L. Wu, C. K. Waang, C. Lin, S. Wang and J. Huang, "Electrochromic properties of nanostructured tungsten oxide films prepared by surfactant-assisted sol–gel process," *Surface & Coatings Technology,* vol. 231, pp. 403-407, 2013.

[171] C. S. Cundy and P. A. Cox, "The hydrothermal synthesis of zeolites: Precursors, intermediates and reaction mechanism," *Microporous and Mesoporous Materials,* vol. 82, no. 1-2, pp. 1-78, 2005.

[172] K. Byrappa and M. Yoshimura, Handbook of Hydrothermal Technology, A Technology for Crystal Growth and Materials Processing, Norwich, NY: William Andrew Publishing, 2001.

[173] W. J. Dawson and R. J. Riman, "Hydrothermal synthesis of advanced ceramic powders," *Advances in Science and Technology,* vol. 45, pp. 184-193, 2006.

[174] L. I. Stepenova, L. S. Ivashkevich and G. A. Branitskii, "Hydrothermal Synthesis of Tungsten and Molybdenum Mixed Oxides," *Russian Journal of Inorganic Chemistry,* vol. 54, no. 10, pp. 1553-1558, 2009.

[175] X. Xing, Q. Xing, R. Yu, J. Meng, J. Chen and G. Liu, "Hydrothermal synthesis of ZrW2O8 nanorods," *Physica B,* vol. 371, pp. 81-82, 2006.

[176] S. Wannapop, T. Thongtem and S. Thongtem, "Characterization of Donut-Like SrMoO4 Produced by Microwave Hydrothermal Process," National Reserach Univeristy of Thailand, 2012.

[177] C. J. Mao, J. Geng, X. C. Wu and J. J. Zhu, "Selective synthesis and luminescence properties of self assembled SrMoO4 superstructures via a facile sonochemical Route," *J. Phys. Chem.,* vol. 114, pp. 1982-1988, 2010.

[178] Y. Mi, Z. Huang, F. Hu, Y. Li and J. Jiang, "Room-Temperature Synthesis and Luminescent Properties of Single-Crystalline SrMoO4 Nanoplates," *J. Phys. Chem.,* vol. 113, pp. 20795-20799, 2009.

[179] J. P. Liu, X. T. Huang, Y. Y. Li and Z. K. Li, *J. Mater.Chem.,* vol. 17, p. 2754, 2007.

[180] X. tang, X. Zhu, J. Dai, J. Yang, L. Hu, L. Chen, X. Zhu, X. Li, H. Jiang, R. Zhang and Y. Sun, "c-Axis oriented SrMoO4 thin films by chemical solution deposition: Self-assembled orientation, grain growth and photoluminescence properties," *Acta Materialia,* vol. 65, pp. 287-294, 2014.

[181] Z. Liu, M. Miyauchi, T. Yamazaki and Y. Shen, "Facile synthesis and NO2 gas sensing of tungsten oxide nanorods assembled microspheres," *Sensors and Actuators B: Chemical,* vol. 140, pp. 514-519, 2009.

[182] M. Amberg, J. R. Gunter and H. Schmalle, "Preparation, crystal structure, and luminescence of magnesium molybdate and tungstate monohydrates, MgMoO4 · H2O and MgWO4 · H2O," *Journal of Solid State Chemistry,* vol. 77, pp. 162-169, 1988.

[183] J. Liu, X. Huang, Y. Li and Z. Li, "A general route to thickness-tunable multilayered sheets of sheelite-type metal molybdate and their self-assembled films," *Journal of Materials Chemistry,* vol. 17, pp. 2754-2758, 2007.

[184] J. C. Sczancoski, L. S. Cavalcante, M. R. Joya, J. A. Varela, P. S. Pizani and E. Longo, "SrMoO4 powders processed in microwave-hydrothermal: Synthesis, characterization and optical properties," *Chemical Engineering Journal,* vol. 140, pp. 632-637, 2008.

[185] W. Hirschwald, in *In Current Topics In Material Science*, vol. 7, 1981, p. 143.

[186] Y. Abraham, N. A. Holzwarth, R. T. Williams and G. E. Matthews, "The electronic structure of oxygen related defects in PbWo4 and CaMoO4 crystals," *Physical Review B,* vol. 64, 2001.

[187] T. Esaka, "Oxide Ion Conduction via Interstitial Sites in the Substituted Scheelite and Spinel-type Oxides," *Electrochemistry,* vol. 78, no. 1, pp. 16-22, 2009.

[188] W. Chen, C. S. Chen and L. Winnubst, "Ta doped SrCo0.8Fe0.2O3-x membrans Phase Stability and oxygen permeation in CO2 atmosphere," *Solid state Ionics,* vol. 196, pp. 30-33, 2011.

[189] Q. Zeng, Y. B. Zuo, C. G. Fan and C. S. Chen, "CO2 tolerant oxygen seperation membrans targeting Co2 capture application," *Journal of membrane Science,* vol. 335, pp. 140-144, 2009.

[190] L. Z. Pei, Y. K. Xie, Y. Q. Pei and C. Z. Yuan, "Synthesis and formation process of zirconium dioxide," *Material Science Poland,* vol. 31, no. 2, pp. 186-192, 2013.

[191] T. Kinoshita, M. Senna, Y. Doshida and H. Kishi, "Synthesis of size controlled phase pure KNbO3 fine particles via a solid-state route from a core-shell structured precursor," *Ceramics International,* vol. 38, pp. 1897-1904, 2012.

[192] A. L. Tiano, C. Koenigsmann, A. C. Santullia and S. S. Wong, "Solution-based synthetic strategies for one-dimensional metal-containing nanostructures," *Chemical Communications,* vol. 46, pp. 8093-8130, 2010.

[193] E. Formo, M. S. Yavuz, E. P. Lee, L. Lane and Y. Xia, "Functionalization of electrospun ceramic nanofibre membranes with noble-metal nanostructures for catalytic applications," *Journal of Materials Chemistry,* vol. 19, no. 23, pp. 3878-3882, 2009.

[194] H. Ogihara, M. Sadakane, Y. Nodasaka and W. Ueda, "Shape-controlled synthesis of ZrO2, Al2O3, and SiO2 nanotubes using carbon nanofibers as templates," *Chemistry of Materials,* vol. 18, no. 21, 2006.

[195] A. A. Al-Ghamdi, F. Al-Hazmi, F. Alnowaiser, R. M. Al-Tuwirqi, A. A. Al-Ghamdi, A. O. Alhartomy, F. El-Tantawy and F. Yakuphanoglu, "A new facile synthesis of ultra fine magnesium oxide nanowires and optical properties," *Journal of J Electroceramics,* vol. 29, pp. 198-203, 2012.

[196] A. Kato, S. Oishi, T. Shishido, M. Yamazaki and S. Lida, "Evaluation of stoichiometric rare-

earth molybdate and tungstate compounds as laser materials," *Journal of Physics and Chemistry of Solids,* vol. 66, no. 11, pp. 2079-2081, 2005.

[197] R. Adhikari, G. Gyawali, H. T. Kim, T. Sekino and W. S. Lee, "Synthesis of Er3þ loaded barium molybdate nanoparticles: A new approach for harvesting solar energy," *Materials Letters,* vol. 91, p. 294–297, 2013.

[198] J. Kubo and W. Ueda, "Catalytic behavior of AMoOx (A = Ba, Sr) in oxidation of 2-propanol," *Materials Research Bulletin,* vol. 44, no. 4, pp. 906-912, 2009.

[199] D. Logvinovich, R. Aguiar, R. Robert, M. Trottmann, S. G. Ebbinghaus, A. Reller and A. Weidenkaff, "Synthesis, Mo-valence state, thermal stability and thermoelectric properties of SrMoO3-xNx (x>1) oxynitride perovskites," *Journal of Solid State Chemistry,* vol. 180, pp. 2649-2654, 2007.

[200] H. H. Wang, D. F. Cui, Y. L. Zhou, Z. H. Chen, F. Chen , T. Zhao, H. B. Lu, G. Z. Yang, M. C. Xu, Y. C. Lan, X. L. Chen, H. J. Qian and F. Q. Liu, "Growth and characterization of SrMoO3 thin films," *Journal of Crystal Growth,* vol. 226, pp. 261-266, 2001.

[201] D. Y. Kim, J. S. Kim, B. H. Park, J. K. Lee, J. H. Kim, H. J. Lee, J. Chang, H. J. Kim, I. Kim and Y. D. Park, "SrFeO3 nanoparticles dispersed SrMoO4 insulating thin films deposited from Sr2FeMoO5 target in oxygen atmosphere," *Applied Physics Letters,* vol. 84, no. 24, 2004.

[202] I. Nagai, S. Ikeda, N. Shirakawa, R. Iwasaki, H. Nishimura and M. Kosaka, "Highest conductivity oxide SrMoO 3 grown by a floating-zone method under ultralow oxygen partial pressure," *Applied Physics Letters,* vol. 87, 2005.

[203] J. A. Rodriguez, "Electronic and chemical properties of mixed-metal oxides: basic principles for the design of DeNOx and DeSOx catalysts," *Catalysis Today,* vol. 85, no. 2-4, pp. 177-

192, 2003.

[204] D. L. Perry, Handbook of Inorganic Compounds, CRC Press, 2010.

[205] N. W. Hurst, S. J. Gentry and A. Jones, "Temperature Programmed Rduction," *Catalysis Reviews,* vol. 24, no. 2, pp. 233-309, 1982.

[206] J. Guo, L. Zhou, H. Wang, T. Shao, Z. M. Qi and X. Yao, "Infrared spectra, Raman spectra, microwave dielectric properties and simulation for effective permittivity of temperature stable ceramics AMoO4–TiO2 (A = Ca, Sr)," *Dalton Transcations,* vol. 42, pp. 1483-1491, 2012.

[207] A. P. Marques, M. T. Tanaka, E. Longo, E. R. Leite and L. L. Rosa, "The Role of the Eu3+ Concentration on the SrMoO4:Eu Phosphor Properties: Synthesis, Characterization and Photophysical Studies," *Journal of Fluorescence,* vol. 21, no. 3, pp. 893-899, 2011.

[208] s. Vidya, A. John, S. Solomon and J. K. Thomas, "Optical and dielectric properties of SrMoO4 powders prepared by the combustion synthesis method," *Advances in Materials Research,* vol. 1, no. 3, pp. 191-204, 2012.

[209] M. Karlsteen, A. Baranzahi, L. A. Spetz, M. Willander and I. Lundstrom, "Electrical Properties of Inhomogeneous SiC MIS Structures," *Join'hal of Electronic Materials,* vol. 24, no. 7, 1995.

[210] U. Hoefer, J. Frank and M. Fleischer, "High temperature Ga2O3 gas sensor and SnO2 gas sensors a comparison," *Sensors and Actuators B: Chemical,* vol. 78, pp. 6-11, 2001.

[211] D. Errandonea, L. Gracia, R. Lacomba-Perales, A. Polian and J. C. Chervin, "Compression of scheelite-type SrMoO4 under quasi-hydrostatic conditions: Redefining the high-pressure

structural sequence," *Journal of Applied Physics,* vol. 113, 2013.

[212] R. Merkle and J. Maier, "How Is Oxygen Incorporated into Oxides? A Comprehensive Kinetic Study of a Simple Solid-State Reaction with SrTiO3 as a Model Material," *Angew Chem Int. Ed. Engl.,* vol. 47, no. 21, pp. 3874-3894, 2008.

[213] E. T. Turkdogan and B. B. Rice, *Metallurgical Transaction,* vol. 5, 1974.

[214] S. J. Lee, S. Y. Jung, S. C. Lee, H. K. Jun, C. K. Ryu and J. C. Kim, "SO2 Removal and Generation of MgO-Based Sorbents Promoted with Titanium Oxide," *Ind. Eng. Chem. Res. ,* vol. 48, pp. 2691-2696, 2009.

[215] S. Sugiyama, T. Miyamoto, H. Hayashi and J. B. Moffat, *Bull. Chem. Soc. Jpn. ,* vol. 69, p. 235, 1996.

[216] J. A. Schwarz, C. I. Contescu and K. Puty, Dekker Encyclopedia of Nanoscience and Nanotechnology.

[217] M. Kandavel and S. Ramaprabhu, "Hydrogen storage properties of Mg-based composites prepared by reaction ball milling,," *J. Phys.: Condens. Matter,* 2006.

[218] R. A. Cox-Galhotra and S. McIntosh, "Unreliability of simultaneously determining kchem and Dchem via conductivity relaxation for surface-modified La0.6Sr0.4Co0.2Fe0.8O3−δ," *Solid State Ionics,* vol. 181, pp. 1429-1436, 2010.

[219] P. Hjalmarsson, M. Søgaard and M. Mogansen, "Oxygen transport properties of dense and porous (La0.8Sr0.2)0.99Co0.8Ni0.2O3-δ," *Solid State Ionics,* vol. 180, pp. 1290-1297, 2009.

[220] Y. Li, "Oxygen Transport Kinetics in Solid Oxide Fuel Cell Cathode," West Virginia

University, Morgantown, 2012.

[221] J. W. Gardner, "A non linear Diffusion Model of Electrical Conductance in Semiconducting Gas Sensors," *Sensors and Actuators B: Chemical,* pp. 166-170, 1990.

[222] G. J. Cadena, J. Riu and F. X. Rius, "Gas sensors based on nanostructured materials," *The Analyst,* Vols. i-SECTION: CRITICAL REVIEW, no. 132, pp. 1083-1099, 2007.

[223] G. Korotcenkov, B. K. Cho, L. Gulina and V. Tolstoy, "Ozone sensors based on SnO2 films modified by SnO2–Au nanocomposites synthesized by the SILD method," *Sensors and Actuators B: Chemical,* vol. 138, no. 2, pp. 512-517, 2009.

[224] M. A. Andio, "Sensor Array Devices Utilizing Nano-structured Metal-oxides for Hazardous Gas Detection," The Ohio State University , Ohio , 2012.

[225] K. Arshak and I. Gaidan, "Development of an array of polymer/MnO2/Fe2O3 mixtures for use in gas sensing applications," *Sensors and Actuators B : Chemical,* vol. 118, pp. 386-392, 2006.

[226] J. Li, Y. Lu, L. Ye, L. Delzeit and M. Meyyappan, "A Gas Sensor Array Using Carbon Nanotubes and Microfabrication Technology," *Electrochemical and Solid-State Letters,* vol. 8, no. 11, pp. H100-H102, 2005.

[227] S. Semancik, R. E. Cavicchi, M. C. Wheeler, J. E. Tiffany, G. E. Poirier, R. M. Walton, J. S. Suehle, B. Panchapakesan and D. L. DeVoe, "Microhotplate platforms for chemical sensor research," *Sensors and Actuators B: Chemical,* vol. 77, no. 1-2, p. 579–591, 2001.

[228] "ASM Handbook," *Mechanical grinding and Polishing,* pp. 257-280, 2004.

[229] W. Chen, C.-s. Chwn and L. Winnubst, "Ta-doped SrCo0.8Fe0.2O3-δ membranes: Phase stability and oxygen permeation in CO2 atmosphere," *Solid State Ionics,* vol. 196, pp. 30-33, 2011.